THE MINISTRY OF SCIENCE AND HIGHER EDUCATION OF THE RUSSIAN FEDERATION

ST. PETERSBURG STATE POLYTECHNICAL UNIVERSITY JOURNAL

Physics and Mathematics

VOLUME 12, No.4, 2019

Peter the Great St. Petersburg
Polytechnic University
2019

**ST. PETERSBURG STATE POLYTECHNICAL UNIVERSITY JOURNAL.
PHYSICS AND MATHEMATICS**

The journal is included in the List of leading peer-reviewed scientific journals and other editions to publish major findings of theses for the research degrees of Doctor of Sciences and Candidate of Sciences.

The publications are presented in the VINITI RAS Abstract Journal and Ulrich's Periodical Directory International Database.

The journal is published since 2008 as part of the periodical edition 'Nauchno-tekhnicheskie vedomosti SPb-GPU'.

The journal is registered with the Federal Service for Supervision in the Sphere of Telecom, Information Technologies and Mass Communications (ROSKOMNADZOR). Certificate ПИ № ФС77-52144 issued December 11, 2012.

The journal is distributed through the CIS countries catalogue, the «Press of Russia» joint catalogue and the «Press by subscription» Internet catalogue. The subscription index is **71823.**

The journal is in the **Web of Science** (Emerging Sources Citation Index) and the **Russian Science Citation Index** (RSCI) databases.

Address: 195251 Politekhnicheskaya St. 29, St. Petersburg, Russia.

Phone: (812) 294-22-85.

http://ntv.spbstu.ru/physics

Contents

Condensed matter physics

Simulation of physical processes

Experimental technique and devices

Physical electronics

Theoretical physics

Mechanics

CONDENSED MATTER PHYSICS

DOI: 10.18721/JPM.12401
UDC 541.64: 678

THERMOACTIVATIONAL SPECTROSCOPY OF THE HIGH IMPACT POLYSTYRENE BASED COMPOSITE FILMS

A.A. Guliakova[1], *Yu.A. Gorokhovatsky*[1], *M.F. Galikhanov*[2], *P. Frübing*[3]

[1]Herzen State Pedagogical University of Russia, St. Petersburg, Russian Federation;

[2]Kazan National Research Technological University,

Kazan, Republic of Tatarstan, Russian Federation;

[3]University of Potsdam, Potsdam, Germany

The relaxation processes in the high impact polystyrene (HIPS) films filled with 2, 4, 6 vol.% of titanium dioxide (TiO_2) of the rutile modification have been studied using the thermally stimulated depolarization current (TSDC) technique. Three relaxation processes were observed in the composite HIPS films. The first one (α-relaxation peak) appeared at about 93 °C and represented the glass transition. The second peak ρ was a high-temperature part of the first one and overlapped it. The ρ peak was caused by the release and subsequent motion of excess charges deposited during the electret preparation or the polarization process. The third peak appeared at about 150 °C and occurred only in the spectra of the composite films. The overlapping peaks were separated by the thermal cleaning technique. The subsequent application of the numerical methods (the Tikhonov regularization technique) allowed to determine the activation energy of the second process and to compare the obtained value with the corresponding data on the dielectric relaxation.

Keywords: thermoactivational spectroscopy, high impact polystyrene, titanium dioxide

Citation: Guliakova A.A., Gorokhovatsky Yu.A., Galikhanov M.F., Frьbing P., Thermoactivational spectroscopy of the high impact polystyrene based composite films, St. Petersburg Polytechnical State University Journal. Physics and Mathematics. 12 (4) (2019) 4–11. DOI: 10.18721/JPM.12401

ТЕРМОАКТИВАЦИОННАЯ СПЕКТРОСКОПИЯ КОМПОЗИТНЫХ ПОЛИМЕРНЫХ ПЛЕНОК НА ОСНОВЕ УДАРОПРОЧНОГО ПОЛИСТИРОЛА

А.А. Гулякова[1], *Ю.А. Гороховатский*[1], *М.Ф. Галиханов*[2], *П. Фрюбинг*[3]

[1] Российский государственный педагогический университет им. А.И. Герцена, Санкт-Петербург, Российская Федерация;

[2] Казанский национальный исследовательский технологический университет,

г. Казань, Республика Татарстан, Российская Федерация;

[3] Потсдамский университет, г. Потсдам, Германия

С помощью метода токов термостимулированной деполяризации (ТСД) исследованы релаксационные процессы в пленках ударопрочного полистирола (УПС) без наполнителя и с различным содержанием диоксида титана TiO_2 (2, 4, 6 об.%). На кривых тока ТСД, полученных для композитных пленок, обнаружено три пика. Первый (α-релаксация) возникает при температуре около 93 °C и соответствует переходу вещества из стеклообразного состояния в высокоэластическое. Второй (ρ-пик) появляется как высокотемпературное плечо α-пика и соответствует процессу высвобождения и

движения избыточных носителей заряда. Наличие третьего пика при температуре около 150 °C характерно только для композитных пленок УПС. Разделение перекрывающихся α- и ρ-пиков проведено методом частичной термоочистки. Последующее применение регуляризующих алгоритмов Тихонова позволило определить энергию активации второго процесса и сравнить полученное значение с результатом, полученным методом диэлектрической спектроскопии.

Ключевые слова: термоактивационная спектроскопия, ударопрочный полистирол, диоксид титана

Ссылка при цитировании: Гулякова А.А., Гороховатский Ю.А., Галиханов М.Ф., Фрюбинг П. Термоактивационная спектроскопия композитных полимерных пленок на основе ударопрочного полистирола // Научно-технические ведомости СПбГПУ. Физико-математические науки. 2019. Т. 12. № 4. С. 9–16. DOI: 10.18721/JPM.12401

Introduction

The thermally stimulated depolarisation current (TSDC) technique is commonly used for the investigation of charge carrier relaxation in dielectrics. It is widely applied as a complement to the frequency domain and the time domain dielectric spectroscopy.

The basic experiment includes two main steps:

the first one is that sample material is polarised in a D.C. field E_p for a time t_p at a high temperature T_p. At this temperature particular dipolar units or charge carriers are free to move, the former orient in the field and the latter drive towards the electrodes or internal boundaries in heterogeneous materials forming a space charge;

the second one is that the sample is shorted at a low temperature. Under this condition the relaxation times of the species of interest are much longer than the measuring time, and finally it is linearly heated, while the depolarisation current is recorded. During the heating, oriented dipolar units turn back to their equilibrium position and accumulated charge carriers return to a uniform distribution. Due to thermal stimulation, the polarisation decay is more and more accelerated [1 – 3].

A TSDC measurement corresponds to a loss-versus-temperature measurement at a very low equivalent frequency of 10^{-2} to 10^{-3} Hz [4]. Here, an attempt is made for a more detailed description of the relaxation processes in the composite high-impact polystyrene films by means of the thermally stimulated depolarization currents (TSDC) method.

Experimental details

High impact polystyrene (HIPS-0801, GOST (Russian State Standard) 28250-89E) without filler as well as composite HIPS films were used in the present study. HIPS contains 4 to 6 % butadiene rubber, the butadiene rubber particles form agglomerates from 0.1 to 1 μm in size, and they are embedded in the polystyrene matrix [5].

Titanium dioxide (TiO_2) powder of the rutile modification (R-01, GOST 9808-65, specific surface area is 15 m^2/g, particle size is from 0.1 to 0.8 μm) was used as a filler. Mixing of HIPS and TiO_2 was performed using a laboratory rolling mill under heating at (175 ± 5) °C for 3 min. Films of pure HIPS as well as HIPS with TiO_2 contents of 2, 4, 6 vol.% were manufactured by melt pressing according to GOST 12019-66 at (170 ± 5) °C for 5 min. The films with thicknesses ranging from 350 to 450 μm were investigated.

For electrical measurements, circular aluminum electrodes (12 mm in diameter, about 50 nm thick) were evaporated onto both sides of the films.

Thermally stimulated depolarization currents (TSDC) were recorded with a Keithley model 5617 electrometer and the Novocontrol QUATRO cryosystem. TSDC measurements (heating rate was 2.8 K/min) were performed after poling with the field $E_p = 0.67 \cdot 10^6$ V/m at T_p = 110 °C for t_p = 10 min, subsequent rapid cooling to room temperature and short-circuiting.

Experimental results

TSDC thermograms of unfilled HIPS and HIPS with 2 and 4 vol.% TiO_2 are shown in Fig. 1. Three peaks could be observed for composite HIPS films. The α peak appears at about 93 °C and denotes the glass transition [6, 7]. The second ρ peak is caused by the release and subsequent motion of excess charges deposited during the electret preparation or the polarization process [3]. It is a high-temperature

part of the α peak and overlaps it. The third peak appeared at about 150 °C occurs only in the composite films.

In order to separate the α and ρ peaks the peak-cleaning technique was applied according to the following procedure: after passing the first peak the heating was interrupted. Then, the sample was quickly cooled down followed by a second heating where only the response of the second process was expected [6].

The results of the peak-cleaning technique applied to the pure HIPS samples with an attempt to separate the α relaxation (related to the glass transition) and the higher-temperature relaxation process is shown in Fig. 2 (blue curves). Fig. 3 represents the results for composite HIPS films with 4 vol.% of TiO_2.

Current, 10^{-13} A Temperature, °C

After the ρ peak was separated from the α peak, the activation energy E_a for the ρ peak was determined using the Tikhonov regularization technique [8, 9]. For this purpose, the TSDC measurement was performed for two different heating rates under identical conditions for composite HIPS films with 4 vol.% of TiO_2 (Fig. 4).

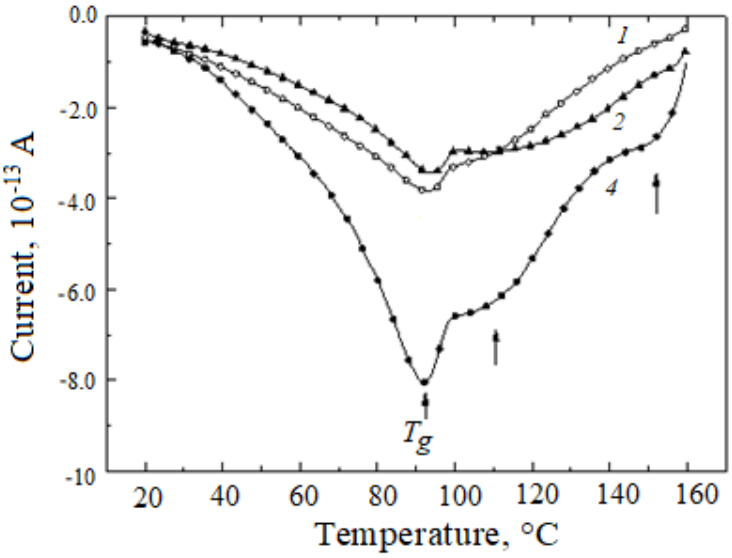

Fig. 1. Thermally stimulated depolarization current (TSDC) spectra of pure HIPS (*1*) as well as of the HIPS with 2 (*2*) and 4 (*4*) vol.% of TiO_2 (heating rate β = 3 K/min); T_g is the glass transition temperature

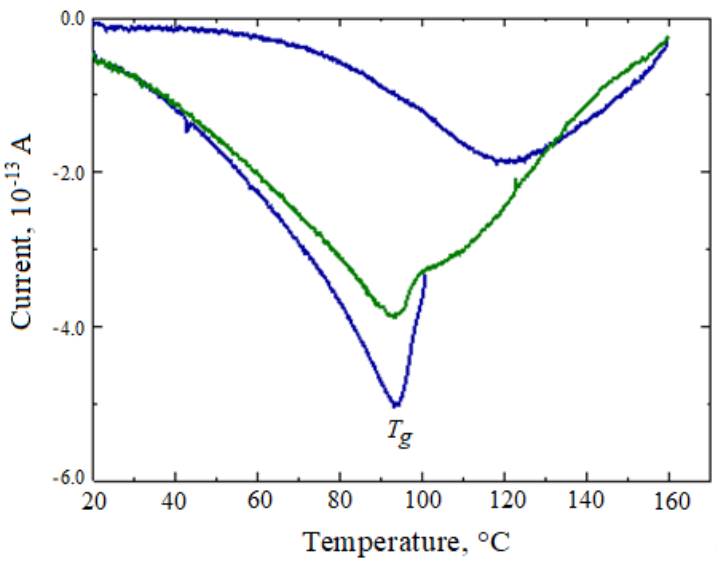

Fig. 2. The peak cleaning technique (blue curves) applied to the pure HIPS samples (heating rate β = 3 K/min) and shown together with the initial TSDC spectrum (a green curve)

This method allows one to obtain information about values of the activation energy E_a and the effective frequency factor ω_e. The energy distribution $G(E)$ was calculated from the current density $J(T)$. The determination of the distribution function $G(E)$ using the experimental TSDC curves represents the ill-posed problem and could be solved by means of numerical calculations (here the Tikhonov regularization technique was used) [8, 9].

The effective frequency factor ω_e was varied until the peak positions of the energy distribution functions $G(E)$ coincide. This procedure was the criterion for the correct choice of the effective frequency factor ω_e. The calculated activation energy value yields $E_a = 1.10 \pm 0.05$ eV for the composite HIPS films with 4, 6 vol.% (Figs. 5 and 6). This value was in a good agreement with the activation energy calculated by means of the dielectric relaxation spectroscopy (DRS). At temperatures from 105 to 130 °C the activation energy of 1.1 eV was found [6, 10].

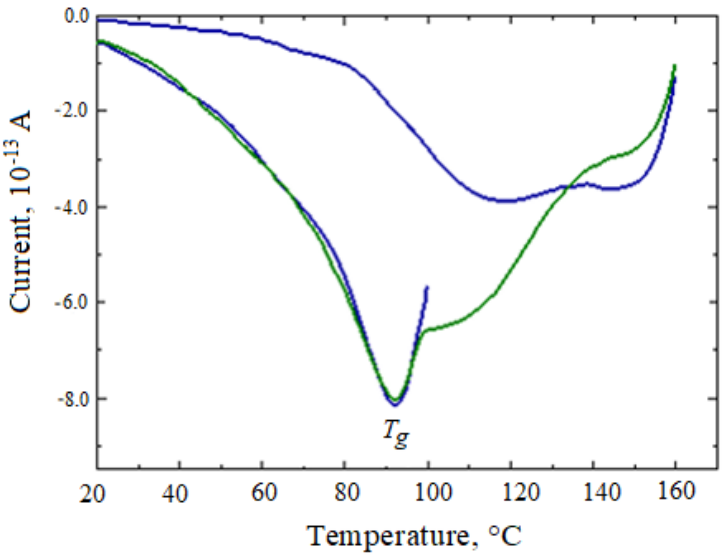

Fig. 3. The peak cleaning technique (blue curves) applied to the HIPS samples with 4 vol.% of TiO_2 (heating rate $\beta = 3$ K/min) and shown together with the initial TSDC spectra (a green curve)

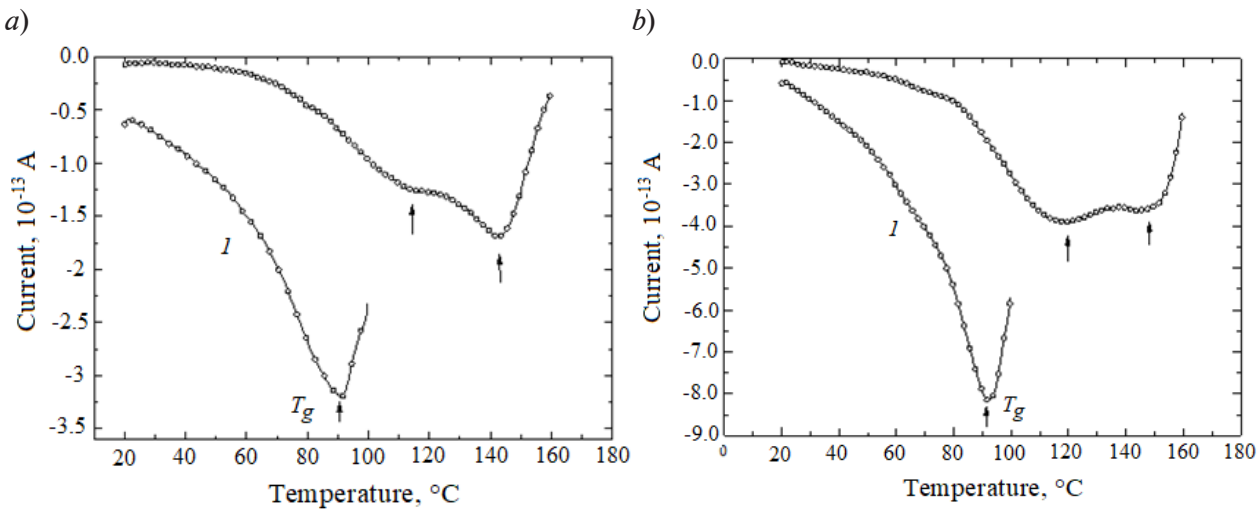

Fig. 4. Thermally stimulated depolarization current (TSDC) spectra (both curves) of the HIPS with 4 vol.% of TiO_2 for two different heating rates β: 1 K/min (*a*) and 3 K/min (*b*); curves *1* show the α peaks obtained before (see explanation in the text)

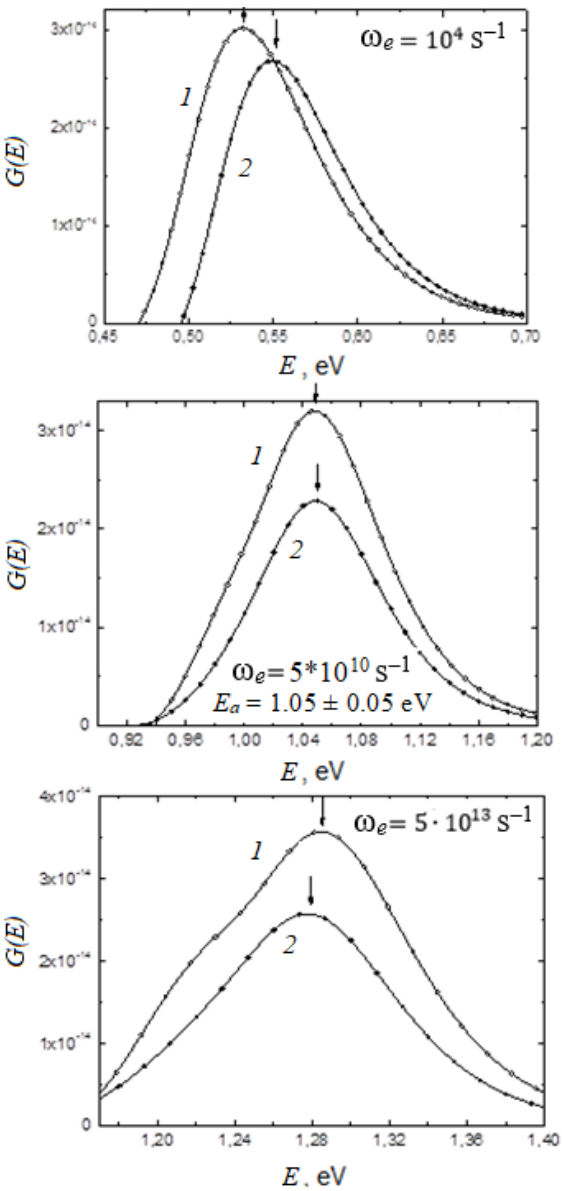

Fig. 5. Determination of the activation energy by means of the Tikhonov regularization technique for HIPS with 4 vol.% of TiO_2 using TSDC curves for 2 heating rates β, K/min: 1.0 (*1*) and 2.8 (*2*); ω_e is the obtained effective frequency factor; E_a = 1.05 ± 0.05 eV

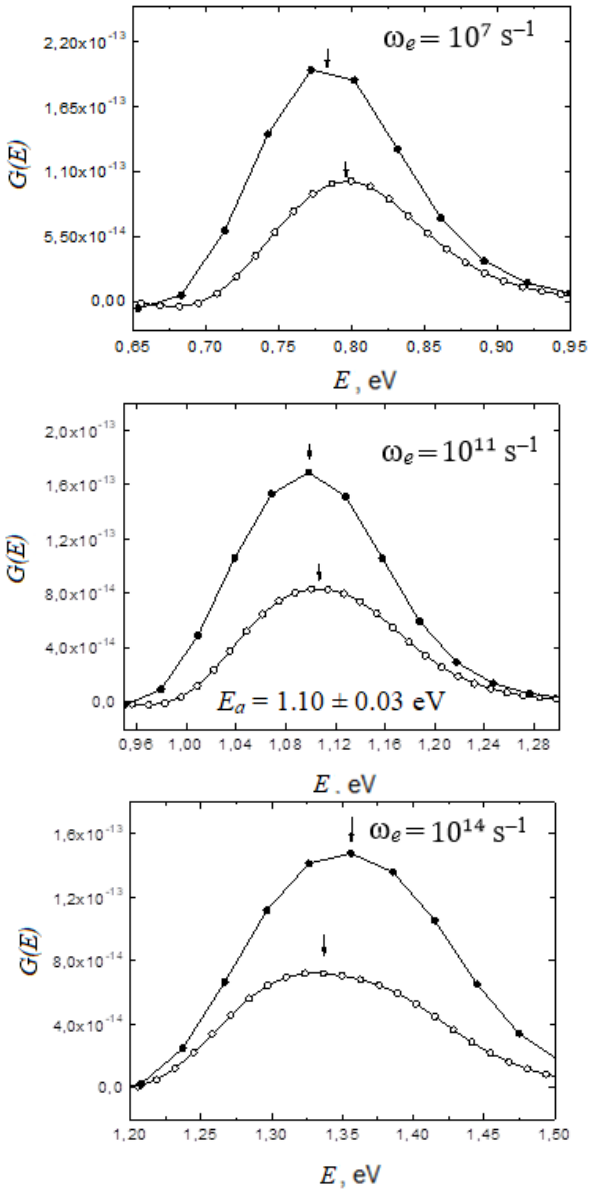

Fig. 6. The data similar to those shown in Fig. 5 but for HIPS with 6 vol.% of TiO_2; E_a = 1.10 ± 0.03 eV

Summary

Three relaxation peak processes have been observed in composite HIPS films with TiO_2 inclusions using the TSDC method:

(*i*) the α peak at about 93 °C which denotes the glass transition;

(*ii*) the ρ peak appears as the high-temperature side of the α peak;

(*iii*) the peak at about 150 °C for composite HIPS films.

The peak-cleaning technique allowed separating the two (α and ρ) superimposed peaks. The Tikhonov regularization technique was applied in order to determine the activation energy for the ρ peak:

$$E_a = 1.10 \pm 0.05 \text{ eV}$$

for HIPS films with 4 and 6 vol.% of TiO_2.

The process with the same activation energy of 1.1 eV has been determined by means of the dielectric relaxation spectroscopy (DRS).

REFERENCES

1. **Frübing P., Weingдrtner J., Brehmer L.,** Thermally stimulated depolarisation currents and pyroelectric measurements using the Novocontrol Cryosystem Quatro, Dielectrics Newsletter. Scientific Newsletter for Dielectric Spectroscopy. 1997. (November) (1997) 1–3.
2. **Teyssedre G., Mezghani S., Bernes A., Lacabanne C.,** Thermally stimulated currents of polymers, In: J.P. Runt, J.J. Fitzgerald (Eds.), Dielectric spectroscopy of polymeric materials, Fundamentals and Applications. Washington, DC: American Chemical Society (1997) 227–258.
3. **Vanderschueren J., Gasiot J.,** Field-induced thermally stimulated currents, In: Bгдunlich P. (Ed.), Thermally stimulated relaxation in solids, Part of the topics in Applied Physics book series, Vol. 37. Springer, Berlin, Heidelberg, New York (1979) 135–223.
4. **Van Turnhout J.,** Thermally stimulated discharge of electrets, In: G.M. Sessler (Ed.), Electrets, 2nd enlarged edition, Springer, Berlin, Heidelberg, New York, 1987.
5. **Kuboki T., Ben Yar P.-Y., Takahashi K., Shinmura T.,** Observation of "black" and "white" crazes in high-impact polystyrene under transmission electron microscopy, Macromolecules, 33 (15) (2000) 5740–5742.
6. **Gulyakova A., Gorokhovatsky Yu.A., Frübing P., Gerhard R.,** Relaxation processes determining the electret stability of high-impact polystyrene/titanium-dioxide composite films, IEEE Transactions on Dielectrics and Electrical Insulation. 24 (4) (2017) 2541–2548.
7. **Gulyakova A., Frübing P., Gorokhovatsky Yu.A.,** Relaxation processes and electret properties of titanium-dioxide filled high-impact polystyrene films, IEEE 14th Int'l. Sympos. Electrets (ISE 14), Montpellier, France (2011) 139–140, 2011.
8. **Samarskii A.A., Vabishchevich P.N.,** Numerical methods for solving inverse problems of mathematical physics, Walter de Gruyter, Berlin (2007) 161.
9. **Tikhonov A.N., Arsenin V.Y.,** Solutions of ill-posed problems, V.H. Winston & Sons, Washington D.C., 1977.
10. **Gulyakova A., Gorokhovatsky Yu.A., Frübing P.,** Dielectric relaxation spectroscopy in the high-impact polystyrene/titanium-dioxide composite films, St. Petersburg Polytechnical State University Journal. Physics and Mathematics. 12 (3) (2019) 9–16.

Received 26.09.2019, accepted 21.11.2019.

THE AUTHORS

GULIAKOVA Anna A.
Herzen State Pedagogical University of Russia
48 Moyka Emb., St. Petersburg, 191186, Russian Federation
a.guliakova@gmail.com

GOROKHOVATSKY Yuriy A.
Herzen State Pedagogical University of Russia
48 Moyka Emb., St.Petersburg, 191186, Russian Federation

yurig@fromru.com

GALIKHANOV Mansur F.
Kazan National Research Technological University
68, Karl Marx street, Kazan, 420015, Russian Federation
mgalikhanov@yandex.ru

FRЬBING Peter
University of Potsdam
9, Am Neuen Palais 10, Potsdam, 14469, Germany
frubing@uni-potsdam.de

СПИСОК ЛИТЕРАТУРЫ

1. **Frübing P., Weingдrtner J., Brehmer L.** Thermally stimulated depolarisation currents and pyroelectric measurements using the Novocontrol Cryosystem Quatro // Dielectrics Newsletter. Scientific Newsletter for Dielectric Spectroscopy. 1997. November. Pp. 1–3.

2. **Teyssèdre G., Mezghani S., Bernès A., Lacabanne C.** Thermally stimulated currents of polymers // Runt J.P., Fitzgerald J.J. (Eds.). Dielectric spectroscopy of polymeric materials. Fundamentals and Applications. Washington, DC: American Chemical Society, 1997. Pp. 227–258.

3. **Vanderschueren J., Gasiot J.** Field-induced thermally stimulated currents // Bгдunlich P. (Ed.). Thermally stimulated relaxation in solids. Part of the topics in Applied Physics book series. Vol. 37. Berlin, Heidelberg, New York: Springer, 1979. Pp. 135–223.

4. **Van Turnhout J.** Thermally stimulated discharge of polymer electrets: a study on nonisothermal dielectric relaxation phenomena // Sessler G.M. (Ed.). Electrets. 2nd enlarged edition. Berlin, Heidelberg, New York: Springer, 1987.

5. **Kuboki T., Ben Yar P.-Y., Takahashi K., Shinmura T.,** Observation of “black” and “white” crazes in high-impact polystyrene under transmission electron microscopy // Macromolecules. 2000. Vol. 33. No. 15. Pp. 5740–5742.

6. **Gulyakova A., Gorokhovatsky Yu.A., Frübing P., Gerhard R.** Relaxation processes determining the electret stability of high-impact polystyrene/titanium-dioxide composite films // IEEE Transactions on Dielectrics and Electrical Insulation. 2017. Vol. 24. No. 4. Pp. 2541– 2548.

7. **Gulyakova A., Frübing P., Gorokhovatsky Yu.A.** Relaxation processes and electret properties of titanium-dioxide filled high-impact polystyrene films// IEEE 14th Int’l. Sympos. Electrets (ISE 14). Montpellier, France. 2011. Pp. 139–140.

8. **Samarskii A.A., Vabishchevich P.N.,** Numerical methods for solving inverse problems of mathematical physics, Walter de Gruyter, Berlin (2007) 161.

9. **Tikhonov A.N., Arsenin V.Y.,** Solutions of ill-posed problems, V.H. Winston & Sons, Washington D.C., 1977.

10. **Gulyakova A., Gorokhovatsky Yu.A., Frübing P.,** Dielectric relaxation spectroscopy in the high-impact polystyrene/titanium-dioxide composite films, St. Petersburg Polytechnical State University Journal. Physics and Mathematics. 12 (3) (2019) 9–16.

Статья поступила в редакцию 26.09.2019, принята к публикации 21.11.2019.

СВЕДЕНИЯ ОБ АВТОРАХ

ГУЛЯКОВА Анна Александровна – *кандидат физико-математических наук, доцент кафедры общей и экспериментальной физики Российского государственного педагогического университета им. А.И. Герцена, Санкт-Петербург, Российская Федерация.*

191186, Российская Федерация, г. Санкт-Петербург, наб. р. Мойки, 48
a.guliakova@gmail.com

ГОРОХОВАТСКИЙ Юрий Андреевич – *доктор физико-математических наук, заведующий кафедрой общей и экспериментальной физики Российского государственного педагогического университета им. А.И. Герцена, Санкт-Петербург, Российская Федерация.*

191186, Российская Федерация, г. Санкт-Петербург, наб. р. Мойки, 48
gorokh-yu@yandex.ru

ГАЛИХАНОВ Мансур Флоридович – *кандидат технических наук, профессор кафедры технологии переработки полимеров и композиционных материалов Казанского национального исследовательского технологического университета, г. Казань, Республика Татарстан, Российская Федерация.*

420015, Российская Федерация, Республика Татарстан, г. Казань, ул. К. Маркса, 68
mgalikhanov@yandex.ru

ФРЮБИНГ Петер – *научный сотрудник группы прикладной физики конденсированного состояния Потсдамского университета, г. Потсдам, Германия.*
9, Am Neuen Palais 10, Potsdam, 14469, Germany
frubing@uni-potsdam.de

DOI: 10.18721/JPM.12402
УДК 537.226

FERROELECTRIC PROPERTIES OF COMPOSITES BASED ON DIISOPROPYLAMMONIUM BROMIDE AND LEAD TITANATE

S.V. Baryshnikov[1], *E.V. Stukova*[2], *T.A. Meredelina*[1]

[1]Blagoveshchensk State Pedagogical University, Blagoveshchensk, Russian Federation;

[2]Amur State University, Blagoveshchensk, Russian Federation

The results of a study of linear and nonlinear dielectric properties, as well as calorimetric measurements of a ferroelectric composite $(C_6H_{16}NBr)_{1-x}/(PbTiO_3)_x$ with a volume fraction x = 0.1, 0.2, 0.3 of lead titanate particles are presented. It has been shown that the addition of lead titanate particles to diisopropylammonium bromide leads to a change in the sequence of structural phase transitions in the diisopropylammonium bromide, an increase in the effective dielectric constant and tanδ values. In a temperature range of 150–138°C, there were two $C_6H_{16}NBr$ phases (ferroelectric $P2_1$ and nonferroelectric $P2_12_12_1$). The proportion among these phases depended on the fraction of lead titanate particles in the composite.

Keywords: ferroelectric, dielectric constant, composite, phase transition

Citation: Baryshnikov S.V., Stukova E.V., Meredelina T.A., Ferroelectric properties of composites based on diisopropylammonium bromide and lead titanate, St. Petersburg Polytechnical State University Journal. Physics and Mathematics. 12 (4) (2019) 12–19. DOI: 10.18721/JPM.12402

СЕГНЕТОЭЛЕКТРИЧЕСКИЕ СВОЙСТВА КОМПОЗИТОВ НА ОСНОВЕ БРОМИДА ДИИЗОПРОПИЛАММОНИЯ И ТИТАНАТА СВИНЦА

С.В. Барышников[1], *Е.В. Стукова*[2], *Т.А. Меределина*[1]

[1]Благовещенский государственный педагогический университет,

г. Благовещенск, Российская Федерация;

[2]Амурский государственный университет, г. Благовещенск, Российская Федерация

В работе приведены результаты исследований линейных и нелинейных диэлектрических свойств, а также калориметрических измерений сегнетоэлектрического композита $(C_6H_{16}NBr)_{1-x}/(PbTiO_3)_x$ с объемной долей частиц титаната свинца в композите x = 0,1; 0,2; 0,3. Показано, что добавка частиц титаната свинца к бромиду диизопропиламмония приводит к изменению последовательности структурных фазовых переходов в бромиде диизопропиламмония, увеличению эффективной диэлектрической проницаемости и значений tgδ композита. В температурном интервал138 – 150°С присутствуют две фазы $C_6H_{16}NBr$ (сегнетоэлектрическая $P2_1$ и несегнетоэлектрическая $P2_12_12_1$), соотношение между которыми зависит от доли частиц титаната свинца в композите.

Ключевые слова: сегнетоэлектрик, диэлектрическая проницаемость, композит, фазовый переход

Ссылка при цитировании: Барышников С.В., Стукова Е.В., Меределина Т.А. Сегнетоэлектрические свойства композитов на основе бромида диизопропиламмония и титаната свинца // Научно-технические ведомости СПбГПУ. Физико-математические науки. 2019. Т. 4 № .12. С. 17–24. DOI: 10.18721/JPM.12402

Introduction

Ferroelectric composites are the focus of considerable attention because heterogeneous materials can exhibit unusual properties compared to homogeneous substances. According to theoretical models, the ferroelectric state is induced by dipole-dipole interaction, allowing to explain the domain structure and the effect of polar impurities on the properties of crystals [1–3]. It was established in [2, 3] that introducing polar impurities to highly polarized matrices can cause the ferroelectric state to appear. In contrast to crystals and solid solutions, polar particles in composites are located at distances of the order of several microns; this brings the question how electrical interactions manifest in such structures.

A number of studies considered the mutual influence of components in ferroelectric composites (see, for example, [4–7] and the references therein), finding that such influence is possible for these objects. An extended temperature range was observed for the ferroelectric phase of potassium nitrate in composites such as $(KNO_3)_{1-x}/(BaTiO_3)_x$, $(KNO_3)_{1-x}/(KNbO_3)_x$ [4, 5]. The interaction effect led to extended temperature range of incommensurate phase of sodium nitrite in the $(NaNO_2)_{1-x}/(BaTiO_3)_x$ composite [6]. A substantial shift in the Curie temperature was found in [7] for the $AgNa(NO_2)_2$ compound in the $[AgNa(NO_2)_2]_{0.9}/[BaTiO_3]_{0.1}$ composite.

A series of organic compounds with a polar point group at room temperature and relatively high melting point (around 177°C) were discovered recently. Such ferroelectrics include diisopropylammonium chloride ($C_6H_{16}NCl$, DIPAC) with $P_s \approx 8.2$ μC/cm^2, $T_c = 167$°C [8]; diisopropylammonium bromide ($C_6H_{16}NBr$, DIPAB) with $P_s \approx 23$ μC/cm^2, $T_c = 153$°C [9]; diisopropylammonium iodide ($C_6H_{16}NI$, DIPAI) with $P_s \approx 5.17$ μC/cm^2, $T_c = 105$°C [10]. In particular, DIPAB has spontaneous polarization close to barium titanate, a high Curie temperature and exhibits good piezoelectric response. These properties make it an alternative to perovskite-like ferroelectrics and ferroelectric polymers.

This study considers the effect of $PbTiO_3$ particles on the temperatures of phase transitions and dielectric properties of the $(C_6H_{16}NBr)_{1-x}/(PbTiO_3)_x$ composite.

Samples and experimental procedure

The $C_6H_{16}NBr$ compound can exist at room temperature in two different polymorphic phases: with spatial symmetry $P2_1$ or $P2_12_12_1$, depending on the conditions in which it was obtained and the thermal history [10]. Monoclinic phase $P2_1$ is ferroelectric, transforming into the nonpolar phase $P2_1/m$ at temperatures above $T_c \approx 152$°C. The ferroelectric transition in $C_6H_{16}NBr$ is a transition of the first kind. The second phase, stable at room temperature, has orthorhombic symmetry with space group $P2_12_12_1$and is not an active ferroelectric phase; it is also transformed to nonpolar monoclinic phase $P2_1/m$ under heating, but with an intermediate polar structure with symmetry $P2_1$, existing in the range from about 148 to 152°C. The structure of $C_6H_{16}NBr$ changes immediately from $P2_1/m$ to $P2_1$ under cooling at 145°C, and the rhombic phase no longer forms.

Diisopropylammonium bromide in our study was obtained as a product of diisopropylammonium reacting with 48% aqueous solution of HBr (1:1 molar ratio) by the technique described in [11], followed by recrystallization from methanol at room temperature. The largest crystals were 2–3 mm in size.

Lead titanate has a tetragonal phase below 490°C, isomorphic to barium titanate, and is a ferroelectric of the first kind. Spontaneous polarization of $PbTiO_3$ at room temperature is approximately $P_s \approx 70$ μC/cm^2, which is significantly higher than for $BaTiO_3$ ($P_s \approx 22$ μC/cm^2). The values of the dielectric constant ε′ along the polar axis lie in the range of $(1.5–2.2)\cdot10^2$ for $PbTiO_3$ at room temperature, while it is $(2–4)\cdot10^3$ for $BaTiO_3$ [12].

We used composite samples of $(C_6H_{16}NBr)_{1-x}/(PbTiO_3)_x$, where x was 10, 20 and 30 wt%, for the experiments. The samples were thoroughly mixed and pressed under about 10^4 kg/cm^2. Average particle size in the composite ranged from 3 to 10 μm. The samples were disc-shaped, with a diameter 10 of mm and a thickness of 1.5 mm; silver electrodes were deposited on their surface.

The characteristics of the given samples were measured automatically using a computer, under heating and subsequent cooling at a rate of 1 deg/min in the temperature range 30–170°C.

The E7-25 immittance meter was used to determine the dielectric properties. The measurements were carried out at frequencies of 10^3, 10^4 и 10^5 Hz at a voltage of 0.7 V. The error in measuring the capacitance of the samples did not exceed 5%. Temperatures were recorded by a TS-6621 digital thermometer with a chromel-alumel thermocouple. The error in measuring the temperature did not exceed 0.1°C.

The setup for studying the nonlinear properties of the composites included an oscillator with a frequency of 2 kHz. The electric field applied to $C_6H_{16}NBr$ samples and $(C_6H_{16}NBr)_{1-x}/(PbTiO_3)_x$ composites was about 10 V/mm. The signal was taken from the resistor series-connected to the sample and fed to the spectrum analyzer. The coefficients of the second and third harmonics were found as the ratio of the harmonic amplitude to the capacitive component of the main signal:

$$\gamma_{2\omega} = u_{2\omega}/u_{\omega},\ \gamma_{3\omega} = u_{3\omega}/u_{\omega}.$$

The technique for nonlinear measurements is described in more detail in [13, 14].Differential scanning calorimetry with the thermoelectric power of about 5 μV was used to measure the heat capacity. The heating and cooling rate was 2 deg/min. The error in measuring the temperature did not exceed 0.1°C.

Experimental results and discussion

The dielectric properties obtained for polycrystalline samples of C 6 $H_{16}NBr$ and $(C_6H_{16}NBr)_{1-x}/(PbTiO_3)_x$ composites with x = 0.1; 0.2 and 0.3 are shown in Fig. 1.

It follows from the ε′(*T*) dependences that, firstly, the maximum dielectric constant ε'_{max} increases with increasing lead titanate content, and, secondly, an additional anomaly appears on the ε′(*T*) curve for the composites under cooling in the range from 133–137°C; this anomaly is absent in the respective curve for pure $C_6H_{16}NBr$.

The table shows the maximum values of the dielectric constant ε'_{max} of the composites with different volume fractions of lead titanate inclusions, at frequencies of 10^3 and 10^5 Hz.

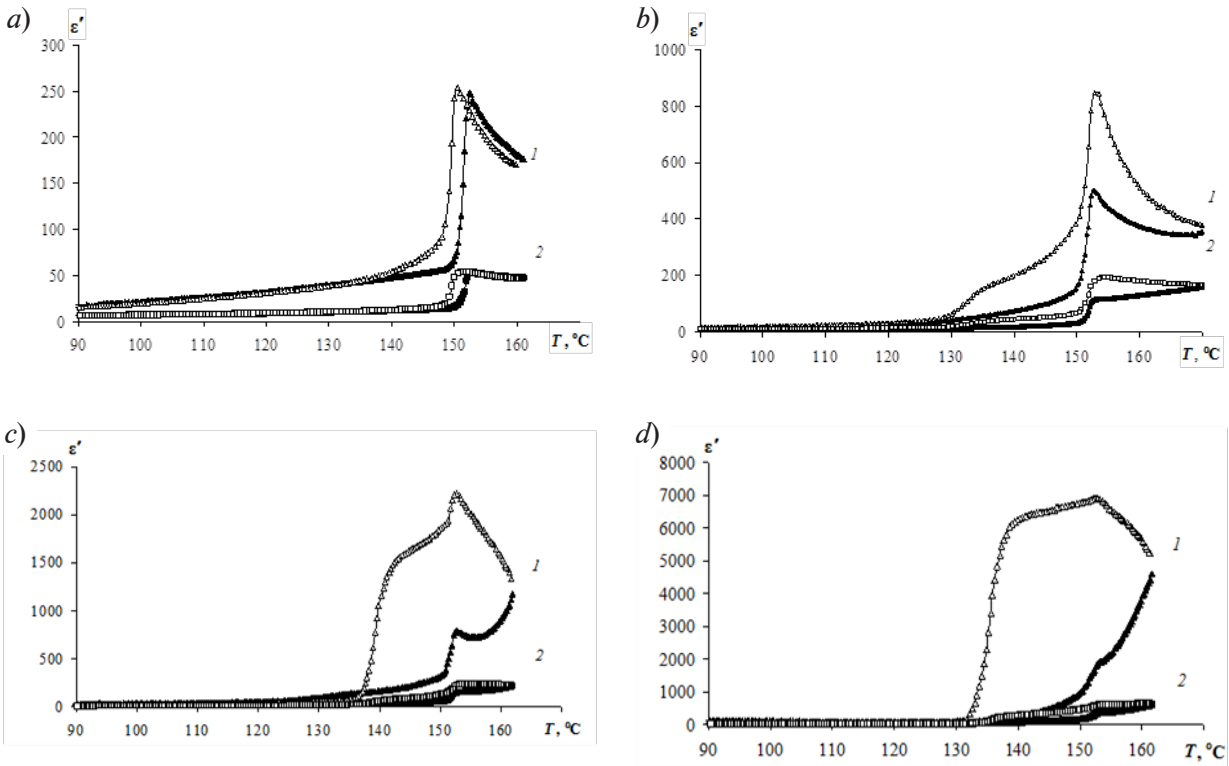

Fig. 1. Temperature evolution of dielectric constant in $(C_6H_{16}NBr)_{1-x}/(PbTiO_3)_x$ composite with x = 0 (*a*), 0.1 (*b*), 0.2 (*c*), 0.3 (*d*), obtained at frequencies of 1 kHz (*1*) and 100 kHz (*2*) under heating (dark symbols) and cooling (light markers)

Calorimetric studies (Fig. 2) indicate that adding lead titanate induces an additional phase transition under cooling. The nature of this phase transition is not yet fully understood. Signal intensity for this additional transition increases with an increase in the proportion of lead titanate particles in the composite.

Nonlinear dielectric spectroscopy (NDS) was used to analyze the structure forming between two phase transition under cooling. Fig. 3 shows the temperature dependences of the main signal at a frequency of 2 kHz and the coefficients of the second (4 kHz) and third (6 kHz) harmonics. It was confirmed in [13] for ferroelectrics with the phase transition of the first kind that nonlinear dielectric permittivities are expressed as

$$\varepsilon_2 = -\left(3\beta + 10\gamma P_s^2\right) P\chi_1^3; \qquad (1)$$

$$\varepsilon_3 = \left[-\beta - P_s^2\left(10\gamma + 18\beta^2\chi_1 + 120\chi_1\beta\gamma P_s^2\right) + \right. \\ \left. + 200\chi_1\gamma^2 P_s^4\right]\chi_1^4, \qquad (2)$$

where χ_1 is the electric susceptibility; P_s is the spontaneous polarization; β, γ are the Landau coefficients.

It can be seen from (2) that third-order permittivity is significantly increased in polar phase due to spontaneous polarization and has a minimum at the phase transition point. Thus, study of temperature dependence of third harmonic generation is a direct method for detecting the ferroelectric state.

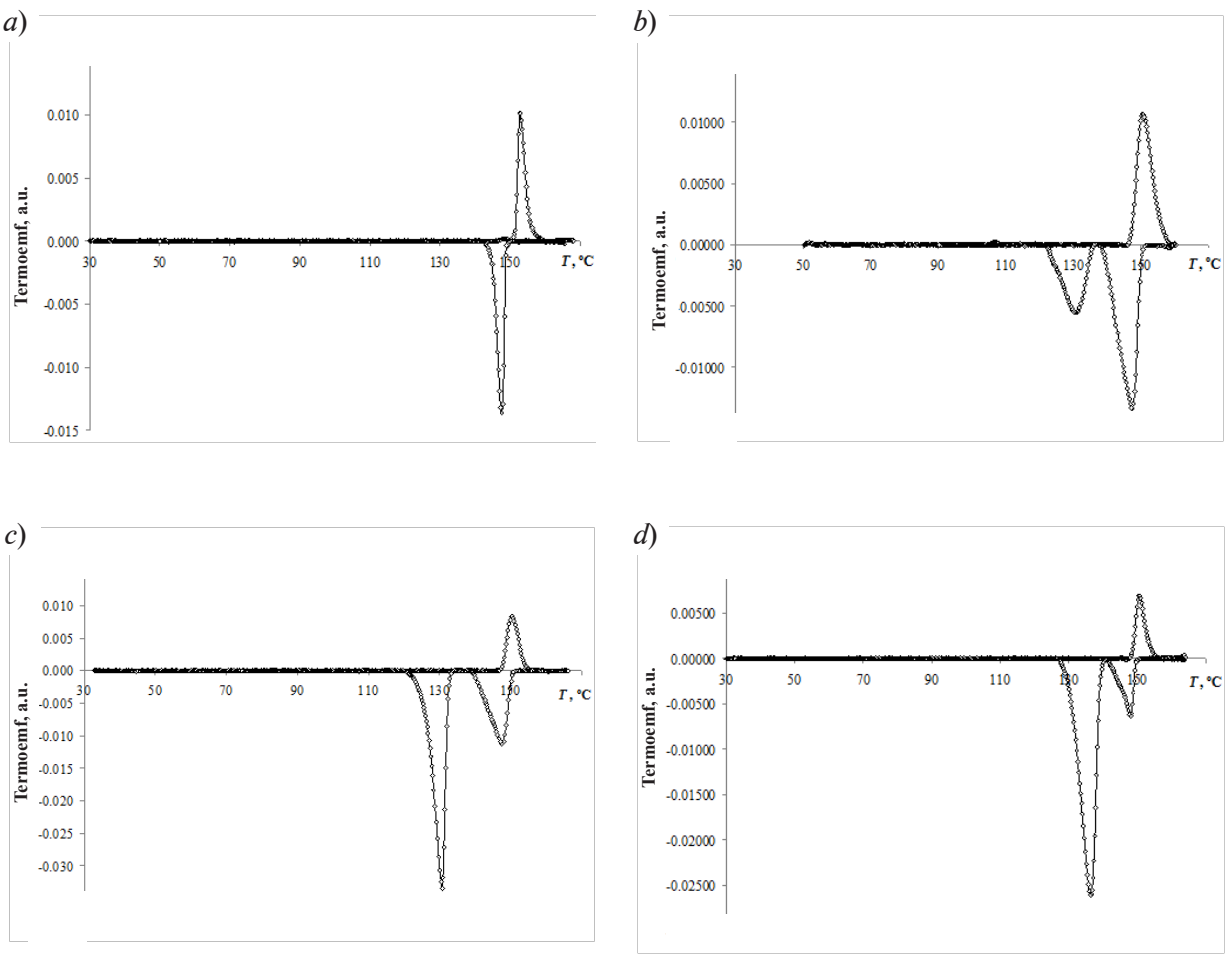

Fig. 2. Relative variation of thermopower for samples of $(C_6H_{16}NBr)_{1-x}/(PbTiO_3)_x$ composite with x = 0 (*a*), 0.1 (*b*), 0.2 (*c*), 0.3 mm (*d*);
positive signal corresponds to heating, negative signal to cooling

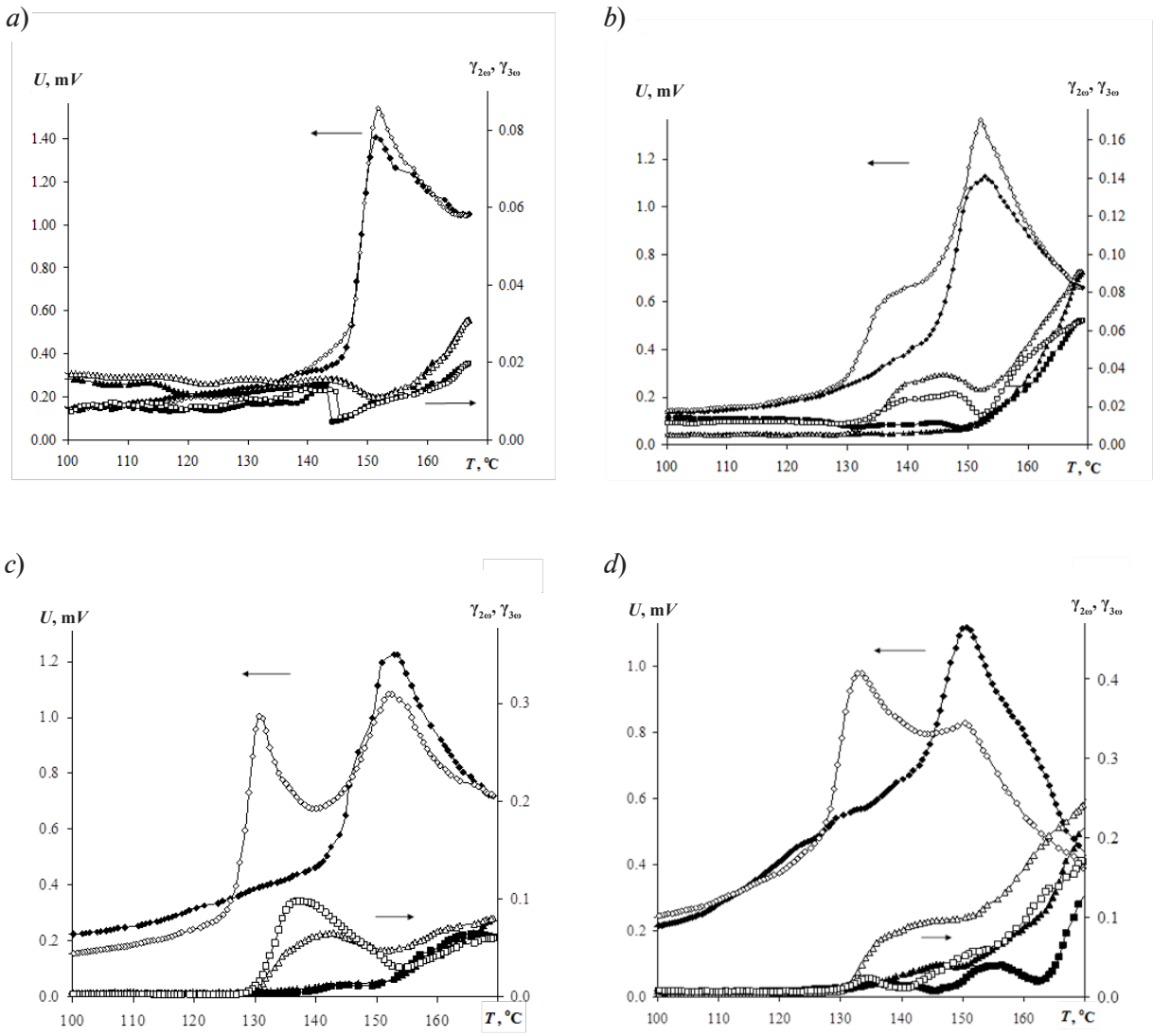

Fig. 3. Temperature dependences for capacitive component of signal at fundamental frequency ω (left axes) and coefficients of second ($\gamma_{2\omega}$) and third ($\gamma_{3\omega}$) harmonics (right axes) for $(C_6H_{16}NBr)_{1-x}/(PbTiO_3)_x$ composites with $x = 0$ (*a*), 0.1 (*b*), 0.2 (*c*), 0.3 (*d*); dark symbols correspond to heating, light symbols correspond to cooling

It follows from the curves in Fig. 3 that a certain anomaly is observed in the behavior of $\gamma_{3\omega}$ for pure $C_6H_{16}NBr$; it is approximately 1.5% near the ferroelectric phase transition. The value of $\gamma_{3\omega}$ for the $(C_6H_{16}NBr)_{0.9}/(PbTiO_3)_{0.1}$ composite under cooling in the temperature range of 133–137°C is about 2.5%, and that of $\gamma_{2\omega}$ is approximately 7.5% The value of $\gamma_{3\omega}$ for the $(C_6H_{16}NBr)_{0.8}/(PbTiO_3)_{0.2}$ composite is about 30% in the temperature range of 133–137 °C, and that of $\gamma_{2\omega}$ is approximately 5%. The value of $\gamma_{3\omega}$ decreases to about 5% with a further increase in lead titanate content in the $(C_6H_{16}NBr)_{0.7}/(PbTiO_3)_{0.3}$ composite, while $\gamma_{2\omega}$ increases to 20%.

The experimental data obtained by NDS confirm that two phases of the $C_6H_{16}NBr$ compound are found in the range of 137–133°C under cooling: ferroelectric $P2_1$ and nonferroelectric $P2_1/m$. The anomalies in phase transitions for the capacitive component of the signal through the sample are more pronounced in comparison with the $\varepsilon'(T)$ dependence, which is due to barrier transitions forming in the composite at the interfaces of $C_6H_{16}NBr$ and $PbTiO_3$ compounds, acting as capacities at low supplied voltages and making a noticeable contribution to the effective dielectric constant. This mechanism does not work with measuring voltages above 3 V, and the effective dielectric constant decreases.

Table

Variation in dielectric properties of composites with increasing lead titanate contents

Composition	ε'_{max}	$(tg\delta)_{max}$	ε'_{max}	$(tg\delta)_{max}$
	10^3 Hz		10^5 Hz	
$C_6H_{16}NBr$	~250	~8	~55	~0.9
$(C_6H_{16}NBr)_{0.9}/(PbTiO_3)_{0.1}$	~900	~30	~190	~2.6
$(C_6H_{16}NBr)_{0.8}/(PbTiO_3)_{0.2}$	~2200	~40	~230	~3.5
$(C_6H_{16}NBr)_{0.7}/(PbTiO_3)_{0.3}$	~7000	~90	~550	~6.0

Conclusion

Studying the dielectric properties of the $(C_6H_{16}NBr)_{1-x}/(PbTiO_3)$ composite, we have found that increasing x leads to smeared phase transitions and increased values of ε' and $tg\delta'$ (see Table). The increase in permeability may be due to barrier mechanisms, which is confirmed by the dependence of dielectric properties on the amplitude of the measuring field and its frequency. Analyzing the data obtained by calorimetric measurements, we have discovered an additional phase transition whose specific heat capacity increases with increasing x. The additional phase transition can be explained by electrical interaction of diisopropylammonium bromide and lead titanate particles in the composite.

The study was financially supported by the RFBR Grant no. 19-29-03004.

REFERENCES

1. **Isupov V.A.,** Nature of physical phenomena in ferroelectric relaxors, Physics of the Solid State. 45 (6) (2003) 1107–1111.

2. **Vugmeister B.E., Glinchuk M.D.,** Some features of the cooperative be-havior of paraelectric defects in strongly polarizable crystals, JETP. 52 (3) (1980) 482–484.

3. **Vugmeister B.E., Glinchuk M.D.,** Cooperative phenomena in crystals containing off-center ions-dipole glass and ferroelectricity, Physics-Uspekhi. 28 (7) (1985) 589–607.

4. **Stukova E.V., Baryshnikov S.V.,** Stabilization of the ferroelectric phase in $(KNO_3)_{1-x}$-$(BaTiO_3)_x$ composites, Inorganic Materials: Applied Research. 2 (5) (2011) 434–438.

5. **Stukova E.V., Baryshnikov S.V.,** Dielektricheskiye issledovaniya segnetoelektricheskikh kompozitov na osnove $(KNO_3)_{1-x}$-$(KNbO_3)_x$ [Dielectric studies of ferroelectric composites based on $(KNO_3)_{1-x}$-$(KNbO_3)_x$], Perspektivnyye Materialy. 13 (2011) 801–805.

6. **Baryshnikov S.V., Stukova E.V., Koroleva E.Yu.,** Dielectric properties of the ferroelectric composite $(NaNO_2)_{0.9}/(BaTiO_3)_{0.1}$, Composites: Part B. 66 (November) (2014) 190–193.

7. **Baryshnikov S., Milinskiy A., Stukova E.,** Dielectric properties of the ferroelectric composites $[AgNa(NO_2)_2]_{0.9}/[NaNO_2]_{0.1}$ and $[AgNa(NO_2)_2]_{0.9}/[BaTiO_3]_{0.1}$, Ferroelectrics. 536 (1) (2018) 91–98.

8. **Fu D.-W., Zhang W., Cai H.-L., et al.,** Diisopropylammonium chloride: a ferroelectric organic salt with a high phase transition temperature and practical utilization level of spontaneous polarization, Advanced Materials. 23 (47) (2011) 5658–5662.

9. **Fu D.-W., Cai H.-L., Liu Y., et al.,** Diisopropylammonium bromide is a high-temperature molecular ferroelectric crystal, Science. 339 (6118) (2013) 425–428.

10. **Jiang C., Tong W-Y., Lin H., et al.,** Effect of counter anions on ferroelectric properties of diisopropylammoniumcation based molecular crystals, Physica Status Solidi, A. 214 (6) (2017) 1700029.

11. **Piecha A., Gagor A., Jakubas R., Szklarz P.,** Room-temperature ferroelectricity in diisopropylammonium bromide, CrystEngComm. 15 (5) (2013) 940–944.

12. **Lines M.E., Glass A.M.,** Principles and application of ferroelectrics and related materials, Oxford, “Clarendon Press Oxford”, 1977.

13. **Ikeda S., Kominami H., Koyama K., Wada Y.J.,** Nonlinear dielectric constant and ferroelectric-to-paraelectric phase transition in copolymers of vinylidene fluoride and trifluoroethylene, Appl. Phys. 62 (8) (1987) 3339–3342.

14. **Baryshnikov S.V., Charnaya E.V., Milinskii A.Yu., et al.,** Dielectric and calorimetric investigations of KNO_3 in pores of nanoporous silica matrices MCM-41, Physics of the Solid State. 54 (3) (2012) 636–641.

Received 30.09.2019, accepted 22.10.2019.

THE AUTHORS

BARYSHNIKOV Sergey V.
Blagoveschensk State Pedagogical University
104 Lenina St., Blagoveshchensk, 675000, Russian Federation
svbar2003@list.ru

STUKOVA Elena V.
Amur State University
21 Ignatievskoe Ave., Blagoveshchensk, 675027, Russian Federation
lenast@bk.ru

MEREDELINA Tatiana A.
Blagoveshchensk State Pedagogical University
104 Lenina St., Blagoveshchensk, 675000, Russian Federation
biofirm@mail.ru

СПИСОК ЛИТЕРАТУРЫ

1. **Исупов В.А.** Природа физических явлений в сегнеторелаксорах // ФТТ. 2003. Т. 6 № .45. С. 1056–1060.

2. **Вугмейстер Б.Е., Глинчук М.Д.** Особенности кооперативного поведения параэлектрических дефектов в сильно поляризуемых кристаллах // ЖЭТФ. 1980. Т. 3 № .79. С. 952–947.

3. **Вугмейстер Б.Е., Глинчук М.Д.** Кооперативные явления в кристаллах с нецентральными ионами – дипольное стекло и сегнетоэлектричество // УФН. 1985. Т. 146. № 3. С. 459–491.

4. **Stukova E.V., Baryshnikov S.V.** Stabilization of the ferroelectric phase in $(KNO_3)_{1-x}$-$(BaTiO_3)_x$ composites // Inorganic Materials: Applied Research. 2011. Vol. 2. No. 5. Pp. 434–438.

5. **Стукова Е.В., Барышников С.В.** Диэлектрические исследования сегнетоэлектрических композитов на основе $(KNO_3)_{1-x}$-$(KNbO_3)_x$ // Перспективные материалы. 2011. № 13. С. 801–805.

6. **Baryshnikov S.V., Stukova E.V., Koroleva E.Yu.** Dielectric properties of the ferroelectric composite $(NaNO_2)_{0.9}/(BaTiO_3)_{0.1}$ // Composites. Part B. 2014. Vol. 66. November. Pp. 190–193.

7. **Baryshnikov S., Milinskiy A., Stukova E.** Dielectric properties of the ferroelectric composites $[AgNa(NO_2)_2]_{0.9}/[NaNO_2]_{0.1}$ and $[AgNa(NO_2)_2]_{0.9}/[BaTiO_3]_{0.1}$ // Ferroelectrics. 2018. Vol. 536. No. 1. Pp. 91–98.

8. **Fu D.-W., Zhang W., Cai H.-L., Ge J.-Z., Zhang Y., Xiong R.-G**. Diisopropylammonium chloride: a ferroelectric organic salt with a high phase transition temperature and practical utilization level of spontaneous polarization // Advanced Materials. 2011. Vol. 23. No. 47. Pp. 5658–5662.

9. **Fu D.-W., Cai H.-L., Liu Y., Ye Q., Zhang W., Zhang Y., Chen X.-Y., Giovannetti G., Capone M., Li J., Xiong R.-G.** Diisopropylammonium bromide is a high-temperature molecular ferroelectric crystal // Science. 2013. Vol. 339. No. 6118. Pp. 425–428.

10. **Jiang C., Tong W-Y., Lin H., Luo C., Peng H., Duan C.-G.** Effect of counter anions on ferroelectric properties of diisopropylammonium cation based molecular crystals // Physica Status Solidi. A. 2017. Vol. 214. No. 6. P. 1700029.

11. **Piecha A., Gagor A, Jakubas R., Szklarz P**. Room-temperature ferroelectricity in diisopropylammonium bromide // CrystEngComm. 2013. Vol. 15. No. 5. Pp. 940–944.

12. **Лайнс М., Гласс А.** Сегнетоэлектрики и родственные им материалы. Пер. с англ. под ред. Леманова В.В., Смоленского Г.А. М.: Мир, 1981. 736 с.

13. **Ikeda S., Kominami H., Koyama K., Wada Y.J.** Nonlinear dielectric constant and ferroelectric-to-paraelectric phase transition in copolymers of vinylidene fluoride and trifluoroethylene // Appl. Phys. 1987. Vol. 62. No. 8. Pp. 3339–3342.

14. **Барышников С.В., Чарная Е.В., Милинский А.Ю., Шацкая Ю.А., Michel D.** Диэлектрические и калориметрические исследования KNO_3 в порах наноразмерных силикатных матриц MCM-41 // ФТТ. 2012. Т. 54. № 3. С. 594–599.

Статья поступила в редакцию 30.09.2019. Принята 22.10.2019.

СВЕДЕНИЯ ОБ АВТОРАХ

БАРЫШНИКОВ Сергей Васильевич – *доктор физико-математических наук, профессор кафедры физического и математического образования Благовещенского государственного педагогического университета.*

675000, Российская Федерация, Амурская область, г. Благовещенск, ул. Ленина, 104
svbar2003@list.ru

СТУКОВА Елена Владимировна – *доктор физико-математических наук, профессор кафедры физики Амурского государственного университета.*

675027, Российская Федерация, Амурская область, г. Благовещенск, Игнатьевское шоссе, 21
lenast@bk.ru

МЕРЕДЕЛИНА Татьяна Александровна – *кандидат физико-математических наук, доцент кафедры физического и математического образования Благовещенского государственного педагогического университета.*

675000, Российская Федерация, Амурская область, г. Благовещенск, ул. Ленина, 104
biofirm@mail.ru

DOI: 10.18721/JPM.12403
УДК 53.093, 53.096, 57.031, 57.033, 57.038

DEHYDRATED FILMS OF PROTEIN SOLUTIONS: STRUCTURAL PROPERTIES

M.A. Baranov, E.N. Velichko, S.V. Rozov

Peter the Great St. Petersburg Polytechnic University, St. Petersburg, Russian Federation

In this paper, the formation of various characteristic dissipative structures in the films of aqueous and aqueous-salt solutions of albumin protein in dehydration processes is considered. It has been shown that a number of parameters for conducting experiments on solution dehydration affect the shape and spatial distribution of two-dimensional structural formations in films of protein solutions. A conclusion was drawn on the importance of the structural self-organization of films in the process of their dehydration.

Keywords: self-organization process, dissipative structure, protein film

Citation: Baranov M.A., Velichko E.N., Rozov S.V., Dehydrated films of protein solutions: structural properties, St. Petersburg Polytechnical State University Journal. Physics and Mathematics. 12 (4) (2019) 20–31. DOI: 10.18721/JPM.12403

СТРУКТУРНЫЕ СВОЙСТВА ДЕГИДРАТИРОВАННЫХ ПЛЕНОК БЕЛКОВЫХ РАСТВОРОВ

М.А. Баранов, Е.Н. Величко, С.В. Розов

Санкт-Петербургский политехнический университет Петра Великого,
Санкт-Петербург, Российская Федерация

В данной работе рассмотрено образование различных характерных диссипативных структур в пленках водного и водно-солевого растворов белка альбумина в процессах дегидратации. Показано, что условия проведения экспериментов по дегидратации растворов влияет на форму и пространственное распределение двумерных структурных образований в пленках растворов белков. Сделан вывод о значении структурной самоорганизации пленок в процессе их дегидратации.

Ключевые слова: процесс самоорганизации, диссипативная структура, белковая пленка

Ссылка при цитировании: Баранов М.А., Величко Е.Н., Розов С.В. Структурные свойства дегидратированных пленок белковых растворов // Научно-технические ведомости СПбГПУ. Физико-математические науки. 2019. Т. 12. № 4. С. 25–37. DOI: 10.18721/JPM.12403

Introduction

The properties of films formed upon dehydration of protein solutions or their fragments (peptides) are currently the focus of much attention. Such materials are used in physics, chemistry, biology, medicine, as well as in electronics and nanotechnologies [1–8]. The conditions for rapid phase transition of substances during dehydration are far from equilibrium; according to classical theory, this should be accompanied by self-assembly and by appearance of ordered spatial structures.

These processes can occur, for example, during dehydration of aqueous solutions of proteins [9–11]. Understanding the mechanisms of protein folding is the key to studying self-assembly processes in biological films [9]. A peculiar ordered morphological structure is observed as water evaporates from protein films [9]. Such evaporated film is an interesting subject as a natural model of a self-organizing system with a rich set of variables affecting the process, depending on its composition, substrate properties, and external conditions [10, 12].

Dehydrated films of biological fluids are commonly used in medical diagnostics, obtained by wedge-shaped dehydration. There is a well-known correlation between the parameters of the structures formed in self-organized films of biofluids and different types of pathologies [13, 14]. Different experimental factors affect the physical component of self-assembly processes in protein films.

To correctly interpret the structures formed in complex biological fluids, we considered aqueous solutions of egg albumin (ovalbumin) with different experimental conditions, analyzing the effect of different dehydration parameters on formation of structures in ovalbumin films.

Description of self-assembly processes

From the standpoint of molecular biology, protein folding occurs during self-assembly, i.e., with the tertiary structure (three-dimensional conformation) evolving in accordance with structural information encoded in the primary structure (sequence of amino acid residues). Physically speaking, self-assembly means that macroscopically ordered spatio-temporal structures form in complex nonlinear systems [15]. Physical and chemical aspects of self-assembly of proteins are described in detail in [16].

Self-assembly processes can only occur in systems with a high level of complexity and a large number of elements. There are several approaches to describing and interpreting the physical nature of these processes. For example, Prigogine offered an approach determining the entropy of open systems [17], while Rudenko formulated an approach from the standpoint of evolutionary catalysis [18]. While both of these approaches are identical in estimating the anti-entropic nature of self-assembly, they differ greatly in interpreting the conditions, causes and driving forces of self-assembly, explaining its mechanisms and establishing its measure. These approaches are close in choice of characteristics of an open system for describing its self-assembly and estimating its measure. However, dissipative flow is considered in the first case and that of internal useful work in the second. In other words, dissipation and its functions serve as measures of self-assembly in the first approach, and internal useful work and its functions do so in the second. The difference between these approaches, the benefits and drawbacks found by comparing them are described in monograph [19].

Study of self-assembly processes should include unstable states of systems and conditions of phase transitions accompanied by diffusion and dissipation of energy. Mathematical modeling, for example, the framework of differential equations, is used to describe these processes [20, 21]. Probability theory combined with computer simulation is used for analyzing processes with a small number of molecules.

Self-assembly during protein folding is described using methods of physical chemistry and optics, i.e., considering the interaction of matter with light in the entire wavelength range: from X-rays to radio waves. Self-assembly of proteins after destruction of their tertiary structure (renaturation) and their structural formation are of particular interest for such fields as drug design, molecular bioelectronics, including biomolecular robotics, and nanotechnology [9, 22].

There are a number of techniques for studying self-assembly processes. X-ray diffraction provides direct information about the arrangement of atoms in molecular crystals. This method was used to describe the structure of some vitamins and also to discover denaturation of protein molecules. Structural formation of proteins at the molecular level is studied by this method. This allows to detect lattices with long-range order with strong covalent chemical bonds [23]. X-ray

diffraction methods are not quite satisfactory for describing systems without long-range order.

Synchrotron radiation is a very promising method for studying biological processes associated with conformational and other structural transformations at molecular and supramolecular levels [20]. The electric field affects a wide range of processes, for example, phase transitions in substances, reducing the evaporation heat of water and increasing the heat transfer rate in liquids. The electric field induces conformational transformation of spiral single-stranded polynucleotide in the solution into clusters, where the degree of transition is a linear function of field strength [24].

Optical methods make it possible to observe the progress of biological processes in real time virtually without interfering with them.

Experimental procedure

The simplest and most accessible method for studying self-assembly is visual (or hardware-based) monitoring of dynamics of protein condensation and its phase transitions under nonequilibrium conditions: in an open protein-water system, far from thermodynamic equilibrium. This technique consists in evaporating water from a colloidal protein-water system (dehydration) with subsequent dynamic visualization of protein condensation and self-assembly under equilibrium and nonequilibrium conditions *in vitro*. Different types of colloidal protein-water systems (with albumin or thrombin) are placed on a solid wetted substrate (glass) and dried in an open system at room temperature and atmospheric pressure. The dynamics of the process is recorded with an optical microscope and a sensitive CCD camera.

Certain reproducible structures form through self-assembly in drying films of aqueous protein solutions. Depending on the chemical composition of the solution of a particular protein and on experimental conditions, these structures can take a variety of shapes and volumes. It was found in [9] that there are two main types of structures: spirals and dendrites. Fig. 1 shows these types of structures.

The next section describes the procedure for obtaining these structures and the results of experimental studies.

Experimental studies

These studies were aimed at analyzing the effect that experimental conditions have on formation of different structures in ovalbumin films. We considered the following factors:

initial volume of solution;
protein concentration in solution;
presence of salt;
acidity of solution.

Ovalbumin with an initial concentration of 20 wt% was selected for the experiments. Next, different samples were prepared in accordance with the experimental design. Liquid samples with a volume of 1, 2, 3, and 4 ml were placed in glass Petri dishes 28 mm in diameter and subjected to dehydration for 48 h at a temperature of 36.6 °C and a humidity of 20%. The temperature selected corresponded to the temperature of the human body under normal conditions. The degree of acidity of the solutions was changed by adding 99% acetic acid to the solution.

Eight measurements were performed for each experimental set. Images of the films with a resolution of 896 × 684 pixels were recorded with an optical microscope and a USB camera connected to it.

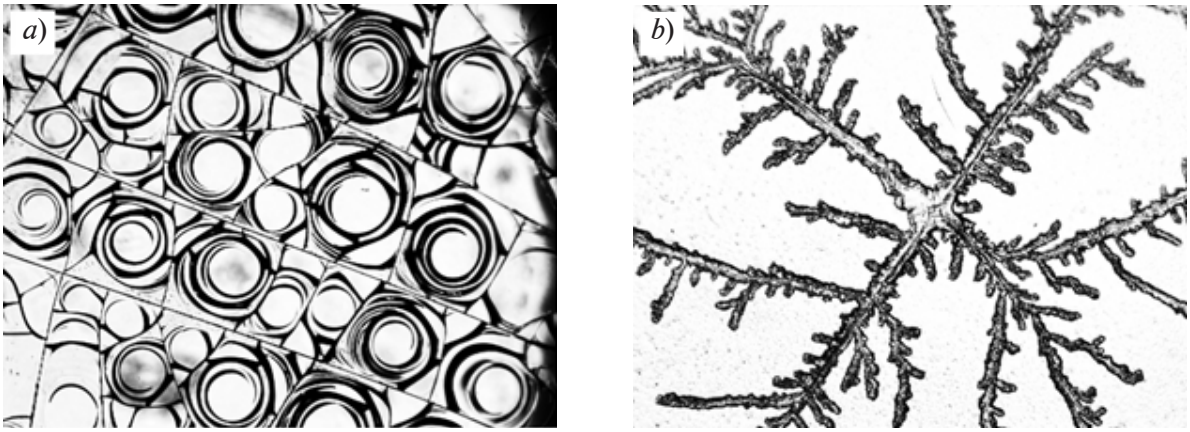

Fig. 1 [9]. Dissipative structures found in dehydrated film of ovalbumin protein: spirals (*a)*; dendrites (*b)*

Transparent protein films formed in Petri dishes as the samples dried. Structures varying in type, shape and size formed In some films, depending on their composition and experimental conditions. The structures were found in separate areas of the Petri dish rather than over its entire surface (Fig. 2). A small spot containing cracks formed in the protein film in the center of the Petri dish (region *3*).

A ring of spiral structures located on polygonal fragments of the film, separated by cracks, formed closer to the edge of the dish (region *2*). Film fragments in this ring had a smaller total area than in the central region. Hemispherical cracks with elongated branch-like structures were observed at the edge of the Petri dish (region *1*).

The reason for this localization was that the colloidal phase (particles) were driven to the periphery as water evaporated.

Dependence of the structures on protein concentration. We considered the structures forming in albumin films depending on the protein concentration both in the initial aqueous solution and in the sodium chloride (NaCl) solution. We used 3 ml samples with different protein concentrations in the solution (wt%): 2.5; 5.0; 10 and 20. The experimental results obtained are shown in Fig. 3. Evidently, the higher the initial protein concentration in aqueous solution given a constant volume, the denser the spiral structures in the protein film. The average geometric dimensions of the spirals and the cells were obtained by calibrating the microscope chamber. The outer circumference and area for spiral structures were approximately 180 μm and 2500 μm^2, respectively. The circumference and area of the cells were about 200 μm and 5000 μm^2.

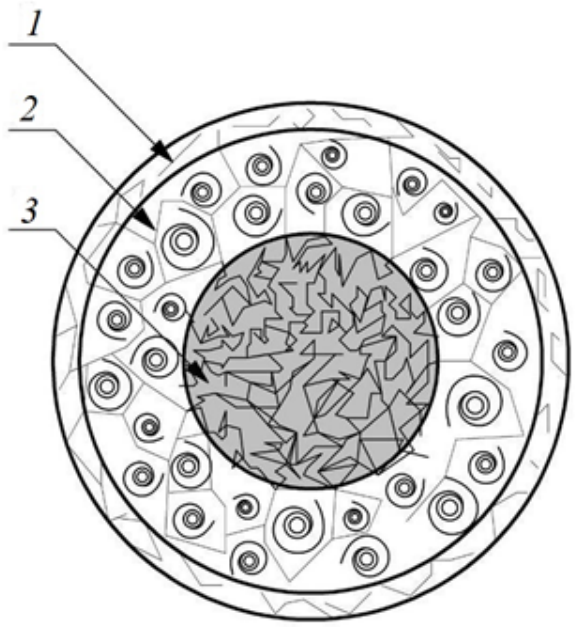

Fig. 2. Schematic of Petri dish with dried egg albumin sample showing different regions of film: dish edge *1* with salt residue; region *2* with spiral structures and cracks; central region *3* with cracks

We also analyzed the structures forming in ovalbumin films depending on protein concentration in dry film. Because protein concentration in the film could not be measured or changed, the samples in these experiments were selected by the initial volume of the aqueous solution. A 20% solution was chosen for the experiment. Solutions of 1, 2, 3, and 4 ml were then placed in Petri dishes and subjected to dehydration for 48 h. The experimental results obtained are shown in Fig. 4.

To assess the nature of film structuring, we calculated the approximate number of structures formed (in one spiral) in the photograph of the film. Fig. 5 illustrates this calculation.

It follows from the data in Figs. 4 and 5 that the larger the initial volume of the solution, the more structures form in protein film and the larger they are. A possible reason for this is that protein concentration in dry film is higher with a larger volume of the initial solution.

Dependence of the structures on solution acidity. We prepared aqueous solutions of albumin with different pH values. Acetic acid was added to the protein solution to obtain a certain degree of acidity. The same as in the previous experiment, 3 ml samples were taken. Fig. 6 shows photographs of ovalbumin films with different pH and similar aqueous solutions.

It follows from the data in Fig. 6 that the closer the pH of the initial solution to 4.8, the less structures are formed in albumin film. Additionally, if the pH of the solution abruptly shifts from 4.8 towards acidic or alkaline values, the structures take the shape of incorrectly formed spirals. Notably, pH = 4.8 is the isoelectric point of the protein (the pH value at which the total charge of the protein molecules is zero).

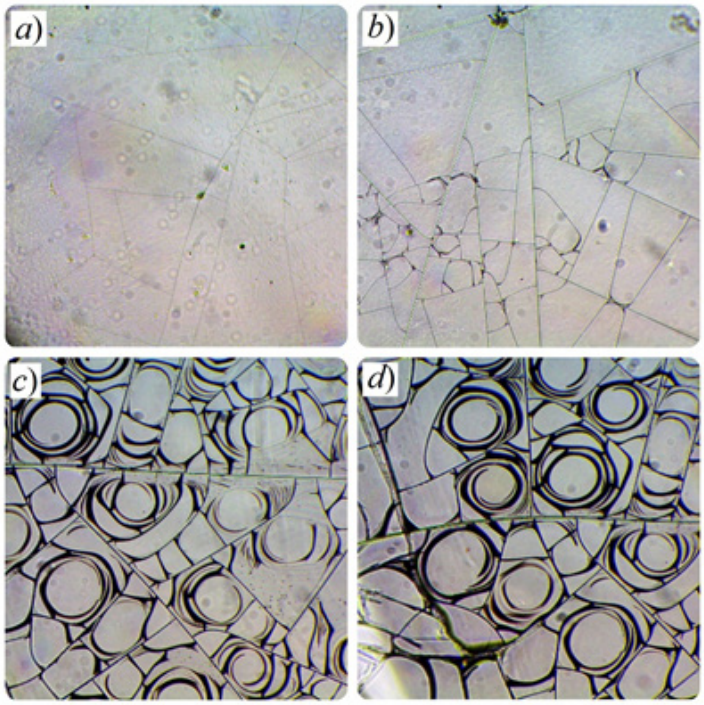

Fig. 3. Structural changes in ovalbumin films depending on ovalbumin concentration in aqueous solution (wt%): 2.5 (*a*), 5.0 (*b*), 10 (*c*) and 20 (*d*)

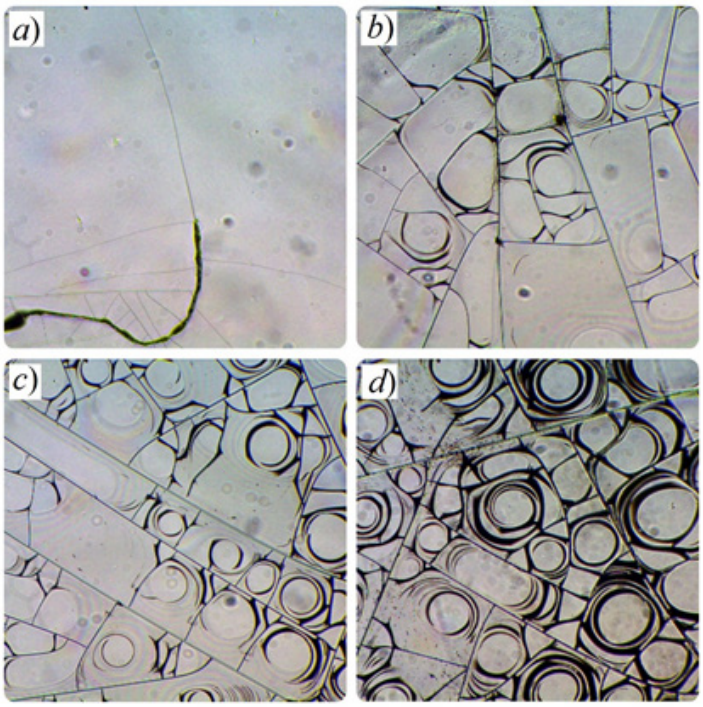

Fig. 4. Structural changes in ovalbumin films depending on volume of initial 20% aqueous solution, ml: 1 (*a*); 2 (*b*), 3 (*c*), 4 (*d*)

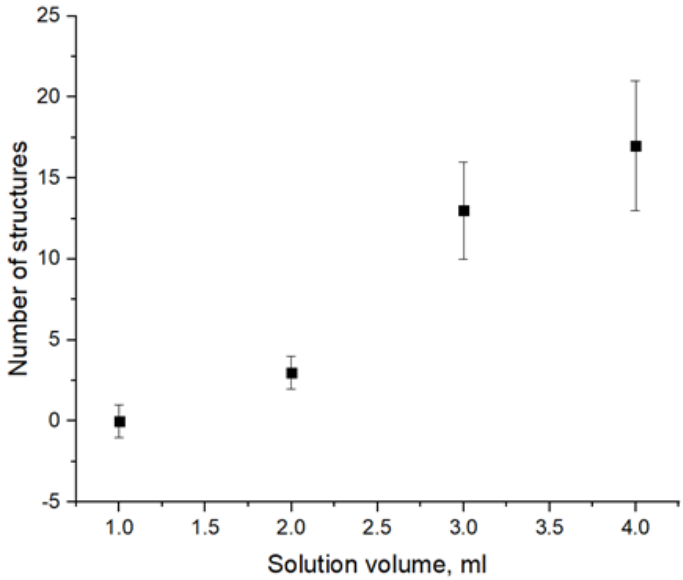

Fig. 5. Number of structures formed in ovalbumin film depending on volume of initial 20% aqueous solution

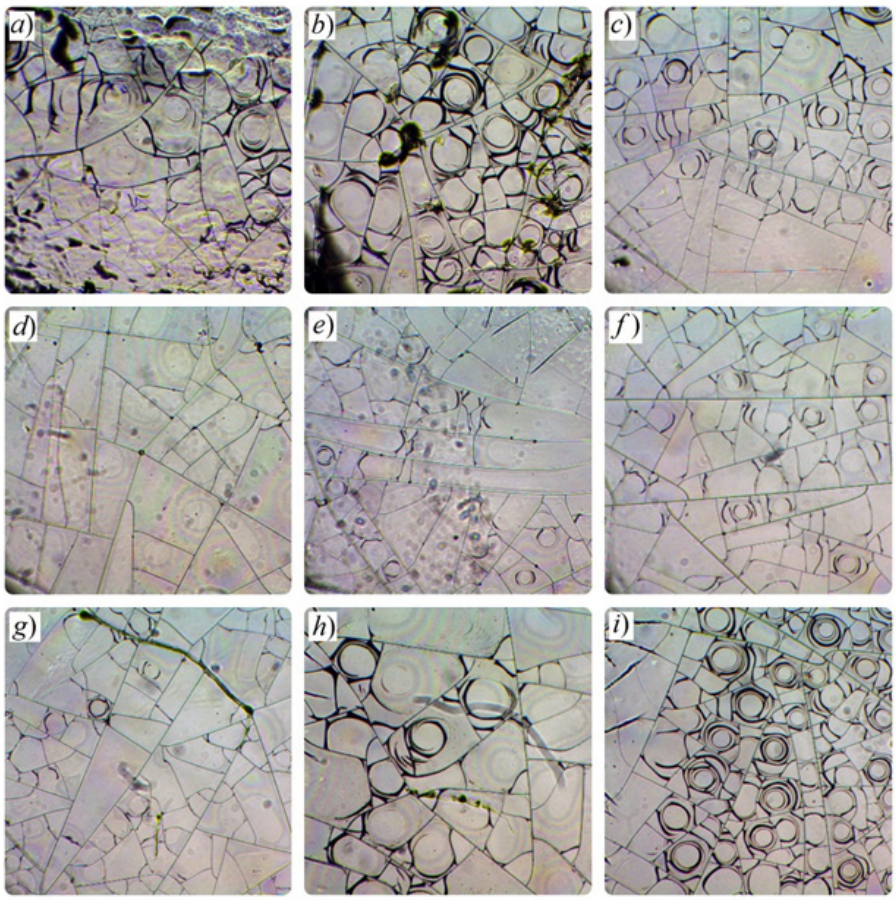

Fig. 6. Structural changes in ovalbumin films depending on pH value of initial aqueous solution: 3.0 (*a*), 4.2 (*b*), 4.4 (*c*), 4.8 (*d*) 5.2 (*e*), 5.8 (*f*), 6.2 (*g*), 7.0 (*h*), 7.8 (*i*)

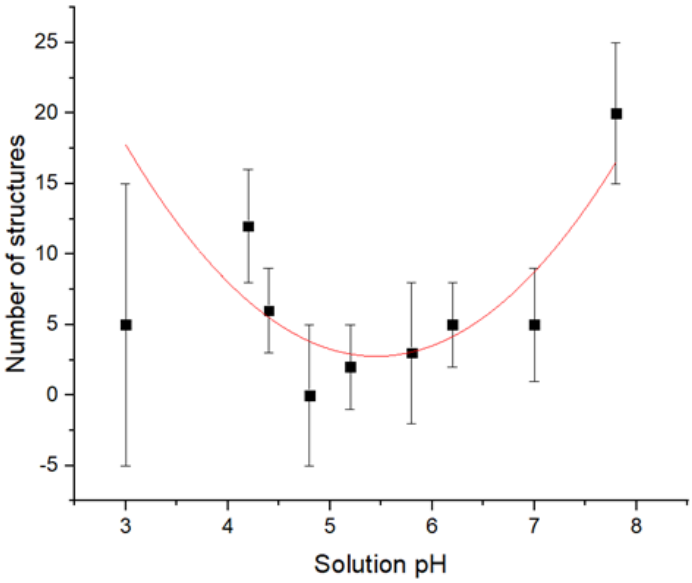

Fig. 7. Number of structures in ovalbumin films depending on pH of initial aqueous solution

Fig. 7 shows the number of structures formed, i.e., the number of structures per unit area, depending on the pH of the initial solution.

It can be seen from Fig. 7 that a large number of structures form if the acidity of the initial solution ranges from 7.0 to 7.8. The same thing happens with pH ranging from 3.0 to 4.4. There are no structures with pH = 4.8. Most likely, structures cannot form near the isoelectric point due to absence of uncompensated charge. We can then conclude that protein's ability to form structures in dehydrated film is directly related to charge of the protein molecule. Even though errors extend beyond the trend, we decided to preserve this line, since this graph shows only measurement errors and does account for the specifics of producing an aqueous protein solution and performing dehydration.

Presence of salts in solution. In addition to films obtained from purely aqueous solutions, we considered structures forming in ovalbumin films from a solution containing NaCl. For this purpose, we prepared protein solutions with different concentrations where an aqueous NaCl solution with a concentration of 0.9% (0.15 M) served as solvent. Experimental samples of 3 ml were dehydrated for 8 h. The experimental results are shown in Fig. 8.

Unlike the structures forming in films prepared from aqueous solution, so-called tree-like structures formed in films prepared from water-salt solution. The higher the concentration of NaCl in the initial solution, the denser the branches. The structure of the 'trees' is disrupted with a very low protein concentration, and a dense field of crystals is formed. The structures shown in Fig. 9 are two-dimensional self-affine fractals. The main property of such structures is invariance after a simultaneous but quantitatively different change in distance along different directions in space. In other words, in contrast to a simple fractal, self-affine fractals cannot be obtained by simple stretching of self-replicating fractals, since the ratios of stretching in different directions should depend on size [26].

However, if protein concentration in the initial water-salt solutions is progressively reduced, fractal structures of a different type form. Examples of such structures are shown in Fig. 9. Evidently, as protein concentration decreases, structures become more and more branched. Fig. 9,*b* shows a NaCl crystal surrounded by fine structures. We used the Witten–Sander model to interpret the results obtained. According to this model, particles are added one after another to a growing cluster. The aggregation process is induced by a fixed initial particle in the original version. The aggregate then keeps growing [26]. The structures shown in Fig. 8 are Witten–Sander aggregates.

Results and discussion

We examined some features of the structures forming in ovalbumin films upon dehydration self-assembly. We confirmed experimentally that two types of film predominantly form as a result of dehydration and accompanying self-assembly of protein solutions. We analyzed how different factors affect the structures forming: acidity of protein solution, presence of NaCl in the solution, protein concentration, and initial volume of aqueous solution. The experiments showed that all of the above conditions influence the structuring of the 'spirals'. As a whole, the nature of protein self-assembly depends on general physicochemical properties of polymer biomacromolecules [16]. However, mechanisms of interaction of protein with water have to be understood to take into account all aspects of the studies conducted.

The protein chain is polar like water and also has total zero charge. Some side groups are also partially charged. Charged amino acid residues are even more polar. Both the peptide groups of the main chain and the polar side groups act as donors and acceptors of hydrogen bonds. They can form bonds with each other or with water molecules; almost all of them create such bonds, since the typical energy of hydrogen bonds is 5 kcal/mol, which is significantly higher than the energy of thermal motion.

If the intramolecular bond between the donor and the acceptor of the hydrogen bond in protein forms in an aqueous medium, it replaces two hydrogen bonds of the protein with water molecules, with a bond simultaneously created between the molecules of the water released.

From a thermodynamic standpoint, the energy balance of the given reaction is close to zero, since the number of hydrogen bonds has not changed [16]. However, the entropy of water generally increases, since water is no longer bound to the protein chain, and molecules with an H-bond can move freely.

Let us consider the so-called hydrophobic effect. Proteins contain many amino acids with hydrocarbon side groups that form the hydrophobic core of the protein globule. The hydrophobic effect plays a crucial role in maintaining the stability of the protein structure, serving to transform the protein chain into a compact dense globule. The effects opposite to 'hardening' are associated with entropy of rotations and displacements of molecules in liquid. This is because each molecule in a liquid moves more or less freely, while it is restrained by the crystal lattice in a solid. As a matter of fact, the entropy of displacements of a molecule does not depend on its size, in contrast to the enthalpy that grows with increasing number of contacts of the molecule

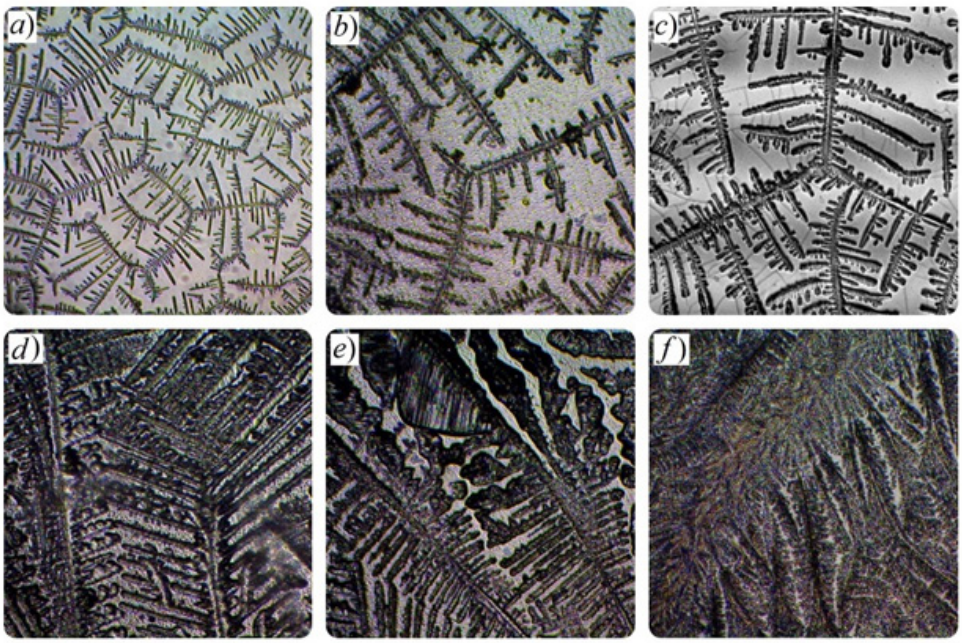

Fig. 8. Changes in dendritic structures in ovalbumin films depending on protein concentration, %: 10 (*a*), 5 (*b*), 2.5 (*c*), 1.0 (*d*), 0.5 (*e*), 0.1 (*f*).
Films were obtained from water-salt solutions (0.1 M NaCl)

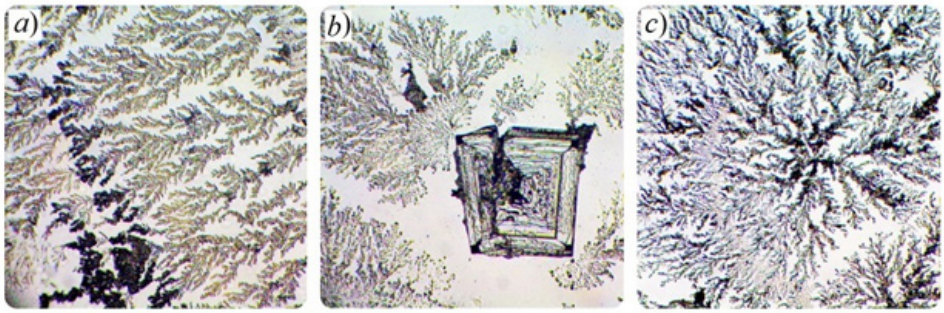

Fig. 9. Changes in dendritic structures in ovalbumin films depending on protein concentration c_p in initial water-salt solutions (0.15 M NaCl); c_p = 0.05% (*a*), 0.02% (*b*), 0.01% (*c*)

with the others. Displacement entropy plays a smaller role in the protein chain, since amino acid residues are linked by a chain, that is, they cannot move independently of each other, making the protein 'harden'.

The hydrophobic effect accounts for 90% of the process in which a protein globule is created. But it cannot produce its own 'solid' protein, generating only a liquid protein globule. Accordingly, we can conclude that aqueous protein solutions should serve as a basis for studying self-assembly of proteins *in vitro*. However, protein concentration should be maintained in a certain range to achieve proper self-assembly [16].

As already established (and confirmed by our experiments), the water content affects the structure of proteins, and the structure is in turn responsible for the functionality of the protein. Thus, if concentration of proteins in aqueous solutions has a known effect on the formation of structures during dehydration, it is possible to estimate the functionality of proteins during dehydration of complex biological fluids in medical diagnostics.

Conclusion

We have carried out experimental studies aimed at understanding how the sizes and shapes of structures in protein films depend on experimental conditions.

Analyzing the results of the experiments conducted, we have reached the following conclusions.

Acidity of the initial solution and the concentration of protein in the solution significantly affected the formation of spiral structures.

We have found that acidity considerably different from the isoelectric point of ovalbumin, neither critically acidic nor alkaline, was required to obtain stable structures in ovalbumin films. The required pH of the solution was less than 3.0 or greater than 8.0.

We determined the specific values of the parameters in experimental conditions. For example, dense structures could form with a sufficiently large volume of the initial solution: 3-4 ml for a Petri dish of 28 mm, i.e., with film thickness in liquid phase at least 4–5 mm.

Notably, self-assembly processes can occur in samples with the smallest volume. However, it is extremely difficult to detect dissipative structures in such samples.

We plan to carry out further quantitative studies of the structures formed in protein films, including by varying the pH value of salt solutions, measuring the geometric parameters of structures, determining whether these parameters correspond to experimental conditions for self-assembly during dehydration.

This paper was prepared with the financial support of RFBR, grant no. 19-32-90130. We wish to express our gratitude to A.N. Skvortsov for help with biophysical aspects.

REFERENCES

1. **Bordag M., Klimchitskaya G.L., Mohideen U., Mostepanenko V.M.,** Advances in the Casimir effect. OUP Oxford, 2009. Vol. 145.

2. **Baranov M.A., Klimchitskaya G.L., Mostepanenko V.M., Velichko E.N.,** Fluctuation-induced free energy of thin peptide films, Physical Review E. 99 (2) (2019) 022410.

3. **Karki S., Kim H., Na S.J., et al.,** Thin films as an emerging platform for drug delivery, Asian Journal

of Pharmaceutical Sciences. 11 (5) (2016) 559–574.

4. **Piedade A.P., Romeu F., Branco R., Morais P.V.,** Thin films for medical and environmental applications, Thin Film Synthesis and Application for Medical and Biological Use, IntechOpen, 2018.

5. **Yoshimura T**., Thin-film organic photonics: molecular layer deposition and applications, CRC Press, 2016.

6. **Malyshko E.V., Tverdislov V.A.,** Khiralnost, strukturnyye iyerarkhii i folding belkov [Chirality, structural hierarchy and protein folding], Report at Intern. Conf. "Molecular, membrane and cell basics of functioning of bio systems", Minsk, Belarus, June 27–29, 2018.

7. **Fukuda K., Takeda Y., Yoshimura Y., et al.,** Fully-printed high-performance organic thin-film transistors and circuitry on one-micron-thick polymer films, Nature Communications. 5 (2014) 4147.

8. **Aggeli B.A., Bell M., Boden N., et al.,** Responsive gels formed by the spontaneous self-assembly of peptides into polymeric β-sheet tapes, Nature. 386 (6622) (1997) 259–262.

9. **Rapis E.,** Self-organization and supramolecular chemistry of protein films from the nano- to the macroscale, Technical Physics. 48 (4) (2004)494–498.

10. **Yakhno T.A., Yakhno V.G., Sanin A.G., et al.,** Protein and salt: Spatiotemporal dynamics of events in a drying drop, Technical Physics. 49 (8) (2004)1055–1063.

11. **Yakhno T.A.,** Sodium chloride crystallization from drying drops of albumin–salt solutions with different albumin concentrations, Technical Physics. 60 (11) (2015) 1601–1608.

12. **Wakamatsu T.**, Forward-light-scattering characterization of pre-crystalline aggregates in crystallizing lysozyme solutions, American Journal of Analytical Chemistry. 5 (9) (2014) 581–582.

13. **Krayevoy S.A., Koltovoy N.A.,** Diagnostika po kaple krovi. Kristallizatsiya biozhidkostey. Kniga 1. Kristallizatsiya syvorotki krovi metodom otkrytoy kapli (uglovaya degidratatsiya) [Blood drop diagnostics. Crystallization of biofluids, Book 1: Crystallization of blood serum by an open drop procedure (angular dehydration)]. Version 6.0, Moscow, Smolensk (2016) 321.

14. **Shabalin V.N., Shatokhina S.N.,** Diagnostic markers in the structures of human biological liquids, Singapore Medical Journal. 48 (5) (2007) 440–442.

15. **Usychenko V.G.,** Electron self-organization in electronic devices //Technical Physics. 49 (11) (2004) 1431–1440.

16. **Finkelshteyn A.V., Ptitsyn O.B.,** Fizika belka: kurs lektsiy, Knizhnyy Dom "Universitet, Moscow, 2002.

17. **Prigogine I., Stengers I.,** Order out of chaos: Man's new dialogue with nature, Verso Books, 2018.

18. **Rudenko A.P.,** Samoorganizatsiya i sinergetika, Slozhnyye Sistemy. (2) (2013) 4–39.

19. **Shcherbakov A.S**., Samoorganizatsiya materii v nezhivoy prirode: Filosofskiye aspekty sinergetiki [Self-organization of matter in the inanimate nature: Philosophical aspects of synergetics], Moscow University Publishing, Moscow, 1990.

20. **Denisevich A.A., Liapzev A.V.,** Computer simulation of processes of self-organization. Structures in a chain of colliding balls, Computer Tools in Education. (4) (2018) 27–34.

21. **Liapzev A.V., Denisevich A.A.,** Computer modelling of processes of self- organization. Analogy to Benar's cells, Computer Tools in Education. (1) (2017) 38–44.

22. **Velichko E.N., Tsybin O.Yu.,** Biomolekulyarnaya elektronika. Vvedeniye [Biomolecular electronics. Introduction], Polytechnical University Publishing, St. Petersburg, 2011.

23. **Rapis E.G.,** Self-assembly of cluster protein films (allotropic nonequilibrium noncrystalline modification) during the process or their condensation, Technical Physics. 45 (1) (2000) 121–131.

24. **Bandman O.L.,** Implementation of large-scale cellular automata models on multicore computers and clusters. High performance computing and simulation (HPCS), 2013 Int. Conf. IEEE Conference Publications. 5 (2013) 304–310.

25. **Yakhno T.A., Yakhno V.G.,** Structural evolution of drying drops of biological fluids, Technical Physics. 54 (8) (2009) 1219–1227.

26. **Jullien R.,** Fractal aggregates, Comm. Cond. Mat. Phys. (Comm. Mod. Phys. Pt. B. 13 (4) (1987) 177–205 (Uspekhi Fizicheskikh Nauk, 1989).

Received 14.10.2019, accepted 30.10.2019.

THE AUTHORS

BARANOV Maksim A.
Peter the Great St. Petersburg Polytechnic University
29 Politechnicheskaya St., St. Petersburg, 195251, Russian Federation
baranovma1993@gmail.com

VELICHKO Elena N.
Peter the Great St. Petersburg Polytechnic University
29 Politechnicheskaya St., St. Petersburg, 195251, Russian Federation
velichko-spbstu@yandex.ru

ROZOV Sergey V.
Peter the Great St. Petersburg Polytechnic University
29 Politechnicheskaya St., St. Petersburg, 195251, Russian Federation
svroz@yandex.ru

СПИСОК ЛИТЕРАТУРЫ

1. **Bordag M., Klimchitskaya G.L., Mohideen U., Mostepanenko V.M.** Advances in the Casimir effect. Oxford: OUP Oxford. Int. Ser. Monogr. Phys. Vol. 145. 2009. 749 p.

2. **Baranov M.A., Klimchitskaya G.L., Mostepanenko V.M., Velichko E.N.** Fluctuation-induced free energy of thin peptide films // Physical Review. E. 2019. Vol. 99. No. 2. P. 022410.

3. **Karki S., Kim H., Na S.J., Shin D.J.K., Lee J.** Thin films as an emerging platform for drug delivery // Asian Journal of Pharmaceutical Sciences. 2016. Vol. 11. No. 5. Pp. 559–574.

4. **Piedade A.P., Romeu F., Branco R., Morais P.V.** Thin films for medical and environmental applications // Thin Film Synthesis and Application for Medical and Biological Use. IntechOpen, 2018. DOI: 10.5772/intechopen.80021.

5. **Yoshimura T.** Thin-film organic photonics: molecular layer deposition and applications. London, New York: CRC Press, 2016. 370 p.

6. **Малышко Е.В., Твердислов В.А**. ХиХ ральность, структурные иерархии и фолдинг белков // Междунар. научн. конф. «Моле/ кулярные, мембранные и клеточные основы функционирования биосистем». г. Минск, Беа ларусь, 27–29 июня 2018 года. 2018. С. 29–29.

7. **Fukuda K., Takeda Y., Yoshimura Y., Shiwaku R., Tran L.T., Sekine T., Tokito S**. Fully-printed high-performance organic thin-film transistors and circuitry on one-micron-thick polymer films // Nature Communications. 2014. Vol. 5. P. 4147.

8. **Aggeli B.A., Bell M., Boden N., Keen J.N., Knowles P.F., McLeish T.C.B., Radford S.E.** Responsive gels formed by the spontaneous self-assembly of peptides into polymeric β-sheet tapes // Nature. 1997. Vol. 386. No. 6622. Pp. 259–262.

9. **Рапис Е.** Самоорганизация и супермолекулярная химия пленки белка от нано- до макромасштаба // Журнал технической физики. 2004. Т. 74. № 4. С. 117–122.

10. **Яхно Т.А.,** Яхно **В.Г., Санин А.Г., Санина О.А.,** Пелюшенко **А.С.** Белок и соль: пространственно-временные события в высыхающей капле // Журнал технической физики. 2004. Т. 8 № .74. С. 108–100.

11. **Яхно Т.А.** Кристаллизация хлорида натрия из высыхающих капель белково-солевых растворов с разным содержанием белка // Журнал технической физики. 2015. Т. 85. № 11. С. 30–37.

12. **Wakamatsu T.** Forward-light-scattering characterization of pre-crystalline aggregates in crystallizing lysozyme solutions // American Journal of Analytical Chemistry. 2014. Vol. 5. No. 9. Pp. 581–582.

13. **Краевой С.А., Колтовой Н.А**. Диагностика по капле крови. Кристаллизация биожидкостей. Книга 1. Кристаллизация сыворотки крови методом открытой капли (угловая дегидратация). Версия 6.0. Москва, Смоленск. 2016. 321 с.

14. **Shabalin V.N., Shatokhina S.N.** Diagnostic markers in the structures of human biological liquids //Singapore Medical Journal. 2007. Vol. 48. No. 5. Pp. 440–442.

15. **Усыченко В.Г.** Самоорганизация электронов в электронных приборах//Журнал технической физики. 2004. Т. 11 № .74. С. 46–38.

16. **Финкельштейн А.В., Птицын О.Б.** Физика белка: курс лекций. М.: Книжный дом «Университет», 365 .2002 с.

17. **Пригожин И., Стенгерс И.** Порядок из хаоса. Новый диалог человека с природой. М.: Прогресс, 432 .1986 с.

18. **Руденко А.П.** Самоорганизация и синергетика // Сложные системы. 2 № .2013. С. 39–4.

19. **Щербаков А.С.** Самоорганизация материи в неживой природе: философские аспекты синергетики. М.: Изд-во МГУ, 110 .1990 с.

20. **Денисевич А.А., Ляпцев А.В.** Компьютерное моделирование процессов самоорганизации. Структуры в одномерной цепочке шаров // Компьютерные инструменты в образовании. 4 № .2018. С. 34–27.

21. **Ляпцев А.В., Денисевич А.А.** Компьютерное моделирование процессов самоорганизации. Аналогия с ячейками Бенара // Компьютерные инструменты в обы разовании. 2017. № 1. С. 38–44.

22. **Величко Е.Н., Цыбин О.Ю**. Биомолекук лярная электроника. Введение // СПб.: Изд-во Политехнического ун-та, 256 .2011 с.

23. **Рапис Е.Г.** Самосборка кластерных пленок белка в процессе конденсации (аллотропная неравновесная некристаллическая его форма) // Журнал технической физики. 2000. Т. 70. № 1. С. 122–133.

24. **Bandman O.L.** Implementation of large-scale cellular automata models on multicore computers and clusters. High performance computing and simulation (HPCS) // 2013 Int. Conf. IEEE Conference Publications. 2013. Vol. 1. Pp. 304–310.

25. **Яхно Т.А., Яхно В.Г.** Основы структурной эволюции высыхающих капель биологических жидкостей // Журнал технической физики. 2009. Т. 79. Вып. 8. С. 133–141.

26. **Жюльен** Р. Фрактальные агрегаты // Успехи физических наук. 1989. Т. 2 № .157. С. 357–339.

Статья поступила в редакцию 14.10.2019, принята к публикации 30.10.2019.

СВЕДЕНИЯ ОБ АВТОРАХ

БАРАНОВ Максим Александрович – *ассистент Высшей школы прикладной физики и космических технологий Санкт-Петербургского политехнического университета Петра Великого.*

195251, Российская Федерация, г. Санкт-Петербург, Политехническая ул., 29
baranovma1993@gmail.com

ВЕЛИЧКО Елена Николаевна – *кандидат технических наук, доцент, директор Высшей школы прикладной физики и космических технологий Санкт-Петербургского политехнического университета Петра Великого.*

195251, Российская Федерация, г. Санкт-Петербург, Политехническая ул., 29
velichko-spbstu@yandex.ru

РОЗОВ Сергей Владимирович – *кандидат технических наук, доцент Высшей школы прикладной физики и космических технологий Санкт-Петербургского политехнического университета Петра Великого.*

195251, Российская Федерация, г. Санкт-Петербург, Политехническая ул., 29
svroz@yandex.ru

DOI: 10.18721/JPM.12404
УДК 538.915+975; 544.22.022.343; 544.225.22+25

ELASTIC CONDUCTIVITY OF SILICENE AND GERMANENE NANORIBBONS

O.S. Lebedeva[1,2], *N.G. Lebedev*[1], *I.A. Lyapkosova*[2]

[1] Volgograd State University, Volgograd, Russian Federation;

[2] Volgograd State Agricultural University, Volgograd, Russian Federation

The theoretical research results for piezoresistive properties of ideal silicene and germanene nanoribbons with different conductivity types have been presented. Within the framework of the Hubbard model, the band structure of the nanoparticles under investigation was simulated and a longitudinal component of their elastoconductivity tensor was analytically calculated. For this tensor, the dependences on the relative strain of longitudinal compression/tension as well on the nanoribbon width were studied.

Keywords: 2D structure, silicene, germanene, stress-strain state, piezoresistive effect, elastroconductivity tensor

Citation: Lebedeva O.S., Elastic conductivity of silicene and germanene nanoribbons, St. Petersburg Polytechnical State University Journal. Physics and Mathematics. 12 (4) (2019) 32–42. DOI: 10.18721/JPM.12404

ЭЛАСТОПРОВОДИМОСТЬ СИЛИЦЕНОВЫХ И ГЕРМАНЕНОВЫХ НАНОЛЕНТ

О.С. Лебедева[1,2], *Н.Г. Лебедев*[1], *И.А. Ляпкосова*[2]

[1] Волгоградский государственный университет, г. Волгоград, Российская Федерация;

[2] Волгоградский государственный аграрный университет,

г. Волгоград, Российская Федерация

Представлены результаты теоретического исследования пьезорезистивных свойств идеальных силиценовых и германеновых нанолент с разным типом проводимости. В рамках модели Хаббарда проведено моделирование зонной структуры исследуемых наночастиц и аналитический расчет продольной компоненты тензора эластопроводимости, а также исследованы его зависимости от величины относительной деформации продольного сжатия (растяжения) и ширины наноленты.

Ключевые слова: двумерная структура, силицен, германен, напряженно-деформированное состояние, пьезорезистивный эффект

Ссылка при цитировании: Лебедева О.С. Эластопроводимость силиценовых и германеновых нанолент // Научно-технические ведомости СПбГПУ. Физико-математические науки. 2019. Т. 12. № 4. С. 38–49. DOI: 10.18721/JPM.12404

Introduction

New carbon-based nanostructures synthesized in 2004, such as graphene and graphene nanoribbons, proved to be materials with a unique set of physicochemical properties that can be used in a wide range of applied problems [1–4]. The electronic characteristics of graphene vary and depend on the nature and concentration of structural defects, atoms and atomic groups adsorbed on its surface. Graphene is one of the main candidates for components of future nanoelectronics, instead of silicon. The main obstacle to widespread use of graphene in electronics is its band structure, characterized by narrow band gap; there is ongoing research focused on expanding it.

Silicene, a material similar to graphene, consisting of a two-dimensional layer of silicon atoms that make up two sublattices displaced relative to each other, was theoretically predicted in 1994 and synthesized for the first time in 2010 [5]. The width of the band gap can be controlled using an electric field, making it possible to construct an effective spin polarizer. This material attracts considerable attention due to its diverse potential applications in silicon electronics and spintronics.

Another material similar to graphene was synthesized in 2014: germanene, which, like silicene, has two atomic sublattices displaced relative to each other. The narrow band gap of germanene can be controlled by electric field, adsorption of different atoms, deformation, and interaction with the substrate [6, 7]. Germanene has great potential for applications in solar cells [8]. The calculated Grüneisen parameter of the new material indicates that the dependence on strain is similar to that for silicene [9].

Density functional theory was used in [10] to conduct a comparative study on the mechanical properties of single-layer silicene, germanene, and stanene. It was found that applying a uniaxial load to each material can alter the electronic nature of buckled structure of the semiconductor to metallic character.

Optical properties of silicene and germanene under uniform compression strain were investigated within density functional theory in [11]. The results indicate that the response of the optical field strongly depends on the magnitude of the applied load. With compression strain applied in silicene and germanene, the band gap decreases at the Dirac points and ultimately reaches zero. Absorption of light along the zigzag direction is greater than in the armchair direction in both structures.

A new direction of condensed matter physics that has evolved in recent years is straintronics. It uses physical phenomena in matter induced by deformations arising in micro-, nano- and heterostructures with external controlling fields, altering the electronic structure of this matter, and, as a result, modifying its electrical, magnetic, optical and other properties [12].

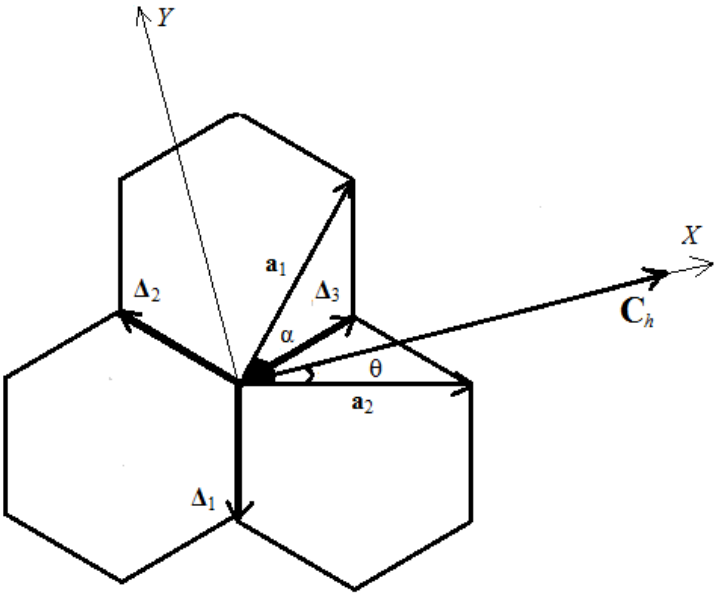

Fig. 1. Fragment of nanoribbon structure with selected coordinate system:
Δ_1, Δ_2, Δ_3 are the vectors of distance between the nearest neighbors; $\mathbf{a}_1$, $\mathbf{a}_2$ are the translation vectors; α is the angle between the translation vectors; θ is the chiral angle; $\mathbf{C}_h$ is the chiral vector

Such effects make it possible to create a new generation of information-sensing devices. For example, a transistor based on graphene with strain-induced suppression of ballistic conductivity (piezoconductivity) was proposed in [13]. Similar transistors can also be developed based on germanene and silicene; effects of strain in these materials are the focus of much research.

This paper presents the results of theoretical study on the piezoresistive properties of perfect silicene (Si) and germanene (Ge) nanoribbons (NR), SiNR and GeNR.

Model of electronic structure of deformed graphene nanoribbons

A two-dimensional hexagonal graphene layer was chosen as a geometric model of the nanoribbon. Fig. 1 shows a fragment of such a crystalline structure, with the chiral vector

$$\mathbf{C}_h = n\mathbf{a}_1 + m\mathbf{a}_2,$$

the angle α between the primitive translation vectors $\mathbf{a}_1$ and $\mathbf{a}_2$, as well as the interatomic distance vectors $\mathbf{\Delta}_i$.

The coordinate system is selected so that the ribbon width is measured along the *OX* axis using the chiral vector $\mathbf{C}_h$, and the *OY* axis is directed along the length of the ribbon. The angle θ between the vectors $\mathbf{C}_h$ and $\mathbf{a}_1$, counted from the translation vector $\mathbf{a}_1$, lies in the range from 0° to 30° and is called the chiral angle [4].

A mathematical model of the electronic structure of undeformed nanoribbons is constructed based on their geometric structure and the band structure of the hexagonal layer. The band structure of nanoribbons within the framework of the strong coupling method using Hückel approximations and approximate nearest neighbors has the following general form [4]:

$$\varepsilon(\mathbf{k}) = \pm\gamma_0 \left\{3+2\cos\left(\mathbf{k}\mathbf{a}_1\right)+ +2\cos\left(\mathbf{k}\mathbf{a}_2\right)+2\cos\left(\mathbf{k}\left(\mathbf{a}_1-\mathbf{a}_2\right)\right)\right\}^{1/2} = \pm\gamma_0 \left\{1+4\cos\left(\frac{\mathbf{k}\left(\mathbf{a}_1+\mathbf{a}_2\right)}{2}\right)\cos\left(\frac{\mathbf{k}\left(\mathbf{a}_1-\mathbf{a}_2\right)}{2}\right) +4\cos^2\left(\frac{\mathbf{k}\left(\mathbf{a}_1-\mathbf{a}_2\right)}{2}\right)\right\}^{1/2}, \quad (1)$$

where γ_0 is the hopping integral, the matrix element of electron transition between neighboring atoms; **k** is the wave vector, one of the components of which is quantized along the width of the ribbon.

The Fermi level in dispersion relation (1) is taken as 0 eV.

The condition for quantization of the wave vector **k** along the direction of the chiral vector $\mathbf{C}_h$ can be written as follows [4]:

$$\mathbf{k}\cdot \mathbf{C}_h = 2\pi q,\ q = 1, 2, \ldots . \quad (2)$$

The components of the wave vector k_x and k_y should be chosen so that they are codirectional with the chiral vector $\mathbf{C}_h$ and the length of the nanoribbon, respectively, i.e.,

$$\mathbf{k}_x \uparrow\uparrow \mathbf{C}_h,\ \mathbf{k}_y \perp \mathbf{C}_h.$$

The magnitude of the chiral vector of undeformed nanoribbons can be represented, in accordance with its definition, in the following known form [1]:

$$\left|\mathbf{C}_{\mathbf{h}0}\right| = \sqrt{n\cdot\mathbf{a}_1^2 + m\cdot\mathbf{a}_2^2 + 2nm\mathbf{a}_1\mathbf{a}_2} = = a\sqrt{n^2+m^2+nm}. \quad (3)$$

Using representation (3) and conditions (2), we can obtain an explicit expression for quantization of the transverse component of the wave vector:

$$k_x a = \frac{2\pi q}{\sqrt{n^2+m^2+nm}}, \quad q = 1,2,\ldots,\left[\sqrt{n^2+m^2+nm}\right]. \quad (4)$$

Arguments of trigonometric functions in expression (1) for band structure can be written, based on geometric transformations corresponding to Fig. 1, as follows:

$$\frac{\mathbf{k}(\mathbf{a}_1+\mathbf{a}_2)}{2} = \left(\frac{1}{\sqrt{n^2+m^2+nm}}\times \left(\frac{3\pi q(n+m)}{2\sqrt{n^2+m^2+nm}} + \frac{\sqrt{3}k_y a(n-m)}{4}\right)\right),$$
$$\frac{\mathbf{k}(\mathbf{a}_1-\mathbf{a}_2)}{2} = \left(\frac{1}{\sqrt{n^2+m^2+nm}}\times \left(\frac{\pi q(n-m)}{2\sqrt{n^2+m^2+nm}} - \frac{\sqrt{3}k_y a(n+m)}{4}\right)\right). \quad (5)$$

As a result, expression (1) and relations (5) completely determine the energy spectrum of electrons of undeformed nanoribbons.

According to theory of electronic structure of graphene nanoribbons [4], a set of dispersion curves of the electronic spectrum, numbered by the integer q, is formed by crossing the two-dimensional energy surface of graphene with parallel planes corresponding to the continuous component of the wave vector. The position of these planes relative to the Brillouin zone is determined by the value of the discrete k_x component of the wave vector (in accordance with quantization condition (2)).

The deformed state of a crystallite is generally characterized by a distortion tensor,

$$u_{\mu\eta} = \partial_\eta \left(\mathbf{r}' - \mathbf{r}\right)_\mu, \left(\mu, \eta = x, y, z\right),$$

where **r, r'** are the radius vectors of the initial and final position of some point of the crystallite [14].

The diagonal elements of the tensor characterize the relative elongation of the sample along the corresponding direction, the off-diagonal elements determine the rotation angle of the linear element under strain.

In accordance with the definition of the distortion tensor, the energy spectrum of deformed nanoribbons is formulated by modifying the scalar products that appear in the arguments of trigonometric functions in expression (1) for the electronic spectrum. The change in the primitive cell of a nanoribbon under tensile load is shown in Fig. 2. The figure illustrates the model where strain induces not only the change in interatomic bond lengths, Δ_i ($\Delta_i = R_0(1 + \delta)$), by their relative elongation δ ($\delta = \Delta R/R_0$) but also in the angle α between the translation vectors ($\alpha = \alpha_0 + \Delta\alpha$, where $\alpha_0 = \pi/3$ is the angle between the translation vectors in the undeformed lattice, $\Delta\alpha$ is the angle change due to deformation), and, therefore, in the projections of the translation vectors $\mathbf{a}_1$ and $\mathbf{a}_2$ on the OX and OY axes of the selected coordinate system.

The expression for the band structure of deformed nanoribbons can be obtained based on geometric transformations (see Fig. 2). As a result, the electronic spectrum of such nanoribbons within the framework of the strong binding method takes the form

$$\varepsilon(\mathbf{k}) = \pm\gamma\left(1 + 4\cos\left[\pi n A_1 + B_1\right]\times \times\cos\left[\pi n A_2 - B_2\right] + +4\cos^2\left[\pi n A_2 - B_2\right]\right)^{1/2}, \quad (6)$$

where the following notations are introduced for the general case:

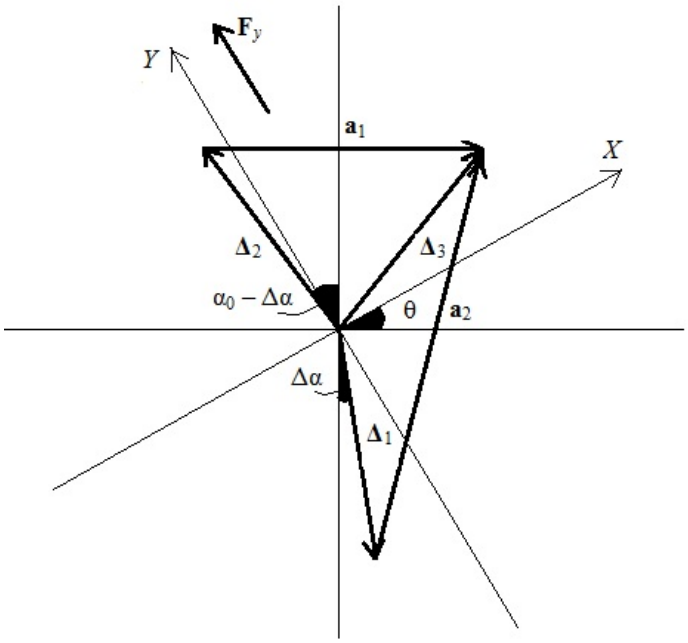

Fig. 2. Positions of interatomic vectors $\mathbf{\Delta}_1$, $\mathbf{\Delta}_2$, $\mathbf{\Delta}_3$ after tensile or compressive strain taking into account their rotation through the angle $\Delta\alpha$; $\mathbf{F}_y$ is the tensile (compressive) force. The remaining notations are given in the caption to Fig. 1

$$A_1 = \frac{F\cos\alpha + G\sin\alpha}{A\cos\alpha + B\sin\alpha},$$
$$B_1 = k_y R_0 (1+\delta)\left(-G\cos\alpha + F\sin\alpha\right),$$
$$A_2 = \frac{-E\cos\alpha}{A\cos\alpha + B\sin\alpha},$$
$$B_2 = k_y R_0 (1+\delta) E\sin\alpha,$$
$$A = n\sin\theta\cos(2\alpha_0) + m\cos\theta\cos\left(\alpha_0/2\right), \quad (7)$$
$$B = \sin\theta\left[n\sin(2\alpha_0) + m\cos\left(\alpha_0/2\right)\right],$$
$$E = \sin\theta\sin\left(\alpha_0/2\right) + \cos\theta\cos\left(\alpha_0/2\right),$$
$$F = \sin\theta\cos(2\alpha_0) + \cos\theta\cos\left(\alpha_0/2\right),$$
$$G = \sin\theta\left[\sin(2\alpha_0) + \cos\left(\alpha_0/2\right)\right].$$

The change in the transverse dimensions (width) of the nanoribbon due to strain is taken into account by modifying the magnitude of the chiral vector $\mathbf{C}_h$, which, in accordance with the definition of Poisson's ratio and direct proportionality of the main geometric dimensions of nanotubes to the lattice parameters, can be calculated by the following formula:

$$C_h = (1 - \boldsymbol{\nu}\cdot\boldsymbol{\delta})\, C_{h0}, \quad (8)$$

where ν is Poisson's ratio whose value varies in the range $\nu = 0.19–0.27$.

Relation (8) and the selected geometric model of deformed nanoribbons make it possible to find the angle α between the translation vectors in the deformed hexagonal lattice included in the expressions for coefficients (7) of the nanoribbon spectrum (6):

$$\sin\alpha = \frac{BC + A\sqrt{B^2 - C^2 + A^2}}{A^2 + B^2}, \quad (9)$$

where

$$C = \frac{1-\nu\delta}{1+\delta}\left[\sin\theta\left(n\cos\alpha_0 + m\cos^2\left(\alpha_0/2\right)\right) + \right.$$
$$\left. + \frac{m}{2}\cos\theta\sin\alpha_0\right],$$

and the coefficients A and B are expressed by Eq. (8).

The procedure for calculating the dependence of the hopping integral γ on the relative strain δ using carbon nanotubes as an example is described in detail in [15–18].

The following values of relative tensile (compressivee) strain were used for theoretical calculations:

$$\delta = +0.250\ ;\pm 0.104\ ;0.069\pm\ ;0.035\pm.$$

Finding the band structure of perfect nanoparticles taking into account scattering effects, for example, the Coulomb interaction of electrons at one site, consists in finding the poles of Green's functions [19] within the Hubbard model [20], which is described in [17] for the case of achiral carbon nanotubes.

The electronic spectrum of the deformed nanoribbon can then be represented as

$$E(\mathbf{k}) = \frac{1}{2}\left[\varepsilon(\mathbf{k}) + U \pm \right.$$
$$\left. \pm\left(\varepsilon(\mathbf{k})^2 - 2\varepsilon(\mathbf{k})U(1-2n_{-\beta}) + U^2\right)^{1/2}\right], \quad (10)$$

where $\varepsilon(\mathbf{k})$ is the band structure of deformed perfect nanoribbons, expressed by Eq. (6); U is the energy of the Coulomb interaction of electrons at one site, which can be estimated, for example, using the semi-empirical MNDO method from quantum chemistry [21]; $n_{-\beta}$ is the number of electrons with opposite spin already located in the zone.

No fundamental qualitative differences could be found for the obtained band structures of semiconductor SiNR and GeNR nanoribbons of the armchair type, in comparison with the energy spectrum of undeformed nanowires. Quantitative analysis points to narrowing band gap, conduction and valence bands, leading to increased density of electronic states in case of compression and, conversely, broadening of these bands (decreased density of states) under tensile strain. A similar result was observed for deformed achiral (armchair and zigzag) nanotubes, as well as for achiral carbon nanotubes studied in [15–18].

Axial tension (compression) also changes the band structure of conducting armchair and zigzag SiNR and GeNR nanoribbons in the manner described above; this does not make them fundamentally different from armchair nanoribbons, except for one notable aspect: the band gap is absent in such nanoribbons and does not appear under small strain. Strain-induced opening of the band gap is observed in mixed nanoribbons, as in the case of chiral carbon nanotubes [23], where Mott-type conductor → semiconductor and semiconductor → conductor transitions due to axial tensile (compressive) strain become possible.

Elastoconductivity of nanoribbons

Simulation of piezoresistive constants, in particular, the axial component of the elastoconductivity tensor of nanowires, was carried by the technique described in detail in [15–17]. In accordance with the definition of the elastic conductivity tensor [22], its longitudinal component for quasi-one-dimensional structures can be expressed by the following formula:

$$M = \frac{\Delta\sigma}{\sigma_0}\frac{1}{\delta}, \tag{11}$$

where M is the longitudinal component of 4th-order elastoconductivity tensor ($M = m_{zzzz}$); σ_0 is the longitudinal component of 2nd-order tensor of specific conductivity σ_{zz} of an undeformed crystal; $\Delta\sigma$ is the change in the longitudinal component of the conductivity tensor due to crystallite strain ($\Delta\sigma = \sigma - \sigma_0$, σ is the longitudinal component of the 2nd-order tensor of specific conductivity σ_{zz} of the deformed crystal).

The longitudinal component of the zero-phonon conductivity tensor of nanoribbons was calculated within the Kubo–Greenwood theory [19] using Green's function method with the Hubbard model Hamiltonian [20]. The final expression for the longitudinal conductivity of nanoribbons used in the calculations of the constant Mhas the following form [17]:

$$\sigma = 2\frac{i\pi e^2}{k_B TV}\sum_{\mathbf{k},\beta}\sum_{\mathbf{q},\lambda} v(\mathbf{k})v(\mathbf{q}) < \\ < n_{\mathbf{k}\beta} > \left[< n_{\mathbf{q}\lambda} > + \delta_{\mathbf{kq}}\delta_{\beta\lambda}\left(1 - < n_{\mathbf{k}\beta} >\right)\right], \tag{12}$$

where V is the crystallite volume; k_B is the Boltzmann constant; T is absolute temperature; e is the elementary charge; $\mathbf{k}$, $\mathbf{q}$ are two-component wave vectors within the Brillouin zone; β, λ are the spin indices; $<n_{\mathbf{k}\beta}>$ is the average number of particles in a quantum state with the wave vector $\mathbf{k}$ and spin β, expressed by the Fermi–Dirac distribution function; v is the longitudinal component of the electron velocity vector in the Brillouin zone.

The velocity vector is found by conventional means using the electronic spectrum (10):

$$\mathbf{v}(\mathbf{k}) = \frac{1}{\hbar}\frac{\partial E(\mathbf{k})}{\partial \mathbf{k}}. \tag{13}$$

Since numerous studies of the transport properties of Dirac materials, for example, graphene nanoribbons, point to ballistic (zero-phonon) nature of electronic conductivity [4], using the Hubbard model, which does not include the electron-phonon interaction, seems appropriate.

Figs. 3 and 4 show the component M of the elastic conductivity tensor depending on the relative strain δ equal to

−0.067, −0.045, −0.022,
+0.022, +0,045, +0.067, +0.250

for armchair (Arm) and zigzag (Zg) SiNR and GeNR nanoribbons of different widths: nArm (n = 9, 10, 50 and 100) and mZg (m = 5 and 10) (the values are given in primitive cells). Numerical results were obtained at T = 300 K. The calculated points are connected by solid lines to visually illustrate the trend in the variation of the constant M. Notably, the point $\delta = 0$ is not defined.

As follows from Figs. 3 and 4, the longitudinal component M of conducting armchair (9Arm) and zigzag (5Zg, 10Zg) nanoribbons is positive, and the behavior of this component completely correlates with the changes in the band structure of the nanoribbons, described above. A common trend for the given conducting nanoribbons is monotonic growth (or decrease) of M with increasing relative tensile (compressive) strain δ. A similar behavior is observed for conducting achiral carbon nanotubes [16, 17]. Despite the increase in the width of the conduction band and the decrease in the density of states at the Fermi level with increasing δ, the specific conductivity of the objects increases, which leads to monotonic growth of the component M. The reason for this effect is that the increasing number of charge carriers with increasing energies contribute to specific conductivity of the crystallite. Thermal fluctuations lead to filling of the conduction band of the nanoribbon by electrons according to the Fermi–Dirac distribution function. Modification of the electronic spectrum leads to a change in specific conductivity, taking into account all possible filled electronic states, and, consequently, to increase in the component M with increasing δ.

The longitudinal component M is negative for semiconductor armchair (10Arm, 50Arm, 100Arm) SiNR and GeNR nanoribbons but also monotonically

a)

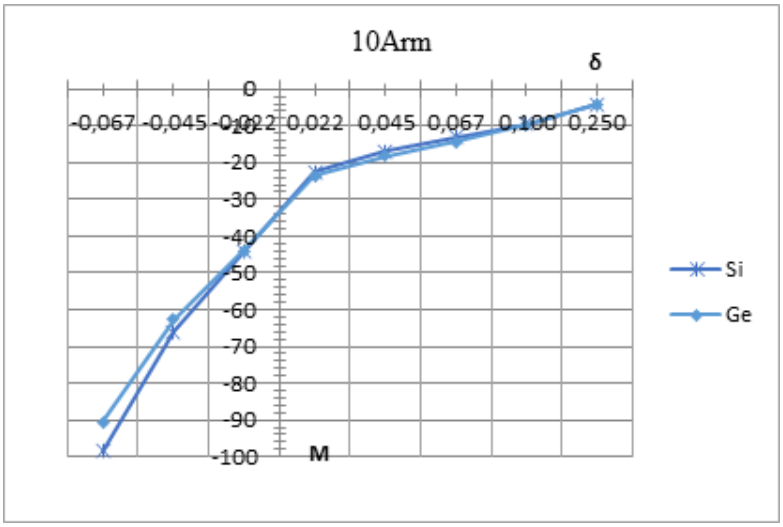

b)

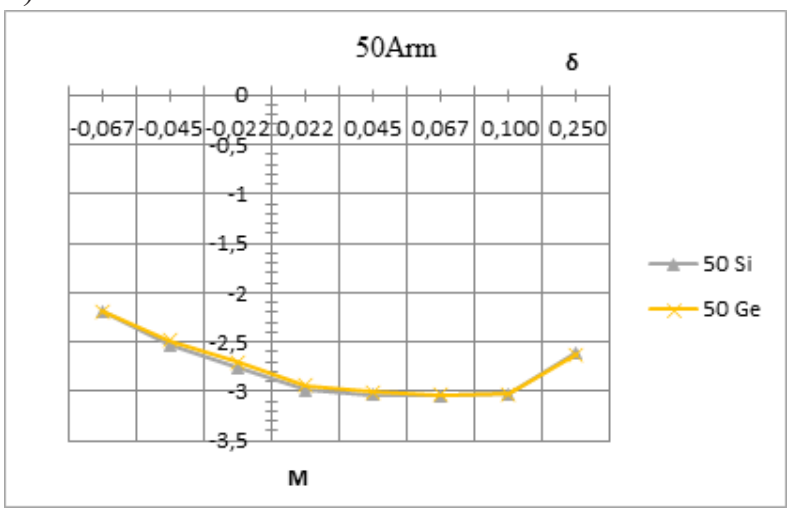

c)

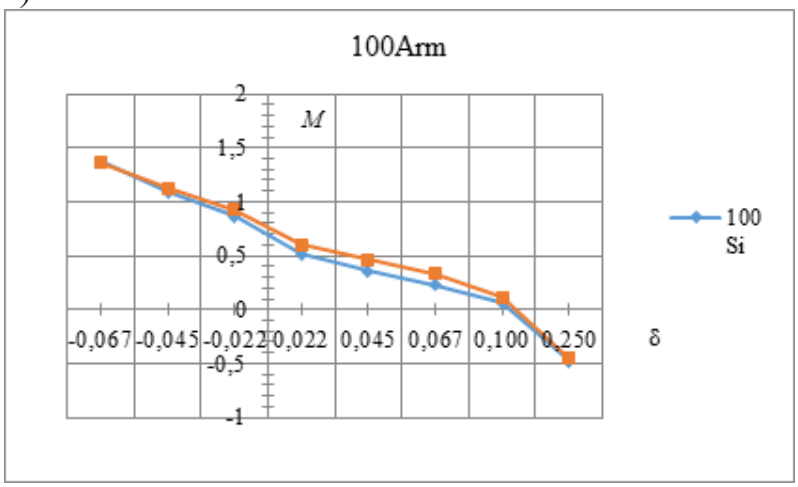

Fig. 3. Longitudinal component M of elastic conductivity tensor of armchair (Arm) SiNR and GeNR nanoribbons with a width of 10 (*a*), 50 (*b*) and 100 (*c*) primitive cells as function of relative strain δ. The point δ = 0 is not defined on all curves.

increases with increasing δ, the same as in case of conducting nanoribbons. The negative value is due to a decrease in conductivity with increasing strain. This effect is also a consequence of the behavior of the band structure of deformed semiconductor nanoribbons, where the band gap broadens and, therefore, the number of occupied states in the conduction band decreases. A similar behavior of the constant *M* is observed for conducting achiral carbon nanotubes [16, 17].

Applying the above-described technique for calculating the longitudinal component of the elastic conductivity tensor to study of piezoresistive properties of carbon nanotubes [16, 17] yielded results that are in good agreement with the data given in literature on the piezoresistive properties of carbon structures [24, 25]. Therefore, it should be expected that due to similar approaches to describing the band structure, graphene nanoribbons (Dirac structures) possess qualitatively identical piezoresistive properties. There are as yet no data in literature relating to nanoribbons of the graphene family, including silicene and germanene.

a)

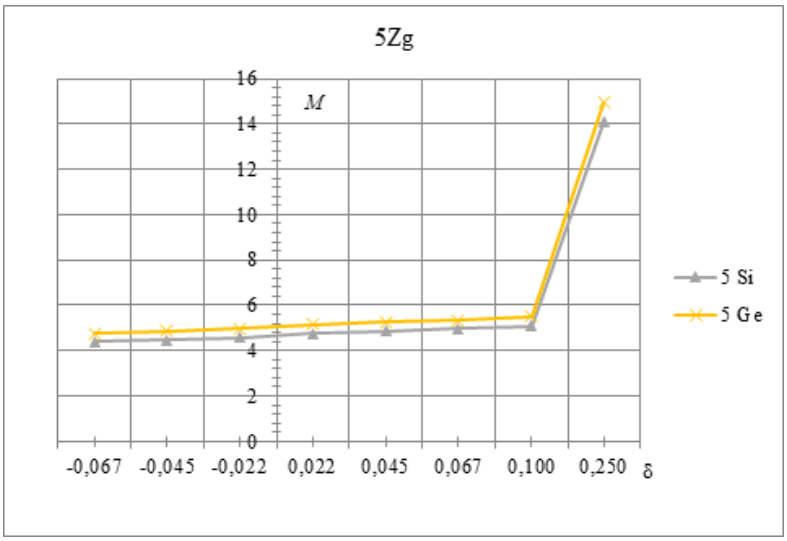

b)

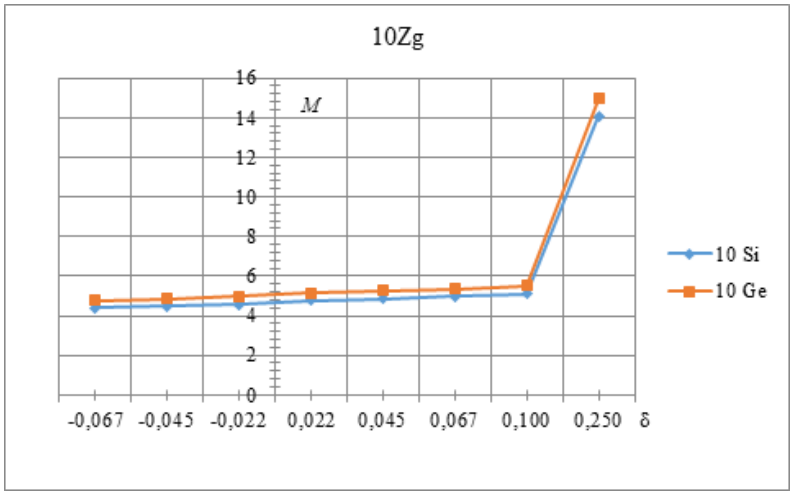

Fig. 4. Longitudinal component *M* of elastic conductivity tensor of zigzag (Zg) SiNR and GeNR nanoribbons with a width of 5 (*a*) and 10 (*b*) primitive cells as function of relative strain δ.
The point δ = 0 is not defined on all curves.

Conclusion

We have carried out theoretical study of piezoresistive properties of perfect silicene and germanene nanoribbons with different types of conductivity within the framework of the Hubbard model, finding several peculiarities in the behavior of the longitudinal component of the elastoconductivity tensor, described above. Quantitative study of the constant M depending on the magnitude of the strain and the width of the nanoribbon yields a more complete picture of the variation in the conductivity of nanoribbons due to tensile or compressive strain. In addition, the longitudinal component of the elastic conductivity tensor of germanene nanoribbons slightly exceeds the component of silicene nanoribbons.

The results obtained can be used for developing electromechanical nanosensors based on the piezoresistive effect, whose main structural element are silicene and germanene nanoribbons.

The study was financially supported by the Russian Foundation for Basic Research as part of scientific project no. 18-31-00130.

REFERENCES

1. **Morozov S.V., Novoselov K.S., Geim A.K.,** Electronic transport in graphene, Phys. Usp. 51 (7) (2008) 744–748.

2. **Lozovik Yu.E., Merkulova S.P., Sokolik A.A.,** Collective electron phenomena in graphene, Phys. Usp. 51 (7) (2008) 727–744.

3. **Chernozatonskii L.A., Sorokin P.B., Artukh A.A.**, New nanostructures based on graphene: physical and chemical properties and applications, Russ. Chem. Rev. 83 (2014) 251–279.

4. Physics of graphene, Edited by Aoki H., Dresselhaus M.S. (Nanoscience and Technology), Springer International Publishing, 2014.

5. **Gert A.V., Nestoklon M.O., Yassievich I.N.,** Band structure of silicene in the tight binding approximation, JETP. 121 (1) (2015) 115–121.

6. **Acun A., Zhang L., Bampoulis P., et al.,** Germanene: the germanium analogue of graphene, Journal of Physics: Condensed Matter. 27 (44) (2015) 443002.

7. **Behzad S.,** Effect of uni-axial and bi-axial strains and vertical electric field on free standing buckled germanene, Journal of Electron Spectroscopy and Related Phenomena. 229 (December) (2018) 13–19.

8. **Ould NE M.L., El hachimi A.G., Boujnah M., et al.,** Comparative study of electronic and optical properties of graphene and germanene: DFT study, Optik. 158 (April) (2018) 693–698.

9. **Kaloni T.P., Schwingenschlugl U.**, Stability of germanene under tensile strain, Chemical Physics Letters. 583 (17 September) (2013) 137–140.

10. **Mortazavi B., Rahaman O., Makaremi M., et al.,** First-principles investigation of mechanical properties of silicene, germanene and stanine, Physica E: Low-dimensional Systems and Nanostructures. 87 (March) (2017) 228–232.

11. **Kazemlou V., Phirouznia A.,** Influence of compression strains on photon absorption of silicene and germanene, Superlattices and Microstructures. 128 (April) (2019) 23–29.

12. **Bukharaev A.A., Zvezdin A.K., Pyatakov A.P., Fetisov Yu.K.,** Straintronics: a new trend in micro- and nanoelectronics and material science, Phys. Usp. 61 (12) (2018) 1175–1212.

13. **McRae A.C., Wei G., Champagne A.R.**, Graphene quantum strain transistors, Physical Review Applied. 11 (5) (2019) 054019.

14. **Landau L.D., Lifshitz E.M.,** Theory of elasticity, 2nd ed., Course of theoretical physics, Vol. 7, Pergamon Press, Oxford, 1981.

15. **Lyapkosova O.S., Lebedev N.G.**, Piezoresistive effect in single-walled carbon nanotubes, Physics of the Solid State. 54 (7) (2012) 1501–1506.

16. **Lebedeva O.S., Lebedev N.G.**, The influence of the stretching and compression deformations on the piezoresistance of the carbon nanotubes and graphene nanoribbons, St. Petersburg State Polytechnical University Journal. Physics and Mathematics. (1(189)) (2014) 26–34.

17. **Lebedeva O.S., Lebedev N.G.**, The piezoresistive effect in doped single-walled carbon nanotubes in the "Hubbard-I" approach, St. Petersburg State Polytechnical University Journal. (2(195)) (2014) 149–161.

18. **Lebedeva O.S., Lebedev N.G.,** Deformation change of the band gap of impurity carbon nanotubes, Russian Journal of Physical Chemistry B: Focus on Physics. 8 (5) (2014) 745–751.

19. **Kvasnikov I.A.,** Termodinamika i statisticheskaja fizika. T. 4: Kvantovaja statistika [Thermodynamics and statistical physics, Vol. 4: Quantum Statistics], KomKniga Publ., Moscow, 2005.

20. **Izyumov Ju.A., Chashhin N.I., Alekseev D.S.,** Teorija sil'no korrelirovannyh sistem. Metod proizvodjashhego funkcionala [The theory of strongly correlated systems. Method of generating functional], Reguljarnaja i Haoticheskaja

Dinamika Publ., Moscow, 2006.

21. **Stepanov N.F.**, Kvantovaya mehanika i kvantovaya himiya [Quantum Mechanics and Quantum Chemistry]. Mir, Moscow, 2001.

22. **Bir G.L., Pikus G.E.**, Symmetry and strain-induced effects in semiconductors, John Wiley & Sons, Inc., New-York, 1974.

23. **Lebedeva O.S., Lebedev N.G., Lyapkosova I.A.**, Piezoconductivity of chiral carbon nanotubes in the framework of the tight-binding method, Mathematical Physics and Computer Simulation. 21 (1) (2018) 53–63.

24. **Li Y., Wang W., Liano K., et. al.,** Piezoresistive effect in carbon nanotube films, Chinese Science Bulletin. 48(2) (2003) 125–127.

25. **Obitayo W., Liu T.,** A review: carbon nanotube-based piezoresistive strain sensors, Journal of Sensors. 2012 (2012), ID 652438, DOI 10.1155/2012/652438.

Received 01.10.2019, accepted 09.12.2019.

THE AUTHORS

LEBEDEVA Olga S.
Volgograd State University
Volgograd State Agricultural University
100, University Ave., Volgograd, 400062, Russian Federation
26, University Ave., Volgograd, 400002, Russian Federation
lebedeva_os@volsu.ru

LEBEDEV Nikolay G.
Volgograd State University
100, University Ave., Volgograd, 400062, Russian Federation
nikolay.lebedev@volsu.ru

LYAPKOSOVA Irina A
Volgograd State Agricultural University
26, University Ave., Volgograd, 400002, Russian Federation
lyapkosova_irina@mail.ru

СПИСОК ЛИТЕРАТУРЫ

1. Морозов С.В., Новоселов К.С., Гейм А.К. Электронный транспорт в графене // Успехи физических наук. 2008. Т. 178. № 7. С. 776–780.

2. Лозовик Ю.Е., Меркулова С.П., Сокоөлик А.А. Коллективные электронные явления в графене // Успехи физических наук. 2008. Т. 178. № 7. С. 758–776.

3. Чернозатонский Л.А., Сорокин П.Б., Артюх А.А. Новые наноструктуры на основе графена: физико-химические свойства и приложения // Успехи химии. 2014. Т. 83. Вып. 3. С. 251–279.

4. Physics of graphene. Edited by Aoki H., Dresselhaus M.S. (Nanoscience and Technology). Switzerland: Springer International Publishing, 2014. 345 p.

5. Герт А.В., Нестоклон М.О., Яссиевич И.Н. Зонная структура силицена в приближении сильной связи // Журнал экспериментальной и теоретической физики. 2015. Т. 148. № 1. С. 133–139.

6. **Acun A., Zhang L., Bampoulis P., et al.,** Germanene: the germanium analogue of graphene // Journal of Physics: Condensed Matter. 2015. Vol. 27. No. 44. P. 443002.

7. **Behzad S.** Effect of uni-axial and bi-axial strains and vertical electric field on free standing buckled germanene // Journal of Electron Spectroscopy and Related Phenomena. 2018. Vol. 229. December. Pp. 13–19.

8. **Ould N.E. M.L., El hachimi A.G., Boujnah M., Benyoussef A., El Kenz A.** Comparative study of electronic and optical properties of graphene and germanene: DFT study // Optik. 2018. Vol. 158. April. Pp. 693–698.

9. **Kaloni T.P., Schwingenschlugl U.** Stability of germanene under tensile strain // Chemical Physics Letters. 2013. Vol. 583. 17 September. Pp. 137–140.

10. **Mortazavi B., Rahaman O., Makaremi M., Dianat A., Cunibertic G., Rabczuk T.** First-principles investigation of mechanical properties of silicene, germanene and stanene // Physica E:

Low-dimensional Systems and Nanostructures. 2017. Vol. 87. March. Pp. 228–232.

11. **Kazemlou V., Phirouznia A.** Influence of compression strains on photon absorption of silicene and germanene // Superlattices and Microstructures. 2019. Vol. 128. April. Pp. 23–29.

12. Бухараев А.А., Звездин А.К., Пяток А.П., Фетисов Ю.К. Стрейнтроника – новое направление микро- и наноэлектроники и науки о материалах // Успехи физических наук. 2018. Т. 188. № 12. С. 1288–1330.

13. **McRae A.C., Wei G., Champagne A.R.** Graphene quantum strain transistors // Physical Review Applied. 2019. Vol. 11. No. 5. P. 054019.

14. Ландау Л.Д., Лифшиц Е.М. Теоретическая физика. Т. VII. Теория упругости. М.: Физматлит, 2003. 264 с.

15. Ляпкосова О.С., Лебедев Н.Г. Пьезорезистивный эффект в однослойных углеродных нанотрубках // Физика твердого тела. 2012. Т. 54. № 7. С. 1412–1416.

16. Лебедева О.С., Лебедев Н.Г. Влияние растяжения и сжатия на пьезорезистивность углеродных нанотрубок и графеновых нанолент // Научно-технические ведомости СПбГПУ. Физико-математические науки. 2014. № 1 (189) С. 26–34.

17. Лебедева О.С., Лебедев Н.Г. Пьезорезистивный эффект в примесных однослойных углеродных нанотрубках в приближении «Хаббард-I» // Научно-технические ведомости СПбГПУ. 2014. № 2 (195). С. 149–161.

18. Лебедева О.С., Лебедев Н.Г. Деформационное изменение запрещенной щели примесных углеродных нанотрубок // Химическая физика. 2014. Т. 33. № 10. С. 73–80.

19. Квасников И.А. Термодинамика и статистическая физика. Т. 4. Квантовая статистика. М.: Комкнига, 2005. 352 с.

20. Изюмов Ю.А., Чащин Н.И., Алексеев Д.С. Теория сильно коррелированных систем. Метод производящего функционала. М.: Регулярная и хаотическая динамика, 2006. 384 с.

21. Степанов Н.Ф. Квантовая механика и квантовая химия. М.: Мир. Изд. Московского ун-та, 2001. 519 с.

22. Бир Г.Л., Пикус Г.Е. Симметрия и деформационные эффекты в полупроводниках. М.: Наука, 1972. 584 с.

23. **Lebedeva O.S., Lebedev N.G., Lyapkosova I.A**. Piezoconductivity of chiral carbon nanotubes in the framework of the tight-binding method // Математическая физика и компьютерное моделирование. 2018. Т. 21. № 1. С. 53–63.

24. **Li Y., Wang W., Liano K., Hu Ch., et. al.** Piezoresistive effect in carbon nanotube films // Chinese Science Bulletin. 2003. Vol. 48. No. 2. Pp. 125–127.

25. **Obitayo W., Liu T.** A review: carbon nanotube-based piezoresistive strain sensors // Journal of Sensors. 2012. Vol. 2012. P. ID 652438, 15 p. DOI 10.1155/ 2012/652438.

Статья поступила в редакцию 01.10.2019, принята к публикации 09.12.2019.

СВЕДЕНИЯ ОБ АВТОРАХ

ЛЕБЕДЕВА Ольга Сергеевна – *кандидат физико-математических наук, ассистент Волгоградского государственного университета,* доцент Волгоградского государственного аграрного университета, г. Волгоград, Российская Федерация.

400062, Российская Федерация, г. Волгоград, Университетский пр., 100.
400002, Российская Федерация, г. Волгоград, Университетский пр., 26.
lebedeva_os@volsu.ru

ЛЕБЕДЕВ Николай Геннадьевич – *доктор физико-математических наук, профессор Волгоградского государственного университета,* г. Волгоград, Российская Федерация.

400062, Российская Федерация, г. Волгоград, Университетский пр., 100.
nikolay.lebedev@volsu.ru

ЛЯПКОСОВА Ирина Александровна – *кандидат сельскохозяйственных наук, доцент Волгоградского государственного аграрного университета,* г. Волгоград, Российская Федерация.

400002, г. Волгоград, Университетский пр., 26.
lyapkosova_irina@mail.ru

DOI: 10.18721/JPM.12405
УДК 532.5+612.13

THE FLOW STRUCTURE IN A THREE-DIMENSIONAL MODEL OF ABDOMINAL AORTIC BIFURCATION: ULTRASONIC AND NUMERICAL STUDY

D.E. Sinitsyna, A.D. Yukhnev, D.K. Zaitsev, M.V. Turkina

Peter the Great St. Petersburg Polytechnic University, St. Petersburg, Russian Federation

A numerical and experimental research of fluid flow structure on a model involving statistical-average bifurcations of the abdominal aorta and iliac arteries with an axisymmetric stenosis in the right common iliac artery has been conducted. It was shown that a two-vortex flow formed in the external iliac artery transforms a downstream into a four-vortex flow. The stenosis in the common iliac artery leads to formation of a recirculation zone behind it, namely, at the inner wall of the vessel. The following spatial bend of the external iliac artery leads to generation of a swirling flow in this vessel. A transitional flow, from a two-vortex to a single-vortex motion, forms in the internal iliac arteries.

Keywords: abdominal aorta's bifurcation, spatial bending of vessel, stenosis, ultrasound Doppler method

Citation: Sinitsyna D.E., Yukhnev A.D., Zaitsev D.K., Turkina M.V., The flow structure in a three-dimensional model of abdominal aortic bifurcation: ultrasonic and numerical study, St. Petersburg Polytechnical State University Journal. Physics and Mathematics. 12 (4) (2019) 43–52 DOI: 10.18721/JPM.12405

УЛЬТРАЗВУКОВОЕ И ЧИСЛЕННОЕ ИССЛЕДОВАНИЕ СТРУКТУРЫ ТЕЧЕНИЯ В ТРЕХМЕРНОЙ МОДЕЛИ БИФУРКАЦИИ БРЮШНОЙ АОРТЫ

Д.Э. Синицына, А.Д. Юхнев, Д.К. Зайцев, М.В. Туркина

Санкт-Петербургский политехнический университет Петра Великого,

Санкт-Петербург, Российская Федерация

Проведено расчетно-экспериментальное исследование структуры стационарного течения жидкости на модели, включающей среднестатистические бифуркации брюшной аорты и подвздошных артерий с осесимметричным стенозом в правой общей подвздошной артерии. Показано, что в наружной подвздошной артерии сначала формируется двухвихревое течение, которое далее, вниз по потоку, трансформируется в течение с четырьмя вихрями. Наличие гемодинамически значимого стеноза в общей подвздошной артерии приводит к формированию за ним отрывной зоны у внутренней стенки сосуда. Следующий за ним пространственный изгиб наружной подвздошной артерии приводит к генерации в ней закрученного течения. Во внутренних подвздошных артериях формируется переходное течение - от двухвихревого к одновихревому.

Ключевые слова: бифуркация брюшной аорты, пространственный изгиб сосуда, стеноз, ультразвуковой доплеровский метод

Ссылка при цитировании: Синицына Д.Э., Юхнев А.Д., Зайцев Д.К., Туркина М.В. Ультразвуковое и численное исследование структуры течения в трехмерной модели бифуркации брюшной аорты // Научно-технические ведомости СПбГПУ. Физико-математические науки. 2019. Т. 4 № .12. С. 50–60. DOI: 10.18721/JPM.12405

Introduction

The abdominal aorta is one of the most important arteries supplying blood to abdominal structures and lower limbs. Aortic occlusion is a common disease of the abdominal aorta occurring near the aortic bifurcation and damaging the surrounding organs, so it requires surgical treatment. Detailed analysis of the structure of flow in this segment of the vascular bed can provide insights into possible locations and causes of pathologies, uncovering data on the exit conditions necessary for simulation of blood flow in femoral arteries downstream.

First studies on flow structure in the abdominal aortic bifurcation were carried out in the 1980s. An experimental study in [1] considered a simplified model of aortic bifurcation, comparing it with with clinical measurements at rest. Velocity profiles in vessels of this model were recorded using magnetic resonance imaging at a Reynolds number Re = 1150. This number is estimated by the average flow rate at the time of maximum flow and by the inlet diameter of the vessel.

Ref. [2] was dedicated to numerical simulation of pulsatile flow in a simplified model of abdominal aortic bifurcation without spatial bends. The sizes of separated regions in the common iliac arteries were considered in two states: at Re = 702 for the resting case and at Re = 1424 for mild exercise (the Reynolds number was estimated by the mean flow velocity averaged over the cardiac cycle and the vessel's inlet diameter).

Generally, different configurations of simplified models of the given region were discussed in literature [2–4]. Flow structure in subsequent bifurcations of iliac arteries was not considered in most cases.

Numerical simulation using patient-specific models based on clinical measurements of the patient's blood vessel geometry is currently the focus of much attention [5, 6]. A number of studies use models with average geometry [7]. However, there are virtually no studies using average models of abdominal aortic bifurcation and subsequent iliac bifurcations; it would prove important to simulate these arteries based on averaged geometry of several groups of patients.

The focus is typically on regions with low shear stresses, associated with formation and development of atherosclerosis, as well as on the effect of wall elasticity on flow structure. For example, it was confirmed in [5] that wall elasticity only insignificantly affects the flow pattern, and the difference in averaged shear stresses in the 'rigid' and 'elastic' simulations does not exceed 10%. Therefore, rigid vessel models can be used as a first approximation in experimental studies [8].

To date, Doppler ultrasound is the most common clinical method for diagnosing blood flow, as it is relatively cheap, non-invasive and easy to use. Ultrasound imaging of the vortex structure of blood flow in vessels with complex spatial configuration opens up new opportunities for doctors, serving to improve the diagnostics of vascular pathologies. Numerical simulation carried out for laminar flow yields detailed information on the velocity fields, making it possible to interpret complex ultrasonic images [9].

This study considers flow structure using a model of the averaged abdominal aortic bifurcation and subsequent iliac bifurcations using the ultrasonic Doppler method and numerical simulation. The study includes analysis of the effect of stenosis in the common iliac artery on the flow structure.

Model of abdominal aortic bifurcation and subsequent bifurcations of the common iliac arteries

The model of the statistically average configuration of abdominal aorta and iliac arteries used in this study was constructed using averaged clinical data [10–15]. This developed model takes into account the characteristic spatial curvature of the vascular region with three bifurcations.

The model includes an outlet segment of the abdominal aorta with a diameter of 18 mm, which is divided into the right and left common iliac arteries with the diameter D = 10.8 mm (Fig. 1).

The common iliac arteries, in turn, are divided into external (diameter of 9.0 mm) and internal (diameter of 5.5 mm) iliac arteries. The total length of the aortic model is 215 mm.

Deviations from the axis of the outlet segment of the abdominal aorta are 20° for the left common illiac artery and 25° for the right one.

The angle between the internal and external iliac arteries is 30° (side view) and 40° (front view).

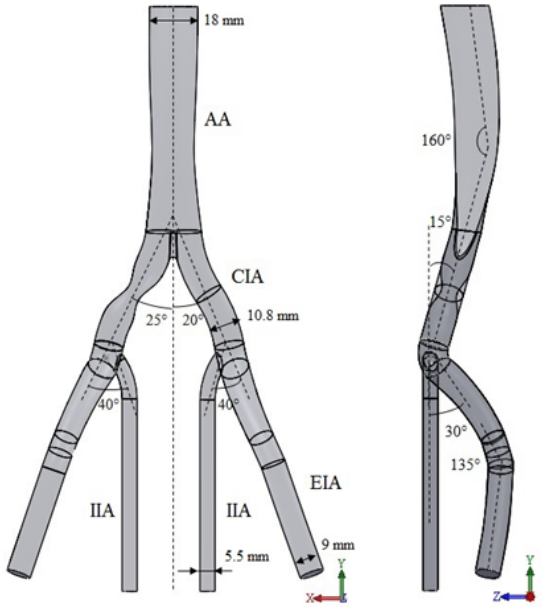

Fig. 1. Model of average bifurcation of abdominal aorta and iliac arteries: abdominal aorta AA, common iliac arteries CIA, external iliac arteries EIA, internal iliac arteries IIA

The angle between the axis of the abdominal aorta and the plane of the common iliac arteries is 160°.

Hemodynamically significant axisymmetric stenosis is located in the right common iliac artery; its length is L_s = 22 mm, drift diameter D_s = 5.9 mm. The stenosis index (by area)

$$\mathrm{STI} = (1 - D_s^2/D^2)\cdot 100\% = 70\%.$$

The variation of the radius R of the vessel in the stenosed region along the vessel axis is given by the formula:

$$R = 0.5D_s + 0.5(D - D_s)\cos^2(\pi y/L_s),$$
$$-L_s/2 \le y \le L_s/2.$$

Since bifurcation of the abdominal aorta is almost symmetric (there is only a slight difference in the deviation angles of the right and left common iliac arteries from the axis of the outlet segment of abdominal aorta), the developed model allowed to carry out a comparative study of the flow in healthy and stenosed branches.

The developed model was designed in the SolidWorks 2016 software package and made using 3D prototyping. The FLGPGR04 photopolymer was used for printing; this made it possible to study the flow using the ultrasonic Doppler method.

Numerical simulation and computational aspects

Numerical simulation of the flow in the given model of a segment of the vascular bed was performed assuming steady-state and laminar nature of the flow. We solved a complete system of Navier–Stokes equations for incompressible Newtonian fluid with constant viscosity.

The following fluid parameters were adopted: dynamic viscosity coefficient μ = 0.004 Pa·s; density ρ = 1050 kg/m^3. The flow rate Q_{AA} = 4 l/min was set at the inlet to the computational domain (this corresponds to maximum flow rate in the abdominal aorta within the cardiac cycle [5]); the flow rates at the outlets from the iliac arteries were set as follows:

0.8 l/min for right EIA,
1.44 l/min for left EIA,
1.04 l/min for left IIA;
zero pressure was set at the outlet from the right IIA.

The values and the ratios of the flow rates in the iliac arteries were selected for the healthy branch based on clinical data [5, 12]. No-slip conditions were imposed on the walls. The characteristic mean flow rates, vessel diameters, and the corresponding Reynolds numbers in the branches of the model are given in Table 1.

The computational domain was mainly covered with a quasi-structured mesh with hexahedral elements with five prismatic layers near the walls. The total number of cells in the

Table 1

Reynolds number Re and mean flow velocities V_b in model branches

Vessel	Re	V_b, cm/s	D, mm
AA	1230	26	18
Right EIA	500	21	9
Right IIA	720	50	5.5
Left EIA	900	38	9
Left IIA	1040	72	5.5

Notation: D is the diameter of the vessel. The names of the vessels are given in caption to Fig. 1.

mesh was about 3 million. The computational mesh was generated using the ICEM 16.2 program. The computations were performed using the ANSYS CFX 16.2 software package, with a second order accuracy of spatial discretization.

Experimental setup and measurement procedure

A setup with a fluid simulating blood circulating in it was assembled for experimental study of the flow structure in the given model. The setup consisted of two closed hydraulic circuits: a working circuit, where the model was installed, and an additional circuit used to fill the working hydraulic circuit with fluid. The experimental setup is shown schematically in Fig. 2.

Centrifugal pump *2* generates constant fluid flow in closed hydraulic circuit *1* at a rate Q = 4 l/min at the inlet to the abdominal aorta. Honeycomb *4*, made of a straight tube 18 mm in diameter, with tubes 2 mm in diameter and 10 mm long glued inside it, is installed at the model inlet to suppress turbulence behind the pump and generate a uniform velocity profile. The flow rate is monitored using sensors *3* of electromagnetic flow meter, installed in front of the honeycomb *4*, on the left external and on both internal iliac arteries. The following

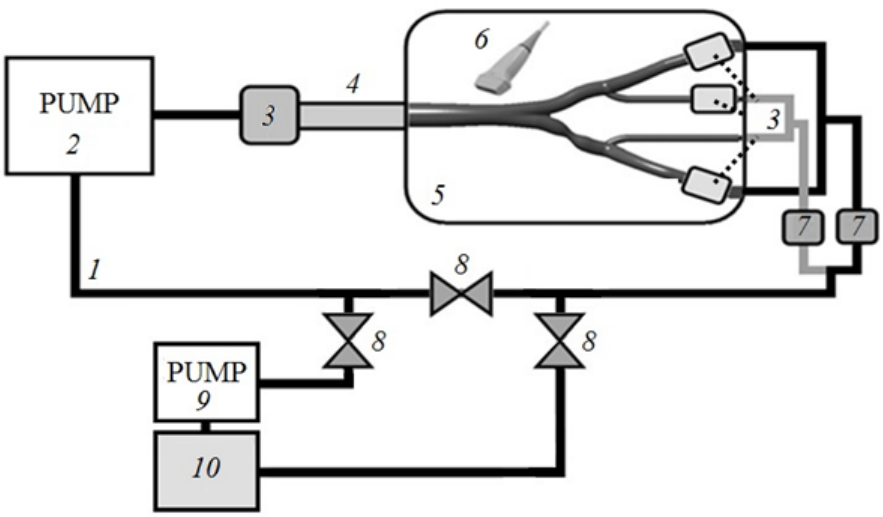

Fig. 2. Schematic of experimental setup:
closed hydraulic circuit *1*; centrifugal and roller pumps *2* and *9*; sensors *3* of electromagnetic flow meter; honeycomb *4*; acoustic tray *5* with model of bifurcations of abdominal aorta and illiac arteries; sensor *6* of ultrasonic scanner; flow control valves *7*; liquid drainage valves *8*; container *10* with fluid simulating blood

flow rate ratios were set at the outlets from the healthy and stenosed branches using regulators 7:

Q_{EIA}/Q_{IIA} = 1.1 in the right branch;

Q_{EIA}/Q_{IIA} = 1.4 in the left branch,

which corresponds to the boundary conditions and the computational results.

The fluid simulating blood was a 36% aqueous glycerin solution with NaCl added (10 g/l), which is necessary for the sensor of the electromagnetic flow meter to operate. The density of the fluid was ρ = 1050 kg/m^3, the viscosity was close to the viscosity of blood and was μ = 0.004 Pa·s.

An ultrasonic LogicScan 64 scanner, equipped with a linear transducer with an operating frequency of 5–7 MHz, was used for measuring the velocity field in the model. The Doppler velocity spectrum was displayed on a computer screen in real time via the EchoWave II interface processing scanner signals. A suspension of gouache paint (5 g/l) was used as scattering ultrasonic particles.

Fields of axial velocity V_n and the projection of transverse velocity V_t on the axis of the ultrasonic sensor were visualized by color Doppler imaging. The ultrasonic sensor was installed at an angle of 60° to the vessel axis to measure the axial velocity, and at an angle of 90° to measure the transverse velocity projection. Shades of red, blue and gray are used as a scale for blood flow velocity in CDI. Red corresponds to the regions with velocities directed toward the sensor, blue to the velocities directed away from the sensor, gray to low velocities that cannot be reliably measured by the ultrasonic sensor.

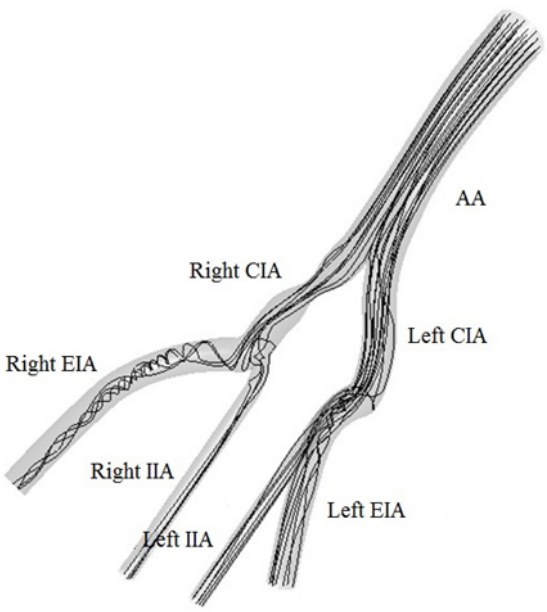

Fig. 3. Calculated streamlines in model of abdominal aortic bifurcation.
Full names of the vessels are given in caption to Fig. 1

Effect of stenosis on flow structure

Computations confirm that a complex vortex structure transforming along the vessel evolves in the given model of the bifurcation of the abdominal aorta and subsequent bifurcations of the iliac arteries. Fig. 3 shows the general picture of the streamlines. Apparently, regular structure of the flow changes considerably behind the stenosis. The positions and sizes of reverse flow regions are determined by the axial velocity fields (Fig. 4). A small region with reverse currents (negative velocities shaded in dark gray, occupying about 10% of the cross-sectional area) is observed behind the bifurcation of the common iliac artery in the branch without stenosis, disappearing at a distance of two calibers downstream.

Stenosis generates a separated region near the inner wall of the common iliac artery, persisting along the entire length of the external iliac artery. Separated regions do not form in the internal iliac arteries, regardless of whether there is stenosis upstream or not (Fig. 4).

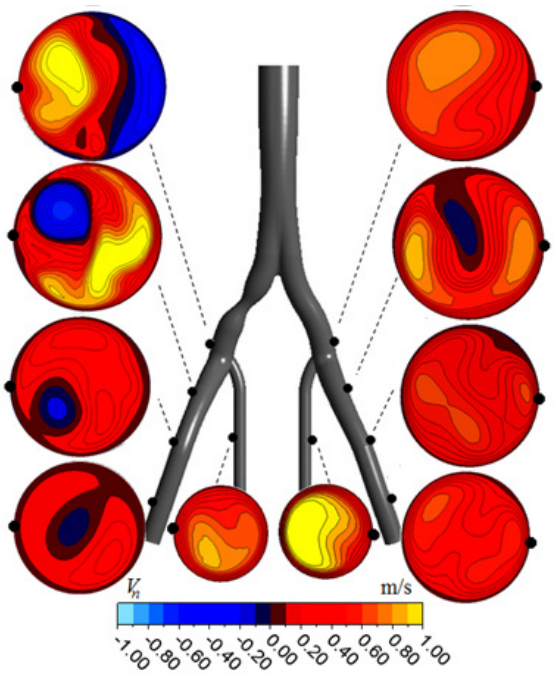

Fig. 4. Calculated effect of stenosis on axial velocity field V_n (m/s)
Scale of blood flow rate in vessel cross-sections: shades of red correspond to axial velocity directed toward the ultrasonic sensor, shades of blue to axial velocity directed away from the sensor, and dark shades to low velocities

Notably, there is a wide variety of vortex structures in the given model (Fig. 5, *a*, *b*).

Computations indicate that two-vortex flow evolves behind the bifurcation of the abdominal aorta in the common iliac arteries. Paired Dean vortices are detected in the branch without stenosis, after the first bifurcation in the common iliac arteries. The vortices are then transformed, generating four-vortex flow at the outlet from the given artery segment.

Two-vortex flow behind the stenosis is transformed into single-vortex, which persists along the entire length of the right external iliac artery.

Transitional flow from two-vortex to single-vortex forms at the outlet of the given segments of the internal iliac arteries; one of the vortices is considerably larger than the other.

Comparison of computational and experimental results

Computed fields of transverse velocity are compared with experimental results in Table 2. The table includes two types of data for the fields of transverse velocity projected onto the axis of the ultrasonic sensor: ultrasound images and computed fields constructed by the CDI scale of the ultrasound scanner. In addition, pictures of computed streamlines of transverse flow are given, allowing to determine the number, location, and shape of the vortices in several cross-sections of the model. The cross-sections compared show diverse vortex structures. The directions of transverse velocity projected onto the axis of the sensor are marked with arrows for each region in the ultrasound images. The sensor is located near the top of the ultrasound images.

The flow narrows in the convergent region in front of the bifurcation of the abdominal aorta; this is characterized by a two-color ultrasound image (cross-section *1*): here the region of negative projection of transverse velocity is closer to the sensor and the region of positive projection is further away from it.

Pronounced swirling flow evolving in the external iliac artery (in the stenosed branch) is characterized by a two-color ultrasound image (cross-section *2*), the boundary between these regions is approximately parallel to the axis of the ultrasonic transducer: the region with negative projection of transverse velocity (blue) is on the left, and the region with positive projection on the right (red).

Two-vortex flow (cross-section *3*) evolves after the bifurcation of the common iliac artery; it is characterized by a combination of several regions in the ultrasound image: positive

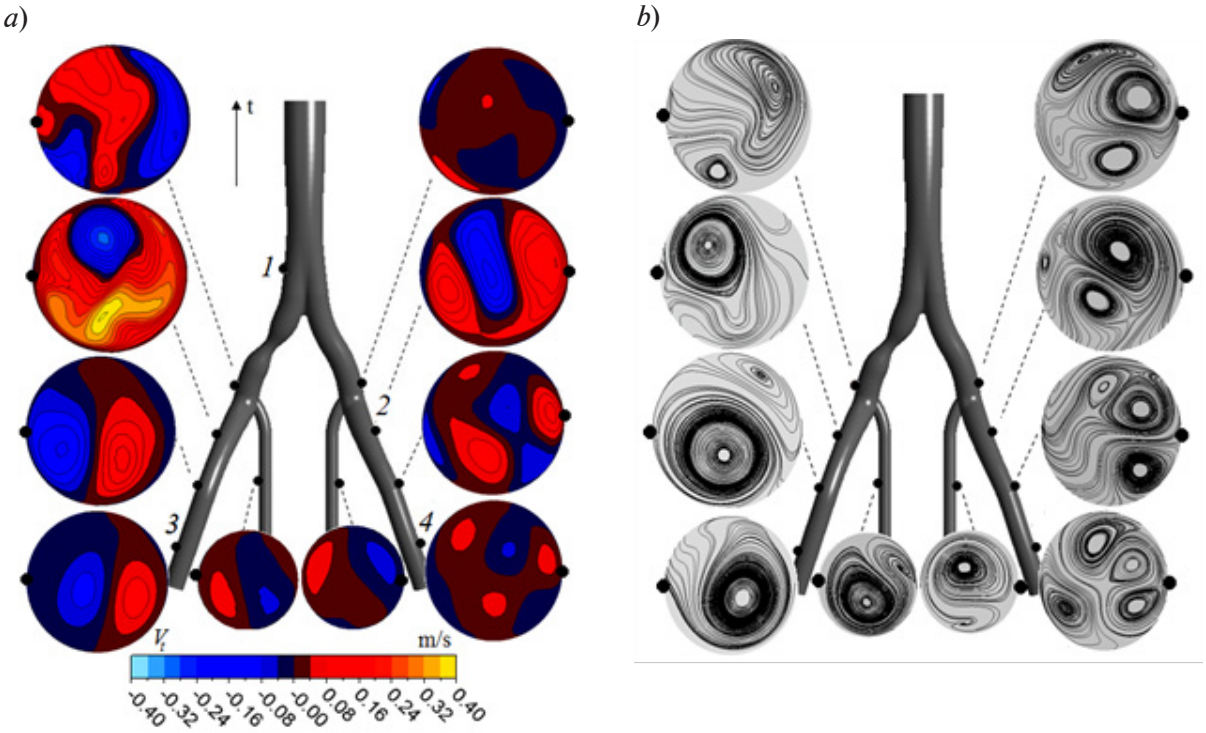

Fig. 5. Calculated effect of stenosis on structure of transverse flow: isolines of velocity (*a*) and streamlines (*b*)

Numbers indicate the cross-sections comparing the calculated results in Table 2 with ultrasonic measurements

Table 2

Comparison of calculated and measured fields of projected transverse velocity

Cross-section	Field of transverse velocity projected on axis of ultrasonic sensor		Streamlines of transverse flow
	Result of ultrasound experiment	Computational result	
	Stenosed flow		
1	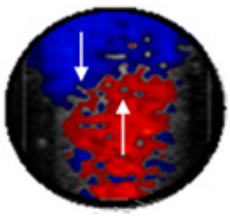	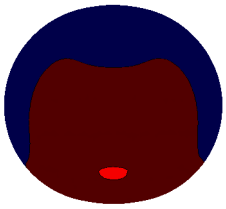	
	Two-vortex flow		
2		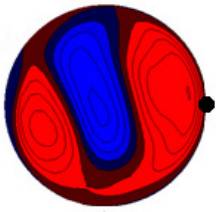	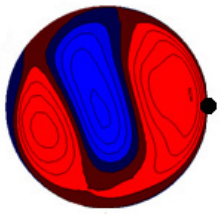
	Single-vortex flow		
3		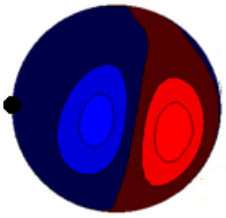	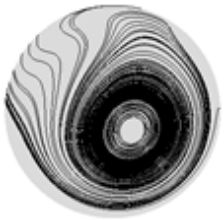
	Four-vortex flow		
4		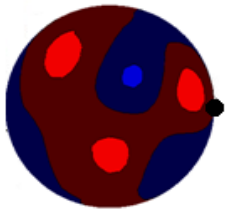	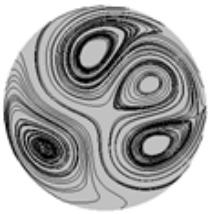
	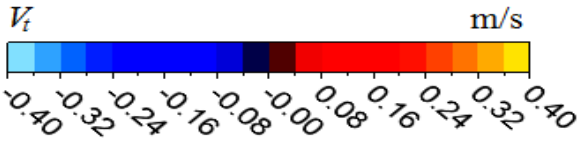		

Note. The locations of numbered cross-sections of the vessels are shown in Fig. 5.

projection on the left (red color), negative at the center (blue) and positive on the right (red)

Analysis of the data indicates that experimental results qualitatively agree with the computational results. Single vortex flow is clearly observed in ultrasound images. The picture becomes more complex if the number of vortices increases to two; the sizes of the region with positive projection of transverse velocity somewhat differe from the computational results. However, in general, the locations of the regions correspond to the computations. More complex flow formed by four vortices with low intensity (cross-section *4*) was difficult to detect by Doppler color imaging.

Conclusion

Numerical simulation and measurements by the ultrasonic Doppler method were used to obtain detailed information on the flow structure in a model including average bifurcation of the abdominal aorta, bifurcation of the common iliac arteries and segments of external and internal iliac arteries.

Two-vortex flow evolves in a spatially curved external iliac artery without stenosis, transforming into four-vortex flow downstream. Hemodynamically significant stenosis in the common iliac artery generates a separated region which is preserved along the entire length of the artery. Spatial bends of the external iliac artery after the stenosis generate swirling flow in the artery. Transitional flow from two-vortex to single-vortex forms at the outlet of the given segments of the internal iliac arteries; one of the vortices is considerably larger than the other.

Numerical modeling confirmed that ultrasound sensors can be used to detect one- and two-vortex structures of transverse flow in a spatial model of the vascular bed. In particular, the direction of rotation, the intensity and the position of the vortices can be determined by the ultrasound method.

This study was financially supported by the Russian Foundation for Basic Research (Title: Spatial and temporal structure of blood flow in bifurcation of healthy abdominal aorta and that with occlusive lesions of iliac arteries), RFBR grant No. 18-01-00629.

REFERENCES

1. **Moore J.E., Ku D.N.,** Hemodynamics in the abdominal aorta: a comparison of *in vitro* and *in vivo* measurements, Journal of Applied Physiology. 76 (4) (1994) 1520–1527.

2. **Lee D., Chen, J.Y.,** Pulsatile flow fields in a model of abdominal aorta with its peripheral branches, Biomedical Engineering: Applications, Basis & Communications. 15 (5) (2003) 170–178.

3. **Long Q., Xu X.Y., Bourne M., Griffith T.M.,** Numerical study of blood flow in an anatomically realistic aorto-iliac bifurcation generated from MRI data, Magnetic Resonance in Medicine. 43 (4) (2000) 565–576.

4. **Lee D., Chen J.Y.,** Numerical simulation of steady flow fields in a model of abdominal aorta with its peripheral branches, Journal of Biomechanics. 35 (8) (2002) 1115–1122.

5. **Ke L., Wentao J., Yu C., et al.,** Fluid-solid interaction analysis on iliac bifurcation artery: a numerical study, international, Journal of Computational Methods. 16 (5) (2018) 1–18.

6. **Soares A.A., Gonzaga S., Oliveira C., et al.,** Computational fluid dynamics in abdominal aorta bifurcation: non-Newtonian versus Newtonian blood flow in a real case study, Computer Methods in Biomechanics and Biomedical Engineering. 20 (8) (2017) 1–10.

7. **Gataulin Y.A., Zaitsev D.K., Smirnov E.M., Yukhnev A.D.,** Structure of unsteady flow in the spatially curved model of the common carotid artery with stenosis: a numerical study, Russian Journal of Biomechanics. 23 (1) (2019) 58–66.

8. **Yukhnev A.D., Sinitsyna D.E.,** The blood vessel models: the technology development for making and following investigation, St. Petersburg State Polytechnical University Journal: Physics and Mathematics. (3(153)) (2012) 75–79.

9. **Gataulin Y.A., Zaitsev D.K., Smirnov E.M., et al.,** Weakly swirling flow in a model of blood vessel with stenosis: numerical and experimental study, St. Petersburg Polytechnical University Journal: Physics and Mathematics. 1 (4) (2015) 364–371.

10. **Lorbeer R., Grotz A., Dцrr M., et al.,** Reference values of vessel diameters, stenosis prevalence, and arterial variations of the lower limb arteries in a male population sample using contrast-enhanced MR angiography, PLoS One. 13 (6) (2018), e0197559. https://doi.org/10.1371/journal.pone.0197559

11. **Cuomo F., Roccabianca S., Dillon-Murphy D., et al.,** Effects of age-associated regional changes in aortic stiffness on human hemodynamics revealed by computational modeling, PLoS One. 12 (3) (2017) e0173177. https://doi.org /10.1371/journal.pone.0173177.

12. **Kurra V., Schoenhagen P., Roselli E.E., et al.,** Prevalence of significant peripheral artery disease in patients evaluated for percutaneous aortic valve insertion: preprocedural assessment with multidetector computed tomography, The Journal of Thoracic and Cardiovascular Surgery. 137 (5) (2009) 1258–1264.

13. **Shah P.M., Scartont H.A., Tsapogas M.J.,** Geometric anatomy of the aortic-common iliac bifurcation, Journal of Anatomy. 126 (Pt. 3) (1978) 451–458.

14. **O'Flynn P.M., O'Sullivan G., Pandit A.S.,** Geometric variability of the abdominal aorta and its major peripheral branches, Annals of Biomedical Engineering. 38 (3) (2010) 824–840.

15. **Yeung J.J., Jin Kim H., Abbruzzese T.A., et al.,** Aortoiliac hemodynamic and morphologic adaptation to chronic spinal cord injury, Journal of Vascular Surgery. 44 (6) (2007) 1254–1265.

Received 01.10.2019, accepted 15.11.2019.

THE AUTHORS

SINITSYNA Daria E.
Peter the Great St. Petersburg Polytechnic University
29 Politechnicheskaya St., St. Petersburg, 195251, Russian Federation
sinicina.daria@yandex.ru

YUKHNEV Andrey D.
Peter the Great St. Petersburg Polytechnic University
29 Politechnicheskaya St., St. Petersburg, 195251, Russian Federation
a.yukhnev@mail.ru

ZAITSEV Dmitrii K.
Peter the Great St. Petersburg Polytechnic University
29 Politechnicheskaya St., St. Petersburg, 195251, Russian Federation
zaitsev-aero@yandex.ru

TURKINA Maria V.
Peter the Great St. Petersburg Polytechnic University
29 Politechnicheskaya St., St. Petersburg, 195251, Russian Federation
turkinamaria@mail.ru

СПИСОК ЛИТЕРАТУРЫ

1. **Moore J.E., JR., Maier S.E., Ku D.N., Boensiger P.** Hemodynamics in the abdominal aorta: a comparison of *in vitro* and *in vivo* measurements // Journal of Applied Physiology. 1994. Vol. 76. No. 4 Pp. 1520–1527.

2. **Lee D., Chen J.Y.** Pulsatile flow fields in a model of abdominal aorta with its peripheral branches // Biomedical Engineering: Applications, Basis & Communications. 2003. Vol. 15. No. 5. Pp. 170–178.

3. **Long Q., Xu X.Y., Bourne M., Griffith T.M.** Numerical study of blood flow in an anatomically realistic aorto-iliac bifurcation generated from MRI data //Magnetic Resonance in Medicine. 2000. Vol. 43. No. 4. Pp. 565–576.

4. **Lee D., Chen J.Y.** Numerical simulation of steady flow fields in a model of abdominal aorta with its peripheral branches // Journal of Biomechanics. 2002. Vol. 35. No. 8. Pp. 1115–1122.

5. **Ke L., Wentao J., Yu C., Xiaobao T., Zhihong Z., Ding Y.** Fluid-solid interaction analysis on iliac bifurcation artery: a numerical study // International Journal of Computational Methods. 2018. Vol. 16. No. 5. Pp. 1–18.

6. **Soares A.A., Gonzaga S., Oliveira C., Simxes A., Rouboa A.I.** Computational fluid dynamics in abdominal aorta bifurcation: non-Newtonian versus Newtonian blood flow in a real case study // Computer Methods in Biomechanics and Biomedical Engineering. 2017. Vol. 20. No. 8. Pp. 1–10.

7. **Гатаулин Я.А., Зайцев Д.К., Смирнов Е.М., Юхнев А.Д.** Структура нестационарного течения в пространственно-извитой модели общей сонной артерии со стенозом: численное исследование // Российский жур-

нал биомеханики. 2019. Т. 23. № 1. С. 69–78.

8. Юхнев А.Д., Синицына Д.Э. РазработА ка технологии изготовления и исследование моделей кровеносных сосудов // Научно-технические ведомости СПбГПУ. Физико-математические науки. 2012. № 3(153). С. 75–79.

9. **Гатаулин Я.А.,** Зайцев Д.К., Смирнов Е.М., Федорова Е.А., Юхнев А.Д. Расчетно-экспериментальное исследование слабозакрученного течения жидкости в модели кровеносного сосуда со стенозом // Научно-технические ведомости СПбГПУ. Физико-математические науки. 2015. № 4 (230). С. 36–47.

10. **Lorbeer R., Grotz A., Dцrr M., Vцlzke H., Lieb W., Kьhn J.-P., Mensel B.** Reference values of vessel diameters, stenosis prevalence, and arterial variations of the lower limb arteries in a male population sample using contrast-enhanced MR angiography // PLoS One. 2018. Vol. 13. No. 6. e0197559. https://doi.org/10.1371 /journal.pone.0197559

11. **Cuomo F., Roccabianca S., Dillon-Murphy D., Xiao N., Humphrey J.D. Figueroa C.A.** Effects of age-associated regional changes in aortic stiffness on human hemodynamics revealed by computational modeling // PLoS One. 2017. Vol. 12. No. 3. e0173177. https://doi.org/10.1371/journal.pone.0173177

12. **Kurra V., Schoenhagen P., Roselli E.E., et al.** Prevalence of significant peripheral artery disease in patients evaluated for percutaneous aortic valve insertion: preprocedural assessment with multidetector computed tomography // The Journal of Thoracic and Cardiovascular Surgery. 2009. Vol. 137. No. 5. Pp. 1258–1264.

13. **Shah P.M., Scartont H.A., Tsapogas M.J.** Geometric anatomy of the aortic-common iliac bifurcation // Journal of Anatomy. 1978. Vol. 126. Pt. 3. Pp. 451–458.

14. **O'Flynn P.M., O'Sullivan G., Pandit A.S.** Geometric variability of the abdominal aorta and its major peripheral branches // Annals of Biomedical Engineering. 2010. Vol. 38. No. 3. Pp. 824–840.

15. **Yeung J.J., Jin Kim H., Abbruzzese T.A., et al.** Aortoiliac hemodynamic and morphologic adaptation to chronic spinal cord injury // Journal of Vascular Surgery. 2007. Vol. 44. No. 6. Pp. 1254–1265.

Статья поступила в редакцию 01.10.2019, принята к публикации 15.11.2019.

СВЕДЕНИЯ ОБ АВТОРАХ

СИНИЦЫНА Дарья Эдуардовна – *аспирантка кафедры «Гидроаэродинамика, горение и теплообмен» Санкт-Петербургского политехнического университета Петра Великого.*
195251, Российская Федерация, г. Санкт-Петербург, Политехническая ул., 29
sinicina.daria@yandex.ru

ЮХНЕВ Андрей Данилович – *заведующий учебной лабораторией кафедры «Гидроаэродинамика, горение и теплообмен» Санкт-Петербургского политехнического университета Петра Великого.*
195251, Российская Федерация, г. Санкт-Петербург, Политехническая ул., 29
a.yukhnev@mail.ru

ЗАЙЦЕВ Дмитрий Кириллович – *доктор физико-математических наук, профессор кафедры «Гидроаэродинамика, горение и теплообмен» Санкт-Петербургского политехнического университета Петра Великого.*
195251, Российская Федерация, г. Санкт-Петербург, Политехническая ул., 29
zaitsev-aero@yandex.ru

ТУРКИНА Мария Валерьевна – *студентка кафедры «Гидроаэродинамика, горение и теплообмен» Санкт-Петербургского политехнического университета Петра Великого.*
195251, Российская Федерация, г. Санкт-Петербург, Политехническая ул., 29
turkinamaria@mail.ru

DOI: 10.18721/JPM.12406
УДК 537.856

THE HEATING OF A DIAPHRAGM SPRING USING INDUCTION TECHNIQUE: PARAMETRIC MODELING

E.R. Mannanov, S.A. Galunin

St. Petersburg Electrotechnical University "LETI", St. Petersburg, Russian Federation

The configuration and work of a system for local heating of a diaphragm spring by induction technique have been studied. The problem-oriented 3D model, developed using ANSYS APDL, made possible to analyze effects of geometric, electrical and positional parameters on temperature distribution over the considered product in its electromagnetic heat treatment. In particular, the temperature fields were obtained varying spring finger number and length, as well as control of finger bend by setting up a heating mode. The main connections between the final temperature distributions and the geometry of the heated product were established. The heating was generated using both longitudinal and transverse magnetic fields.

Keywords: induction heating, numerical simulation, optimization, heat treatment, diaphragm spring

Citation: Mannanov E.R., Galunin S.A., The heating of a diaphragm spring using induction technique: parametric modeling, St. Petersburg Polytechnical State University Journal. Physics and Mathematics. 12 (4) (2019) 53–60. DOI: 10.18721/JPM.12406

ПАРАМЕТРИЧЕСКОЕ МОДЕЛИРОВАНИЕ ПРОЦЕССА НАГРЕВА ДЕМПФЕРНОЙ ПРУЖИНЫ ИНДУКЦИОННЫМ МЕТОДОМ

Э.Р. Маннанов, С.А. Галунин

Санкт-Петербургский государственный электротехнический университет «ЛЭТИ»

имени В.И. Ульянова (Ленина), Санкт-Петербург, Российская Федерация

Исследованы конфигурация и работа системы для локального нагрева демпферной пружины индукционным методом. Проблемно-ориентированная 3D модель, разработанная на базе ANSYS APDL, позволила изучить влияние геометрических, электрических и позиционных параметров на температурное распределение по рассматриваемому изделию при его электромагнитной термообработке. В частности, получены температурные поля при вариации количества и длины пальцев демпферной пружины, при регулировании зоны отгиба пальцев с настройкой режима нагрева. Установлены основные связи конечных температурных распределений с геометрией нагреваемого изделия. Нагрев осуществляли с использованием как продольного, так и поперечного магнитных полей.

Ключевые слова: индукционный нагрев, численное моделирование, оптимизация, термообработка, демпферная пружина

Ссылка при цитировании: Маннанов Э.Р., Галунин С.А. Параметрическое моделирование процесса нагрева демпферной пружины индукционным методом // Научно-технические ведомости СПбГПУ. Физико-математические науки. 2019. Т. 4 № .12. С. 61–68. DOI: 10.18721/JPM.12406

Introduction

Numerous studies have been dedicated to electromagnetic and thermal processes occurring induction heat treatment of products, focusing, in particular, on products with rotational symmetry. For example, heating of metal workpieces shaped as disks or rings is widely used in different industrial technologies; it is particularly important for design of induction coils [1–10].

Most cases of heating require either achieving a uniform temperature distribution throughout the entire volume of the object or maintaining a local temperature region. A classical spiral or loop induction coil is typically used as a disk, located under the object. The configuration of the induction system can be single or multi-turn; eddy currents in the disk then have rotational symmetry. This provides an additional opportunity to control the temperature field by rotating the disk. Eddy currents have a dead zone in the center in this problem statement, and different cooling conditions should be expected in the heated area during heat treatment of a disk with a complex profile. After heating or cooling the product, a heterogeneity of the temperature field naturally appears.

The characteristics of a diaphragm spring depend on its geometric dimensions. The operational characteristics of the mechanism equipped with such a spring (for example, a car clutch) generally change as well.

Since the geometry of the workpiece cannot be altered to achieve the goals of heating and obtain the desired parameters for residual stresses, calculations establishing the necessary level of strength and elasticity are performed first [1]. The optimal shape of the diaphragm spring serves to distribute loads (dynamic and static, constant and thermocyclic, bending loads); heat treatment of this spring is aimed at achieving a balance between the necessary strength in the fingers and the ductility of the diaphragm spring disk. Because of this, not only the geometric parameters of the workpiece but also the technology by which it is manufactured are important for selecting the temperature for heat treatment.

This paper presents a numerical study of induction heating of diaphragm springs for trucks. Such springs are produced by die stamping. The clutch assembly of the truck is hardened by a single stroke with the stamping die, modeling the workpiece into the required shape; the assembly is then heated to 450 °C for subsequent tempering.

Parametric studies of electrothermal processes

The standard number of fingers (Fig. 1) located around the circumference of the diaphragm spring disk was 24, 20, 18, and 12.

The given system is symmetric, so rather than simulate the complex geometry of the workpiece, we decided to simulate only a single section using azimuthal periodicity of the workpiece structure.

We used the following initial data for simulating the diaphragm spring:

Number of fingers.....12, 18, 20, 24

Corresponding computational domains deg(min).....15(0), 10(0), 9(0), 7(5)

The experimental data from [2] is used for the rest of the initial data (design and electrical parameters of the induction coil, mutual positioning and heating time), the heating problem, the criterion for assessing whether the target set (the given temperature level) is achieved.

The nonlinear coefficients used in the simulated system are related to the dependences of the properties of metal workpieces on temperature and electromagnetic field strength, which explains the relationship between electromagnetic and thermal problems. We provided a detailed description for the algorithm for direct simulation of the problem with a coupled electrothermal solution of induction heating of a disk in [3, 9].

Fig. 1 shows a schematic of the diaphragm spring. The initial computational domain *2* is a flat sector of a circle with a central angle of 9°. This means that the basic design of the diaphragm spring has 20 fingers. The estimated time required for calculation with the given accuracy is thus reduced by 40 times. The total height of the unloaded spring is taken equal to the height of the loaded one. In other words, the workpiece does not have the curvature necessary for operation, and has a flat shape under load. This aspect is not particularly important for the heat treatment procedure; actually, in order to maintain uniform local heating, the turns of the heater should be located:

a) on one axis;

b) strictly parallel to the plane relative to the heating zone.

An arrangement complying with the above requirements allows to adjust the input power by changing the current in the induction coil, turn pitch and the width of the air gap.

The parametric study is performed based on the developed parametric 3D model (Fig. 2).

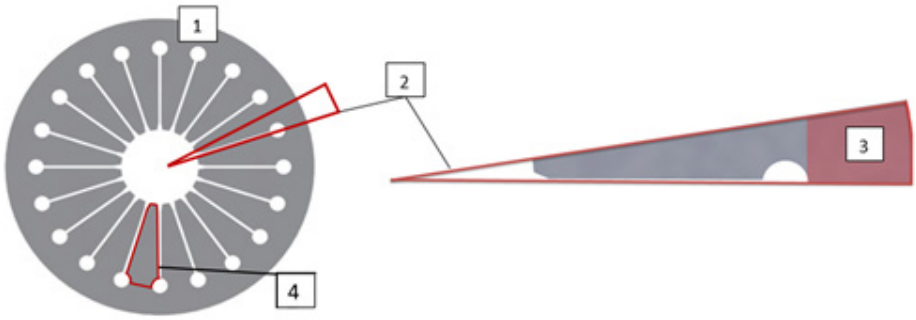

Fig. 1. Schematic problem statement:
general view of workpiece *1;* simulation zone *2;* heating zone *3;* finger *4* of diaphragm spring

Fig. 2. Finite-element 3D system: induction coil *1*, diaphragm spring *2*

It is assumed that the bend zone of the fingers is the most critical in terms of hot spots appearing. The effect that the shape of the finger bend had on the temperature field was estimated at the first stage of the study to account for this risk. Fig. 3 shows a comparison of calculated temperature distributions in the workpiece for poor and desirable quality of processing in the finger bend. The workpiece was heated in a longitudinal magnetic field.

Simulation allowed to estimate the probability with which hot spots appeared in the finger bend, using a configuration similar to that described in [2, 3] for the induction coil, where it was used to heat a disk with a simple profile. According to our estimate, the highest density of induced currents should be reached in the finger bend zone due to random walks of eddy currents. Because the workpiece has a complex shape, the heat dissipation conditions vary and depend on the measurement point. The edges of the disk have the best heat dissipation due to their small thickness, and this prevents overheating in finger bend zones. Comparing our experimental data [2] and the results of numerical simulation, we can confirm that the final temperature profile on the surface in the heating zone is satisfactorily uniform with a minimal temperature difference around the disk circumference.

We studied the heating process based on the developed parametric finite-element 3D model, taking into account the main factors affecting the temperature field by varying the current system parameters. This study included the following factors affecting the temperature distribution of the workpiece:

overall dimensions of the diaphragm spring (Figs. 4–6);

number of fingers of the given spring when regulating the computational domain (Figs. 4–6);

heating in a transverse magnetic field; anti-parallel connection is set for the turns of the induction coil for this purpose (Fig. 6).

Analysis of the obtained simulation data allowed us to draw the following conclusions.

1. The effective current affects only the maximum temperature level but not the temperature distribution.

2. Making the fingers of the diaphragm spring longer improves heat dissipation from the heating zone, which ensures a high temperature difference and provides a decrease in temperature relative to the target temperature level set.

3. Regulating the number of fingers by varying the computational domain leads to qualitative change in the generated temperature field.

4. The dimensions of the diaphragm spring (outer diameter, disk thickness, width of its heating zone) play a significant role in generating the temperature distribution. The increase in mass of the workpiece is accompanied by an increase in the energy input required to ensure heating to a given temperature level, and vice versa (its decrease is accompanied by a decrease in energy input). For example, a source power of 44 kW is required to provide effective heating to the required temperature level for a workpiece with a diaphragm spring with an external diameter of 420 mm, a thickness of 3 mm, a frequency of the heating electromagnetic field of 2.5 kHz, and an air gap of 10–11 mm between the workpiece and the induction coil; power of 15 kW is sufficient if the diameter is reduced to 268 mm.

5. A uniform temperature distribution over the given area in the range of the target temperature level can be achieved by induction heating in a longitudinal magnetic field.

The study has allowed to develop practical recommendations for optimizing the heating process. In particular, we recommend to use rounded chamfers in finger bend zone in order to avoid heat concentration and hot spots.

Modifying the properties of the material when selecting the heat treatment temperature is of great interest for calculating the nonlinear operating characteristic of elasticity of materials in a wide temperature range. Treatment temperatures differ depending on the grade of steel and its purpose, so the mechanical properties of the heat-treated workpiece obtained can vary significantly. This is true for a number of technologies: hardening, forging, annealing, normalizing, tempering, as well as combinations of different heat treatments (for example, preliminary heating – quenching – tempering, normalizing – tempering, quenching – self-tempering, quenching – aging, etc.). If necessary, study and analysis of specific cases should be carried out in advance to optimize the properties of the material for a given purpose. The temperature and the heating zone for tempering should be determined taking into account the required properties of the material.

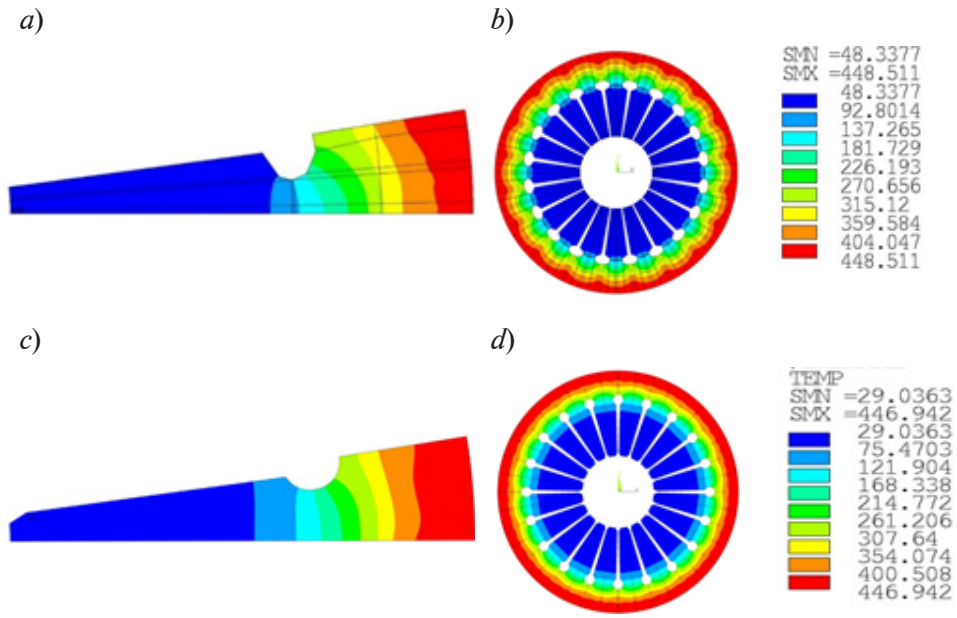

Fig. 3. Final temperature distributions over computational domain of 9° (*a*, *c*) and over workpiece (*b*, *d*) after heating in longitudinal magnetic field with poor (*a*, *b*) and desired (*c*, *d*) surface treatment of diaphragm spring in finger bend zone.

Diaphragm spring has 20 fingers

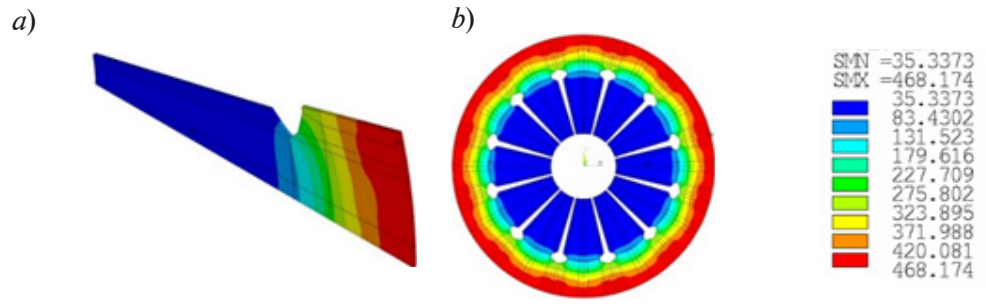

Fig. 4. Final temperature distribution after heating of diaphragm spring 405 mm in diameter in longitudinal magnetic field with effective current of 300 A: computational domain *a,* 15°, complete finite-element solution *b*
Diaphragm spring has 12 fingers

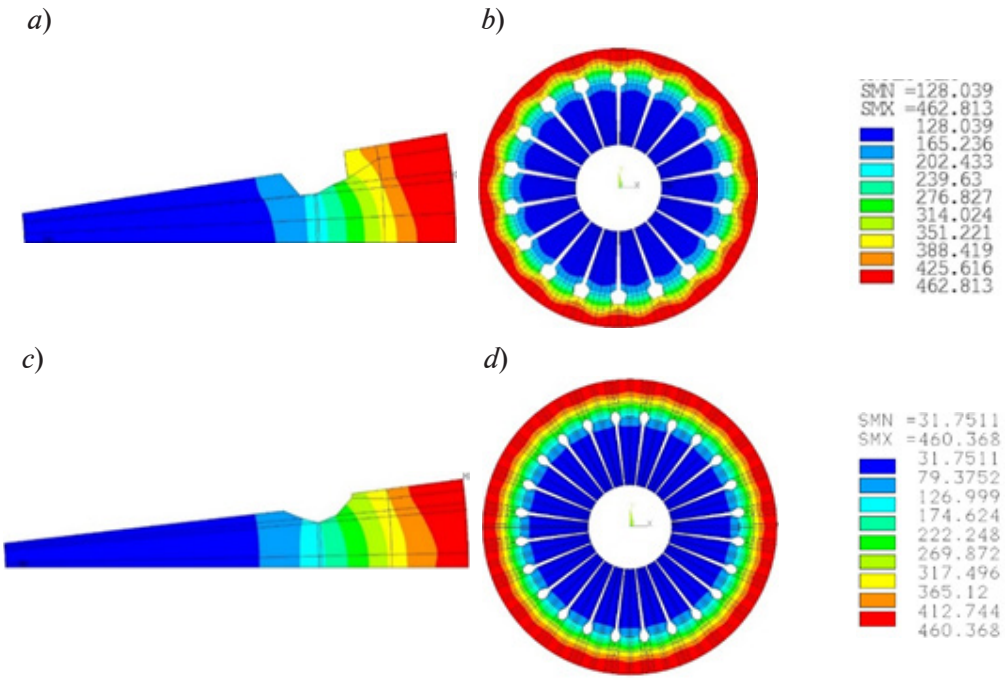

Fig. 5. Final temperature distributions after heating of diaphragm spring 350 mm in diameter in longitudinal magnetic field with effective current of 185 A (*a*, *b*) и 288 A (*c*, *d*)
Computational domains are 10°0’ (*a*) and 7°5’ (*c*)
Diaphragm spring has 18 (*a*, *b*) and 24 (*c*, *d*) fingers

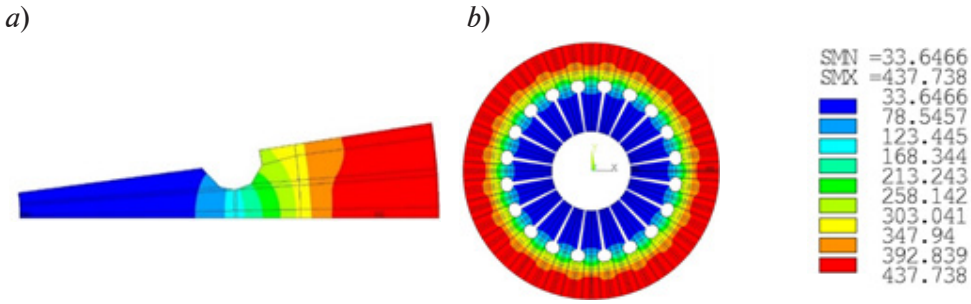

Fig. 6. Final temperature distribution after heating of diaphragm spring 405 mm in diameter in longitudinal magnetic field with effective current of 450 A
Computational domain is 9°
Diaphragm spring has 20 fingers.

Conclusion

Parametric modeling of induction heating of a diaphragm spring was successfully used to study and search for geometric, positional and electrical configurations of the system comprising an induction coil and a workpiece for solving the problem on local heating of the diaphragm spring for tempering. The model developed can be applied to searching for optimal system configurations in order to perform induction heat treatment of diaphragm springs in a wide range of typical sizes, as well as metal blanks shaped as disks or rings, and other axisymmetric metal workpieces with simple and complex profiles.

REFERENCES

1. **Rupnar A.,** Design and analysis of diaphragm spring of a single plate dry clutch, International Journal of Science Technology & Engineering. 2(12) (2016) 26–30.

2. **Mannanov E.R., Galunin S.A., Nikanorov A.N., et al.,** Development of induction systems for disk heating, St. Petersburg Polytechnical State University Journal. Physics and Mathematics. 12 (2) (2019) 23–31.

3. **Mannanov E.R., Yermekova M.R., Mazalov V.O. Galunin S.A.,** Chislennoye modelirovaniye elektroteplovykh protsessov pri induktsionnom otpuske izdeliya koltseobraznoy formy [Numerical simulation of electrothermal processes in the induction tempering of a ring-shaped product], In: "Science. Engineering. Innovation" Collected volume in 10 parts (2017) 128–131.

4. **Mannanov E.R, Galunin S.A.,** Svidetelstvo o gosudarstvennoy registratsii programmy dlya EVM № 2019614128 "Chislennaya problemno-oriyentirovannaya 3D elektroteplovaya model nagreva diska induktsionnym metodom" [Sertificate No. 2019614128 on the state recording of a computer program "Numerical problem-oriented 3D electrothermal model of disk heating by induction technique"], Copyright holder is St. Petersburg Electrotechnical University "LETI", Stated on March 24, 2019, registered on April 1, 2019.

5. **Mannanov E.R, Galunin S.A.,** Svidetelstvo o gosudarstvennoy registratsii programmy dlya EVM № 2019614441 "Chislennaya problemno-oriyentirovannaya 3D elektroteplovaya model nagreva izdeliy slozhnogo profilya induktsionnym metodom" [Sertificate No. 2019614441 on the state recording of a computer program "Numerical problem-oriented 3D electrothermal model of a complex product by induction technique"], Stated on March 25, 2019, registered on April 4, 2019.

6. **Shepelyakovskiy K.Z.**, Uprochneniye detaley mashin poverkhnostnoy zakalkoy pri induktsionnom nagreve [Mashine parts strengthening by shell hardening in the induction heating], Mashinostroyeniye, Moscow, 1972.

7. **Lepeshkin S.A.,** Modelirovaniye i issledovaniye raspredeleniy temperatur vo vrashchayushchikhsya diskakh s uchetom vzaimnogo vliyaniya [Simulation and study of a temperature distribution in the rotating discs taking into account the mutual influence], In collected book "Energy- and Resourse- Saving – The 21th Century", Proceedings of the 13th International Theoretical and Practical Internet Conf. (2014) 77–79.

8. **Galunin S.A., Zlobina M.V., Blinov K.Y.,** Numerical model approaches for in-line strip induction heating, IEEE Eurocon 2009, St. Petersburg (2009) 1607–1610, **DOI:** 10.1109/EURCON.2009.5167857.

9. **Mannanov E., Galunin S., Nikanorov A., Nacke B.,** Simulation algorithm for induction heating of rotated workpieces with complex shape, Proceedings of the 18th International UIE-Congress "Electrotechnologies for Material Processing", Hannover (Germany), June 6–9 (2017) 491–496.

10. **Schlesselmann D., Nacke B., Nikanorov A., Galunin S.,** Coupled numerical multiphysics simulation methods in induction surface hardening, "Coupled Problems 2015", Proceedings of the 6th International Conference on Coupled Problems in Science and Engineering, May 18–20, 2015, San Servolo Island, Venice, Italy (2015) 392–403.

Received 12.09.2019, accepted 13.12.2019.

THE AUTHORS

MANNANOV Emil R.
St. Petersburg Electrotechnical University "LETI"
5 Professora Popova St., 197376, St. Petersburg, Russian Federation
emil-mannanov@mail.ru

GALUNIN Sergei A.
St. Petersburg Electrotechnical University "LETI"
5 Professora Popova St., 197376, St. Petersburg, Russian Federation
galunin@mail.ru

СПИСОК ЛИТЕРАТУРЫ

1. **Rupnar A.** Design and analysis of diaphragm spring of a single plate dry clutch // International Journal of Science Technology & Engineering, 2016. Vol. 2. No. 12. Pp. 26–30.

2. **Маннанов Э.Р., Галунин С.А., Никаноров А.Н., Наке Б., Козулина Т.П.** Разработка индукционных систем для нагрева дисков // Научно-технические ведомости СПбГПУ. Физико-математические науки. 2019. Т. № .12 2. С. 31–23.

3. **Маннанов Э.Р., Ермекова М.Р., Мазалов В.О., Галунин С.А.** Численное моделирование электротепловых процессов при индукционном отпуске изделия кольцеобразной формы // Наука. Технологии. Инновации. Сб. научных трудов в 10 ч. Под ред. Б.Ю. Лемешко, А.А. Попова, М.Э. Рояка, В.С. Тимофеева. Новосибирск: Изд-во НГТУ, 2017. Ч. 2. С. 131–128.

4. **Маннанов Э.Р., Галунин С.А.** Свидетельство о государственной регистрации программы для ЭВМ № 2019614128. «Численная проблемно-ориентированная 3D электротепловая модель нагрева диска индукционным методом». Правообладатель ФГАОУ ВО СПбГЭТУ «ЛЭТИ»; заявл. 24.03.2019; зарегистр. 1 .01.04.2019 с.

5. **Маннанов Э.Р., Галунин С.А.** Свидетельство о государственной регистрации программы для ЭВМ № 2019614441. «Численная проблемно-ориентированная 3D электротепловая модель нагрева изделий сложного профиля индукционным методом». Правообладатель ФГАОУ ВО СПбГЭТУ «ЛЭТИ»; заявл. 25.03.2019; зарегистр. 1 .04.04.2019 с.

6. **Шепеляковский К.З.** Упрочнение деталей машин поверхностной закалкой при индукционном нагреве. М.: Машиностроение, 287 .1972 с.

7. **Лепешкин С.А.** Моделирование и исследование распределений температур во вращающихся дисках с учетом взаимного влияния // «Энерго- и ресурсосбережение – XXI век». Сб. материалов XII Межд. науч.-практ. Интернет-конф., 2014. С. 77–79.

8. **Galunin S.A., Zlobina M.V., Blinov K.Yu.** Numerical model approaches for in-line strip induction heating // IEEE Eurocon 2009. St. Petersburg, 2009. Pp. 1607–1610. **DOI:** 10.1109/EURCON.2009.5167857.

9. **Mannanov E., Galunin S., Nikanorov A., Nacke B.** Simulation algorithm for induction heating of rotated workpieces with complex shape // Proccedings of the 18th International UIE-Congress "Electrotechnologies for Material Processing", Hannover (Germany), June 6 – 9, 2017. Pp. 491–496.

10. **Schlesselmann D., Nacke B., Nikanorov A., Galunin S.** Coupled numerical multiphysics simulation methods in induction surface hardening // "Coupled Problems 2015". Proceedings of the 6th International Conference on Coupled Problems in Science and Engineering. May 18 – 20, 2015. San Servolo Island, Venice, Italy. Pp. 392–403.

Статья поступила в редакцию 12.09.2019, принята к публикации 13.12.2019.

СВЕДЕНИЯ ОБ АВТОРАХ

МАННАНОВ Эмиль Рамилевич – *аспирант кафедры электротехнологической и преобразовательной техники Санкт-Петербургского государственного электротехнического университета «ЛЭТИ» имени В.И. Ульянова (Ленина).*

197376, Российская Федерация, г. Санкт Петербург, ул. Профессора Попова, 5.
emil-mannanov@mail.ru

ГАЛУНИН Сергей Александрович – *кандидат технических наук, заведующий кафедрой электротехнологической и преобразовательной техники Санкт-Петербургского государственного электротехнического университета «ЛЭТИ» имени В.И. Ульянова (Ленина).*

197376, Российская Федерация, г. Санкт Петербург, ул. Профессора Попова, 5.
galunin@mail.ru

DOI: 10.18721/JPM.12407
УДК 544.582

SAMPLE PREPARATION FOR MASS-SPECTROMETRIC ANALYSIS OF $^{13}C/^{12}C$ ISOTOPE FRACTIONATION FROM ENVIRONMENT TO THE PLANT CARBON POOL

T.E. Kuleshova[1], E.S. Pavlova[1], Yu.A. Titov[2], A.G. Kuzmin[2], N.R. Gall[1]

[1] Ioffe Physical Technical Institute of the Russian Academy of Sciences,
St. Petersburg, Russian Federation

[2] Institute for Analytical Instrumentation, St. Petersburg, Russian Federation

In order to study the differences in the ^{13}C and ^{12}C isotopes assimilation degree related to the rate of photosynthetic reactions, we have developed a number of procedures of sample gasification and a hardware experimental complex for sample preparation before mass-spectrometric isotope analysis of carbon involved in plant life. A setup for concentrating the carbon dioxide located around the plant was designed and made. The setup makes catalytic afterburning of organic microimpurities available for increasing the carbon content more than a hundred times. A reaction procedure for oxidation of leaf glucose by yeast generating carbon dioxide was suggested, reagent concentrations selected. The collected samples were free from impurities (not exceeding 10^{-5}). The developed sample preparation technique was used to study the effect of the light exposure characteristics on the carbon isotope interchange between atmospheric CO_2 and the plant carbon pool.

Keywords: carbon isotopes, plant, sample preparation, mass-spectrometric analysis, CO_2 concentration

Citation: Kuleshova T.E., Pavlova E.S., Titov Yu.A., Kuzmin A.G., Gall N.R., Sample preparation for a mass-spectrometric analysis of $^{13}C/^{12}C$ isotope fractionation from environment to the plant carbon pool, St. Petersburg Polytechnical State University Journal. Physics and Mathematics. 12 (4) (2019) 61–70. DOI: 10.18721/JPM.12407

ПРОБОПОДГОТОВКА ДЛЯ МАСС-СПЕКТРОМЕТРИЧЕСКОГО АНАЛИЗА ФРАКЦИОНИРОВАНИЯ ИЗОТОПОВ $^{13}C/^{12}C$ ИЗ ОКРУЖАЮЩЕЙ СРЕДЫ В УГЛЕРОДНЫЙ ПУЛ РАСТЕНИЙ

Т.Э. Кулешова[1], Е.С. Павлова[1], Ю.А. Титов[2], А.Г. Кузьмин[2], Н.Р. Галль[1]

[1] Физико-технический институт им. А.Ф. Иоффе РАН,
Санкт-Петербург, Российская Федерация;

[2] Институт аналитического приборостроения РАН,
Санкт-Петербург, Российская Федерация

С целью изучения различий в степени ассимиляции изотопов ^{13}C и ^{12}C в ходе жизнедеятельности растений (различия связаны со скоростью протекания фотосинтетических реакций), разработан ряд методик и создан аппаратный комплекс для сбора и подготовки пробы, предшествующих масс-спектрометрическому изотопному анализу углерода. Спроектирована и изготовлена установка для концентрирования углекислого газа, находящегося вокруг растения, с каталитическим дожиганием органических микропримесей, позволяющая повысить его относительное содержание

более чем в 100 раз. Предложена методика проведения реакции окисления глюкозы листьев растений дрожжами с образованием углекислого газа, подобраны концентрации реагентов. Полученные пробы свободны от интерферирующих примесей, доля которых не превышала 10^{-5}. Разработанная методика пробоподготовки использована для изучения влияния спектральных характеристик световой среды на взаимообмен изотопов углерода между атмосферным воздухом и углеродным пулом растений.

Ключевые слова: изотопы углерода, растение, пробоподготовка, масс-спектрометрический анализ, концентрирование углекислоты, окисление дрожжами

Ссылка при цитировании: Кулешова Т.Э., Павлова Е.С., Титов Ю.А., Кузьмин А.Г., Галль Н.Р. Пробоподготовка для масс-спектрометрического анализа фракционирования изотопов $^{13}C/^{12}C$ из окружающей среды в углеродный пул растений // Научно-технические ведомости СПбГПУ. Физико-математические науки. 2019. Т. 12. № 4. С. 69–78. DOI: 10.18721/JPM.12407

Introduction

Photosynthesis is accompanied by fractionation of isotopes of the elements constituting organic products; in particular, plants selectively absorb stable carbon isotopes ^{12}C and ^{13}C [1 –5]. The distribution of isotopes between carbon dioxide in the air and the products of photosynthesis depends on the reactivity of molecules of different isotopic compositions; notably, the isotope whose participation accelerates the reaction is accumulated in the reaction products. Plants rapidly accumulate the ^{12}C isotope: its relative content in plant tissues is 15–25‰ higher than in the atmosphere. Differentiation of isotopes during photosynthesis presumably consists of two stages: the first is preferential absorption of carbon dioxide $^{12}CO_2$ from atmospheric air and its dissolution in the cytoplasm of plants, which is due to the kinetic effect; in turn, the fraction enriched with the ^{12}C isotope is extracted from carbon dioxide CO^2 dissolved in cytoplasm at the second stage, during synthesis of organic compounds [6]. Analysis of isotopic composition is of great interest for studies on distribution of carbon in the plant–soil–atmosphere continuum [7, 8], and on the reactions of plant organisms to changing external conditions [9].

Electrochemical gas sensors are used to monitor gas exchange processes in the plant - root system; analysis of carbon dioxide flows in closed chambers is performed using processing and modeling algorithms [10]; the Warburg apparatus is used to study dark respiration in plants [11]. The radioactive isotope 14C [11, 12] is widely used as an indicator of metabolism, movement of carbon and formation of photosynthesis products. However, these methods are not applicable to analysis of isotopic processes occurring during conversion of carbon dioxide from the air to the carbon pool of a growing plant.

Mass spectrometry is the most common and effective method for measuring the $^{13}C/^{12}C$ isotopic ratio. However, standard methods and hardware systems for collecting and preparing samples for such measurements are not suitable for studies of living plants.

Thus, the goal of of this study was to develop a technique for collecting and preparing samples that is suitable for studying the interchange of carbon isotopes between a plant and the atmosphere by conducting mass-spectrometric analysis of the $^{13}C/^{12}C$ ratio simultaneously in atmospheric carbon dioxide around the plant, and in tissues of the living plant.

Technique and devices used for preparing samples for mass-spectrometric analysis of carbon isotopes participating in plant life cycle

We proposed a technique for studying the isotopic composition of carbon in plant tissues and the degree of its fractionation from the air, and created a hardware system that allows to prepare the samples for mass-spectrometric isotopic analysis of carbon involved in the life cycle of plants.

The measured difference of the isotopic ratio of the sample from the standard is usually expressed as $\delta^{13}C$:

$$\delta^{13}C = [(^{13}C/^{12}C)_{smp}/(^{13}C/^{12}C)_{stnd} - 1]\cdot 10^3‰,$$

where $^{13}C/^{12}C$ is the isotopic ratio of carbon; the subscripts *smp* and *stnd* correspond to the sample and the standard, respectively.

We used the commonly accepted standard Belemnitella Americana (PDB) from the Peedee Formation (South Carolina), dating from the Cretaceous period, with the isotopic ratio

$^{13}C/^{12}C = 1123.72 \cdot 10^{-5}$, to compare data in isotopic analysis of carbon.

The $^{13}C/^{12}C$ ratio is determined in CO_2 whose concentration in the sample should be sufficiently high (more than 2–3%) and constant. We face the following problems in working with plants:

the concentration of carbon dioxide in the air surrounding the plants is low (~$3 \cdot 10^{-4}$% $^{13}CO_2$);

organic matter of plant tissues has to be transformed to gaseous state.

Therefore, the gas mixture should be enriched for mass-spectrometric analysis, which we implemented by freezing in nitrogen vapors (see below). Furthermore, to convert solid matter into gaseous state, we proposed and implemented a method alternative to thermal decomposition, which consists in using yeast as oxidizing agents for carbon-containing compounds.

The analysis of the $^{13}C/^{12}C$ ratio was carried out with Helicomass, a specialized static magnetic mass spectrometer, developed at the Ioffe Insitute (St. Petersburg, Russia) [13]. We used a laboratory standard calibrated against PDB with a Thermo Scientific Delta mass spectrometer (by Thermo Fisher Scientific, USA).

The three-collector detection system operating in spectrograph mode allows to detect molecular ions of carbon dioxide (CO_2^+) with the following mass-to-charge ratios:

$m/z = 44$ is the value corresponding to the main isotopic modification of $^{12}C^{16}O^{16}O$;

$m/z = 45$ to the sum of isotopic modifications of $^{13}C^{16}O^{16}O$ and $^{12}C^{17}O^{16}O$;

$m/z = 46$ to the sum of isotopic modifications of $^{12}C^{18}O^{16}O$ and very insignificant additions of $^{13}C^{17}O^{16}O$.

We only used the m/z values equal to 44 and 45 as carriers of analytical information about the $^{13}C/^{12}C$ isotopic ratio.

Given the isotopic abundance of carbon

$$^{13}C\ /^{12}C = 0.01123 : 1{,}000,$$

oxygen

$$^{18}O : {}^{17}O : {}^{18}O : = 2.004810^{-3} : 3.909310^{-4} : 1{,}000,$$

and the detector characteristics, we calculated $\delta^{13}C$ by the following algorithm:

Step 1. Find signal intensity for ^{13}C and ^{12}C isotopes taking into account the contribution of oxygen isotopes

$$^{13}C = (I_{45}/33) - 2I_{44} \cdot 3.9093 \cdot 10^{-4};$$

$$^{12}C = I_{44} + 2I_{44} \cdot 2.0048 \cdot 10^{-3} + + 2I_{44} \cdot 3.9093 \cdot 10^{-4},$$

where I_{45}, I_{44} are the signal intensities for the m/z values of 45 and 44, respectively.

Step 2. Calculate the normalization coefficient k by the formula

$$k = 0.0106956/R_e,$$

where R_e is the average value of $^{13}C/^{12}C$ for laboratory reference gas, normalized by a coefficient of 0.0106956, which is the absolute content of the ^{13}C isotope in laboratory standard and measured against the PDB standard.

Step 3. Calculate $\delta^{13}C$ values by the formula

$$\delta^{13}C = [(kR_s/R_{PDB}) - 1] \cdot 10^3,$$

where R_s is the measured $^{13}C\ /^{12}C$ ratio for the sample; R_{PDB} is the $^{13}C/^{12}C$ ratio for the PDB standard, equal to 0.0112372.

We used a TEKHMAS MS7-100 quadrupole mass spectrometer developed at the Institute for Analytical Instrumentation of RAS (St. Petersburg, Russia) for molecular analysis of the composition of gas mixtures obtained in preparing samples, determining the concentrations of individual components and recording them in dynamic mode. The device allows to determine the composition of the gas mixture in the range of mass numbers from 2 to 100 amu, making it possible to detect substances and fragments of molecules interfering with carbon dioxide.

Setup for enriching carbon dioxide and determining the isotopic ratio of carbon in the air surrounding the plant

The gas mixture is enriched with carbon dioxide for mass-spectrometric analysis of carbon in the atmosphere surrounding the plants. Freezing is one of the methods for concentrating carbon dioxide. Carbon dioxide transforms to solid state at an absolute pressure of 760 mm Hg and a temperature of −78.9 °C. Freezing is carried out in thermal mode, so that carbon dioxide is crystallized on the walls of the collection tank, and in the absence of snow in airflow. In this case, the temperature difference between the air and the walls should not exceed 30 °C, and the gas flow rate should not exceed 3 m/s (to prevent the deposited crystals from getting separated and carried away).

In view of the described conditions, we have developed a technique for enriching the gas mixture with carbon dioxide. The setup for concentrating carbon dioxide is shown schematically in Fig. 1. Small streams of atmospheric air were pumped through test tube *3* placed in heat-insulating vessel *4*, filled approximately one-third with

liquid nitrogen. The tube was placed in nitrogen vapor so that its bottom temperature was about −100 °C. Desiccator *1* was used as a sealed chamber for the test plant.

The freezing system consisted of two circuits, where the temperature just below zero was maintained in loop *2* ensuring deposition of water and dehumidification of the gas mixture, while the temperature below −100 °C was maintained in refrigerating heat exchanger *3*, made in the form of a glass tube with a volume of 235 cm^3, allowing to transform carbon dioxide to solid phase. Flow rate did not exceed 0.5 m^3/ h, so solid carbon dioxide could be desorbed on the walls of the tube. A system of pneumatic tubes connecting all the components of the setup and flow controller *5* allowed the gas mixture to circulate from the plant through a system of containers back to the chamber with the test object.

After a freezing cycle lasting 15 min, concentrated carbon dioxide in tube was transformed to gaseous state by heating at room temperature. The tube was equipped with a 35 × 1 mm platinum catalytic chamber, maintaining a temperature over 900 °C at a heating current of 3.5 A. Catalytic combustion of impurities was performed in the test tube after defrosting for $\tau \approx$ 600 s. We estimate that the total concentration of impurities that can interfere in carbon isotope measurements for target ions with m/z 44 and 45 did not exceed about 10^{-5}.

Technique for determining the isotopic ratio for glucose carbon in plant tissues

Based on the developed technique for studying the fractionation of carbon isotopes by heterotrophic microorganisms [14], we proposed using oxidation by yeast to transform simple plant sugars to gaseous phase with carbon dioxide forming in order to determine the isotopic composition of glucose carbon in plant tissues.

Yeast mainly consume glucose by two pathways:

glycolytic splitting, that is, two pyruvate molecules are formed from a glucose molecule;

partial oxidation of glucose in oxidative pentose phosphate cycle, when three carbon dioxide molecules and pyruvate are formed from a glucose molecule [14].

Pyruvate synthesized through both of these pathways for glucose metabolism can then be oxidized in tricarboxylic acid cycle with the carbon dioxide molecule removed and coenzyme A (CoA) added to form acetyl-CoA:

$$CH_3{-}CO{-}COOH + SH\text{-}CoA + NAD \rightarrow$$
$$\rightarrow CO_2 + CH_3{-}CO{-}S\text{-}CoA + NAD{\cdot}H_2.$$

Alcohol fermentation proceeds in the absence of oxygen; its total equation has the following form:

$$C_6H_{12}O_6 \rightarrow 2CO_2 + 2C_2H_5OH.$$

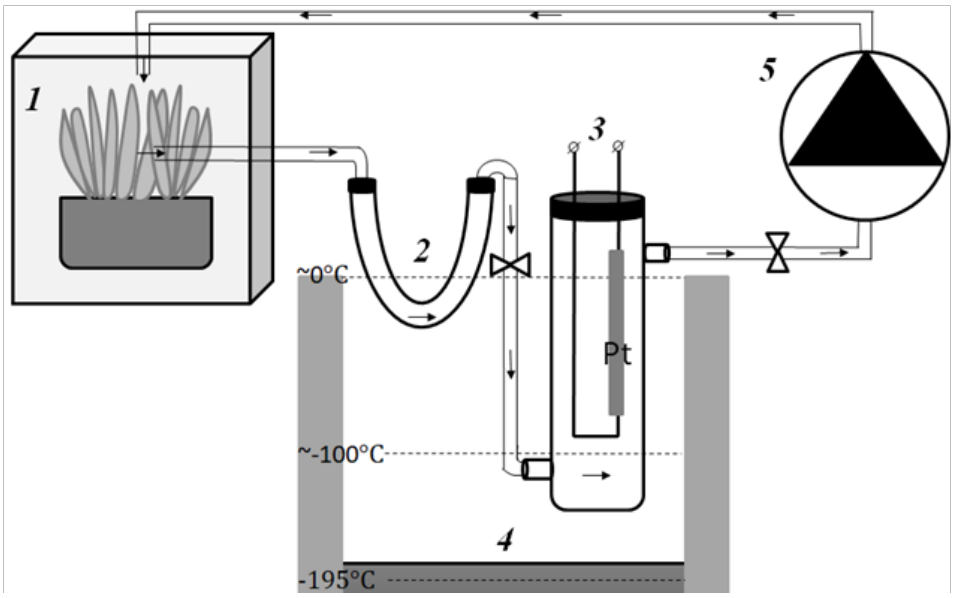

Fig. 1. Setup for enriching carbon dioxide from atmosphere surrounding the plant: sealed chamber *1* with air exhaust and supply pipes, *U*-shaped tube *2* for draining the gas mixture, Wurtz flask *3* for depositing carbon dioxide in nitrogen vapor with integrated catalytic chamber for afterburning organic impurities, heat-insulating vessel *4* with liquid nitrogen, flow controller *5* Temperature is controlled by a thermocouple

The acetaldehyde formed during the reaction has a molar mass of 44 g/mol, which does not allow it to be separated from the target compound, carbon dioxide. However, since glucose is the starting material for the carbon constituting acetaldehyde CH_3COH, this substance does not introduce errors in the isotopic composition of the plant. Ethyl alcohol with a molar mass of 46 g/mol begins to form approximately 24 h after the start of the reaction, after yeast have consumed the nutrients represented in our case by glucose in plant tissues.

The technique was as follows: ground plant tissue, water and dry yeast were placed in a sealed test tube (Fig. 2); after a 30-minute reaction, the synthesized carbon dioxide was taken for mass-spectrometric analysis.

The complete mass spectrum of the gas mixture formed in the reaction tube during oxidation by yeast was recorded with an MS 7-100 quadrupole mass spectrometer (Fig. 3). Gases in atmospheric air exhibited increased peak intensity in the mass spectrum for $m/z = 44$ (CO_2) (by 53 times) and for $m/z = 50–70$ (by 5–10 times) during the reaction (within 15 min).

According to [15], mainly signals from fragment ions lie in the range $m/z = 50–70$, and there are no data on the peaks related to interference of fragments at $m/z = 45$ (this mass corresponds to the CO_2 molecule with the ^{13}C isotope). In addition, the absence of a peak at $m/z = 46$ indicates the absence of ethanol vapor, which is usually the main interfering agent in isotopic measurements of carbon, in the gas mixture. In our estimation, the total concentration of impurities whose molecular or fragment ions are capable of interfering with the target ions used in isotopic measurements at mass numbers 44 and 45 did not exceed the level of 10^{-5}, providing the necessary measurement accuracy of 1‰.

The ratio of reaction components for alcohol fermentation should be as follows: 1 kg of sugar, 4–5 l of water, 100 g of pressed yeast or 20 g of dry yeast. Because the concentration of sugars in the tested plant tissues is not known exactly, we conducted an experiment to select the concentrations of reagents (see Table). We could find no significant differences of in $\delta^{13}C$ values of leaves. The standard deviation for the obtained values was 1.3‰. For example, the $\delta^{13}C$ value for 1 mg of plant tissue per 1 ml of water (second row of Table) was −35.3 ± 0.9‰ 60 min after the start of the reaction, and −33. 6 ± 0.9‰ after 90 min.

In addition to studying plant sugars, we obtained and analyzed the isotopic composition of sugars corresponding to different types of photosynthesis and used as substrate for yeast.

The isotopic ratio obtained for yeast oxidation of beet sugar isolated from C3 plants (fixing carbon dioxide by the C3 mechanism of photosynthesis [16]) was

$$\delta^{13}C = -‰1.9 \pm 33.4.$$

The value for cane sugar synthesized from a C4 plant (higher plants with C4 photosynthesis [16]) was

$$\delta^{13}C = -‰1.6 \pm 14.6.$$

The values obtained are in agreement with the data given in literature for these types of photosynthesis, which means that the proposed technique can be applied for a wide range of objects.

Application of developed technique for preparing the samples

The given methods were used to study the effect of the spectral characteristics of lighting on the degree of exchange of carbon isotopes between atmospheric air and plant organs that carry out photosynthesis. Apparently, isotopic composition of the leaves substantially depends on the spectrum of light that the growing plant was exposed to. For example, when the spectrum changed from

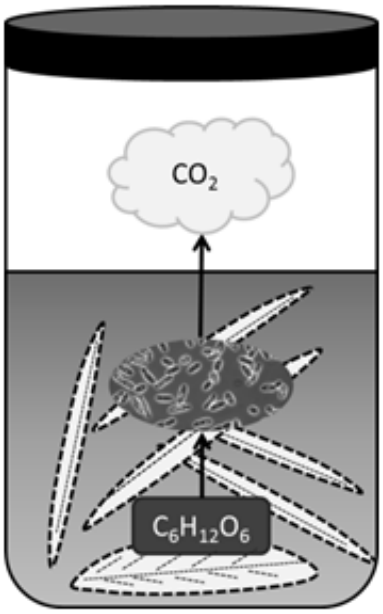

Fig. 2. Glucose from plant leaves oxidated by yeast until carbon dioxide is obtained in reaction tube

Table

Dependence $\delta^{13}C$ for glucose in leaves on reagent concentration in oxidation by yeast

Amount of reagent (mg) per 1 ml of water		$\delta^{13}C$,‰
Plant tissue	Yeast	
0.5	1.05	–33.6 ± 0.9
1.0	1.04	–33.6 ± 0.9
2.0	1.05	–33.6 ± 0.9

red to blue, the $^{13}C/^{12}C$ ratio changed in the range from −35 to −‰23, and the dependence on wavelength was nonmonotonic. The difference between the carbon isotope composition in the air surrounding the plants and in their leaves varies from 7 to 19‰ depending on the spectral composition of light and characterizes the rate of carbon assimilation due to photosynthetic reactions and photorespiration. This difference reflects the degree of isotope fractionation during the life of plants and can be used as a phytomonitoring parameter. We plan to publish more detailed findings later.

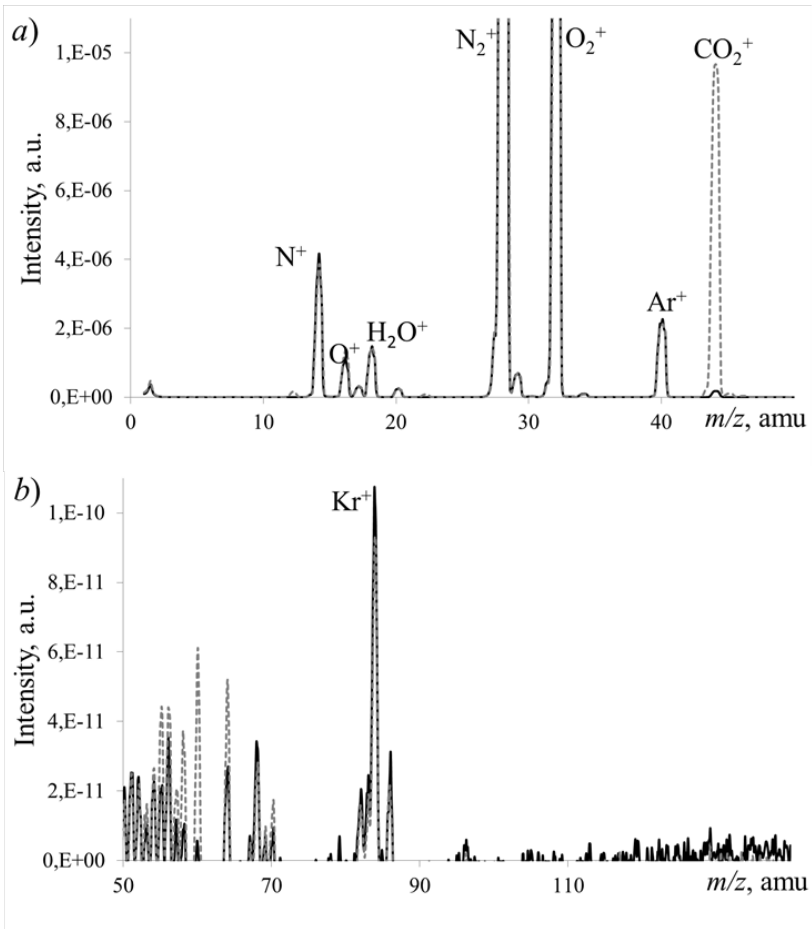

Fig. 3. Mass spectra of air in reaction tube (solid curve) and in gas mixture formed during oxidation of glucose in plant leaves by yeast (dashed curve) in m/z ranges of 0–45 amu (*a*) and 45–95 amu (*b*)

Brief results and conclusions

We have developed a system for collecting and preparing samples for mass-spectrometric analysis of fractionation of $^{13}C/^{12}C$ isotopes from the environment into the carbon pool of plants. Development of the system comprised the following stages:

constructing a setup for collecting and enriching a carbon dioxide sample from the air surrounding the plant *in vivo* by freezing carbon dioxide at a temperature of liquid nitrogen vapor;

developing and applying a technique for obtaining carbon dioxide samples from glucose contained in leaves via biochemical oxidation by yeast.

As a result of experimental studies conducted using this setup by the developed technique, we have found that the ratio of carbon isotopes in carbon dioxide released during oxidation of plant tissue by yeast remained unchanged for three hours.

The isotopic ratios obtained for oxidation by yeast were

$$\delta^{13}C = -33.6 \pm 0.9‰$$

for a leaf of a C3 plant;

$$\delta^{13}C = -‰0.9 \pm 33.6$$

for beet sugar isolated from C3 plants;

$$\delta^{13}C = -‰1.6 \pm 14.6$$

for cane sugar synthesized from a C4 plant.

These values are in agreement with the data given in literature for these types of photosynthesis, which means that the proposed technique can be applied for a wide range of objects.

The developed system for collecting and preparing the samples provided a significant increase in the accuracy of isotope measurements due to concentration of carbon dioxide from the atmosphere surrounding the plant and elimination of interfering organic impurities.

The technique for preparing the samples was successfully used to measure the dependence of isotopic ratio on the spectral composition of the light that the plants were exposed to during growth. We have found significant differences in the isotopic composition of carbon dioxide in the atmosphere and in plant leaves.

Thus, we can recommend to use the $^{13}C/^{12}C$ isotopic ratio as an important indicator of the photosynthesis reaction rate, while the difference between the $\delta^{13}C$ values for the air surrounding the plant and involved in its metabolism and $\delta^{13}C$ values of the carbon pool of plant tissue may reflect the degree of isotope fractionation during plant life cycle.

REFERENCES

1. **O'Leary M.H.,** Carbon isotope fractionation in plants, Phytochemistry. 20 (4) (1981) 553–567.

2. **Brugnoli E., Farquhar G.D.,** Photosynthetic fractionation of carbon isotopes, In: Leegood R.C., Sharkey T.D., von Caemmerer S. (Eds.), Photosynthesis: Physiology and metabolism. Springer, Kluwer, Dordrecht (2000) 399–434.

3. **Gessler A., Ferrio J.P., Hommel R., et al.,** Stable isotopes in tree rings: towards a mechanistic understanding of isotope fractionation and mixing processes from the leaves to the wood, Tree Physiology. 34 (8) (2014) 796–818.

4. **Lehmann M.M., Ghiasi S., George G.M., et al.,** Influence of starch deficiency on photosynthetic and post-photosynthetic carbon isotope fractionations, Journal of Experimental Botany. 70 (6) (2019) 1829–1841.

5. **Galimov E.M.,** Geokhimiya stabilnykh izotopov ugleroda [Geochemistry of stable carbon isotopes], "Nedra" Publishing, 1968.

6. **Park R., Epstein S.,** Carbon isotope fractionation during photosynthesis, Geochimica et Cosmochimica Acta. 21 (1–2) (1960) 110–120.

7. **Brüggemann N., Gessler A., Kayler Z., et al.,** Carbon allocation and carbon isotope fluxes in the plant-soil-atmosphere continuum: a review, Biogeosciences. 8 (11) (2011) 3457–3489.

8. **Hagedorn F., Joseph J., Peter M., et al.,** Recovery of trees from drought depends on belowground sink control, Nature plants. 2 (8) (2016) 16111.

9. **Gessler A., Cailleret M., Joseph J., et al.,** Drought induced tree mortality – a tree-ring isotope based conceptual model to assess mechanisms and predispositions, New Phytologist. 219 (2) (2018) 485–490.

10. **Hoffmann M., Jurisch N., Borraz E.A., et al.,** Automated modeling of ecosystem CO_2 fluxes based on periodic closed chamber measurements: a standardized conceptual and practical approach, Agricultural and Forest

Meteorology. 200 (January) (2015) 30–45.

11. **Zalenskiy O.V., Semikhatova O.A., Voznesenskiy V.L.,** Metody primeneniya radioaktivnogo ugleroda C^{14} dlya izucheniya fotosinteza [Radioactive carbon-14 application method for a photosynthesis study], USSR Academy of Sciences Publishing House, Moscow, 1955.

12. **Dieuaide-Noubhani M., Alonso A.P., Rolin D., et al.,** Metabolic flux analysis: recent advances in carbon metabolism in plants, Plant Systems Biology, Birkhäuser Basel (2007) 213–243.

13. **Blashenkov N.M., Sheshenya E.S., Solov'ev S.M., et al.,** Development of a dedicated isotope mass spectrometer for the noninvasive diagnostics of humans infected with Helicobacter Pylory, Technical Physics. 58 (6) (2013) 836–840.

14. **Zyakun A.M.,** Teoreticheskiye osnovy izotopnoy mass-spektrometrii v biologii [Theoretical basis for isotopic mass spectrometry in biology], «Foton-vek», Pushchino, 2010.

15. **Anufriyev G.S., Boltenkov B.S., Kapitonov I.N., Ryabinkov A.I.,** Issledovaniye ostatochnogo gaza pri pomoshchi mass-spektrometra vysokogo razresheniya [Residual gas investigation using high-resolution mass spectrometer], Ioffe Physical Technical Institute of the Russian Academy of Sciences, Leningrad, 1990.

16. **Edwards G., Walker D.,** C3, C4: mechanisms, and cellular and environmental regulation, of photosynthesis, University of California Press, 1983.

Received 26.08.2019, accepted 09.09.2019.

THE AUTHORS

KULESHOVA Tatiana E.
Ioffe Physical Technical Institute of the Russian Academy of Sciences
26 Polytekhnicheskaya St., St. Petersburg, 194021, Russian Federation
www.piter.ru@bk.ru

PAVLOVA Ekatherina S.
Ioffe Physical Technical Institute of the Russian Academy of Sciences
26 Polytekhnicheskaya St., St. Petersburg, 194021, Russian Federation
sheshenayket@gmail.com

TITOV Yuriy A.
Institute for Analytical Instrumentation
31–33, Ivana Chernykh St., St. Petersburg, 198095, Russian Federation
titov.uriy@gmail.com

KUZMIN Alexey G.
Institute for Analytical Instrumentation
31–33, Ivana Chernykh St., St. Petersburg, 198095, Russian Federation
agqz55@rambler.ru

GALL Nicholas R.
Ioffe Physical Technical Institute of the Russian Academy of Sciences
26 Polytekhnicheskaya St., St. Petersburg, 194021, Russian Federation
gall@ms.ioffe.ru

СПИСОК ЛИТЕРАТУРЫ

1. **O'Leary M.H.** Carbon isotope fractionation in plants // Phytochemistry. 1981. Vol. 20. No. 4. Pp. 553–567.

2. **Brugnoli E., Farquhar G.D.** Photosynthetic fractionation of carbon isotopes // Leegood R.C., Sharkey T.D., von Caemmerer S. (Eds.). Photosynthesis: Physiology and metabolism. Kluwer, Dordrecht: Springer, 2000. Pp. 399–434.

3. **Gessler A., Ferrio J.P., Hommel R., Treydte K., Werner R.A., Monson R.K.** Stable isotopes in tree rings: towards a mechanistic understanding of isotope fractionation and mixing processes from the leaves to the wood //Tree Physiology. 2014. Vol. 34. No. 8. Pp. 796–818.

4. **Lehmann M.M., Ghiasi S., George G.M., Cormier M.A., Gessler A., Saurer M., Werner R.A**. Influence of starch deficiency on photosynthetic and post-photosynthetic carbon isotope fractionations // Journal of Experimental Botany. 2019. Vol. 70. No. 6. Pp. 1829–1841.

5. **Галимов Э.М.** Геохимия стабильных изотопов углерода. М.: Изд-во «Недра», 1968. 226 с.

6. **Park R., Epstein S.** Carbon isotope fractionation during photosynthesis // Geochimica et Cosmochimica Acta. 1960. Vol. 21. No. 1–2. Pp. 110–120.7. **Brüggemann N., Gessler A., Kayler Z., et al.** Carbon allocation and carbon isotope fluxes in the plant-soil-atmosphere continuum: a review // Biogeosciences. 2011. Vol. 8. No. 11. Pp. 3457–3489.

8. **Hagedorn F., Joseph J., Peter M., et al.** Recovery of trees from drought depends on belowground sink control // Nature Plants. 2016. Vol. 2. No. 8. P. 16111.

9. **Gessler A., Cailleret M., Joseph J., et al.** Drought induced tree mortality – a tree ring isotope based conceptual model to assess mechanisms and predispositions //New Phytologist. 2018. Vol. 219. No. 2. Pp. 485–490.

10. **Hoffmann M., Jurisch N., Borraz E.A., Hagemann U., Drцsler M., Sommer M., Augustin J.** Automated modeling of ecosystem CO_2 fluxes based on periodic closed chamber measurements: A standardized conceptual and practical approach //Agricultural and Forest Meteorology. 2015. Vol. 200. January. Pp. 30–45.

11. **Заленский О.В., Семихатова О.А., Вознесенский В.Л.** Методы применения радиоактивного углерода C^{14} для изучения фотосинтеза. М.: Изд-во Академии наук СССР, 1955. 90 с.12. **Dieuaide-Noubhani M., Alonso A.P., Rolin D., Eisenreich W., Raymond P.** Metabolic flux analysis: recent advances in carbon metabolism in plants // Plant Systems Biology. Birkhдuser Basel, 2007. Pp. 213–243.

13. **Блашенков Н.М., Шешеня Е.С., Соловьев С.М., Галль Л.Н., Саченко В.М., Заруцкий И.В., Галль Н.Р.** Разработка специализированного изотопного масс-спектрометра для неинвазивной диагностики инфицированности человека *Helicobacter Pylori* // Журнал технической физики. 2013. Т. 83. № 6. С. 60–65.

14. **Зякун А.М.** Теоретические основы изотопной масс-спектрометрии в биологии. Пущино: «Фотон-век», 224 .2010 с.

15. **Ануфриев Г.С., Болтенков Б.С., Капитонов И.Н., Рябинков А.И.** Исследование остаточного газа при помощи масс-спектрометра высокого разрешения. Ленинград: Изд-во ФТИ, 35 .1990 с.

16. **Эдвардс Д., Уокер Д.** Фотосинтез С3- и С4-растений: механизмы и регуляция: Пер. с англ. М.: Мир, 1986. 590 с.

Статья поступила в редакцию 26.08.2019, принята к публикации 09.09.2019.

СВЕДЕНИЯ ОБ АВТОРАХ

КУЛЕШОВА Татьяна Эдуардовна – *младший научный сотрудник Физико-технического института им. А.Ф. Иоффе РАН*

194021, Российская Федерация, г. Санкт-Петербург, Политехническая ул., 26

www.piter.ru@bk.ru

ПАВЛОВА Екатерина Сергеевна – *младший научный сотрудник Физико-технического института им. А.Ф. Иоффе РАН*

194021, Российская Федерация, г. Санкт-Петербург, Политехническая ул., 26

sheshenayket@gmail.com

ТИТОВ Юрий Алексеевич – *младший научный сотрудник Института аналитического приборостроения* РАН
198095, Российская Федерация, г. Санкт-Петербург, ул. Ивана Черных, 31–33.
titov.uriy@gmail.com

КУЗЬМИН Алексей Георгиевич – *кандидат физико-математических наук, ведущий специалист* Института аналитического приборостроения РАН
198095, Российская Федерация, г. Санкт-Петербург, ул. Ивана Черных, 31–33.
agqz55@rambler.ru

ГАЛЛЬ Николай Ростиславович – *доктор физико-математических наук, ведущий научный сотрудник Института аналитического приборостроения РАН*
190103, Российская Федерация, г. Санкт-Петербург, Рижский пр., 26
gall@ms.ioffe.ru

DOI: 10.18721/JPM.12408
УДК 628.94, 617-7

OPTIMIZATION OF SURGICAL FIELD ILLUMINATION TO MAXIMIZE THE CONTRAST FOR VISUALIZING BIOLOGICAL OBJECTS

A.V. Aladov[1], V.P. Valyukhov[2], A.L. Zakgeim[1], V.D. Kuptsov[2], A.V. Mamoshin[3,4], E.V. Potapova[3], A.E. Chernyakov[1], A.E. Fotiadi[2]

[1] Submicron Heterostructures for Microelectronics Research and Engineering Center of RAS, St. Petersburg, Russian Federation;

[2] Peter the Great St. Petersburg Polytechnic University, St. Petersburg, Russian Federation;

[3] Research and Development Center of Biomedical Photonics, Orel, Russian Federation;

[4] Orel Regional Clinical Hospital, Orel, Russian Federation

The optimal lighting conditions for contrast imaging of biological tissues during surgical operations have been studied. In so doing a special experimental setup based on a dynamically controlled led lighting system was used. The operating team selected the optimal illumination of the operating field during work with individual organs and tissues of animals (rats); simultaneously experimental investigations of the spectral characteristics of these biological objects were carried out. Relying on such experimental data, an analysis of luminance and color contrasts, including a comparison with a halogen lamp effect. According to results of studies the need to use special lighting with optimization of its intensity and a wavelength spectrum was confirmed. Such a measure will increase the contrast during surgical operations.

Keywords: LEDs, RGB-mixing, dynamic light control, surgical lamp, contrast visualization of biological tissues

Citation: Aladov A.V., Valyukhov V.P., Zakgeim A.L., Kuptsov V.D., Mamoshin A.V., Potapova E.V., Chernyakov A.E., Fotiadi A.E., Optimization of surgical field illumination to maximize the contrast when biological objects being visualized, St. Petersburg Polytechnical State University Journal. Physics and Mathematics. 12 (4) (2019) 71–80. DOI: 10.18721/JPM.12408

ОПТИМИЗАЦИЯ ОСВЕЩЕНИЯ ОПЕРАЦИОННОГО ПОЛЯ С ЦЕЛЬЮ ПОЛУЧЕНИЯ МАКСИМАЛЬНОГО КОНТРАСТА ПРИ ВИЗУАЛИЗАЦИИ БИОЛОГИЧЕСКИХ ОБЪЕКТОВ

А.В. Аладов[1], В.П. Валюхов[2], А.Л. Закгейм[1], В.Д. Купцов[2], А.В. Мамошин[3,4], Е.В. Потапова[3], А.Е. Черняков[1], А.Э. Фотиади[2]

[1] Научно-технологический центр микроэлектроники и субмикронных гетероструктур Российской академии наук, Санкт-Петербург, Российская Федерация;

[2] Санкт-Петербургский политехнический университет Петра Великого, Санкт-Петербург, Российская Федерация;

[3] Научно-технологический центр биомедицинской фотоники Орловского государственного университета им. И.С. Тургенева», г. Орёл, Российская Федерация;

[4] Орловская областная клиническая больница, г. Орёл, Российская Федерация

Исследованы оптимальные условия освещения для контрастной визуализации биологических тканей при хирургических операциях. При этом использована специальная экспериментальная установка на основе светодиодной, динамически управляемой

системы освещения. Операционная бригада проводила подбор оптимального освещения операционного поля при работе с отдельными органами и тканями животных (крысы), одновременно выполнялись экспериментальные исследования спектральных характеристик этих биологических объектов. На основе полученных данных проведен анализ яркостного и цветового контрастов, который включал сравнение с освещением объектов светом от галогеновой лампы накаливания. По результатам исследований подтверждена необходимость использовать специальное освещение с подбором оптимальных интенсивности и спектра длин волн для повышения контраста при проведении хирургических операций.

Ключевые слова: светодиод, RGB-смешение, динамическое управление светом, хирургический светильник, контрастная визуализация биологических тканей

Ссылка при цитировании: Аладов А.В. Валюхов В.П., Закгейм А.Л., Купцов В.Д., Мамошин А.В., Потапова Е.В., Черняков А.Е., Фотиади А.Э. Оптимизация освещения операционного поля с целью получения максимального контраста при визуализации биологических объектов // Научно-технические ведомости СПбГПУ. Физико-математические науки. 2019. Т. 12. № 4. С. 80–89. DOI: 10.18721/JPM.12408

Introduction

Color perception of objects and precise detection of tissue boundaries, even if they only slightly differ in color (which is especially important in surgery) considerably reduces the risk of inaccuracies during operative treatment [1, 2]. Until recently, white light with a high color-rendering index from halogen or xenon lamps, allowing to reproduce the color of tissues with the greatest accuracy, was considered to be the best type for operating rooms. Color contrast between observed objects can be increased by using accent color lighting accounting for the spectral dependences of the reflection coefficient of the objects, in particular, different biological tissues. This can be implemented with multi-color LEDs with adjustable spectral color characteristics. The technique was first proposed in [3], where a controllable surgical lamp was used for contrast imaging of tumor masses and necrotic tissues; apparently, such masses and tissues were localized not only near the surface but also at a certain depth, under a layer of healthy tissues. There is growing interest towards increasing the imaging contrast of biological tissues in surgery by using special lighting [4–6].

The goal of this study consisted in determining the optimal lighting modes that provide maximum contrast of objects during surgical operations. We considered the spectral color characteristics of biological tissues and the emission spectra of a dynamically controlled lamp.

Setup and experimental procedure

Animal tests were conducted in laboratory conditions at the Oryol State University named after I.S. Turgenev (Oryol, Russia) using a surgical lamp.

Experimental studies were carried out with clinically healthy male rats (2 Wistar rats aged 6 months) in accordance with the Principles of Good Laboratory Practice (GOST 33647-2015). The study was approved by the Ethics Committee of the OSU (protocol No. 10 dated 16.10.2017). The animals were quarantined for 2 weeks in a clean environment controlled for temperature and humidity. Rats were anesthetized with Zoletil 100 (Vibrac, France) in standard dosages and restrained on a special table. The experiments were carried out on areas of depilated skin, on subcutaneous fat, and on muscle tissues of abdominal organs (intestines and liver). The animals were then removed in accordance with experimental standards.

A spectrally tunable surgical lamp was mounted above a special operating table for small laboratory animals at a distance of 70 cm, generating a uniform light field measuring at least 20 × 20 cm (Fig. 1). The spectral parameters of the lamp's LED array were varied via software. The RGBW(RGBWLED) array included four large chips with different colors: red (R), green (G), blue (B), and phosphor-coated W chips generating white light with a correlated color temperature (6500 K). The lighting parameters of the lamp were controlled via a remote PC. The optimal lighting of the surgical field for tissues

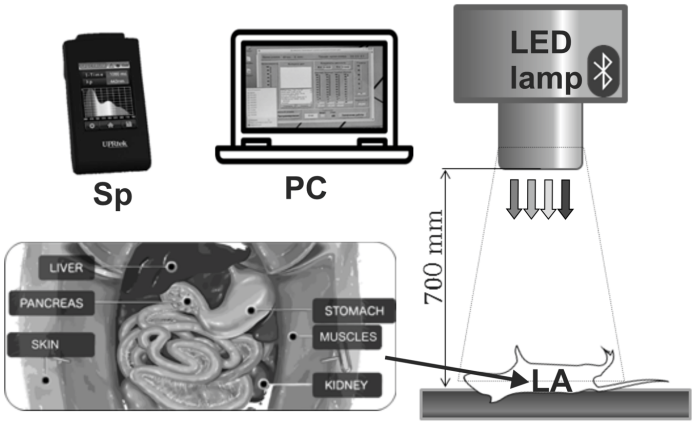

Fig. 1. Schematic layout for installed surgical lamp:
controllable LED lamp, MK350 spectrometer (Sp),
personal computer (PC), laboratory animal (LA);
the animal's internal organs are shown and marked on the insert

and organs was selected based on subjective visual assessment given by the surgical team. The spectral composition of the emitted light was monitored by a portable MK350 spectrometer.

The reflection coefficients were measured by the following procedure: a biological sample was placed in a beam of incident light; the luminous flux reflected from it was taken as the incident flux in the absence of the sample. All the rays scattered in different directions had to be collected in case of diffuse reflection or transmission.

The spectral characteristics of tissues were obtained using the OL 770-LED High-speed LED Test and Measurement system [7] (Fig. 2).

Samples were prepared at the Oryol State University by the following procedure.

A set of glasses with samples from two rats was used. In accordance with the GLP principles and the 3Rs concept (replacement, reduction and refinement) [8], specifically, minimizing the number of animals participating in the experiment, the smallest number of rats possible, i.e., two, was considered.

Preliminary experiments were carried out to compare the spectral characteristics of different biological tissues. We then measured the same parameter of the given part of the biological object several times (10) to reduce the relative error. Measurement results given below correspond to reflection curves obtained as the arithmetic mean of two similar samples.

Ten types of biological tissues were selected: pancreas, liver, spleen, skin, heart, brain, muscle, kidney, subcutaneous fat, bladder. A thin tissue slice 1 mm thick (obtained with a scalpel) was placed on a glass slide measuring 77 × 26 × 1 mm. Slides with objects were mounted in the OL770-71 adapter to measure the reflection spectra. The sample was covered by a second thin glass.

Experimental results

The optimal lighting of the surgical field was selected for each type of biological tissue using a dynamically controlled LED system based on subjective visual assessment of the operating team. The following indicators served as the criteria for choosing contrast imaging:

brightness contrast against the surrounding tissues;anatomical structure of tissue and small details can be clearly detected (i.e., without blending together).

Additional factors taken into account were:

comfortable visual perception;

optimal brightness;

lack of glare and shadow.

The LED array used to select the optimal spectrum (RGBWLED) was compared with illumination from a halogen lamp (HL) and an array of white LEDs (WLED) with a correlated color temperature of 2800 K. The spectral characteristics of these sources are shown in Fig. 3,*a*.

Distinctly differentiated reflection spectra obtained from different biological tissues are shown in Fig. 3,*b*.Notably, analysis of the reflection spectra of individual tissues of different organs provides deeper insights into

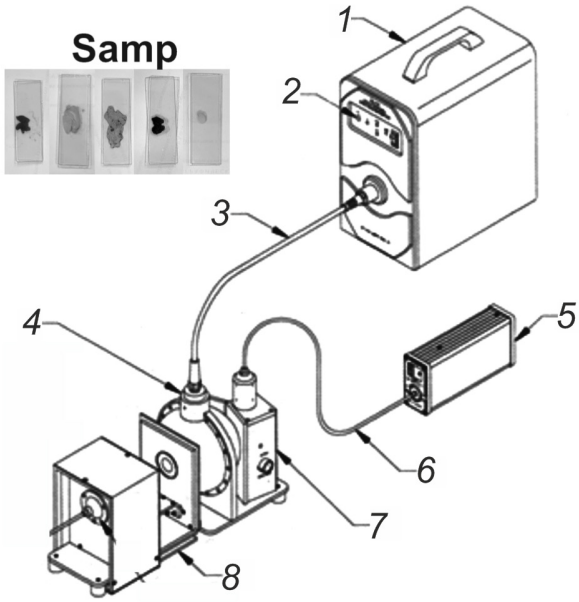

Fig. 2. Adapted OL-770 system for meauring spectral characteristics of biological tissues:
spectroradiometer *1*; window *2* for connecting optical fiber from light source;
optical fibers *3* and *6* for recording signal and light coupling to the sample, respectively;
adapter *4* for measuring integral (diffuse and specular) reflection spectra;
light source *5*; input coupler *7* for measuring reflection; sample position *8*, tissue samples Samp

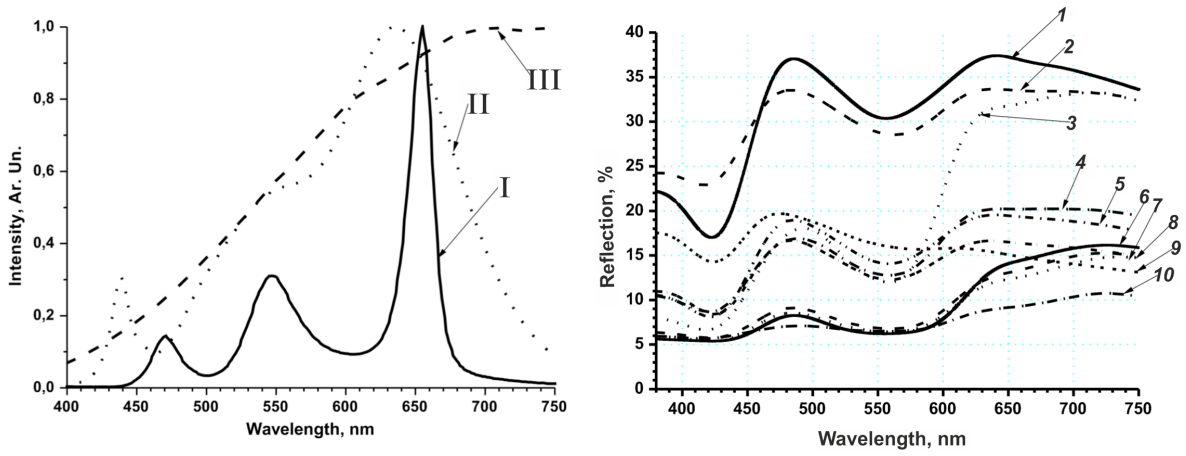

Fig. 3. Emission spectra for sources (*a*) and reflection of different biological tissues (*b*):
RGBWLED (I), WLED (II); HL (III);
brain *1*, skin *2*, lung *3*, pancreas *4*, muscle *5*, heart *6,*
liver *7*, kidney *8*, bladder *9*, spleen *10*

the problem of optical recognition of biological tissues, making it possible to assess different morphological and structural changes in biological organs consisting of identical cells.

Assessment of contrast imaging of biological objects based on experiment

The human visual system identifies boundaries of biological tissues by brightness and color of adjacent organs. The brightness contrast of one biological organ against another gives a reliable estimate of the boundaries of organs in shades of gray and is determined, according to [9], by the following expression:

$$\alpha = \frac{\Phi_{1biotis} - \Phi_{1biotis}}{\Phi_{1biotis} + \Phi_{1biotis}},$$

where $\Phi_{1,2biotis}$ are the relative fluxes of visual exposure to light reflected from the first (1) and second (2) organs adjacent to each other.

The values $\Phi_{1,2biotis}$ are determined by the integrals of spectral flux density of visual light exposure. The last integral is equal to the product of three factors: the spectrum of the light source $E_{source}(\lambda)$, the spectrum of the reflection coefficient $R_{1,2biotis}$ and the luminous efficiency function of the human eye, $V(\lambda)$:

$$\Phi_{i\ biotis} = \int_{380}^{780} \Phi_{i\ sp\ biotis}(\lambda)\, d\lambda =$$

$$= \int_{380}^{780} E_{sourse}(\lambda) \cdot R_{i\ biotis}(\lambda) \cdot V(\lambda)\, d\lambda.$$

Integration is carried out in the wavelength range of optical radiation visible to the human eye: 380–780 nm.

Calculated brightness contrasts of a liver tissue sample against other organs under illumination by three types of sources are given in Table 1.

The spectral density peaks for visual light exposure adjacent tissues are located at different wavelengths and have different amplitudes; the brightness contrast in the liver tissue sample against the pancreas, nerve fibers and subcutaneous fat is virtually independent of the spectral composition of the light source. On the other hand, contrast of blood vessels in the liver strongly depends on the spectral composition of the light source, which makes it possible to optimize the spectral composition of the light from the lamp in order to increase the brightness contrast of the blood vessels. The location of spectral density peaks of visual light exposure at different wavelengths indicates a considerable color contrast.

The color difference of two contacting objects depends on the difference in coordinates in the CIE 1931 color space [10].

Relative spectral flux densities of visual light exposure from two adjacent biological tissues (numbered i = 1, 2) in XYZ color space are found by the expressions [10]:

$$\Phi_{X\ sp\ i}(\lambda) = E_{sourse}(\lambda) \cdot R_{i\ biotis}(\lambda) \cdot X(\lambda);$$

$$\Phi_{Y\ sp\ i}(\lambda) = E_{sourse}(\lambda) \cdot R_{i\ biotis}(\lambda) \cdot Y(\lambda);$$

$$\Phi_{Z\ sp\ i}(\lambda) = E_{sourse}(\lambda) \cdot R_{i\ biotis}(\lambda) \cdot Z(\lambda),$$

Table 1

Brightness contrast of liver tissue specimen against other biological tissues under lighting from different sources

Light source	Pancreas	Nerve fiber	Blood vessels (veins)	Subcutaneous fat
HL	0.2570	0.5985	–0.0096	0.2972
RGBWLED	0.2548	0.5962	0.0012	0.2945
WLED	0.2542	0.5962	0.0066	0.2961

Note. The values of α (see the formula in the text) are compared in relative units.

where $X(\lambda)$, $Y(\lambda)$, $Z(\lambda)$ are the color matching functions of the *XYZ* color space.

Relative color coordinates (chromaticity coordinates) x_i, y_i of visual light exposure of biological tissues are found by the expressions:

$$x_i = \frac{\Phi_{X\,sp\,i}}{\Phi_{X\,sp\,i} + \Phi_{Y\,sp\,i} + \Phi_{Z\,sp\,i}},$$

$$y_i = \frac{\Phi_{Y\,sp\,i}}{\Phi_{X\,sp\,i} + \Phi_{Y\,sp\,i} + \Phi_{Z\,sp\,i}}.$$

Each color can be represented by a point in the *XYZ* color space with two color coordinates *x* and *y*; the coordinate *z* always linearly depends on *x* and *y*.

The distance between two points in the *XY* diagram characterizes the color difference between the two light fluxes and can be used as a measure of contrast. Thus, the color contrast of one biological tissue ($i = 1$) against another ($i = 2$) is found by the expression

$$\alpha_{color} = \sqrt{(x_1 - x_2)^2 + (y_1 - y_2)^2}.$$

If α_{color} extends beyond the perimeter of MacAdam ellipses [11, 12], the adjacent tissues can be distinguished by color; the colors do not necessarily differ in the opposite case.

We calculated the color contrasts for a practically important case of imaging the liver against other tissues under illumination with three light sources (Table 2). Fig. 4 shows calculated chromaticity coordinates *x*, *y* of the same biological tissues.

According to our results, the color contrasts α_{color} were outside the perimeter of MacAdam ellipses in all cases. The highest value of color contrast was observed for tissues illuminated with the RGBWLED array, which is consistent with expert assessment of practicing surgeons.

Table 2

Color contrast α_{color} of liver tissue (relative units) against other biological tissues from different light sources

Color coordinate and contrast	Liver	Pancreas	Subcutaneous fat	Veins	Nerve fibers
Halogen lamp					
x	0.482	0.460	0.475	0.575	0.460
y	0.396	0.396	0.410	0.405	0.351
α_{color}	0	0.026	0.012	0.103	0.031
RGBWLED array					
x	0.461	0.440	0.457	0.576	0.438
y	0.410	0.427	0.420	0.351	0.435
α_{color}	0.0256	0.032	0.015	0.124	0.039
White LED					
x	0.500	0.480	0.494	0.589	0.478
y	0.400	0.415	0.409	0.351	0.422
α_{color}	0	0.026	0.012	0.101	0.032

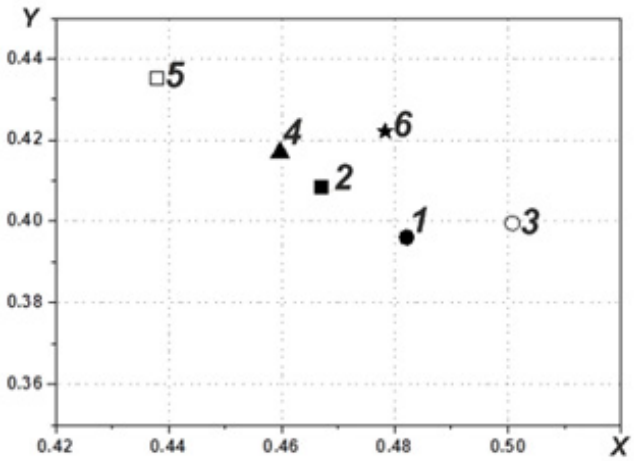

Fig. 4. CIE 1931 chromaticity diagram, color coordinates of liver (*1–3*) and nerve fibers (*4–6*) in different light: halogen lamp (HL)(*1*, *4*); RGBWLED array (*2*, *5*); white LED (3, *6*)

Conclusion

We have considered methods for improving visual detection and differentiation of morphological characteristics of biological tissues and organs *in vivo*. We have solved this problem by using LEDs whose spectral color characteristics can be varied over a wide range, providing optimal lighting for contrast imaging of objects (tissues) that the surgeon is currently working with.

Considering the spectral characteristics of biological tissues, we have found pronounced differentiation in biological tissues by reflection spectra; we have then chosen the spectral color parameters for optimal imaging contrast. Experimental studies using different lamp and LED light sources (HL, RGBWLED and WLED) confirmed that the best contrast is achieved using RGBWLED based on a LED array with specially tailored lighting spectrum. Notably, this lighting may differ from the emission spectrum of white light. This difference means that using different types of lighting for tissue imaging is a promising direction.

A surgical lamp should include a lighting system generating high-quality white light and a dynamically controlled system generating specialized lighting that provides contrast imaging of biological tissues.

The studies were partially supported by the Subsidy Agreement with the Ministry of Education and Science of the Russian Federation (Agreement No. EB 075-02-2018-929, internal agreement number 14.604.21.0187, project ID RFMEFI60417X0187).

REFERENCES

1. **Blinov N.I., Khromov B.M.,** Oshibki, opasnosti i oslozhneniya v khirurgii [Mistakes, dangers and complications in the surgery], Medicine Publishing, Leningrad, 1972.

2. **Knulst A.J., Stassen L.P.S., Grimbergen C.A., Dankelman J.,** Choosing surgical lighting in the LED era, Surgical Innovation. 16 (4) (2009) 317–323.

3. **Aladov A.V., Biryuchiskiy S.B., Dubina M.V., et al.,** Tsvetodinamicheski upravlyayemyy operatsionnyy svetilnik s polnotsvetnym svetodiodom [Color-dynamically controlled operating lamp with a full-color LED], Light and Engineering (Svetotekhnika). (2) (2012) 13–18.

4. **Murai K., Kawahira K., Haneishi H.,** Improving color appearance of organ in surgery by optimally designed LED illuminant, Proc. World Congr. Med. Phys. Biomed. Eng., Berlin, Germany: Springer. 39 (2013) 1010 – 1013.

5. **Wang H., Cuijpers R.H., Luo M.R., et al.,** Optimal illumination for local contrast enhancement based on the human visual system, J. Biomed Opt. 20 (1) (2015) 015005-1– 015005-8.

6. **Kurabuchi Y., Nakano K., Ohnishi T., et al.,** Optimization of surgical illuminant spectra for organ microstructure visualization, IEEE Access. (May) (2019) 70733–70741.

7. **Zakgeim A.L., Chernyakov A.E.,** Izmeritelnyy kompleks dlya polucheniya spektroradiometricheskikh, fotokolorimetricheskikh i teplovykh kharakteristik

poluprovodnikovykh izluchateley [Measuring complex for obtaining spectroradiometric, photocolorimetric and thermal characteristics of semiconductor emitters], Light and Engineering (Svetotekhnika). (4) (2013) 51–56.

8. **Russell W.M.S., Burch R.L.,** The principles of human experimental technique, Methuen Publishing Ltd, London, 1959, 60 p.

9. **Koschan A., Abidi M.,** Digital color image processing, John Wiley & Sons, New York, USA (2008) 11–12.

10. **Yustova E.N.,** Tsvetovyye izmereniya (kolorimetriya) [Color measurement (colorimetry)], St. Petersburg University Publishing, St. Petersburg, 2003.

11. **Guild J.,** The colorimetric properties of the spectrum, Philosophical Transactions of the Royal Society of London, Series A. 230 (1931) 149–187.

12. **MacAdam D.L.,** Visual sensitivities to color differences in daylight, J. Opt. Soc. Am. 32 (5) (1942) 247–274.

Received 18.10.2019, accepted 01.11.2019.

THE AUTHORS

ALADOV Andrey V.
Submicron Heterostructures for Microelectronics, Research & Engineering Center, RAS
26 Politechnicheskaya St., St. Petersburg, 195251, Russian Federation
aaladov@mail.ioffe.ru

VALYUKHOV Vladimir P.
Peter the Great St. Petersburg Polytechnic University
29 Politechnicheskaya St., St. Petersburg, 195251, Russian Federation
Valyukhov@yandex.ru

ZAKGEIM Alexader L.
Submicron Heterostructures for Microelectronics Research and Engineering Center of the RAS
26 Politekhnicheskaya St., St. Petersburg, 194021, Russian Federation
zakgeim@mail.ioffe.ru

KUPTSOV Vladimir D.
Peter the Great St. Petersburg Polytechnic University
29 Politechnicheskaya St., St. Petersburg, 195251, Russian Federation
vdkuptsov@yandex.ru

MAMOSHIN Andrian V.
Research and Development Center of Biomedical Photonics
95 Komsomolskaya St., Orel, 302026, Russian Federation;
Orel Regional Clinical Hospital
10 Pobedy Ave., Orel, 302028, Russian Federation
dr.mamoshin@mail.ru

POTAPOVA Elena V.
Research and Development Center of Biomedical Photonics
95 Komsomolskaya St., Orel, 302026, Russian Federation
potapova_ev_ogu@mail.ru

CHERNYAKOV Anton E.
Submicron Heterostructures for Microelectronics Research and Engineering Center of the RAS
26 Politekhnicheskaya St., St. Petersburg, 194021, Russian Federation
chernyakov.anton@yandex.ru

FOTIADI Alexander E.
Peter the Great St. Petersburg Polytechnic University
29 Politechnicheskaya St., St. Petersburg, 195251, Russian Federation
fotiadi@rphf.spbstu.ru

СПИСОК ЛИТЕРАТУРЫ

1. **Блинов Н.И., Хромов, Б.М.** Ошибки, опасности и осложнения в хирургии. Ленинград: Изд-во «Медицина», 213 .1972 с.

2. **Knulst A.J., Stassen L.P.S., Grimbergen C.A., Dankelman J.** Choosing surgical lighting in the LED era // Surgical Innovation. 2009. Vol. 16. No. 4. Pp. 317–323.

3. **Аладов А.В., Бирючиский С.Б., Дубина М.В., Закгейм А.Л., Мизеров М.Н.** Цветодинамически управляемый операционный светильник с полноцветным светодиодом // Светотехника. 2012. Вып. 2. С. 13–18.

4. **Murai K., Kawahira K., Haneishi H.** Improving color appearance of organ in surgery by optimally designed LED illuminant // Proc. World Congr. Med. Phys. Biomed. Eng. Vol. 39. Berlin, Germany: Springer, 2013. Pp. 1010– 1013.

5. **Wang H., Cuijpers R.H., Luo M.R., Heynderickx I., Zheng Z.** Optimal illumination for local contrast enhancement based on the human visual system // J. Biomed Opt. 2015. Vol. 20. No. 1. Pp. 015005-1–015005-8.

6. **Kurabuchi Y., Nakano K., Ohnishi T., Nakaguchi T., Hauta-Kasari M., Haneishi H.** Optimization of surgical illuminant spectra for organ microstructure visualization // IEEE Access. 2019. May. Pp. 70733–70741.

7. **Закгейм А.Л., Черняков А.Е.** Измерительный комплекс для получения спектрорадиометрических, фотоколориметрических и тепловых характеристик полупроводниковых излучателей // Светотехника. 2013. Вып. 4. С. 51–56.

8. **Russell W.M.S., Burch R.L.** The principles of human experimental technique. London: Methuen Publishing Ltd., 1959. 60 p.

9. **Koschan A., Abidi M.** Digital color image processing. New York, USA: John Wiley & Sons, 2008. Pp. 11–12.

10. **Юстова Е.Н.** Цветовые измерения (колориметрия). СПб.: Изд-во СПбГУ, 2003. 397 с.

11. **Guild J.** The colorimetric properties of the spectrum // Philosophical Transactions of the Royal Society of London. Series A. 1932. Vol. 230. Pp. 149–187.

12. **MacAdam D.L.** Visual sensitivities to color differences in daylight // J. Opt. Soc. Am. 1942. Vol. 32. No. 5. Pp. 247–274.

Статья поступила в редакцию 18.10.2019, принята к публикации 01.11.2019.

СВЕДЕНИЯ ОБ АВТОРАХ

АЛАДОВ Андрей Вальменович – *старший научный сотрудник Научно-технологического центра микроэлектроники и субмикронных гетероструктур Российской академии наук.*
194021, Российская Федерация, г. Санкт-Петербург, Политехническая ул., 26.
aaladov@mail.ioffe.ru

ВАЛЮХОВ Владимир Петрович – *доктор технических наук, профессор Высшей школы прикладной физики и космических технологий Санкт-Петербургского политехнического университета Петра Великого.*
195251, Российская Федерация, г. Санкт-Петербург, Политехническая ул., 29
Valyukhov@yandex.ru

ЗАКГЕЙМ Александр Львович – *кандидат технических наук, ученый секретарь, заведующий лабораторией Научно-технологического центра микроэлектроники и субмикронных гетероструктур Российской академии наук.*
194021, Российская Федерация, г. Санкт-Петербург, Политехническая ул., 26.
zakgeim@mail.ioffe.ru

КУПЦОВ Владимир Дмитриевич – *доктор технических наук, доцент Высшей школы прикладной физики и космических технологий Санкт-Петербургского политехнического университета Петра Великого,* Санкт-Петербург, Российская Федерация.
195251, Российская Федерация, г. Санкт-Петербург, Политехническая ул., 29
vdkuptsov@yandex.ru

МАМОШИН Андриан Валерьивич – *кандидат медицинских наук, доцент, старший научный сотрудник Научно-технологического центра биомедицинской фотоники Орловского государственного университета имени И.С. Тургенева*, врач-хирург Орловской областной клинической больницы**.*
*302026, Российская Федерация, г. Орлл, Комсомольская ул., 95
**302028, Российская Федерация, г. Орлл, бульвар Победы, 10
dr.mamoshin@mail.ru

ПОТАПОВА Елена Владимировна – *кандидат технических наук, доцент, старший научный сотрудник Научно-технологического центра биомедицинской фотоники Орловского государственного университета имени И.С. Тургенева, г. Ор□л,* Российская Федерация.
302026, Российская Федерация, г. Орлл, Комсомольская ул., 95
potapova_ev_ogu@mail.ru.

ЧЕРНЯКОВ Антон Евгеньевич – *кандидат физико-математических наук, старший научный сотрудник Научно-технологического центра микроэлектроники и субмикронных гетероструктур Российской академии наук.*
194021, Российская Федерация, г. Санкт-Петербург, Политехническая ул., 26.
chernyakov.anton@yandex.ru

ФОТИАДИ Александр Эпаминондович – *доктор физико-математических наук, профессор Высшей инженерно-физической школы Санкт-Петербургского политехнического университета Петра Великого.*
195251, Российская Федерация, г. Санкт-Петербург, Политехническая ул., 29
fotiadi@rphf.spbstu.ru

DOI: 10.18721/JPM.12409
УДК 538.956 и 621.317.7

AN AUTOMATIC SYSTEM FOR MEASURING THE FERROELECTRIC HYSTERESIS LOOPS USING THE MODIFIED SAWYER–TOWER CIRCUIT

A.F. Vakulenko[1], *S.B. Vakhrushev*[2], *A.V. Filimonov*[1]

[1] Peter the Great St. Petersburg Polytechnic University, St. Petersburg, Russian Federation;

[2] The Ioffe Institute of the Russian Academy of Sciences, St. Petersburg, Russian Federation

In the article, an equipment and practical application of an automatic system (created by the authors) for measuring the ferroelectric hysteresis loops using the Atmega328 microcontroller have been considered. The modern approaches to the classical Sawyer–Tower circuit's application was analyzed, and practical need for such development was proven. The schematic diagram and description of the main device's components were given. Test results on measuring the hysteresis loops in a barium titanate single crystal were presented, and they were compared with the data published earlier. Moreover, the results on measuring the ferroelectric hysteresis loops of an [110]-oriented $0.8Pb(Mb_{1/3}Nb_{2/3})O_3$–$0.2PbTiO_3$ single crystal in a temperature range of 120 –300 K at frequencies from 2 to 50 Hz were presented.

Keywords: polarization, ferroelectric, hysteresis, Sawyer–Tower circuit

Citation: Vakulenko A.F., Vakhrushev S.B., Filimonov A.V., An automatic system for measuring the ferroelectric hysteresis loops using the modified Sawyer – Tower circuit, St. Petersburg Polytechnical State University Journal. Physics and Mathematics. 12 (4) (2019) 81–87. DOI: 10.18721/JPM.12409

УСТАНОВКА ДЛЯ ИЗМЕРЕНИЯ ПЕТЕЛЬ СЕГНЕТОЭЛЕКТРИЧЕСКОГО ГИСТЕРЕЗИСА НА ОСНОВЕ МОДИФИЦИРОВАННОГО МЕТОДА СОЙЕРА – ТАУЭРА

А.Ф. Вакуленко[1], *С.Б. Вахрушев*[2], *А.В. Филимонов*[1]

[1] Санкт-Петербургский политехнический университет Петра Великого, Санкт-Петербург, Российская Федерация;

[2] Физико-технический институт им. А.Ф. Иоффе РАН, Санкт-Петербург, Российская Федерация

В статье рассматривается устройство и практическое применение созданного авторами автоматического измерителя петель сегнетоэлектрического гистерезиса на основе микроконтроллера Atmega328. Проанализированы современные подходы к использованию классической схемы Сойера – Тауэра и показана практическая необходимость в выполненной разработке прибора. Приводится принципиальная схема и описание основных узлов созданного устройства. Представлены результаты тестовых измерений петель гистерезиса в монокристалле титаната бария, которые сравниваются с ранее опубликованными данными. Изложены также результаты измерения петель сегнетоэлектрического гистерезиса в монокристалле твердого раствора $(PbMg_{1/3}Nb_{2/3}O_3)_{0,8}$-$(PbTiO_3)_{0,2}$ (PMN-PT20) в температурном диапазоне 130 – 300 K.

Ключевые слова: поляризация, сегнетоэлектрик, гистерезис, схема Сойера – Тауэра

Ссылка при цитировании: Вакуленко А.Ф., Вахрушев С.Б., Филимонов А.В. Установка для измерения петель сегнетоэлектрического гистерезиса на основе модифицированного метода Сойера – Тауэра // Научно-технические ведомости СПбГПУ. Физико-математические науки. 2019. Т. 12. № 4. С. 90–98. DOI: 10.18721/JPM.12409

Introduction

Polarization as function of the external electric field in ferroelectrics is a hysteresis loop; it is one of the main characteristics of ferroelectric materials. First studies on measuring hysteresis loops were carried out by Sawyer and Tower in the 1930s. The measurement method named after the researchers has been used ever since. The initial version of the circuit was a high-voltage generator series-connected to a flat sample capacitor and a reference capacitor connected to the deflection plates of the cathode ray tube. This measurement circuit was modified many times: with new methods proposed for compensating for parasitic effects in the sample [1], for measuring the output signal [2], and for special types of applied measuring voltage [3–5].

Sinusoidal or triangular measuring signal is used in the classical circuit. In this case, one of the main problems in measuring hysteresis loops is phase rotation of the measured signal due to parasitic effects in the sample, for example, high conductivity. This is expressed as distortion of the loop or as a loop appearing in the material where it should not, which is described in detail in [6]. This problem can be solved by using a measuring signal with a complex shape, for example, by applying pairs of pulses of each polarity. This method is called Positive Up - Negative Down (PUND) or sometimes the Double-wave method (DWM) [3] in literature. Polarization is switched during primary pulses (half-waves), and all effects that were not preserved when the external electric field was removed are measured during the secondary half-waves. There are more complex measuring signals but describing them is beyond the scope of our study.

Although the original measurement circuit is fairly popular due to its simplicity, it has many drawbacks. The most important one is that data collection is complicated. The only way to record the measured loops before widespread use of digital oscilloscopes was to photograph the oscilloscope screen or transfer the image to translucent paper (film).

One of the main advantages of a digital oscilloscope is that it can record the numerical data of the measured signal. While all modern digital oscilloscopes can perform this function, not all models necessarily allow to record the numerical values of measurements taken in *XY* mode required for applying the Sawyer–Tower circuit. In most cases, only the values from both channels of the oscilloscope as functions of time can be recorded, which is inconvenient and requires constant switching between the two modes. Besides, this method becomes much more complicated if special forms of the measuring signal are used in case of modified circuits. For example, there are relatively long pauses between half-waves in the double-wave method, in order to discharge the reference capacitor, and the oscilloscope may not have sufficient memory to record such a long measurement process.

Another considerable drawback in using an oscilloscope is that an operator has to be personally present, since most devices are not equipped with an automated data storage system synchronized with some external process. Hundreds of hysteresis loops may be measured in real experiments over long periods of time, for example, during long passes over the temperature range. In this case, some universal digital system should be used for data collection. Such systems are very common nowadays.

This study describes a system for data collection that is easy to manufacture. The system is based on widely available, inexpensive components. An example of the system's practical application is study of polarization of a PMN-20PT ferroelectric single crystal.

Circuit diagram and operating principles of the device

The proposed system for measuring ferroelectric hysteresis loops is based on the Atmega328 microcontroller, which is part of the Arduino Uno debug board. The circuit diagram of the device is shown in Fig. 1. The hysteresis loop can be measured with at least one output and one input analog voltage channel. The output channel in the diagram is based on the DAC8512 DAC chip, which has an integrated reference voltage source, a 12-bit resolution and an output voltage in the range from 0 to 4.095 V. An operational amplifier (op-amp) is used to expand the range of output voltages to ±10 V; it is a four-channel LM324 op-amp in this device. The supply voltage of the op-amp, which is 12± V, provides the necessary output signal amplitude. An AD1580 shunt diode with a stabilized voltage of 1.225 V, a stabilized current from 50 μA to 10 mA and an output impedance of 0.5 Ω was chosen as a reference source for shifting the output signal during range scaling. Trimmer potentiometers for range limits (R7) and zero (R5) have 25 revolutions, so output voltage scaling can be

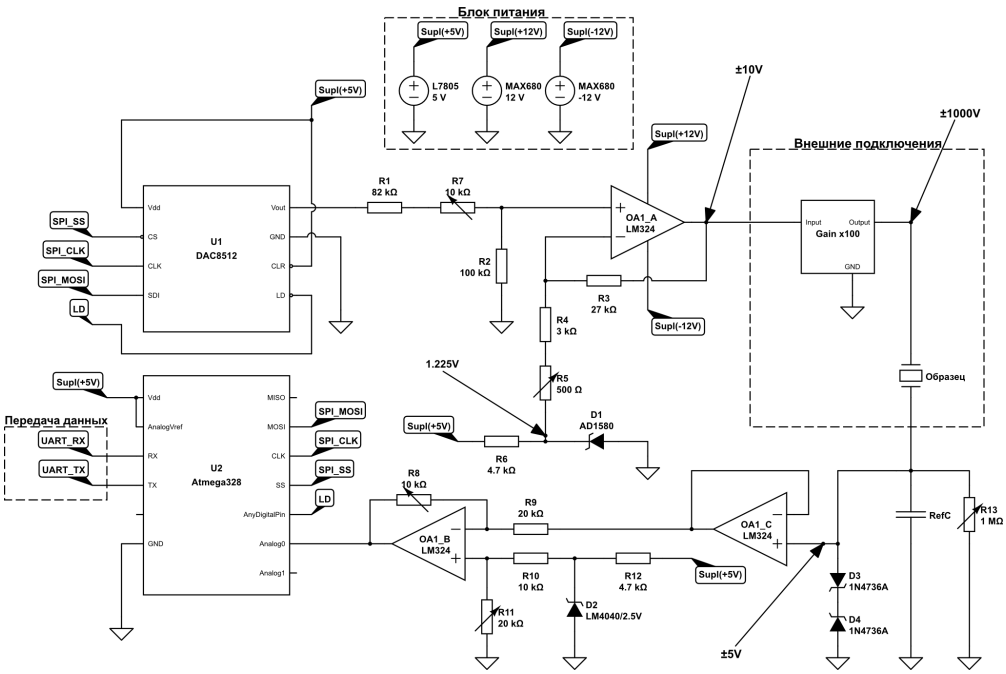

Fig. 1. Circuit diagram of main nodes of system for measuring hysteresis loops

adjusted with an accuracy no worse than 0.5%. The input channel measures the voltage drop across the reference capacitor and has a range of ±5 V. The built-in Atmega328 converter with 6 channels, a 10-bit resolution and reference voltage supplied to the AnalogVref input (5 V) is used as an ADC. Since the voltages in the test sample can significantly exceed the admissible input values, safeguards against sample breakdown (Zener diodes, TVS diodes, etc.) are installed on the input channel. Unfortunately, this solution has its drawbacks, for example, leakage currents of Zener diodes parallel-connected to the reference capacitor affect measurements like a phase-shifting variable resistor R13, which is not always acceptable. Better protection can be achieved by installing a high-linearity optocoupler, for example, HCNR201. The power supply unit is based on L78L05, L78L06 and MAX680 microchips and provides power supply of +5 and 12± V.

The diagram shows an example of external connections: a voltage amplifier with a gain of 100 and the installed sample (a flat capacitor with the given material). If the voltage amplifier is non-linear or has unstable parameters, its output voltage should also be measured. Another analog input channel (similar to the one described above) is constructed for this purpose, connected via a divider to the output of the high-voltage amplifier. In this case, the shape of voltage pulses from the output channel is selected based on the known behavior of the amplifier, and the voltages on the sample and on the reference capacitor are measured simultaneously by two input channels during operation.

The capacity for the reference capacitor is chosen so that the voltage drop across it remains within the acceptable range but at the same time occupies a significant part of the input voltage range. A block of capacitors is usually assembled to simplify the selection of this quantity; the capacitors can be connected to the circuit with either a manual wafer switch or with electromagnetic relays controlled by a microcontroller.

Resistor R13 is used to compensate for the phase shift between the applied voltage and the voltage generated on the reference capacitor if the sample has considerably high conductivity. The resistor can also be used as a current-measuring resistance. In the latter case, the reference capacitor is disconnected from the circuit, and the voltage drop across the resistor R13 is converted into the current flowing through it, so that the current hysteresis loops can be measured. Values of this resistance are typically tens of megaohms for compensated phase rotation and tens of hundreds of ohms for current measurements. It is convenient to use dual potentiometers as current-measuring resistors: one half of the device can be connected to another ADC channel of the

microcontroller as a voltage reference divider; the microcontroller can then measure the resistance of the current-measuring resistor at any time for instant conversion of voltage into current.

The microcontroller can communicate with a computer by the RS232 standard (the circuit should be equipped with a UART-RS232 level converter for this purpose) or in virtual COM port mode via the USB interface built into the debug board, with the data transfer rate of up to 1 Mbps. The microcontroller can be programmed in the standard Arduino IDE, which does not require a separate programmer, or in AVR Studio using the I2C/SPI programmer.

Experimental studies

The ferroelectric hysteresis loops were measured on two samples: single crystals of $BaTiO_3$ (BTO) and $0.8Pb(Mg_{1/3}Nb_{2/3})O_3$-$0.2PbTiO_3$ (PM-20PT) ferroelectrics.

Single crystals were prepared as follows: first, large samples were cut into plates with a [110] plane orientation and thicknesses of 70 μm for PMN-20PT and 600 μm for BTO, then the surfaces of the plates were polished with a DiaPro Nap R diamond suspension to a roughness less than 1 μm. Chromium-gold conductive electrodes 84 nm thick (Cr 4 nm, Au 80 nm) were deposited on both sides of the plates; Moorfield Minilab 080, a vacuum system for deposition of thin films, was used for this purpose. A Struers Accutom 50 machine was used for cutting, and a SuperNova X-ray diffractometer for measuring crystallographic orientation.

A single crystal of barium titatnate ($BaTiO_3$), which is a well-studied material, was chosen as a sample for testing and tuning the device constructed. Fig. 2 shows the obtained hysteresis loops (dark squares) and the signal of the secondary half-waves (light circles). A significant difference between the signals of the first and second pass indicates that polarization is switched in the sample, and the effect persists even when the external field is removed. The positive and negative parts of the loop are shifted relative to each other because the reference capacitor was discharged to zero after each half-wave was applied. The results obtained correspond to the hysteresis loops measured in [7] on the same material with good accuracy (of the order of 10–15%).

Measurements of hysteresis loops in PMN-20PT from our study [8] are given below as an example application of the device constructed. Numerous studies of polarization switching in PMNPT solid solutions [9, 10] point to a linear temperature dependence of the coercive electric field. The temperature model of hysteresis in ferroelectrics was described in [11]: the temperature dependence of the coercive electric field was found to be nonlinear. We assume that the temperature range in these experimental studies was not wide enough to observe non-linearity.

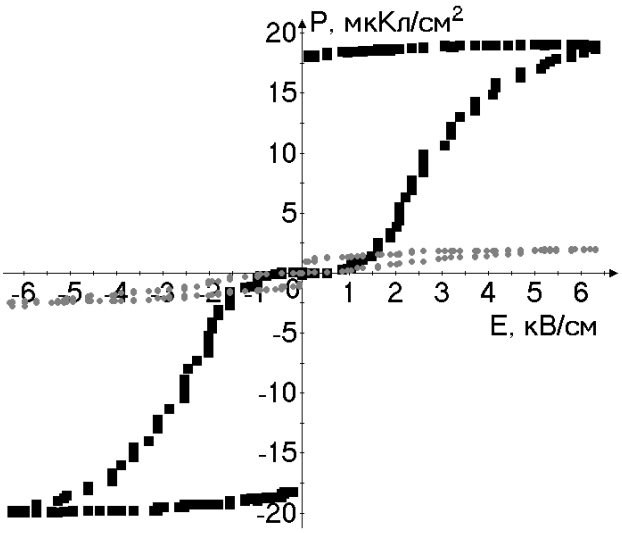

Fig. 2. Hysteresis loop obtained by double-wave method for $BaTiO_3$ single crystal; measuring system we constructed was used

The amplitude and frequency of the measuring signal were 400 V and 50 Hz, respectively; dark squares correspond to the signal of the primary half-waves, light circles to the signal of the secondary half waves

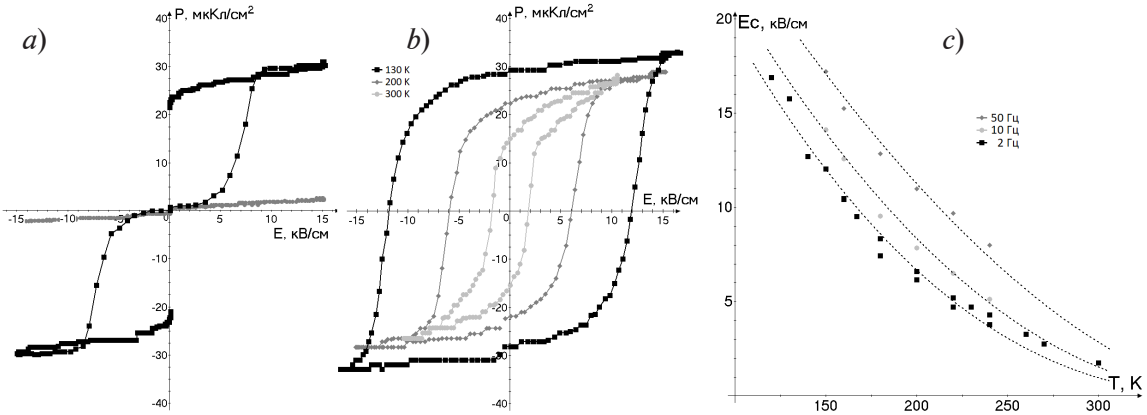

Fig. 3. Double-wave hysteresis loop in PMN-20PT single crystal (*a*) measured by DWM; hysteresis loops measured by conventional method at different temperatures (*b*). Dependence of coercive fields on temperature at different measuring frequencies (*c*). Dark dots in Fig. 3,*a* correspond to signals of the primary half-waves, light dots to signals of the secondary half-waves

Using the system constructed, we measured the ferroelectric hysteresis loops in the temperature range from 130 K to 300 K. Fig. 3,*a* shows quasistatic (measured at a frequency of 2 Hz) ferroelectric hysteresis loops at different temperatures. The double wave method (DWM) was used to increase the measurement accuracy. Fig. 3,*b* shows the results obtained for the primary (dark dots) and secondary (light dots) half-waves. A significant difference between the signals of the first and second pass means that the steps of the measured hysteresis loops are induced by polarization switching, while the parasitic effects are small and can be ignored. The magnitudes of the coercive electric fields were obtained using the measured hysteresis loops (Fig. 3,*c*).

The temperature dependences of the coercive electric fields we obtained are nonlinear, which corresponds to the model of ferroelectric hysteresis described in [11]. According to this model, the magnitude E_c of the coercive electric field is expressed as

$$E_c = E_h\left(1-\frac{T}{T_C}\right)^P, \qquad (1)$$

where E_h is the displacement field [12], T_c is the Curie temperature, p is the dimensionless constant.

Using expression (1), we performed regression analysis of the obtained dependences. The coefficients included in this expression were as follows (determined by the least squares method):

$$E_h = 40.1 \text{ kV/cm}; \; T_c = 380 \text{ K};$$

$$P = 2.4 \text{ at 2 Hz}; \; p = 2.1 \text{ at 10 Hz};$$

$$P = 1.7 \text{ at 50 Hz}.$$

It is difficult to estimate and compare the obtained coefficients, as our experimental study, carried out for a PMN-20PT single crystal using the above model, is the first in this direction.

Conclusion

We have developed and constructed a simple and effective device for measuring ferroelectric hysteresis loops, based on both the classical Sawyer–Tower circuit and the modified double wave method. We have given a circuit diagram of the main components of the measuring system. We have tested the system for a single crystal of barium titanate, yielding good accuracy of measurements. We have confirmed that the system we constructed could be used for a real scientific task, obtaining the hysteresis loops and values of coercive fields of a PMN-20PT single crystal in the temperature range from 130 to 300 K.

REFERENCES

1. **Hikam M., Rachmat A., Ode L., et al.,** The electrical hysteresis loop and polarization value of $BaZr_xTi_{1-x}O_3$ multilayer films material at different annealing temperature (x = 0.1 and 0.08) based on Sawyer – Tower circuit, Proceedings of the 2014 International Conference on Physics and its Applications (ICOPIA-14), Atlantis Press (2014) 41–48.

2. **Pecherskaya E.A.,** Primeneniye metoda Soyera –Tauera i yego modifikatsiy dlya izmereniya elektricheskikh parametrov segnetoelektrikov [Applying the Sawyer – Tower technique and its modification for measuring the electric parameters of ferroelectrics], Izmeritelnaya Tekhnika (Measuring Technique). (10) (2007) 54–58.

3. **Fukunaga M., Noda Y.,** New technique for measuring ferroelectric and antiferroelectric hysteresis loops, Journal of the Physical Society of Japan. 77 (6) (2008) 064706.

4. **Fina I., Fabrega L., Langenberg E., et al.,** Nonferroelectric contributions to the hysteresis cycles in manganite thin films: A comparative study of measurement techniques, Journal of Applied Physics. 109 (7) (2011) 074105.

5. **Liu J., Zhao Y., Chen C., et al.,** Study on the polarization and relaxation processes of ferroelectric polymer films using the Sawyer–Tower circuit with square voltage waveform, The Journal of Physical Chemistry, C. 121 (23) (2017) 12531–12539.

6. **Tylczynski Z.,** A collection of 505 papers on false or unconfirmed ferroelectric properties in single crystals, ceramics and polymers, Frontiers of Physics. 14 (6) (2019) 63301.

7. **Wongdamnern N., Ngamjarurojana A., Laosiritaworn Y., et al.,** Dynamic ferroelectric hysteresis scaling of $BaTiO_3$ single crystals, Journal of Applied Physics. 105 (4) (2009) 044109.

8. **Vakulenko A.F., Vakhrushev S.B., Filimonov A.V.,** Investigation of polarization switching processes in 0.8PMN-0.2PT single crystal in a temperature range from 100 K to 300 K, Ferroelectrics. 542 (1) (2019) 77–84.

9. **Zhang Y., Chen Z., Cao W., Zhang Z.,** Temperature and frequency dependence of the coercive field of $0.71PbMb_{1/3}Nb_{2/3}O_3$–$0.29PbTiO_3$ relaxor-based ferroelectric single crystal, Applied Physics Letters. 111 (17) (2017) 172902.

10. **Chen I.W., Wang Y.,** A domain wall model for relaxor ferroelectrics, Ferroelectrics. 206 (1) (1998) 245–263.

11. **Raye J.K., Smith R.C.,** A temperature-dependent hysteresis model for relaxor ferroelectric compounds, “Smart Structures and Materials 2004: Modeling, Signal Processing, and Control” (International Society for Optics and Photonics), 5383 (2004) 1–10.

12. **Smith R.C., Seelecke S., Ounaies Z., Smith J.,** A free energy model for hysteresis in ferroelectric materials, Journal of intelligent material systems and structures. 14 (11) (2003) 719–739.

Received 25.10.2019, accepted 05.11.2019.

THE AUTHORS

VAKULENKO Aleksandr F.
Peter the Great St. Petersburg Polytechnic University
29 Politechnicheskaya St., St. Petersburg, 195251, Russian Federation
vakulenko705@gmail.com

VAKHRUSHEV Sergey B.
Ioffe Institute of the Russian Academy of Sciences
26 Polytekhnicheskaya St., St. Petersburg, 194021, Russian Federation
s.vakhrushev@mail.ioffe.ru

FILIMONOV Alexey V.
Peter the Great St. Petersburg Polytechnic University
29 Politechnicheskaya St., St. Petersburg, 195251, Russian Federation
filimonov@rphf.spbstu.ru

СПИСОК ЛИТЕРАТУРЫ

1. **Hikam M., Rachmat A., Ode L., Bambang S., Arief S.** The electrical hysteresis loop and polarization value of $BaZr_xTi_{1-x}O_3$ multilayer films material at different annealing temperature (x = 0.1 and 0.08) based on Sawyer – Tower circuit // Proceedings of the 2014 International Conference on Physics and its Applications (ICOPIA-14). Atlantis Press, 2014. Pp. 41–48.

2. Печерская Е.А. Применение метода Сойера – Тауэра и его модификаций для измерения электрических параметров сегнетоэлектриков // Измерительная техника. 2007. № 10. С. 54–58.

3. **Fukunaga M., Noda Y.** New technique for measuring ferroelectric and antiferroelectric hysteresis loops // Journal of the Physical Society of Japan. 2008. Vol. 77. No. 6. P. 064706.

4. **Fina I., Fabrega L., Langenberg E., Marti X., Sanchez F., Varela M., Fontcuberta J.** Nonferroelectric contributions to the hysteresis cycles in manganite thin films: A comparative study of measurement techniques //Journal of Applied Physics. 2011. Vol. 109. No. 7. P. 074105.

5. **Liu J., Zhao Y., Chen C., Wei X., Zhang Z.** Study on the polarization and relaxation processes of ferroelectric polymer films using the Sawyer–Tower circuit with square voltage waveform //The Journal of Physical Chemistry. C. 2017. Vol. 121. No. 23. Pp. 12531–12539.

6. **Tylczynski Z.** A collection of 505 papers on false or unconfirmed ferroelectric properties in single crystals, ceramics and polymers //Frontiers of Physics. 2019. Vol. 14. No. 6. P. 63301.

7. **Wongdamnern N., Ngamjarurojana A., Laosiritaworn Y., Ananta S., Yimnirun R.** Dynamic ferroelectric hysteresis scaling of $BaTiO_3$ single crystals // Journal of Applied Physics. 2009. Vol. 105. No. 4. P. 044109.

8. **Vakulenko A.F., Vakhrushev S.B., Filimonov A.V.** Investigation of polarization switching processes in 0.8PMN-0.2PT single crystal in a temperature range from 100 K to 300 K // Ferroelectrics. 2019. Vol. 542. No. 1. Pp. 77–84.

9. **Zhang Y., Chen Z., Cao W., Zhang Z.** Temperature and frequency dependence of the coercive field of $0.71PbMb_{1/3}Nb_{2/3}O_3$–$0.29PbTiO_3$ relaxor-based ferroelectric single crystal //Applied Physics Letters. 2017. Vol. 111. No. 17. P. 172902.

10. **Chen I.W., Wang Y.** A domain wall model for relaxor ferroelectrics //Ferroelectrics. 1998. Vol. 206. No. 1. Pp. 245–263.

11. **Raye J.K., Smith R.C.** A temperature-dependent hysteresis model for relaxor ferroelectric compounds //Smart Structures and Materials 2004: Modeling, Signal Processing, and Control. International Society for Optics and Photonics, 2004. Vol. 5383. Pp. 1–10.

12. **Smith R.C., Seelecke S., Ounaies Z., Smith J.** A free energy model for hysteresis in ferroelectric materials // Journal of intelligent material systems and structures. 2003. Vol. 14. No. 11. Pp. 719–739.

Статья поступила в редакцию 25.10.2019, принята к публикации 05.11.2019.

СВЕДЕНИЯ ОБ АВТОРАХ

ВАКУЛЕНКО Александр Феликсович – *инженер научно-образовательного центра «Физика нанокомпозитных материалов электронной техники» Санкт-Петербургского политехнического университета Петра Великого.*

195251, Российская Федерация, г. Санкт-Петербург, Политехническая ул., 29
sasha705@mail.ru

ВАХРУШЕВ Сергей Борисович – *доктор физико-математических наук, заведующий лабораторией нейтронных исследований Физико-технического института им. А.Ф. Иоффе РАН.*

194021, Российская Федерация, г. Санкт-Петербург, Политехническая ул., 26
s.vakhrushev@mail.ioffe.ru

ФИЛИМОНОВ Алексей Владимирович – *доктор физико-математических наук, профессор Высшей инженерно-физической школы, директор научно-образовательного центра «Физика нанокомпозитных материалов электронной техники» Санкт-Петербургского политехнического университета Петра Великого.*

195251, Российская Федерация, г. Санкт-Петербург, Политехническая ул., 29
filimonov@rphf.spbstu.ru

DOI: 10.18721/JPM.12410
УДК 533.9.01

POSITIVE COLUMN OF A DIRECT CURRENT DISCHARGE IN LASER TUBES OF VARIABLE DIAMETER

A.E. Fotiadi, V.A. Kozhevnikov, V.E. Privalov

Peter the Great St. Petersburg Polytechnic University,

St. Petersburg, Russian Federation

A positive column of a direct current discharge in monoatomic gas is considered and expressions are obtained that relate the external parameters of the column (varying radius of the discharge channel, gas pressure and discharge current) to the "internal" characteristics (concentration of charged particles, electron temperature, and longitudinal electric field strength).

Keywords: positive column plasma characteristic, variable diameter laser tube, active element geometry

Citation: Fotiadi A.E., Kozhevnikov V.A., Privalov V.E., Positive column of a direct current discharge in laser tubes of variable diameter, St. Petersburg Polytechnical State University Journal. Physics and Mathematics. 12 (4) (2019) 88–98. DOI: 10.18721/JPM.12410

ПОЛОЖИТЕЛЬНЫЙ СТОЛБ РАЗРЯДА ПОСТОЯННОГО ТОКА В ЛАЗЕРНЫХ ТРУБКАХ ПЕРЕМЕННОГО ДИАМЕТРА

А.Э. Фотиади, В.А. Кожевников, В.Е. Привалов

Санкт-Петербургский политехнический университет Петра Великого,

Санкт-Петербург, Российская Федерация

Рассмотрены процессы в положительном столбе разряда постоянного тока в газе и получены выражения, связывающие внешние параметры столба (меняющийся радиус разрядного канала, давление напуска газа и разрядный ток) с «внутренними» характеристиками (концентрация заряженных частиц, электронная температура, напряженность «продольного» электрического поля).

Ключевые слова: характеристика плазмы положительного столба, лазерная трубка переменного диаметра, геометрия активного элемента

Ссылка при цитировании: Фотиади А.Э., Кожевников В.А., Привалов В.Е. Положительный столб разряда постоянного тока в лазерных трубках переменного диаметра // Научно-технические ведомости СПбГПУ. Физико-математические науки. 2019. Т. 12. № 4. С. 97–107. DOI: 10.18721/JPM.12410

Gas-discharge lasers such as, for example, helium-neon (He-Ne) or helium-cadmium (He-Cd), are one of the most common types, using a positive column (PC) of low-pressure direct-current glow discharge in cylindrical tubes. The laser's gain medium is placed in an optical cavity with sphere-plane geometry. The shape of the caustic in such a cavity is considerably different from cylindrical. Because of this, some of the excited atoms produced in the cylindrical discharge do not contribute to the 'effective' gain determining the laser's output power. Conical tubes were first considered in 1969 as a means for improving the efficiency of the gain medium and increasing its mode volume in gas lasers [1, 2]. This model was supported by calculations of the gain [3] and confirmed experimentally [4].

The 'geometric' part of the gain k were based on the formula

$$k = \frac{1}{S}\int_V k_0 \cdot f_s dV,$$

where k_0 is the unsaturated gain on the tube axis, f_S is the gain distribution function over the column cross-section, S is its cross-sectional area.

It was assumed that the function f_S is similar to the distribution of the concentration of excited atoms in the discharge [5, 6]. This formulation implies that the quantities k_0, f_S and S are independent of the longitudinal coordinate z of the column. This is questionable to say the least for discharge in a conical tube, since the area S and such important characteristics of the PC as electron concentration and temperature, determining the population inversion, change with the changing radius of the discharge channel.

An earlier study [7] considered the reaction of the parameters of the positive column to an abrupt change in the radius of the discharge tube. However, there is practically no data in literature for tubes with a 'smoothly changing' radius of the discharge channel, especially in GDLs. Our study is dedicated to this problem.

Let us consider a direct current PC of length l in monatomic gas. Gas inlet pressure p does not exceed 10 mm Hg, discharge current I lies in the range of 10–100 mA. The radius R of the discharge channel is a smooth function of the coordinate z ($0 \le z \le l$):

$$|dR/dz| << 1.$$

The axis z is directed along the axis of the discharge tube:

$$R = R(z) = R_0 f_R(z),$$

where R_0 is the radius of the channel R at the point $z = 0$; $f_R(z = 0) = 1$;

$$1 \text{ mm} \le R_0 \le 5 \text{ mm}.$$

We assume that the given positive column under these discharge conditions is three-component plasma consisting of neutral atoms of the same kind, singly charged positive ions, and electrons. The concentrations of these particles are denoted, respectively, as n_a, n_i, n_e, and their masses as m_a, m_i, m_e; $m_a = m_i$.

The ion mean free path λ_i is much smaller than the tube radius: $\lambda_i << R$. Therefore, the processes in the discharge can be considered within Schottky's diffusion theory of the positive column.

We assume that the column plasma is quasi-neutral in these discharge conditions, i.e., $n_e \approx n_i = n$, and is weakly ionized:

$$\nu_{ee}, \nu_{ei}, \nu_{ii} << \nu_{ea}, \nu_{ia},$$

i.e., the frequencies with which charged particles collide with each other, ν_{ee}, ν_{ei}, ν_{ii}, are much lower than the frequencies of electron-atom (ν_{ea}) and ion-atom (ν_{ia}) collisions.

Such processes as stepwise ionization, bulk recombination, and electron attachment are unlikely under this assumption.

Next let us assume the energy distributions of electrons, ions, and neutral atoms to be Maxwellian, with temperatures $T_\alpha \equiv T_e$, T_i, T_a, respectively. We also assume that

particle temperatures are related as $T_e >> T_i \approx T_a$;

the electron temperature is uniform over the column cross-section but is a function of the coordinate z: $T_e = \text{const}\ (r,\theta)$, $T_e = T_e(z)$;

the ion temperature is distributed uniformly both over the column cross-section and along the longitudinal coordinate: $T_e = \text{const}\ (r,\theta,z)$.

The distributions of gas pressure in the column, equal to the inlet pressure p, gas temperature, and, consequently, the concentration of neutral particles $n_a = p/kT_a$ are assumed to be uniform both over the cross-section of the column and along its length: T_a, $n_a = \text{const}\ (r,\theta,z)$.

The concentrations of charged particles are azimuthally uniform but are functions of the radial and longitudinal coordinates:

$$n_e = \text{const}(\theta),\ n_e = n_e(r,z),$$
$$n_i = \text{const}(\theta),\ n_i = n_i(r,z).$$

The electric field **E** is also azimuthally uniform and is a function of the radial and longitudinal coordinates:

$$\mathbf{E} = \text{const}(\theta),\ \mathbf{E} = \mathbf{E}(r,z).$$

We assume that the main mechanism for producing charged particles is direct ionization by electron impact from the ground state of atoms. The ionization frequency is $\nu_i = n_a\langle\sigma_{0i},\nu_e\rangle$, where $\langle\sigma_{0i},\nu_e\rangle$ is the product $\sigma_{0i}\nu_e$, averaged over the electron distribution function $f_e(\nu_e)$; σ_{0i} is the cross-section of this ionization process; ν_e is the electron velocity.

We assume that the main mechanism for the decay of charged particles is their diffusive escape to the walls of the discharge tube.

The current density $\mathbf{j} = \mathbf{j}(r,z)$ is equal to the difference in the density of ion fluxes $\mathbf{\Gamma}_i = n_i\mathbf{u}_i$ and electron fluxes $\mathbf{\Gamma}_e = n_e\mathbf{u}_e$:

$$\mathbf{j} = e(\mathbf{\Gamma}_i - \mathbf{\Gamma}_e) = e\,(n_i\mathbf{u}_i - n_e\mathbf{u}_e) = en(\mathbf{u}_i - \mathbf{u}_e). \quad (1)$$

The discharge current I is determined by the zth component of the current density $\mathbf{j}_z$ associated with the drift of charged particles in the field $\mathbf{E}_z$ (the longitudinal potential gradient in the column) depending on the longitudinal coordinate:

$$\mathbf{E}_z(z) = \mathbf{E}_{0z}f_{E_z}(z),$$

where $\mathbf{E}_{0z} = \mathbf{E}_z(z = 0)$; $f_{E_z}(z = 0) = 1$.

We assume that all energy is supplied to the PC from electrons accelerated in this electric field $\mathbf{E}_z$.

The following problem is formulated:

obtain relatively simple expressions linking easily controlled external parameters of the column (discharge current I, radius R(z) of the discharge channel and gas inlet pressure p) with its main internal characteristics (charged particle concentration $n_e(z)$, electron temperature $T_e(z)$ and strength of the longitudinal electric field $\mathbf{E}_z(z)$).

Based on the methods developed in [7, 8, 12], we use the following equations to solve this problem.

Equations of motion of charged particles, which, provided that

$$\nu_{ee},\ \nu_{ei},\ \nu_{ii} << \nu_{ea},\ \nu_{ia},$$

and neglecting the thermal power, have the form:

$$-e\mathbf{E} - \frac{\nabla\left(n_e kT_e\right)}{n_e} - \mu_{ea}\nu_{ea}\mathbf{u}_e = 0$$

for electrons;

$$e\mathbf{E} - \frac{\nabla\left(n_i kT_i\right)}{n_i} - \mu_{ia}\nu_{ia}u_i = 0$$

for ions.

Here μ_{ea}, μ_{ia} are the normalized masses of electrons and ions, respectively.

Equations of balance of charged particles:

$$\frac{\partial n_e}{\partial t} + \nabla\left(n_e\mathbf{u}_e\right) = \frac{\delta n_e}{\delta t}$$

for electrons;

$$\frac{\partial n_i}{\partial t} + \nabla\left(n_i\mathbf{u}_i\right) = \frac{\delta n_i}{\delta t}$$

for ions.

The equation of electron energy balance:

$$IE_z = P_\nu + P_w,$$

where IE_z is the power expended by the longitudinal electric field to heat the electrons and maintain the total energy balance in the column; P_ν is the power lost by electrons in elastic collisions with atoms (gas heating); P_w is the power transferred to the wall by ions.

The power lost by electrons in inelastic collisions with atoms is not taken into account in the balance equation.

Let us consider these equations in more detail.

The expressions for the directed velocities of electrons and ions for a direct-current discharge are written as follows assuming that plasma is quasi-neutral and that ion temperatures are independent of the coordinates:

$$\mathbf{u}_e = -b_e\mathbf{E} - D_e\left(\frac{\nabla n}{n} + \frac{\nabla T_e}{T_e}\right); \quad (2)$$

$$\mathbf{u}_i = +b_i\mathbf{E} - D_i\frac{\nabla n}{n}. \quad (3)$$

Here $b_e = e/\mu_{ea}\nu_{ea}$, $b_i = e/\mu_{ia}\nu_{ia}$ are the mobilities of electrons and ions; $D_e = kT_e/\mu_{ea}\nu_{ea} = b_e kT_e/e$, $D_i = kT_i/\mu_{ia}\nu_{ia} = b_i kT_i/I$ are the diffusion coefficients of electrons and ions, respectively; ν_{ea} is the frequency of elastic electron-atom collisions, equal to

$$\nu_{ea} = n_a\left\langle\sigma_{ea}\nu_e\right\rangle,$$

where $\langle\sigma_{ea},\nu_e\rangle$ is the product $\sigma_{ea}\nu_e$, averaged over the electron distribution function $f_e(\nu_e)$; σ_{ea} is the cross-section of elastic electron-atom collisions, ν_e is the electron velocity.

In general, the expression $\langle\sigma_{ea},\nu_e\rangle$ is also a function of the longitudinal coordinate z, because $T_e = T_e(z)$. We also assume that

$$\langle \sigma_{ea} v_e \rangle = \mathrm{const}(z),$$

which is true to a first approximation, at least for discharge in helium, since $\sigma_{ea} v_{ea} \approx \mathrm{const}(T_e)$ in the variation range of electron energy characteristic for these discharge conditions [11].

The frequency of elastic ion-atom collisions has the form

$$\nu_{ia} \nu_{ia} = n_a \langle \sigma_{ia} v_{ia} \rangle,$$

where the quantity $\langle \sigma_{ia}, \nu_{ia} \rangle$ can be represented for the case of weakly ionized plasma as

$$\langle \sigma_{ia} v_{ia} \rangle \approx \sigma_{ia} \langle v_{T_a} \rangle = \sigma_{ia} \sqrt{3 \frac{kT_a}{m_a}} = \mathrm{const}(z).$$

The current density in DC plasma is then written as

$$\mathbf{j} = en\left[b_i \mathbf{E} - D_i \frac{\nabla n}{n} + b_e \mathbf{E} + D_e \left(\frac{\nabla n}{n} + \frac{\nabla kT_e}{kT_e} \right) \right]. \quad (4)$$

We then obtain the expression for the electric field **E**:

$$\mathbf{E} = \frac{\mathbf{j}}{en(b_i + b_e)} - \left(\frac{D_e - D_i}{b_i + b_e} \cdot \frac{\nabla n}{n} + \frac{D_e}{b_i + b_e} \cdot \frac{\nabla kT_e}{kT_e} \right) = \mathbf{E}_{con} + \mathbf{E}_{sc}.$$

In other words, the electric field **E** in column plasma is determined by two terms. The first one is the electric field of 'conductivity' $\mathbf{E}_{con}$, that is, the 'external' field generating the current flux **j** in a medium with the conductivity σ:

$$E_{con} = \frac{\mathbf{j}}{en(b_i + b_e)} = \frac{\mathbf{j}}{\sigma}.$$

The second term is the 'space charge' field $\mathbf{E}_{sc}$:

$$\mathbf{E}_{sc} = -\left(\frac{D_e - D_i}{b_i + b_e} \cdot \frac{\nabla n}{n} + \frac{D_e}{b_i + b_e} \cdot \frac{\nabla kT_e}{kT_e} \right) = \left(\mathbf{E}_{\hat{i}\varsigma_{\nabla n}} + \mathbf{E}_{\hat{i}\varsigma_{\nabla T_e}} \right),$$

where

$$\mathbf{E}_{sc_{\nabla n}} = -\frac{D_e - D_i}{b_i + b_e} \cdot \frac{\nabla n}{n},$$

$$\mathbf{E}_{sc_{\nabla T_e}} = -\frac{D_e}{b_i + b_e} \cdot \frac{\nabla kT_e}{kT_e}.$$

The expression for the current density can then be written as

$$\mathbf{j} = en\left[(b_i + b_e)(\mathbf{E}_{con} + \mathbf{E}_{sc}) + (D_e - D_i) \frac{\nabla n_e}{n_e} + D_e \frac{\nabla kT_e}{kT_e} \right] \Rightarrow$$

$$\Rightarrow \mathbf{j} = en(b_i + b_e)\left[\mathbf{E}_{con} - \frac{D_e - D_i}{b_i + b_e} \cdot \frac{\nabla n}{n} - \frac{D_e}{(b_i + b_e)} \frac{\nabla kT_e}{kT_e} \right] + en\left[(D_e - D_i) \frac{\nabla n_e}{n_e} + D_e \frac{\nabla kT_e}{kT_e} \right] \Rightarrow$$

$$\Rightarrow \mathbf{j} = \mathbf{j}_{\hat{i}\partial} + \mathbf{j}_{\nabla_n} + \mathbf{j}_{\nabla_{T_e}},$$

where

$$\mathbf{j}_{con} = en(b_i + b_e)\mathbf{E}_{con} = \sigma \mathbf{E}_{con};$$

$$\mathbf{j}_{\nabla n} = en\left[(D_e - D_i) - (b_i + b_e) \frac{D_e - D_i}{b_i + b_e} \right] \frac{\nabla n}{n};$$

$$\mathbf{j}_{\nabla_{Te}} = en\left[D_e - (b_i + b_e) \frac{D_e}{(b_i + b_e)} \right] \frac{\nabla kT_e}{kT_e}.$$

Evidently, the current densities $\mathbf{j}_{\nabla_n}$ and $\mathbf{j}_{\nabla_{T_e}}$, generated by diffusion of charged particles under the influence of their concentration gradients and electron temperature, are equal to zero.

The following conclusions can be drawn from this.

First, ambipolar diffusion is prevalent in the given discharge. Indeed, using the obtained expressions for the diffusion flows of charged particles, we obtain:

$$\mathbf{u}_{e_{sc}} = \mathbf{u}_{i_{sc}} = -\left[\frac{(b_i D_e + b_e D_i)}{b_i + b_e} \right] \frac{\nabla n}{n} - \frac{b_i D_e}{b_i + b_e} \times \frac{\nabla kT_e}{kT_e} = -D_{a_{\nabla n}} \frac{\nabla n}{n} - D_{a_{\nabla T_e}} \frac{\nabla kT_e}{kT_e},$$

where

$$D_{a_{\nabla n}} = \frac{(b_i D_e + b_e D_i)}{b_i + b_e}, \quad D_{a_{\nabla T_e}} = \frac{b_i D_e}{b_i + b_e}$$

are the respective coefficients of ambipolar diffusion.

Given that $D_e >> D_i$, $b_e >> b_i$, $T_e >> T_i$, we obtain:

$$D_{a_{\nabla n}} \approx D_{a_{\nabla T_e}} = D_a = b_i \frac{kT_e}{e}.$$

Secondly, the current density in DC plasma, equal to the sum $\mathbf{j} = \mathbf{j}_{con} + \mathbf{j}_{sc,}$ depends in this case only on the conductivity current density:

$$\mathbf{j} = en\left(\mathbf{u}_i - \mathbf{u}_e\right) = \mathbf{j}_{con} = en\left(b_i + b_e\right)\mathbf{E}_{con} \approx$$
$$\approx enb_e\mathbf{E}_{cjn} = \sigma_e\mathbf{E}_{con}.$$

The current density $\mathbf{j}_{con}$ can be represented as the sum

$$\mathbf{j}_{con} = \mathbf{j}_{con_r r} + \mathbf{j}_{con_z}.$$

Since the longitudinal component of the conductivity current density $\mathbf{j}_{conz}$ is associated with electron drift along the column axis in the longitudinal electric field $\mathbf{E}_{conz} = \mathbf{E}_z(z)$, the detected discharge current I can be written as

$$I = \int_0^{2\pi}\int_0^{R_z} \mathbf{j}_{con_z} r dr d\theta =$$
$$= 2\pi e b_e E_z\left(z\right)\int_0^{R_z} n\left(r,z\right) r dr = \mathrm{const}\left(z\right), \quad (5)$$

where R_z is the radius R at the point with the coordinate z.

Let us now consider the equations of balance of charged particles:

$$\frac{\partial n_e}{\partial t} = -\nabla\left(n_e\mathbf{u}_e\right) + \frac{\delta n_e}{\delta t};$$
$$\frac{\partial n_i}{\partial t} = -\nabla\left(n_i\mathbf{u}_e\right) + \frac{\delta n_i}{\delta t}.$$

The following condition should be satisfied to maintain quasi-neutral plasma in steady state:

$$\frac{\partial n_{\grave{a}}}{\partial t} = \frac{\partial n_i}{\partial t}.$$

In our case, the generation terms $\frac{\delta n_i}{\delta t}$ and $\frac{\delta n_e}{\delta t}$ of the equations (absence of bulk recombination and stepwise ionization) are determined only by direct ionization of atoms by electron impact with the ionization frequency

$$\nu_i = n_a\left\langle \sigma_{0_i} v_e \right\rangle.$$

Since bulk ionization and recombination on the walls of the tube lead to simultaneous production or decay of an ion-electron pair, which is expressed as

$$\frac{\delta n_e}{\delta t} = \frac{\delta n_i}{\delta t} = \frac{\delta n}{\delta t} = n\nu_i,$$

we obtain the following equalities: $\nabla n\mathbf{u}_e = \nabla n\mathbf{u}_i = n\nu_i$.

Then, assuming that plasma is quasi-neutral and that the mobilities of electrons and ions, as well as the temperatures of ions are independent of the coordinates, we use expressions (2), (3) for directed velocities of electrons and ions, making simple transformations, excluding $\mathbf{E}$ and provided that $\nabla n\mathbf{u}_e = \nabla n\mathbf{u}_i = n\nu_i$, and obtain the following equation:

$$n\nu_i\left(b_i + b_e\right) + \left(b_i D_e + b_e D_i\right)\Delta n +$$
$$+\left(b_i D_e \frac{\nabla T_e}{T_e}\right)\nabla n +$$
$$+b_i\left[\nabla D_e \cdot \frac{\nabla T_e}{T_e} + D_e \nabla\left(\frac{\nabla T_e}{T_e}\right)\right] n = 0.$$

Since n = const(θ), n_a = const(r,θ,z), T_e = const(r,θ), and the atom concentration and the electron temperature are independent of the radial coordinates, which in turn means that the electron diffusion coefficient and the ionization frequency are independent of the coordinate r, this equation can be represented as

$$n\nu_i + \frac{\left(b_i D_e + b_e D_i\right)}{\left(b_i + b_e\right)}\left(\Delta_r n + \Delta_z n\right) +$$
$$+\left(\frac{b_i D_e}{\left(b_i + b_e\right)}\frac{\nabla_z T_e}{T_e}\right)\nabla_z n + \frac{b_i}{\left(b_i + b_e\right)} \times$$
$$\times\left\{\left[\nabla_z D_e \cdot \frac{\nabla_z T_e}{T_e} + D_e \nabla_z\left(\frac{\nabla_z T_e}{T_e}\right)\right]\right\} n = 0.$$

Then, since $b_e >> b_i$, $T_e >> T_i$ and

$$D_{\grave{a}} = \frac{b_i D_e + b_e D_i}{b_i + b_e} \approx b_i \frac{D_e}{b_e} = b_i \frac{kT_e}{e},$$

we obtain the following equation:

$$n\nu_i\left(b_i + b_e\right) + \left(b_i D_e + b_e D_i\right)\Delta n +$$
$$+\left(b_i D_e \frac{\nabla T_e}{T_e}\right)\nabla n +$$
$$+b_i\left[\nabla D_e \cdot \frac{\nabla T_e}{T_e} + D_e \nabla\left(\frac{\nabla T_e}{T_e}\right)\right] n = 0.$$

After transforming it, we obtain:

$$\left(\Delta_r n+\Delta_z n\right)+\frac{2}{D_a}\left(\nabla_z D_a\right)\nabla_z n+$$
$$+\frac{1}{D_a}\left[\nabla_z\left(\nabla_z D_a\right)+\nu_i\right]n=0.$$

Let us transform this equation so it takes the following form:

$$\frac{\partial^2 n}{\partial r^2}+\frac{1}{r}\frac{\partial n}{\partial r}+\frac{\partial^2 n}{\partial z^2}+$$
$$+\frac{2}{D_a}\frac{dD_a}{dz}\frac{dn}{dz}+\frac{1}{D_a}\left(\frac{d^2 D_a}{dz^2}+\nu_i\right)n=0. \quad (6)$$

Now we introduce the dimensionless concentration

$$N(r,z)=\frac{n(r,z)}{n_0}=f_{n_r}(r)\cdot f_{n_z}(z),$$

where $n_0 = n(0,0)$ is the concentration of charged particles on the axis of the discharge ($r = 0$) at the point $z = 0$; $f_{nr}(r) = \text{const}(z)$ is the function of radius only, $f_{nz}(z) = \text{const}(r)$ is the function of the longitudinal coordinate only, with boundary conditions:

$$f_{n_r}(r=0)=f_{n_z}(z=0)=f_{R_z}(z=0)=1;$$
$$f_{n_r}(R_z)=0; f_{n_z}(l)=\frac{n(0,l)}{n_0}; f_{R_z}=\frac{R_z}{R_0}.$$
$$0\le r\le R_z;\ \ 0\le z\le l;$$

The concentration $n(0,z)$ on the axis ($r = 0$) at the point z is equal to:

$$n(0,z)=n_{0z}(z)=n_0 f_{n_z}(z)=\text{const}(r),$$

and the expression for $n(r,z)$ is written as

$$n(r,z)=n_{0_z}(z)\cdot f_{n_r}(r)=n_0 f_{n_r}(r)f_{n_z}(z).$$

Eq. (6) is converted to the following form:

$$f_{n_z}(z)\frac{d^2 f_{n_r}(r)}{dr^2}+f_{n_z}(z)\frac{1}{r}\frac{df_{n_r}(r)}{dr}+$$
$$+f_{n_r}(r)\frac{d^2 f_{n_z}(z)}{dz^2}+2\frac{f_{n_r}(r)}{D_a}\frac{dD_a}{dz}\frac{df_{n_z}(z)}{dz}+$$
$$+\frac{1}{D_a}\left\{\left[\frac{d^2 D_a}{dz^2}\right]+\nu_i\right\}f_{n_z}(z)f_{n_r}(r)=0,$$

then,

$$\frac{1}{f_{n_r}(r)}\frac{d^2 f_{n_r}(r)}{dr^2}+\frac{1}{f_{n_r}(r)}\cdot\frac{1}{r}\frac{df_{n_r}(r)}{dr}=$$
$$=-\frac{1}{f_{n_z}(z)}\cdot\frac{d^2 f_{n_z}(z)}{dz^2}-\frac{2}{f_{n_z}(z)}\times$$
$$\times\frac{1}{D_a}\frac{dD_a}{dz}\cdot\frac{df_{n_z}(z)}{dz}-\frac{1}{D_a}\left[\frac{d^2 D_a}{dz^2}+\nu_i\right]=-\lambda,$$

or, in a different notation, we obtain a system of equations taking the form

$$\begin{cases}\dfrac{d^2 f_{n_r}(r)}{dr^2}+\dfrac{1}{r}\dfrac{df_{n_r}(r)}{dr}+\lambda f_{n_r}(r)=0\\ \dfrac{d^2 f_{n_z}(z)}{dz^2}+\dfrac{2}{D_a}\dfrac{dD_a}{dz}\cdot\dfrac{df_{n_z}(z)}{dz}+\\ +\dfrac{1}{D_a}\left[\dfrac{d^2 D_a}{dz^2}+\nu_i\right]f_{n_z}(z)-\\ -f_{n_z}(z)\lambda=0\end{cases}\Rightarrow$$

$$\Rightarrow\begin{cases}r^2\dfrac{d^2 f_{n_r}(r)}{dr^2}+r\dfrac{df_{n_r}(r)}{dr}+\\ +\left(r\sqrt{\lambda}\right)^2 f_{n_r}(r)=0\\ \dfrac{d^2 f_{n_z}(z)}{dz^2}+\dfrac{2}{D_a}\dfrac{dD_a}{dz}\cdot\dfrac{df_{n_z}(z)}{dz}+\\ +\dfrac{1}{D_a}\left[\dfrac{d^2 D_a}{dz^2}+\nu_i-D_a\lambda\right]f_{n_z}(z)=0\end{cases}$$

If $\lambda = \text{const}(r)$, the first equation is the zero-order Bessel equation. Its solution is known:

$$f_{n_r}(r)=J_0\left(r\sqrt{\lambda}\right).$$

Then, due to the boundary condition $f_{nr}(R_z) = 0$, we obtain $J_0(R_z\sqrt{\lambda}) = 0$, if

$$\lambda=\left(\frac{2.405}{R_z}\right)^2.$$

Given the expression obtained for λ, the second equation takes the following form after transformations:

$$\frac{d}{dz}\left(D_a\frac{df_{n_z}(z)}{dz}\right)+\frac{d}{dz}\left(f_{n_z}(z)\frac{dD_a}{dz}\right)+$$
$$+\left[\nu_i-D_a\left(\frac{2.405}{R_z}\right)^2\right]f_{n_z}(z)=0. \quad (7)$$

Since the main mechanism for decay of charged particles in discharge is diffusive escape to the tube wall, it is natural to assume that the discharge is stable only at a certain ratio of the ionization frequency ν_i, determining the production time τ_i of charged particles per unit of discharge length, $\tau_i = 1/\nu_i$, and the ambipolar diffusion coefficient D_a, determining the time for diffusive escape of particles from the discharge to the wall of the tube of radius R_z:

$$\tau_{D_a} = R_z^2 / D_a.$$

We assume that the concentration of particles on the wall is equal to zero, and since the distribution of electron concentration over the radius is a zero-order Bessel function whose first root is reached with the argument equal to 2.455, we can take

$$R_z\sqrt{\frac{\nu_i}{D_a}} = 2.405 \text{ or } \left(\frac{2.405}{R_z}\right)^2 - \frac{\nu_i}{D_a} = 0. \quad (8)$$

In other words, we obtained a 'classical' relationship between the ionization frequency and the ambipolar diffusion coefficient for the Schottky's positive column of a direct-current discharge in a cylindrical discharge channel [7, 10] with the radius R_0 replaced by $R_z = R_0 f_R(z)$.

Eq. (7) can then be written as

$$\frac{d}{dz}\left(D_a \frac{df_{n_z}(z)}{dz}\right) + \frac{d}{dz}\left(f_{n_z}(z)\frac{dD_a}{dz}\right) = 0.$$

It can be converted to the form:

$$\frac{d}{dz}\left[D_a f_{n_z}(z)\right] = C \Rightarrow D_a(z) f_{n_z}(z) =$$
$$= Cz \Rightarrow D_a(z) f_{n_z}(z) = Cz + G.$$

Given that $f_{nz}(z = 0) = 1$, we obtain the following expression:

$$D_a(z) f_{n_z} = Cz + D_a(0) \Rightarrow$$
$$\Rightarrow f_{n_z}(z) = \frac{Cz + D_a(0)}{D_a(z)} = \frac{C_1 z + T_e(0)}{T_e(z)}.$$

As established above (see Eq. (5)), the current in the column, equal to the difference in the electron and ion fluxes, depends only on the drift fluxes of charged particles in an external electric field, i.e., only on the conductivity current:

$$I = 2\pi e b_e E_z(z) \int_0^{R_z} n(r,z) r dr =$$
$$= \text{const}(z) \Rightarrow$$
$$\Rightarrow I_d = 2\pi e b_e E_z(z) n_0 f_{n_z}(z) \times$$
$$\times \int_0^{R_z} f_{n_r}(r) r dr = \text{const}(z).$$

Then, since

$$f_{n_r}(r) = J_0\left(r\sqrt{\lambda}\right),$$
$$\lambda = \left(\frac{2.405}{R_z}\right)^2 = \left(\frac{2.405}{R_0 f_R(z)}\right)^2,$$

using the boundary conditions for R_z and E_z, we obtain:

$$I = 1.36 R_z^2 e b_e n_0 f_{n_z}(z) E_z(z) \Rightarrow$$
$$\Rightarrow n_0 f_{n_z}(z) =$$
$$= \frac{0.737 I_\delta}{R_0^2 f_R^2(z) e b_e E_{0z} f_{E_z}(z)} \Rightarrow$$
$$\Rightarrow n_0 = \frac{0.737 I_d}{R_0^2 e b_e E_{0z}} \Rightarrow$$
$$\Rightarrow f_{n_z}(z) = \frac{1}{f_R^2(z) f_{E_z}(z)}.$$

The average electron concentration over the discharge cross-section is expressed as

$$\overline{n}_z(z) = \frac{\int_0^{R(z)} r n_e dr}{\int_0^{R(z)} r dr} = 0.43 n_0 f_{n_z}(z) =$$
$$= \frac{0.317 I_\delta}{e b_e R_0^2 f_R^2(z) E_{0z} f_{E_z}(z)}.$$

Let us return to expression (8). We obtained that the ionization frequency of atoms $\nu_i(z)$ for the case of 'diffusion' discharge in a tube with variable radius is written as follows:

$$\nu_i = D_a\left(\frac{2.405}{R_z}\right)^2 \Rightarrow \nu_i = b_i \frac{kT_e}{e}\left(\frac{2.405}{R_z}\right)^2.$$

Since we assumed from the very beginning that only 'direct' ionization occurs in the discharge, the ionization frequency ν_i of atoms (their concentration is denoted as n_a) by electron impact from the ground state is written as

$$\nu_i = n_a \left\langle \sigma_{0_i} v_e \right\rangle,$$

where $\langle\sigma_{0_i} v_e\rangle$ is the ionization reaction rate constant, i.e., the product $\sigma_{0_i} v_e$, averaged over the electron energy distribution function.

In case of Maxwellian electron energy distribution, the direct ionization cross-section $\sigma_{0_i}(\varepsilon_e)$ as function of electron energy ε_e should be approximated by such a straight line

$$\sigma_{0i} = C_i (\varepsilon_e - \varepsilon_i),$$

which, with $\varepsilon_e \geq \varepsilon_i$, is characterized by the constant C_i.

With this approximation, we obtain the following expression for the ionization frequency:

$$\nu_i(z) = C_i n_a \left[\varepsilon_i + 2kT_e(z)\right] \times$$
$$\times \sqrt{\frac{8kT_e(z)}{\pi m_e}} \cdot \exp\left(-\frac{\varepsilon_i}{kT_e(z)}\right),$$

then,

$$\nu_i = C_i n_a \sqrt{\frac{8kT_e(z)}{\pi m_e}} \cdot \left(\varepsilon_i + 2kT(z)_e\right) \times$$
$$\times \exp\left(-\frac{\varepsilon_i}{kT_e(z)}\right) = b_i \frac{kT_e(z)}{e} \left(\frac{2{,}405}{R_z(z)}\right)^2.$$

As a result, we obtain the well-known formula [7, 10] relating kT_e in a PC of a diffusion cylindrical discharge to the concentration of ionizable atoms and the radius of the discharge channel replacing R with $R_z(z) = R_0 f_R(z)$:

$$\frac{\sqrt{\frac{\varepsilon_i}{kT_e(z)}} \cdot \exp\left(\frac{\varepsilon_i}{kT_e(z)}\right)}{\left(1 + \frac{\varepsilon_i}{2kT_e(z)}\right)} =$$
$$= 0.552 \frac{e}{\sqrt{m_e}} \left(\frac{C_i \sqrt{\varepsilon_i}}{b_i n_a}\right) n_a^2 \times$$
$$\times \left[R_0 f_R(z)\right]^2 (z).$$

Now let us consider the definition of the field $E_z(z)$. For this purpose, we use the equation of energy balance per unit of column length, following prominent Russian physicists in their classic studies [7, 12]:

$$IE_z = P_\nu + P_w,$$

where IE_z is the power expended by the longitudinal electric field generated by an external source to accelerate ('heat') the electrons in the column. As noted above, P_ν is the power associated with the energy acquired by electrons that they spend in elastic collisions with atoms (gas heating); P_w is the power that ions transfer to the wall.

The expressions for P_ν and P_w can be written as [7, 12]:

$$P_\nu = \frac{3}{2} \pi R^2(z) \cdot \bar{n}(z) \chi_{ea} \nu_{ea}(z) kT_e(z);$$

$$P_w = 2\pi R(z) j_{i_w} \cdot \left(U_i + 1.7 \frac{kT_e(z)}{e} + U_w\right),$$

where χ_{ea} is the energy transfer coefficient in elastic electron-atom collisions, $\chi_{ea} = 2m_e/m_a$; j_{iw} is the ion current to the tube wall; U_i is the atomic ionization potential; U_w is the near-wall jump in potential.

Then the power lost by electrons in elastic collisions is expressed as

$$P_\nu(z) = 4.05 \frac{m_e}{m_a} n_0(z) \cdot kT_e(z) \times$$
$$\times R_z^2(z) \cdot \nu_{ea} = 3 \frac{I_\partial}{m_a b_e^2 E_z(z)} \cdot kT_e(z).$$

The expression for the near-wall potential jump U_w is found from the condition that electron fluxes Γ_{eg} and ion fluxes Γ_{ig} are equal at the interface between the plasma and the tube wall [7, 8].

Assuming that the coefficient of reflection of electrons and ions from the tube wall is negligible, the directional velocity of ions in the layer is determined by the ambipolar field, and the velocity of electrons by their random velocity, we obtain:

$$\Gamma_{eg} = \frac{1}{\sqrt{2\pi}} n_{eg} \sqrt{\frac{kT_e(z)}{m_e}} \times$$
$$\times \exp\left(-\frac{eU_w(z)}{kT_e(z)}\right) = \Gamma_{ig} = n_{ig} \sqrt{\frac{kT_e(z)}{m_i}}$$

Here n_{eg}, n_{ig} are the concentrations of electrons and ions at the layer interface. It follows from this equation that

$$U_w(z) = \frac{kT_e(z)}{e} \ln 0.4 \sqrt{\frac{m_i}{m_e}}.$$

The wall current of ions can be written in accordance with the expressions given in [7, 8]:

$$j_{iw}(z) = -en_{(r\approx R_z)} D_a \frac{1}{n_{(r\approx R_z)}} \left(\frac{\partial n}{\partial r}\right)_{(r\approx R_z)} =$$

$$= -eD_a n_0(z) \left(\frac{\partial}{\partial r} f_{n_{e_r}}\right)_{(r\approx R_z)} =$$

$$= -eD_a n_0(z) \left[\frac{\partial}{\partial r} J_0\left(\frac{2.405}{R_z} r\right)\right]_{(r\approx R_z)} =$$

$$= eD_a n_0(z) \frac{2.405}{R(z)} J_1(2.405) \Rightarrow$$

$$\Rightarrow j_{w_i}(z) \approx 3\overline{n}(z) b_i \frac{kT_e(z)}{R_0 f_R(z)}.$$

The power that ions transfer to the wall is then written as

$$P_w(z) == 6\pi R_z \overline{n}(z) \frac{kT_e(z)}{R_0 f_R(z)} b_i \times$$

$$\times \left(U_i + 1.7\frac{kT_e(z)}{e} + U_w(z)\right),$$

or

$$P_w(z) = \frac{6I}{\left[R_0 f_R(z)\right]^2 E_z(z)} \frac{b_i}{b_e} \cdot \frac{kT_e(z)}{e^2} \times$$

$$\times \left[\mathring{a}U_i + kT_e(z)\left(1,7 + \mathbf{ln}\, 0.4\sqrt{\frac{m_a}{m_e}}\right)\right].$$

The total energy balance then takes the form:

$$IE_z(z) = P_v(z) + P_w(z) =$$

$$= 3\frac{I}{m_{\grave{a}} b_e^2 E_z(z)} \cdot kT_e(z) +$$

$$+ \frac{6I}{\left[R_0 f_R(z)\right]^2 E_z(z)} \frac{b_i}{b_e} \cdot \frac{kT_e(z)}{e^2} \times$$

$$\times \left[\mathring{a}U_i + kT_e(z)\left(1.7 + \ln 0.4\sqrt{\frac{m_a}{m_e}}\right)\right].$$

From here we obtain:

$$(eE_z)^2 = 3kT_e(z)\frac{m_e \nu_{ea}}{m_a} \times$$

$$\times \left\{m_e \nu_{ea} + \frac{4}{\left[R_0 f_R(z)\right]^2 \nu_{ia}} \times\right.$$

$$\left.\times \left[eU_i + kT_e(z)\left(1.7 + \mathbf{ln}\, 0.4\sqrt{\frac{m_i}{m_e}}\right)\right]\right\}.$$

Let us summarize our main results.

Considering the processes in a positive column of direct current discharge under typical discharge conditions in tubes of variable diameter, we obtained equations for the electron concentration (as function of longitudinal and transverse coordinates), electron temperature, and electric field projection, relating them to radius of the discharge channel depending on the longitudinal coordinate. The system of equations obtained provides a solution to the problem. The study presents relatively simple expressions that relate easily controlled external parameters of the column.

REFERENCES

1. **Privalov V.E., Fridrikhov S.A.,** The ring gas laser, Sov. Phys, Usp. 12 (3) (1969) 153–167.

2. **Privalov V.E., Fridrikhov S.A.,** HeNe laser with a conical discharge tube, Journal of Applied Spectroscopy. 12 (5) (1970) 700–702.

3. **Privalov V.E., Fridrikhov S.A.,** Zavisimost moshchnosti izlucheniya He-Ne lazera ot geometrii secheniya razryadnogo promezhutka [The radiation power of He-Ne laser as a function of a cross-section geometry of a discharge gap], Technical Physics. 37(12) (1968) 2080–2084 (in Russian).

4. **Fedotov A.A.,** Abstract of Ph.D. thesis, Leningrad, LETI, 1974.

5. **Troitskiy Yu.V., Chebotayev V.P.,** Radialnoye raspredeleniye usileniya v He-Ne smesi [Radial distribution of amplification in the He-Ne mixture], Optics and Spectroscopy. 20 (2) (1966) 362–365 (in Russian).

6. **Molchanov M.I., Savushkin A.F.,** Izmereniye koeffitsiyenta usileniya v smesi He-Ne [Measurement of amplification factor in the He-Ne mixture], Journal of Communications, Technology and Electronics. 15 (8) (1970) 1544–1546.

7. **Granovskiy V.L.,** Elektricheskiy tok v gaze. Ustanovivshiysya tok [Electric current in the gas. Steady current], Nauka, Moscow, 1971.

8. **Golant V.E., Zhilinskiy A.P., Sakharov I.E.** Osnovy fiziki plazmy [Fundamentals of plasma physics], "Lan" Publishing, St. Petersburg, 2011.

9. **Rayzer Yu.P.**, Fizika gazovogo razryada [Gas discharge physics], "Intellekt" Publishing House, Moscow, 2009.

10. **Cherrington B.E.,** Gaseous electronics and gas lasers, Pergamon press, Oxford, 1979.

11. **Brawn S.C.**, Introduction to electrical discharges in gases, John Wilay & Sons, New York, 1966.

12. **Klyarfeld B.N.,** Polozhitelnyy stolb gazovogo razryada i yego ispolzovaniye dlya polucheniya sveta [Positive gas discharge column and its use to get light], Proceedings of the All-Soviet-Union Electrotechnical Institute, Electronic and Ionic devices, Edited by P.V. Timofeyev, Gosenergoizdat, Moscow, (41) (1940) 165–235.

Received 16.10.2019, accepted 31.10.2019.

THE AUTHORS

FOTIADI Alexander E.
Peter the Great St. Petersburg Polytechnic University
29 Politechnicheskaya St., St. Petersburg, 195251, Russian Federation
fotiadi@rphf.spbstu.ru

KOZHEVNIKOV Vadim A.
Peter the Great St. Petersburg Polytechnic University
29 Politechnicheskaya St., St. Petersburg, 195251, Russian Federation
vadim.kozhevnikov@gmail.com

PRIVALOV Vadim E.
Peter the Great St. Petersburg Polytechnic University
29 Politechnicheskaya St., St. Petersburg, 195251, Russian Federation
vaevpriv@yandex.ru

СПИСОК ЛИТЕРАТУРЫ

1. **Привалов В.Е., Фридрихов С.А.** Кольцевой газовый лазер // Успехи физических наук. 1969. Т. 97. № 3. С. 377–402.

2. **Привалов В.Е., Фридрихов С.А.** HeNe лазер с разрядной трубкой конусообразного сечения // Журнал прикладной спектроскопии. 1970. Т. 12. № 5. С. 937–939.

3. **Привалов В.Е., Фридрихов С.А.** Зависимость мощности излучения He-Ne лазера от геометрии сечения разрядного промежутка // Журнал технической физики. 1968. Т. 37. № 12. С. 2080–2084.

4. **Федотов А.А.** Автореферат кандидатской диссертации. Л.: ЛЭТИ, 1974.

5. **Троицкий Ю.В., Чеботаев В.П.** Радиальное распределение усиления в He-Ne смеси // Оптиу ка и спектроскопия. 1966. Т. 20. № 2. С. 362–365.

6. **Молчанов М.И., Савушкин А.Ф.** Измерение коэффициента усиления в смеси He-Ne // Радиотехника и электроника. 1970. Т. 15. № 8. С. 1544–1546.

7. **Грановский В.Л.** Электрический ток в газе. Установившийся ток. М.: Наука. Гл. ред. физ.-мат. лит-ры, 1971. 545 с.

8. **Голант В.Е., Жилинский А.П., Сахаров И.Е.** Основы физики плазмы. СПб.: «Лань», 2011. 448 с.

9. **Райзер Ю.П.** Физика газового разряда. М.: Издательский дом «Интеллект», 2009. 736 с.

10. **Cherrington B.E.** Gaseous electronics and gas lasers. Oxford: Pergamon Press, 1979. 266 с.

11. **Brawn S.C.** Introduction to electrical discharges in gases. New York, USA, John Wiley & Sons, 1966. 320 p.

12. **Клярфельд Б.Н.** Положительный столб газового разряда и его использование для получения света // Труды Всесоюзного электротехнического института. Электронные и ионные приборы. Вып. 41. Под ред. П.В. Тимофеева. М.: Госэнергоиздат, 1940. С. 165–235.

Статья поступила в редакцию 16.10.2019, принята к публикации 31.10.2019.

СВЕДЕНИЯ ОБ АВТОРАХ

ФОТИАДИ Александр Эпаминондович – *доктор физико-математических наук, профессор Высшей инженерно-физической школы Санкт-Петербургского политехнического университета Петра Великого.*

195251, Российская Федерация, г. Санкт-Петербург, Политехническая ул., 29
fotiadi@rphf.spbstu.ru

КОЖЕВНИКОВ Вадим Андреевич – *старший преподаватель Высшей инженерно-физической школы Санкт-Петербургского политехнического университета Петра Великого.*

195251, Российская Федерация, г. Санкт-Петербург, Политехническая ул., 29
vadim.kozhevnikov@gmail.com

ПРИВАЛОВ Вадим Евгеньевич – *доктор физико-математических наук, профессор Высшей инженерно-физической школы Санкт-Петербургского политехнического университета Петра Великого.*

195251, Российская Федерация, г. Санкт-Петербург, Политехническая ул., 29
vaevpriv@yandex.ru

DOI: 10.18721/JPM.12411
УДК 538.911

RADIATION OF 375 MEV ELECTRONS AND POSITRONS DURING CHANNELING IN STRAIGHT AND PERIODICALLY BENT DIAMOND CRYSTALS

A.V. Pavlov[1], *V.K. Ivanov*[1], *A.V. Korol*[2], *A.V. Solov'yov*[2]

[1] Peter the Great St. Petersburg Polytechnic University, St. Petersburg, Russian Federation

[2] MBN Research Center UG, Frankfurt am Main, Germany

The paper presents the results of calculation and analysis of the trajectories and emission spectra of ultrarelativistic electrons and positrons with an energy of 375 MeV channeling in straight and periodically bent diamond crystals with a length of 20 and 40 μm. The numerical simulation of planar channeling of particles along the crystallographic plane (110) is carried out using the MBN Explorer package. The parameters of the particle beams and the orientation of the crystals are chosen close to the experimental conditions at the MAMI accelerator (Mainz, Germany). The comparison between the results obtained for electrons and positrons is performed.

Keywords: ultrarelativistic electrons and positrons, periodically bent diamond crystal, channeling radiation

Citation*:* Pavlov A.V., Ivanov V.K., Korol A.V., Solov'yov A.V., Radiation of 375 MeV electrons and positrons during channeling in straight and periodically bent diamond crystals, St. Petersburg Polytechnical State University Journal. Physics and Mathematics. 12 (4) (2019) 99–108. DOI: 10.18721/JPM.12411

ИЗЛУЧЕНИЕ ПОЗИТРОНОВ И ЭЛЕКТРОНОВ С ЭНЕРГИЕЙ 375 МЭВ ПРИ КАНАЛИРОВАНИИ В ПРЯМЫХ И ПЕРИОДИЧЕСКИ ИЗОГНУТЫХ КРИСТАЛЛАХ АЛМАЗА

А.В. Павлов[1], *В.К. Иванов*[1], *А.В. Король*[2], *А.В. Соловьев*[2]

[1] Санкт-Петербургский политехнический университет Петра Великого,

Санкт-Петербург, Российская Федерация;

[2]Научно-исследовательский центр мезобионаносистем (MBN),

г. Франкфурт-на-Майне, Германия

В работе представлены результаты расчета и анализа траекторий и спектров излучения ультрарелятивистских электронов и позитронов с энергией 375 МэВ, каналирующих в прямых и периодически изогнутых кристаллах алмаза длиной 20 и 40 мкм. Численное моделирование процессов планарного каналирования частиц вдоль кристаллографической плоскости (110) проводилось с помощью пакета MBN Explorer. Параметры пучков частиц и ориентация кристаллов были выбраны близкими к экспериментальным условиям на ускорителе MAMI (г. Майнц, Германия). Проведено сравнение полученных результатов для электронов и позитронов.

Ключевые слова: ультрарелятивистские электроны и позитроны, периодически изогнутый кристалл алмаза, излучение при каналировании

Ссылка при цитировании: Павлов А.В., Иванов В.К., Король А.В., Соловьев А.В. Излучение позитронов и электронов с энергией 375 МэВ при каналировании в прямых и периодически изогнутых кристаллах алмаза // Научно-технические ведомости СПбГПУ. Физико-математические науки. 2019. Т. 12. № 4. С. 108–118. DOI: 10.18721/JPM.12411

Introduction

Lindhard predicted in the mid-1960s that charged ultrarelativistic particles can travel anomalously large distances in oriented crystals, moving inside a potential channel generated by the electrostatic field of atomic planes or axes [1]. This phenomenon is called channeling. Channeling is stable if the transverse energy of the particles in the channel does not exceed the height of the potential barrier. Ever since channeling was discovered, it has been the subject of a great number of theoretical and experimental studies, valuable from both applied (constructing new types of emitters) and fundamental (understanding the propagation and emission of channeled particles) perspectives, see [2] and references therein.

Planar channeling describes the case when a particle oscillates in a channel parallel to a set of planes, leading to additional electromagnetic radiation, i.e., channeling radiation (ChR), whose intensity is greater than that of bremsstrahlung in the corresponding amorphous medium by orders of magnitude. The emission spectra for channeling of ultrarelativistic electrons range from hundreds of keV to several MeV.

Channeling can also happen in a periodically bent crystal. In this case, particle motion is composed of two components: channeling oscillations and propagation along the centerline of the bent crystal. The latter results in additional synchrotron radiation.

Modern technologies make it possible to grow crystals with quasiperiodic bending. Systems combining a periodically bent crystal with a beam of ultrarelativistic particles are often called crystalline undulators (CU) [2–8]. It was only recently confirmed that CUs could be constructed in practice. Motion of charged particles in a CU generates a new type of spontaneous ondulator radiation (CUR) [2, 5–8]. Perfect crystals and modern particle accelerators can be used to obtain peak brilliance of CUR up to 10^{25} photons/s·(mrad)^2·mm^2·0.1% BW for photons with energies of 10^{-2}–10^{1} MeV [2]. Notably, such brilliance cannot be obtained with conventional magnet undulators [9].

Many theoretical [2, 10–18] and experimental [5, 8, 19–27] studies published recently were aimed at exploring the channeling mechanisms and obtaining the emission spectra of electrons and positrons in straight and bent silicon and diamond crystals. Recent measurements include experiments at the Mainzer Microtron (MAMI, [20, 21]), CERN [28], SLAC [29].

The goal of this study consisted in theoretically describing channeling of 375 MeV electrons and positrons in straight and periodically bent diamond crystals. Finding the parameters of these processes, such as the characteristic length, emission spectrum, etc., holds considerable potential not only for constructing new sources of coherent radiation but also for experimental studies on channeling of electrons with ultrarelativistic energies in such crystals [20, 21]. Channeling of electrons and positrons was simulated using MBN Explorer, a versatile software package [30, 31].

Channeling simulation

Simulation of the channeling process consisted of two stages: three-dimensional trajectories of particle motion in the crystal were computed and channeling parameters were found at the first, and particle emission spectra were computed at the second based on particle trajectories.

We used relativistic molecular dynamics implemented in MBN Explorer to obtain three-dimensional motion trajectories for ultrarelativistic particles in a crystalline medium [31]. The following alterations were introduced to the standard molecular dynamics algorithm [2]. First, relativistic equations of motion were used to describe particle motion. Secondly, the interaction of an ultrarelativistic particle with individual atoms was taken into account, while the crystalline environment was dynamically generated in the direction of particle motion. The motion of ultrarelativistic particles was described within the semiclassical approximation, since quantum corrections are small at such energies. The algorithm for solving these equations is described in detail in [2, 10, 11, 14, 31, 32]. This computational approach was confirmed to be effective, so the simulation results were compared with the

experimental data obtained earlier [2, 10–12, 14, 15]. Applying the computational algorithms used in the MBN Explorer package in modern supercomputers provides a predictive power comparable to experimental measurements.

We considered a diamond crystal oriented along the (110) crystallographic plane. The propagation direction z was chosen along the <10, −10, 0> axis to avoid axial channeling [33]. It was assumed that the particle beam has zero divergence; in other words, the transverse velocity components were equal to zero.

The interaction between ultrarelativistic particles and lattice atoms was simulated using Molière's interatomic potential [34]. The simulation included thermal vibrations of lattice atoms at a temperature of 300 K. The parameters of the crystal and the beam of incident particles were chosen in accordance with the conditions of experiments conducted with electrons on the MAMI accelerator [20, 21]. The bending profile $S(z)$ had a harmonic shape for periodically bent crystals:

$$S(z) = a\cos(2\pi z/\lambda_u),$$

where the coordinate z determines the direction of particle propagation; a is the bending amplitude of the crystal ($a = 0$ E for a straight crystal, $a = 2.5$ and 4.0 E for a periodically bent crystal); λ_u is the bending period taken to be 5 μm.

Examples of systems with such geometry can be found in [15]. The particle distribution in our simulations was analyzed in crystals of length $L_{cr} = 20$ and 40 μm (4 and 8 undulator periods, respectively).

We analyzed 6000 trajectories for each set of parameters. Because we chose a random position for the particle at the entrance to the crystal and a random arrangement of atoms around the particle due to thermal fluctuations, each trajectory corresponded to propagation in a unique crystalline environment.

The trajectories are statistically independent and can be used to determine channeling parameters and calculate electromagnetic spectra. The spectral distribution of electromagnetic radiation for each trajectory was integrated over the angle $\theta_0 = 0.24$ mrad. This value is much smaller than the natural emission angle $\gamma^{-1} = 1.36$ mrad, so only 'forward radiation' was collected.

The spectrum for a specific set of parameters was obtained by averaging the spectrum over all trajectories to take into account the contribution from both the regions where the particle was traveling in channeling mode and the regions of free motion above the barrier.

Results and discussion

An important observable for channeling of relativistic particles in crystals is the spectra of electromagnetic radiation (see, for example, [21]). A particle channeled in a periodically bent crystal experiences two types of quasiperiodic motion: oscillations in the channel and motion along the channel's bending profile.

Quasiperiodic motion induces electromagnetic radiation, which can be generally represented as a set of harmonics. For example, the spectral distribution for emission angle consists of a set of narrow equidistant peaks. The radiation frequency ω_n of the nth harmonic in the region of radiated energies $\hbar\omega$, which are significantly lower compared to the primary particle energy, can be found from the relation

$$\omega_n = \frac{2\gamma^2\Omega}{1+\gamma^2\theta^2+K^2/2}n,$$

$$n = 1, 2, 3, \ldots,$$

where the Ω is the frequency of the corresponding oscillations (Ω_{ch} is the oscillation frequency for channeling or $\Omega = 2\pi/\lambda_u$ is the frequency corresponding to the undulator period λ_u); θ is the radiation collection angle; K^2 is the mean square of the undulator parameter.

If particle motion consists of two types of quasiperiodic motion that do not correlate in frequency, the total value of K^2 is determined by the sum of the squared undulator parameters:

$$K^2 = K_u^2 + K_{ch}^2,$$

where $K_u = 2\pi\gamma a/\lambda_u$ is the undulator parameter of a periodically bent crystal; $K_{ch} = 2\gamma^2\langle v_\perp^2\rangle/c^2$ is the undulator parameter responsible for motion in the channel ($\langle v_\perp^2\rangle$ is the mean-square velocity of transverse motion inside the channel, see [2] for more details).

Figs. 1 and 2 show the energy dependences of spectral density $dE/\hbar d\omega$ for electrons and positrons channeled in crystals 20 and 40 μm long, respectively. The emission spectra for a straight crystal (Fig. 1,*a* and 2,*a*) are dominated by ChR peaks whose spectral density is much higher than the bremsstrahlung density in amorphous media. Because electron oscillations in the channel are strongly anharmonic, the electron emission spectra are considerably broadened (Fig. 1,*a*) compared with the narrow spectral line for positrons (Fig. 2,*a*). The ChR peak in the spectrum for positrons is near the energy $\hbar\omega \approx 1.1$ MeV, while this value

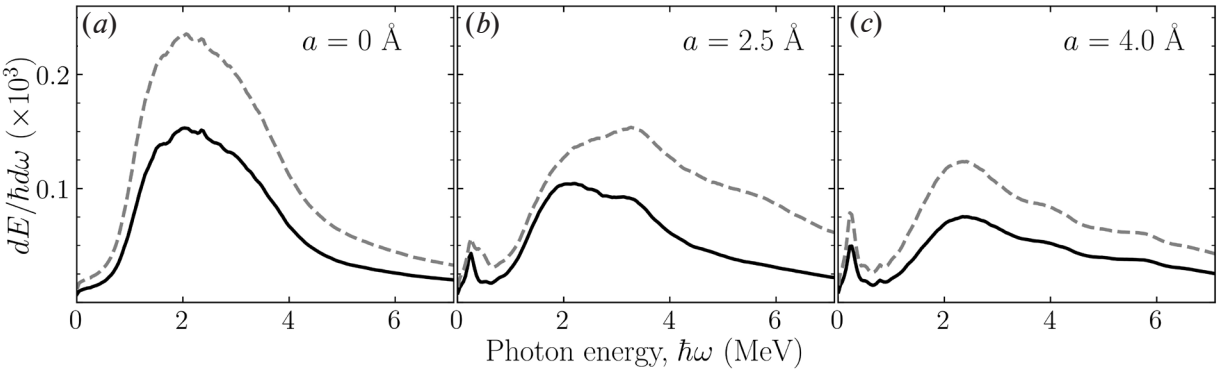

Fig. 1. Spectral distributions of electromagnetic radiation for electrons with energy of 375 MeV passing through straight crystal (*a*) and periodically bent crystal (*b*, *c*) with bending amplitudes a = 2.5 E (*b*) and a = 4.0 E (*c*), depending on photon energy.
The solid line corresponds to the dependences for L_{cr} = 20 μm, the dashed line to L_{cr} = 40 μ

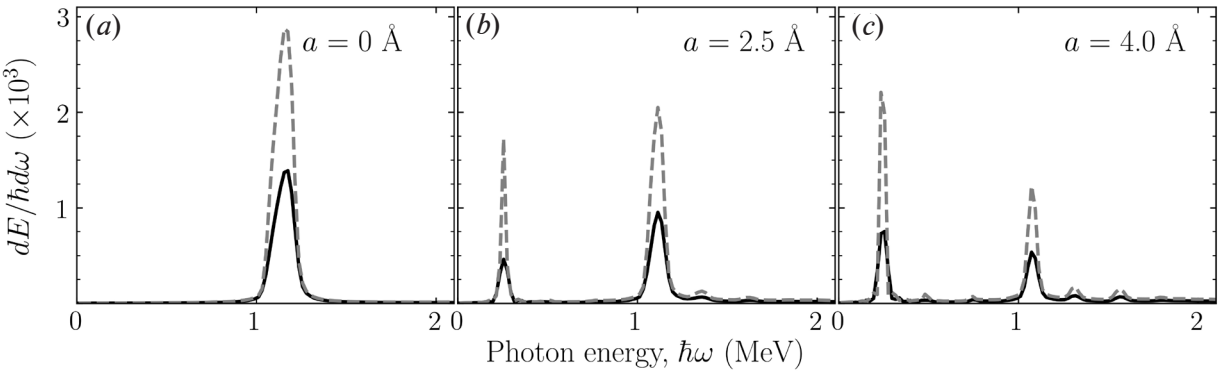

Fig. 2. Spectral distributions of electromagnetic radiation depending on photon energy, the same as in Fig. 1 but for positrons. The notations are the same as in Fig. 1

for electrons shifts toward higher energies and amounts to $\hbar\omega \approx 2$ MeV due to anharmonicity.

The emission spectra of particles channeling in periodically bent crystals (Fig. 1,*b*,*c* and 2,*b*,*c*) exhibit additional peaks at an energy $\hbar\omega \approx 0.25$ MeV. These peaks correspond to coherent undulator radiation (CUR). They are generated as a result of particle motion in a periodically bent crystal, and the frequency of radiation quanta Ω_u depends on the bending period of the crystal and the longitudinal energy of the charged particle [2–8, 14]. Notably, the spectral density of positrons is higher than that of channeled electrons by an order of magnitude.

Let us now discuss the most remarkable features observed in the emission spectra.

Additional peaks appear in the emission spectrum in case of positron channeling in a PBC. Additional harmonics are more pronounced for larger bending amplitudes (see additional peaks in Fig. 2,*c*).

CUR and ChR intensities increase with increasing crystal thickness to varying degrees for electrons and positrons.

ChR intensity decreases with increasing bending amplitude for both types of particles.

A possible explanation for the first effect is that the undulator parameter for positrons with an energy of 375 MeV propagating in periodically bent diamond crystals with the above parameters is

$$K \sim K_u = 2\pi\gamma a/\lambda_u \leq 1.$$

In this case, the theory of undulator radiation predicts that the emission spectrum should consist of a series of equidistant harmonics whose intensity rapidly decreases with the harmonic number n.

The properties of particle channeling should be considered before analyzing the change in the emission spectra depending on the bending amplitude and the crystal thickness. The trajectories of particles in the crystal are the first result obtained in the calculations, making it possible to study the properties in question directly. In particular, the number of channeling particles can be found at any depth of the crystal. Such data cannot be obtained

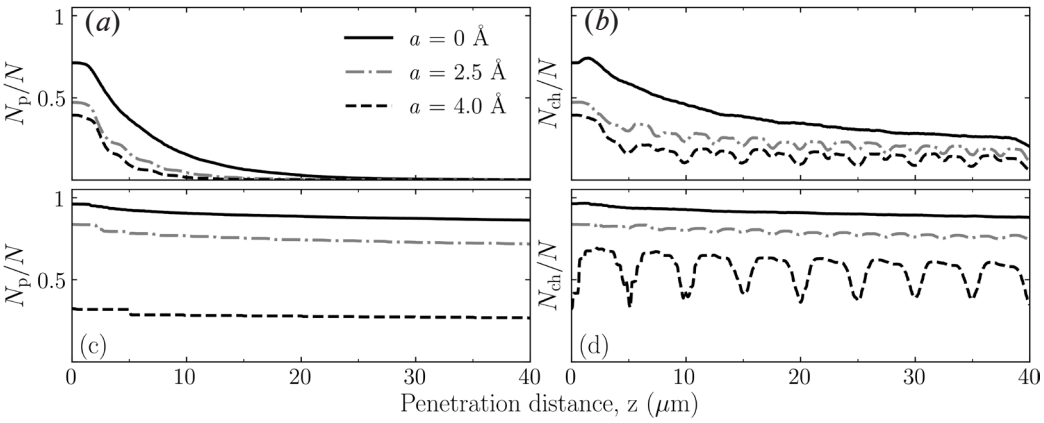

Fig. 3. Distributions of channeling particles with energy of 375 MeV in straight (a = 0 E) (a, c) and periodically bent diamond crystals (110) (b,d) depending on penetration depth of particles in the crystal. Fractions of electrons (a) and positrons (c) trapped into the channel at the entrance to the crystal are given, as well as fractions of channeling electrons (b) and positrons (d) taking into account rechanneling

experimentally, however, they can be useful in analysis of the data obtained, providing at least a qualitative explanation of the dependences.

An important characteristic of the channeling process is the particle trapping coefficient A (acceptance). It is the ratio of the number of particles N_{acc} trapped in the channel at the entrance to the crystal to the number of all incident particles N_0:

$$A = N_{acc}/N_0.$$

The parameter A has the greatest value for a straight crystal and gradually decreases with increasing curvature of a bent crystal due to an increase in centrifugal forces acting on the particle [35].

A value of the length characterizing the channeling process can be given for statistical analysis of channeling.

We introduce the value L_p which is the mean penetration depth. It describes the average distance that particles trapped at the channel entrance travel. The number of such particles is denoted as N_p.

The mean channeling length L_{ch} is the length of all channeling segments averaged over the number of trajectories N.

The number of channeled particles at a certain penetration depth in the crystal is denoted as N_{ch}.

Fig. 3 shows N_p/N and N_{ch}/N for electrons (Fig. 3,a,b) and positrons (Fig. 3,c,d) depending on depth z of penetration into the crystal.

The acceptance A in the figures corresponds to the values N_p/N and N_{ch}/N at the point z = 0. For example, the parameter A for positrons in a straight crystal is equal to 0.96. The values of L_p and L_{ch} can be found by averaging these dependences over the depth z of penetration into the crystal.

Let us first consider positron channeling. A positron travels in a channel between two crystallographic planes. Collisions with lattice atoms lead to an increase in its transverse motion energy, and the positron dechannels when a certain critical value of this energy is reached. The reverse process, rechanneling, takes place when a positron is trapped into the channel due to collisions with lattice atoms. With large crystal thicknesses, for example, $L_{cr} \approx$ 300 μm, the positron can undergo dechanneling and rechanneling several times during propagation inside the crystal. However, dechanneling and rechanneling rarely happen at small crystal thicknesses. Positron rechanneling in periodically bent crystals can occur in parts of the crystal with a small curvature [15] (see the curve corresponding to the oscillating particles in Fig. 3,d).

CUR intensity can be estimated as a value proportional to the product $I \propto A \cdot L_p \cdot a^2$ [16]. It follows then that the particles trapped at the entrance to the crystal make the main contribution to CUR intensity. N_p/N for the given crystal lengths is practically independent of the depth z (see the dependence $N_p/N(z)$ in Fig. 3,a).

Thus, peak intensity should increase with increasing crystal thickness proportional to the increase in L_p. The acceptance and the average penetration depth decrease slightly with an increase in the bending amplitude, however, this decrease is compensated by an increase in the squared bending amplitude, which leads to an increase in CUR intensity. Given a large pene-

tration depth, as the crystal length increases by 2 times, the CUR intensity for the case a = 4.0 E (see Fig. 2,*c*) increases more than twofold. This is a consequence of constructive interference.

Analysis of the energy dependence for ChR should take into account the change in the oscillation amplitude during channeling [16]. Periodic bending of the crystal reduces the amplitude of the oscillations in the channel, since the depth of the potential well of the channel effectively falls under the action of the centrifugal force. As a result, the spectral density of ChR decreases with increasing bending amplitude. ChR intensity increases with increasing crystal thickness, since the average number of particles in the channel practically does not change with depth (see Fig. 3,*c*).

The dependences of channeling parameters on the bending amplitude for electrons have a different character. Since electron trajectories pass in the immediate vicinity of the lattice ions, electrons are much more likely to experience collisions with ions and dechannel as a result. This explains why the penetration depths L_p and the total channel lengths L_{ch} are smaller by almost an order of magnitude compared with the same values for positrons. The number of electrons trapped in the channel in a straight crystal rapidly decreases with distance (see Fig. 1,*a*). Dechanneling is even faster in a periodically bent crystal. The situation is slightly different in case of rechanneling: additional channeling segments, most often rather short, appear, effectively increasing the time that electrons spend in the channel.

As a result of dechanneling of the electrons trapped at the entrance to the channel, CUR intensity grows slightly with increasing crystal thickness, compared with the case for positrons. The intensity also changes only slightly with a change in the amplitude of a periodically bent crystal, since an increase in the squared amplitude is compensated by a decrease in two other parameters.

Accounting for rechanneling is important in analyzing the behavior of ChR intensity. As noted above, electrons rechannel in the regions of the crystal with a small bending amplitude, so as a result they can move in these regions with an oscillation amplitude that is much larger than that possible in segments with a large bending amplitude. This process entails a less pronounced decrease in ChR intensity with an increase in the bending amplitude than in case of positrons. As crystal thickness increases, ChR intensity increases only slightly, since the average length that a particle travels in channeling mode is greater in a longer crystal.

Thus, electrons and positrons have different dynamics of channeling/dechanneling/rechanneling. The centrifugal force exerts a great influence on the properties of channeling and radiation in periodically bent crystals. It leads to suppression of ChR with an increase in the bending amplitude, and is also responsible for oscillation of the number of particles in channeling mode. Additional questions concerning channeling in periodically bent diamond crystals at other energies of incident electrons and positrons were considered in [15, 16].

Conclusion

We have carried out computer simulations of planar channeling of electrons and positrons in periodically bent diamond crystals. Electron and positron beams with an energy of 375 MeV were directed along the (110) crystallographic plane of diamond. The characteristics of the emission spectra associated with particle oscillations in the channel and with undulator motion were explained using statistical analysis of particle trajectories obtained in a numerical experiment.

A low-energy peak associated with CUR appears near 0.25 MeV for particles in a periodically bent channel. Even though the bent crystal had a small number of periods (4 and 8), CUR had a pronounced intensity, which may prove useful in constructing gamma emitters.

Our findings indicate, in particular, that increased thickness of the crystalline undulator significantly increases CUR intensity for positrons but this increase is much less for electrons. As the bending amplitude of the periodically bent crystal increases, ChR intensity drops for both electrons and positrons. These results can be used for planning future experiments, for example, for selecting the optimal parameters of the crystal, energy and particle type.

Acknowledgment

We express our gratitude to Peter the Great Supercomputer Center at Peter the Great St. Petersburg Polytechnic University for the computing resources provided and assistance in running the computations.

This study was financially supported as part the Alexander von Humboldt Foundation Linkage Grant and the HORIZON 2020 RISE-PEARL project.

REFERENCES

1. **Lindhard J., Winther A., Dan K.,** Influence of crystal lattice on motion of energetic charged particles, Kongel. Dan. Vidensk. Selsk., Mat.-Fys. Medd. 34(14) (1965) 1–64.

2. **Korol A.V., Solov'yov A.V., Greiner W.,** Channeling and radiation in periodically bent crystals, 2nd edition, Springer Verlag, Berlin Heildeberg, 2014.

3. **Korol A.V., Solov'yov A.V., Greiner W.,** Coherent radiation of an ultrarelativistic charged particle channelled in a periodically bent crystal, Journal of Physics G: Nuclear and Particle Physics. 24(5) (1998) L45.

4. **Korol A.V., Solov'yov A.V., Greiner W.,** Photon emission by an ultra-relativistic particle channeling in a periodically bent crystal, International Journal of Modern Physics, E. 8(01) (1999) 49–100.

5. **Wistisen T.N., Andersen K.K., Yilmaz S., et al.,** Experimental realization of a new type of crystalline undulator, Phys. Rev. Lett. 112 (25) (2014) 254801.

6. **Backe H., Krambrich D., Lauth W., et al.,** Future aspects of X-ray emission from crystal undulators at channeling of positrons, Nuovo Cimento, C. 34 (4) (2011) 175.

7. **Sushko G.B., Korol A.V., Greiner W., Solov'yov A.V.,** Sub-GeV electron and positron channeling in straight, bent and periodically bent silicon crystals, Journal of Physics: Conf. Ser. 438(1) (2013) 012018.

8. **Wistisen T.N., Uggerh_j. U.I., Hansen J.L., et al.,** Radiation collimation in a thick crystalline undulator, Eur. Phys. J., D. 71(5) (2017) 124.

9. **Yabashi M., Tanaka H.,** The next ten years of X-ray science, Nature Photonics. 11(1) (2017) 12 –14.

10. **Sushko G.B., Bezchastnov V.G., Korol A.V., et al.,** Simulations of electron channeling in bent silicon crystal, Journal of Physics: Conf. Ser. 438(1) (2013) 012019.

11. **Sushko G.B., Korol A.V., Solov'yov A.V.,** Multi-GeV electron and positron channeling in bent silicon crystals, Nucl. Instrum. Meth. B. 355 (15 July) (2015) 39–43.

12. **Polozkov R.G., Ivanov V.K., Sushko G.B., et al.,** Radiation emission by electrons channeling in bent silicon crystals, Eur. Phys. J., D. 68 (9) (2014) 268–277.

13. **Shen H., Zhao Q., Zhang F.S., et al.,** Channeling and radiation of 855 MeV electrons and positrons in straight and bent tungsten (110) crystals, Nucl. Instrum. Meth. B. 424 (1 June) (2018) 26–36.

14. **Agapev K.B., Ivanov V.K., Korol A.V., Solov'yov A.V.,** Channeling of ultrarelativistic particles in a diamond crystal, St. Petersburg State Polytechnical University Journal. Physics and Mathematics. 11 (2) (2018) 139 –150.

15. **Korol A.V., Bezchastnov V.G., Solov'yov A.V.,** Channeling and radiation of the 855 MeV electrons enhanced by the rechanneling in a periodically bent diamond crystal, Eur. Phys. J., D. 71 (6) (2017) 174.

16. **Pavlov A.V., Korol A.V., Ivanov V.K., Solov'yov A.V.,** Interplay and specific features of radiation mechanisms of electrons and positrons in crystalline undulators, Journal of Physics, B: Atomic, Molecular and Optical Physics. 52 (11) (2019) 11–16.

17. **Kostyuk A.,** Crystalline undulator with a small amplitude and a short period, Phys. Rev. Lett. 110 (11) (2013) 115503.

18. **Korol A.V., Bezchastnov V.G., Sushko G.B., Solov'yov A.V.,** Simulation of channeling and radiation of 855 MeV electrons and positrons in a small-amplitude short-period bent crystal, Nucl. Instrum. Meth., B. 387 (15 November) (2016) 41–53.

19. **Backe H., Lauth W.,** Channeling experiments with sub-GeV electrons in flat silicon single crystals, Nucl. Instrum. Meth., B. 355 (15 July) (2015) 24–29.

20. **Backe H., Lauth W.,** Channeling experiments with electrons at the Mainz Microtron MAMI, 4th Int. Conf. "Dynamics of Systems on the Nanoscale" (Bad Ems., Germany, Oct. 3–7 2016), Book of Abstracts. 2016. P. 58.

21. **Backe H., Lauth W., Tran Thi T.N.,** Channeling experiments at planar diamond and silicon single crystals with electrons from the Mainz Microtron MAMI, Journal of Instrumentation. 13(04) (2018) C04022.

22. **Wistisen T.N., Uggerh_j. U.I., Wienands U., et al.,** Channeling, volume reflection, and volume capture study of electrons in a bent silicon crystal, Phys. Rev. Acc. Beams. 19 (7) (2016) 071001.

23. **Bagli E., Bandiera L., Bellucci V., et al.,** Experimental evidence of planar channeling in a periodically bent crystal, Eur. Phys. J., C. 74 (10) (2014) 3114.

24. **Bandiera L., Bagli E., Germogli G., et al.,** Investigation of the electromagnetic radiation emitted by sub-GeV electrons in a bent crystal, Phys. Rev. Lett. 115 (2) (2015) 025504.

25. **Wienands U., Markiewicz T.W., Nelson J., et al.,** Observation of deflection of a beam of

multi-GeV electrons by a thin crystal, Phys. Rev. Lett. 114 (7) (2015) 074801.

26. **Mazzolari A., Bagli E., Bandiera L., et al.,** Steering of a sub-GeV electron beam through planar channeling enhanced by rechanneling, Phys. Rev. Lett. 112 (13) (2014) 135503.

27. **Uggerhoj U.I., Wistisen T.N.,** Intense and energetic radiation from crystalline undulators, Nucl. Instrum Meth., B. 355 (15 July) (2015) 35–38.

28. **Boshoff D., Copeland M., Haffejee F., et al.,** The search for diamond crystal undulator radiation, 4th Int. Conf. "Dynamics of Systems on the Nanoscale" (Bad Ems., Germany, Oct. 3 –7 2016), Book of Abstracts, 2016, P. 38.

29. **Wienands U.,** Channeling of electrons and positrons at SLAC, A talk at "Channeling 2016 – Charged & Neutral Particles Channeling Phenomena" (Sirmione del Garda, Italy, Sept. 25 –30 2016), 2016.

30. **Solov'yov I.A., Yakubovich A.V., Nikolaev P.V., et al.,** MesoBioNano explorer – a universal program for multiscale computer simulations of complex molecular structure and dynamics, J. Comput. Chem. 33 (30) (2012) 2412–2439.

31. **Sushko G.B., Bezchastnov V.G., Solov'yov I.A., et al.,** Simulation of ultra-relativistic electrons and positrons channeling in crystals with MBN Explorer, J. of Comp. Phys. 252 (1 November) (2013) 404–418.

32. **Sushko G.B., Bezchastnov V.G., Korol A.V., et al.,** Simulations of electron channeling in bent silicon crystal, Journal of Physics: Conf. Ser. 438 (1) (2013) 012019.

33. **Sushko G.B., Korol A.V., Solov'yov A.V.,** Electron and positron propagation in straight and periodically bent axial and planar silicon channels, St. Petersburg State Polytechnical University Journal. Physics and Mathematics. (3(225)) (2015) 173–184.

34. **Moliere G.,** Theorie der Streuung schneller geladener Teilchen I. Einzelstreuung am abgeschirmten Coulomb-Feld, Zeitschrift fьr Naturforschung A. 2 (3) (1947) 133–145.

35. **Tsyganov E.N,** Some aspects of the mechanism of a charge particle penetration through a monocrystal, Fermilab TM-682 (1976) 1–5.

Received 18.10.2019, accepted 15.11.2019.

THE AUTHORS

PAVLOV Alexander V.
Peter the Great St. Petersburg Polytechnic University
29 Politechnicheskaya St., St. Petersburg, 195251, Russian Federation
a.pavlov@physics.spbstu.ru

IVANOV Vadim K.
Peter the Great St. Petersburg Polytechnic University
29 Politechnicheskaya St., St. Petersburg, 195251, Russian Federation
ivanov@physics.spbstu.ru

KOROL Andrey V.
MBN Research Center UG
Altenhoferallee 3, 60438 Frankfurt am Main, Germany
korol@mbnexplorer.com

SOLOV'YOV Andrey V.
MBN Research Center UG
Altenhoferallee 3, 60438 Frankfurt am Main, Germany
solovyov@mbnresearch.com

СПИСОК ЛИТЕРАТУРЫ

1. **Lindhard J., Winther A., Dan K.** Influence of crystal lattice on motion of energetic charged particles // Kongel. Dan. Vidensk. Selsk., Mat.-Fys. Medd. 1965. Vol. 34. No. 14. Pp. 1– 64.

2. **Korol A.V., Solov'yov A.V., Greiner W.** Channeling and radiation in periodically bent crystals. 2nd edition. Berlin, Heildeberg: Springer Verlag, 2014. 240 p.

3. **Korol A.V., Solov'yov A.V., Greiner W.** Coherent radiation of an ultrarelativistic charged particle channelled in a periodically bent crystal // Journal of Physics. G: Nuclear and Particle

Physics. 1998. Vol. 24. No. 5. P. L45.

4. **Korol A.V., Solov'yov A.V., Greiner W.** Photon emission by an ultra-relativistic particle channeling in a periodically bent crystal // International Journal of Modern Physics. E. 1999. Vol. 8. No. 1. Pp. 49–100.

5. **Wistisen T.N., Andersen K.K., Yilmaz S., et al.** Experimental realization of a new type of crystalline undulator // Phys. Rev. Lett. 2014. Vol. 112. No. 25. P. 254801.

6. **Backe H., Krambrich D., Lauth W., et al.** Future aspects of X-ray emission from crystal undulators at channeling of positrons // Nuovo Cimento. C. 2011. Vol. 34. No. 4. Pp. 175 –180.

7. **Sushko G.B., Korol A.V., Greiner W., Solov'yov A.V.** Sub-GeV electron and positron channeling in straight, bent and periodically bent silicon crystals // Journal of Physics: Conf. Ser. 2013. Vol. 438. No. 1. P. 012018.

8. **Wistisen T.N., Uggerh_j U.I., Hansen J.L., et al.** Radiation collimation in a thick crystalline undulator // Eur. Phys. J. D. 2017. Vol. 71. No. 5. P. 124.

9. **Yabashi M., Tanaka H.** The next ten years of X-ray science // Nature Photonics. 2017. Vol. 11. No. 1. Pp. 12 –14.

10. **Sushko G.B., Bezchastnov V.G., Korol A.V., et al.** Simulations of electron channeling in bent silicon crystal // Journal of Physics: Conf. Ser. 2013. Vol. 438. No. 1. P. 012019.

11. **Sushko G.B., Korol A.V., Solov'yov A.V.** Multi-GeV electron and positron channeling in bent silicon crystals // Nucl. Instrum. Meth. B. 2015. Vol. 355. 15 July. Pp. 39–43.

12. **Polozkov R.G., Ivanov V.K., Sushko G.B., et al.** Radiation emission by electrons channeling in bent silicon crystals // Eur. Phys. J. D. 2014. Vol. 68. No. 9. Pp. 268–277.

13. **Shen H., Zhao Q., Zhang F. S., et al.** Channeling and radiation of 855 MeV electrons and positrons in straight and bent tungsten (110) crystals // Nucl. Instrum. Meth. B. 2018. Vol. 424. 1 June. Pp. 26–36.

14. Агапьев К.Б., Иванов В.К., Король А.В., Соловьев А.В. Каналирование ультрарелятивистских частиц в кристалле алмаза // Научно-технические ведомости СПбГПУ. Физико-математические науки. 2018. Т. 11. № 2. С. 139–150.

15. **Korol A.V., Bezchastnov V.G., Solov'yov A.V.** Channeling and radiation of the 855 MeV electrons enhanced by the re-channeling in a periodically bent diamond crystal // Eur. Phys. J. D. 2017. Vol. 71. No. 6. P. 174.

16. **Pavlov A.V., Korol A.V., Ivanov V.K., Solov'yov A.V.** Interplay and specific features of radiation mechanisms of electrons and positrons in crystalline undulators // Journal of Physics, B: Atomic, Molecular and Optical Physics. 2019. Vol. 52. No. 11. Pp. 11–16.

17. **Kostyuk A.** Crystalline undulator with a small amplitude and a short period // Phys. Rev. Lett. 2013. Vol. 110. No. 11. P. 115503.

18. **Korol A.V., Bezchastnov V.G., Sushko G.B., Solov'yov A.V.** Simulation of channeling and radiation of 855 MeV electrons and positrons in a small-amplitude short-period bent crystal // Nucl. Instrum. Meth. B. 2016. Vol. 387. 15 November. Pp. 41–53.

19. **Backe H., Lauth W.** Channeling experiments with sub-GeV electrons in flat silicon single crystals // Nucl. Instrum. Meth. B. 2015. Vol. 355. 15 July. Pp. 24–29.

20. **Backe H., Lauth W.** Channeling experiments with electrons at the Mainz Microtron MAMI // 4th Int. Conf. "Dynamics of Systems on the Nanoscale" (Bad Ems. Germany. Oct. 3–7 2016). Book of Abstracts, 2016. P. 58.

21. **Backe H., Lauth W., Tran Thi T.N.** Channeling experiments at planar diamond and silicon single crystals with electrons from the Mainz Microtron MAMI // Journal of Instrumentation. 2018. Vol. 13. No. 4. P. C04022.

22. **Wistisen T.N., Uggerh_j U.I., Wienands U., et al.** Channeling, volume reflection, and volume capture study of electrons in a bent silicon crystal // Phys. Rev. Acc. Beams. 2016. Vol. 19. No. 7. P. 071001.

23. **Bagli E., Bandiera L., Bellucci V., et al.** Experimental evidence of planar channeling in a periodically bent crystal // Eur. Phys. J. C. 2014. Vol. 74. No. 10. P. 3114.

24. **Bandiera L., Bagli E., Germogli G., et al**. Investigation of the electromagnetic radiation emitted by sub-GeV electrons in a bent crystal // Phys. Rev. Lett. 2015. Vol. 115. No. 2. P. 025504.

25. **Wienands U., Markiewicz T.W., Nelson J., et al.** Observation of deflection of a beam of multi-GeV electrons by a thin crystal // Phys. Rev. Lett. 2015. Vol. 114. No. 7. P. 074801.

26. **Mazzolari A., Bagli E., Bandiera L., et al.** Steering of a sub-GeV electron beam through planar channeling enhanced by rechanneling // Phys. Rev. Lett. 2014. Vol. 112. No. 13. P. 135503.

27. **Uggerhoj U.I., Wistisen T.N.** Intense and energetic radiation from crystalline undulators// Nucl. Instrum Meth. B. 2015. Vol. 355. 15 July. Pp. 35–38.

28. **Boshoff D., Copeland M., Haffejee F., et al.** The search for diamond crystal undulator radiation // 4th Int. Conf. "Dynamics of Systems

on the Nanoscale" (Bad Ems. Germany, Oct. 3–7, 2016). Book of Abstracts, 2016. P. 38.

29. **Wienands U.** Channeling of electrons and positrons at SLAC. A talk at "Channeling 2016 – Charged & Neutral Particles Channeling Phenomena" (Sirmione del Garda, Italy. Sept. 25–30, 2016). 2016.

30. **Solov'yov I.A., Yakubovich A.V., Nikolaev P.V., et al.** MesoBioNano explorer – a universal program for multiscale computer simulations of complex molecular structure and dynamics // J. Comput. Chem. 2012. Vol. 33. No. 30. Pp. 2412–2439.

31. **Sushko G.B., Bezchastnov V.G., Solov'yov I.A., et al.** Simulation of ultra-relativistic electrons and positrons channeling in crystals with MBN Explorer// J. of Comp. Phys. 2013. Vol. 252. 1 November. Pp. 404–418.

32. **Sushko G.B., Bezchastnov V.G., Korol A.V., et al.** Simulations of electron channeling in bent silicon crystal //Journal of Physics: Conf. Ser. 2019. Vol. 438. No. 1. P. 012019.

33. **Sushko G.B., Korol A.V., Solov'yov A.V.** Electron and positron propagation in straight and periodically bent axial and planar silicon channels // St. Petersburg State Polytechnical University Journal. Physics and Mathematics. 2015. No. 3 (225). Pp. 173–184.

34. **Moliere G.** Theorie der Streuung schneller geladener Teilchen I. Einzelstreuung am abgeschirmten Coulomb-Feld // Zeitschrift fьr Naturforschung. A. 1947. Band 2. Num. 3. S. 133–145.

35. **Tsyganov E.N.** Some aspects of the mechanism of a charge particle penetration through a monocrystal // Fermilab TM-682. 1976. Pp. 1– 5.

Статья поступила в редакцию 18.10.2019, принята к публикации 15.11.2019.

СВЕДЕНИЯ ОБ АВТОРАХ

ПАВЛОВ Александр Валерьевич – *аспирант кафедры экспериментальной физики Санкт-Петербургского политехнического университета Петра Великого.*

195251, Российская Федерация, г. Санкт-Петербург, Политехническая ул., 29
a.pavlov@physics.spbstu.ru

ИВАНОВ Вадим Константинович – *доктор физико-математических наук, профессор кафедры экспериментальной физики Санкт-Петербургского политехнического университета Петра Великого.*

195251, Российская Федерация, г. Санкт-Петербург, Политехническая ул., 29
ivanov@physics.spbstu.ru

КОРОЛЬ Андрей Владимирович – *кандидат физико-математических наук, доцент, научный сотрудник Научно-исследовательского центра мезобионаносистем (MBN).*

Altenhoferallee 3, 60438 Frankfurt am Main, Germany
korol@mbnexplorer.com

СОЛОВЬЕВ Андрей Владимирович – *доктор физико-математических наук, ведущий научный сотрудник Научно-исследовательского центра мезобионаносистем (MBN).*

Altenhoferallee 3, 60438 Frankfurt am Main, Germany
solovyov@mbnresearch.com

DOI: 10.18721/JPM.12413
УДК 532.529:532.59:534.2

THE INTERACTION OF A SHOCK WAVE WITH A PERMEABLE LAYER: AN EXPERIMENTAL STUDY

S.V. Bulovich[1], *A.V. Masiukevich*[2]

[1] Peter the Great St. Petersburg Polytechnic University, St. Petersburg, Russian Federation;

[2]The Ioffe Institute of the Russian Academy of Sciences, St. Petersburg, Russian Federation

In the paper, the interaction of a shock wave with a granular layer of spherical particles has been experimentally studied in an atmospheric shock tube. A near-edge space of pure gas was located between the porous layer and the tube's end wall. Two problem statements were considered. In the first embodiment, the structure and position of the porous layer remained unchanged. In the second one, the granular layer was destroyed under the action of the incident shock wave and turned into a mobile cloud of particles. For both variants, wave structures that occur both in front of the porous layer of granular particles and in the gap between the granular layer and the end wall of the shock tube were derived and analyzed. The initial information was obtained by measuring and recording equipment, which included piezoelectric pressure sensors and a multichannel ADC board for data collection.

Keywords: shock wave, permeable material layer, nonstationary gas filtration, wave structure

Citation: Bulovich S.V., Masiukevich A.V., The interaction of a shock wave with a permeable layer: an experimental study, St. Petersburg Polytechnical State University Journal. Physics and Mathematics. 12 (4) (2019) 109–117. DOI: 10.18721/JPM.12413

ЭКСПЕРИМЕНТАЛЬНОЕ ИССЛЕДОВАНИЕ ВЗАИМОДЕЙСТВИЯ УДАРНОЙ ВОЛНЫ СО СЛОЕМ ПРОНИЦАЕМОГО МАТЕРИАЛА

С.В. Булович[1], *А.В. Масюкевич*[2]

[1] Санкт-Петербургский политехнический университет Петра Великого,

Санкт-Петербург, Российская Федерация;

[2] Физико-технический институт им. А.Ф. Иоффе РАН, Санкт-Петербург, Российская Федерация

В работе экспериментально исследовано взаимодействие ударной волны с гранулированным слоем сферических частиц в атмосферной ударной трубе. Между пористым слоем и торцевой стенкой трубы располагалась приторцевая область чистого газа. Были рассмотрены две постановки задачи. В первом варианте структура и положение пористого слоя предполагались неизменными. Во втором – гранулированный слой разрушался под действием падающей ударной волны и превращался в подвижное облако частиц. Для обоих вариантов получены и проанализированы волновые структуры, которые возникают как перед пористым слоем гранулированных частиц, так и в приторцевой области между гранулированным слоем и торцевой стенкой ударной трубы. Исходная информация была получена при помощи измерительно-регистрирующей аппаратуры, которая включала пьезоэлектрические датчики давления и многоканальную плату АЦП для сбора информации.

Ключевые слова: ударная волна, проницаемый слой материала, нестационарная фильтрация газа, волновая структура

Ссылка при цитировании: Булович С.В., Масюкевич А.В. Экспериментальное исследование взаимодействия ударной волны со слоем проницаемого материала // Научно-технические ведомости СПбГПУ. Физико-математические науки. 2019. Т. 12. № 4. С. 135–144. DOI: 10.18721/JPM.12413

Introduction

Determining aerodynamic loads on the surface is an important applied aspect in studies of transient processes such as shock waves or pulsed jets. The problem becomes increasingly complex assuming a gas-permeable barrier that can consist of perforated elements, gratings, woven meshes, spongy structures, layers of granular media, etc. As waves propagate through such barriers, their amplitude typically decreases and wave profiles transform. The barrier can be deformed by intense impacts, including irreversible ones. There is much interest towards lattice barriers that allow substantial deformations, enhancing the dynamic effects on the barrier in certain circumstances [1, 2]. The boundary case, for example, when the porous layer in granular media is destroyed and two-phase flow is generated, is no less significant [3, 4].

The primary data obtained in experimental studies are important for this type of problem, allowing to characterize the key phenomena and discover the main trends. Experimental data can be used to refine existing mathematical models and construct new ones, describing the processes with varying degrees of completeness.

Multifactor studies of unsteady seepage began in the 1950s; fairly systematic review of these studies is given, for example, in monograph [5]. The key issues of mechanics of heterogeneous media for destructible lattices are discussed in [6, 7]. Let us consider the experimental studies providing data on granular flows. In particular, [8, 9] generalized the experimental studies, allowing to modify the model based on the Stokes drag. The effect of the medium's compressibility and general unsteady behavior of the given phenomenon was described in [10].

Representative data were given in [3, 4], considering wide variation ranges of geometric factors and flow parameters. Refs. [11, 12] served as a basis for formulating the laws governing shock waves passing through layers of dense mixture taking into account several mechanisms of particle collision [13–15]. Additionally, [16, 17] used sensors located directly in the porous layer to study the pressure variation in gas and in a gas-particle mixture. It was found that the pressure amplitude of the transmitted wave depends on a number of parameters characterizing different properties of the porous layer: length (depth), diameter and shape of the elements, thermal characteristics of the material (density, heat capacity, etc.), potential compression and reordering of structural elements.

The focus of modern studies in this area is on numerical simulation [18, 19]. There are two main directions. On the one hand, efforts are made to provide more complete and detailed descriptions of the processes under consideration; on the other hand, algorithms for numerical integration of differential equations for the given range of problems are improved and new algorithms are developed.

Reviewing the literature on the subject, we note that no studies so far have been carried out on direct comparison of flow regimes for retained and destructible porous layers under identical conditions. There are also no studies considering how the location of porous layers (retained and destroyed) relative to an impervious surface affects the instantaneous and integral characteristics of the attenuating dynamic response to this surface.

The subject of this study is the interaction of a shock wave with a layer of granular material in two problem statements.

The layer remains stationary in the first statement and the lattice structure of the porous layer is preserved; as the structure of the porous layer is destroyed, a mobile cloud of particles forms in the second statement. The size of the region free of granules between the porous layer and the impervious wall plays a certain role in the second case, with diverse effects on the integral characteristics [1]. The

momentum transmitted to the particle cloud and the subsequent shock-wave interaction of this cloud with the 'gas cushion', which is a region filled with pure gas, is an important factor in this case.

Experimental test bed and experimental procedure

The experiments were carried out in an atmospheric shock tube 55 mm in diameter, placed horizontally. The tube is peculiar in that the initial level of air pressure in the high-pressure chamber coincides with the ambient pressure. The schematic of the shock tube with the locations of the holes for the pressure sensors is shown in Fig. 1 (linear dimensions in mm). The pressure sensors G1 and G2 were located opposite each other in the same cross-section of the tube to ensure that the processes and the obtained results were uniform in the circumferential direction.

Piezoelectric pressure sensors with a time constant of 10^{-4} s were used in the experiment. The signal from the sensors was amplified using cathode repeaters and fed to the ADC board, which worked as a multiplexer with a sampling frequency of 100 kHz per channel. The same regime of gas flow was maintained in the shock tube in all experiments by pumping the air out of the low pressure chamber (LPC) to a pressure lower than atmospheric by 10 times. The diaphragm separating the high pressure chamber (HPC) from the evacuated part of the shock tube was destroyed by a mechanical punch. The Mach number of the shock wave for the selected pressure ratio in the chambers of the shock tube was equal to 1.7.

Polyurethane particles of regular spherical shape were used to create a porous layer. The density of the material was 200 kg/m^3. Particles had different sizes, ranging from 2 to 3 mm. The thickness of the granular layer was 30 mm. The granular layer was located at equal distances from sensors G3 and G4 for the given series of experiments in the shock tube.

Different types of containers (depending on the purpose they were intended for) were constructed for holding the granular material in a horizontally arranged setup. To make the granulated layer indestructible, the container holding it consisted of a thin-walled metal support of a cylindrical shape and two meshes covering its end faces. To make the granular layer destructible, one of the meshes was replaced with tracing paper, which was easily destroyed by the shock wave. The longitudinal size of the container was 30 mm. The mesh was made of textile fabric and had a cell size of approximately 0.5×0.5 mm. The effect of the mesh and the paper on the wave structure was considered separately. Experiments were conducted in an empty tube and in a tube with empty containers, without a granular layer. We found that the influence of a container with two meshes does not exceed 15%, which is a small disturbance if the meshes are used to hold granular materials (see the section below).

The illustrations given below for the empty tube, the tube with an empty container, and different configurations with a granular layer correspond to one of the cases of initial data from the signals received from the sensors G1–G5 rather than an average value for the series of experiments. The trends observed in each series of experiments were fully reproducible and the results were obtained with the required repeatability.

Experiments without granular layer

The pressures here and in the graphs are given in relative units. The initial pressure in the low-pressure chamber was chosen for normalizing the function. Time was counted from the moment when the signal in the sensor G5 deviated from its initial level by a threshold value, i.e., when the sensor detected an incident shock wave.

Fig. 1. Schematic of experimental shock tube:
Pressure sensors G1–G5; high and low pressure chambers HPC and LPC, respectively; linear dimensions are given in mm

Fig. 2,*a* shows the pressure variations over time for sensors G1–G5 in the empty low-pressure chamber without a container and a granular layer. Each of the sensors detects two shock wave in the given time interval: a compression wave and a rarefaction wave. In particular, two abrupt changes in pressure to a level of 30 kPa and then to a level of 70 kPa correspond to the sensors detecting an incident shock wave and a shock wave reflected from the end of the low-pressure chamber. The decrease in pressure observed starting from the fourth millisecond corresponds to the rarefaction wave detected. The smooth increase in pressure above the level of 70 kPa preceding the rarefaction wave corresponds to a compression wave appearing in the interaction of the reflected shock wave with fragments of the contact surface.

The term 'contact surface' should be further clarified. If we use a simplified description for the structure of gas flow in the shock tube, the contact surface is represented as a plane separating the high and low pressure gases starting from the initial time. However, when air enters the low-pressure chamber, the final velocities of diaphragm fracture generate intense gas flow in both axial and radial directions. This leads, in addition to front bending with a jump in density and temperature, to partial mixing of air from different chambers of the shock tube. The reflected shock wave actually interacts with the region consisting of fragments of the contact surface in this case.

The gas pressure behind the incident and reflected shock waves (readings from sensors G1–G5) is in good agreement with

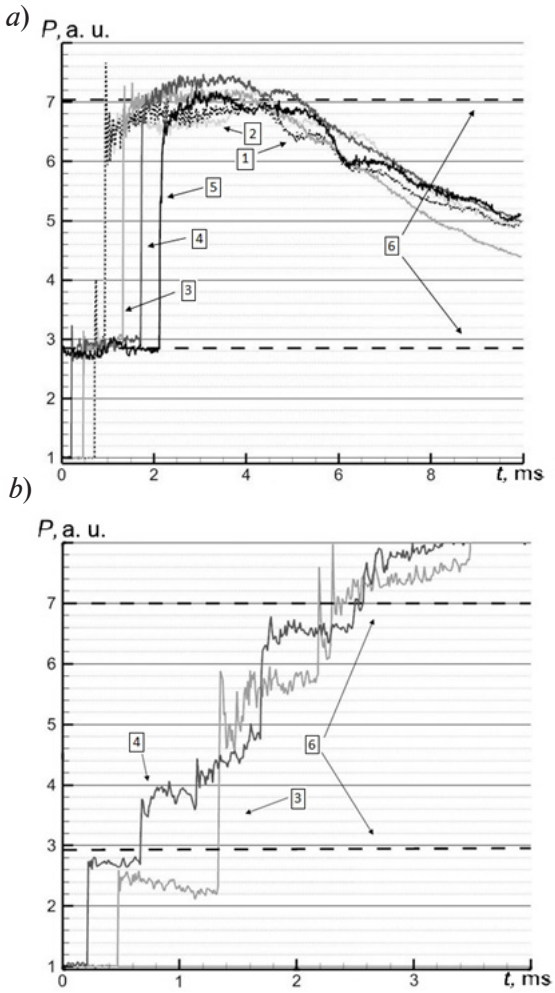

Fig. 2. Pressure variation over time in monitored points in low-pressure shock tube without container (*a*) and in same tube with empty container (*b*):
sensors *1–5*, analytical solutions *6*

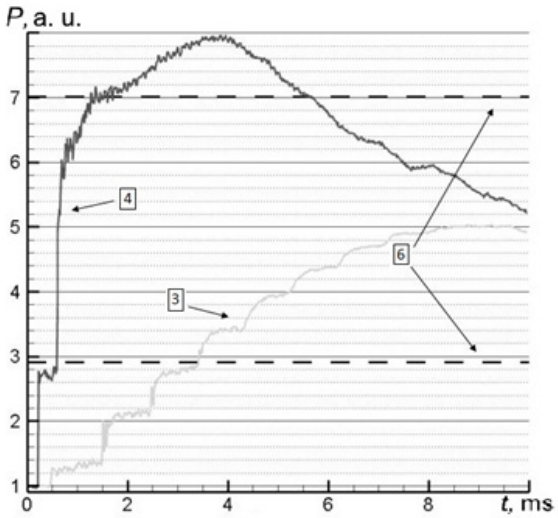

Fig. 3. Pressure variation over time in monitored points for sensors G3 and G4 for configuration with indestructible granular layer: sensors *3*, *4*, analytical solution *6*

the pressure calculated using the analytical dependence. The calculations were carried out based on elementary theory of a shock tube, using the solution of the Riemann problem on the decay of an arbitrary discontinuity [20]. Notably, the difference in the readings from the sensors G1 and G2 has the level of error of a single measurement for this problem statement when gas flow is known to be axially symmetric.

Fig. 2,*b* shows pressure variation over time for sensors G3 and G4 when an empty container is installed in the tube. It is somewhat difficult to interpret these results, since the wave structure is formed not only from the interaction of the shock wave with the end face of the low-pressure chamber and the contact surface but also from the effect of two meshes generating multiple wave reflections inside the empty container. However, it is still possible to determine the level of pressure in the incident shock wave and in the wave reflected from the end face of the LPC. The corresponding pressure levels in the empty tube act as reference values. The attenuation of the incident wave caused by the structural elements of the container can be assessed by the data for the first millisecond; comparing the values of the functions by the second millisecond, when the sensors G3 and G4 detect a shock wave reflected from the end face of the low-pressure chamber, the effect of the two meshes on pressure is no more than 15% of the measured quantity.

Experiments with stationary granular layer

Fig. 3 shows pressure variations over time for sensors G3 and G4, located on opposite sides of the granular layer that remained stationary during this experiment. The first pressure increase to a level of 30 kPa for sensor G4 corresponds to an incident shock wave. A reflected and transmitted shock wave appear in the interaction with the granular layer. Compared to reflection from the end face of the tube, the amplitude of the shock wave reflected from the surface of the granular layer is lower and detected by the sensor G4 at a level of 60–65 kPa. The same as in the tube without a granular layer, the reflected shock wave interacts with the elements of the contact surface. With the given position of the granular layer, the compression wave is reflected multiple times both from the contact surface and from the layer surface, leading to an increase in pressure to a higher level (80 kPa). The subsequent decrease in pressure for the sensor G4 is from a rarefaction wave passing.

Sensor G3 is located in the region between the porous layer and the end face of the low-pressure chamber. The readings from sensor G3 point to a wave structure in the form of a traveling wave reflected multiple times from both the surface of the granular layer and the end face of the low-pressure chamber. This is confirmed by the stepwise dependence of pressure on time. The intensity of the shock wave decays over time. The increase in pressure is associated with continuous flow of gas into the

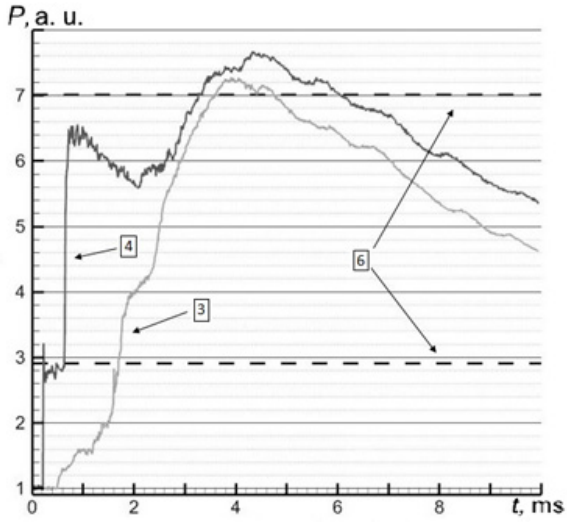

Fig. 4. Pressure variation over time
for sensors G3 and G4 for configuration with destructible granular layer:
sensors *3*, *4*, analytical solution *6*

near-edge region through the granular layer. The mechanism for supplying gas is based on seepage, i.e., mass flow of gas is a function of pressure drop across the thickness of the granular layer. As pressures on opposite sides of the granular layer are equalized and the pressure gradient is subsequently inverted, reverse seepage of gas occurs, that is, the gas in the granular layer changes the flow direction and moves away from the end face of the low-pressure chamber.

Experiments with destructible granular layer

Fig. 4 shows the pressure variations over time for sensors G3 and G4, located on different sides of the granular layer at the initial time. Let us point out some important aspects explaining the behavior of the curves given by in this figure. The granular layer is destroyed and turns into a cloud of particles as a result of interaction with the incident shock wave. There are two stages of particle dispersal in the cloud:

'instantaneous', associated with the front of the shock wave, when the particle gains momentum due to a shock wave passing a spherical particle;

'slow', associated with different velocities of the particle and the medium, that is, primarily with the Stokes drag.

The boundaries of the mobile porous layer have different velocities, i.e., the cloud not only moves toward the end face of the low-pressure chamber but also increases in size. As the cloud grows, the permeability of the mobile porous layer increases. Shock waves or rarefaction waves can still be reflected until the cloud has significantly increased in size from the boundaries of the porous layer.

Sensor G4, located in front of the granular layer, detects several processes. The scenario with sensor G4 detecting the incident and reflected shock waves completely coincides with the case of an indestructible granular layer at the initial stages. Sensor G4 detects a rarefaction wave at subsequent times. The intensity of the rarefaction wave depends on two processes. Firstly, the mass of gas passing through the granular layer increases. Secondly, the displaced boundary of the porous layer generates a rarefaction wave, similar to that behind a moving piston.

Readings from sensor G3 can be used to assess the pressure variations in the near-edge region. This process is more intense for the case when the granular layer is destroyed. Firstly, more gas enters the near-edge region due to increased permeability of the granular layer. Secondly, the size of the near-edge region with pure gas decreases as the particle cloud shifts. In this case, the boundary of the porous layer acts as a piston pushed into the region. A linear slope is observed on the pressure versus time curve after the second millisecond. At this point in time, sensor G3 is surrounded by a cloud of particles, i.e., is located in the region of two-phase flow. Both sensors G3 and G4 are located on one side of the particle cloud after two and a half milliseconds, and their readings reach the same level.

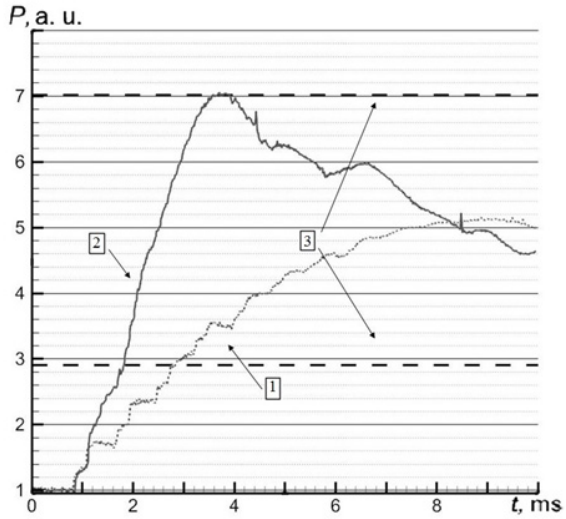

Fig. 5. Pressure variations over time for sensor G2 for both types of granular layer:
1, *2* correspond to indestructible and destructible layers, respectively;
3 is the analytical solution

Fig. 5 shows pressure variations over time for the two types of granular layer from the readings of sensor G2, which is closest to the end face of the tube.

The following patterns were observed for the waves. As follows from the behavior of the functions, the pressure in the near-edge region increases according to the same pattern in the first moments. This means that seepage laws differ little for the retained and destructible granular layers until the granules have gained a certain level of velocities. As noted above, the reason for subsequent discrepancies in the behavior of the pressure at the end face of the tube is that gas in the near-edge region is compressed by a cloud of particles in case of a destructible granular layer, in addition to an increase in pressure due to unsteady seepage. Using integral estimates, we can observe a decrease in the momentum of the impact on the end face of the shock tube in both cases, compared with the empty tube, and a decrease in absolute pressure in case of an indestructible granular layer.

Conclusion

We have carried out experiments on the interaction of a shock wave with a granular layer. We have established the main patterns in the behavior of unsteady seepage of gas through destructible granular layers and those preserving their structure. We have obtained the dependences of the dynamic effect of a passing shock wave on an impervious surface for two cases of porous layers.

The study was carried out within the framework of project 3.3314.2017/4.6 of State Task of the Ministry of Education and Science of the Russian Federation for 2017–2019.

REFERENCES

1. **Kitagawa K., Takayama K.,** Attenuation of shock waves propagating in polyurethane foams, Shock Waves. 15 (6) (2006) 437–445.

2. **Seitz W.M., Skews B.W.,** Effect of compressible foam properties on pressure amplification during shock wave impact, Shock Waves. 15 (3–4) (2006) 177–197.

3. **Boiko V.M., Kiselev V.P., Kiselev S.P., et al.,** Shock wave interaction with a cloud of particles, Shock Waves. 7 (5) (1997) 275–285.

4. **Rogue X., Rodriguez G., Haas J.F., Saurel R.,** Experimental and numerical investigation of the shock-induced fluidization of a particles bed, Shock Waves. 8 (1) (1998) 29–45.

5. **Barenblatt G.I., Entov V.M., Ryzhik V.M.,** Theory of nonstationary flow of liquids and gases in porous media [in Russian], Nedra, Moscow, 1972.

6. **Nigmatulin R.I.,** Dynamics of multiphase media, Vol. 1, Hemisphere, New York, 1990.

7. **Nigmatulin R.I.,** Dynamics of multiphase media, Vol. 2, Hemisphere, New York, 1990.

8. **Britan A., Elperin T., Igra O., Jiang J.P.,** Acceleration of a sphere behind planar shock waves, Experiments in Fluids. 20 (2) (1995) 84–90.

9. **Sun M., Saito T., Takayama K., Tanno H.,** Unsteady drag on a sphere by shock wave loading, Shock Waves. 14 (1–2) (2004) 3–9.

10. **Parmar M., Haselbacher A., Balachandar S.,** Modeling of the unsteady force for shock-particle interaction, Shock Waves. 19 (4) (2009) 317–329.

11. **Wagner J.L., Beresh S.J., Kearney S.P., et al.,** A multiphase shock tube for shock wave interactions with dense particle fields, Experiments in Fluids. 52 (6) (2012) 1507–1515.

12. **Ling Y., Wagner J.L., Beresh S.J., et al.,** Interaction of a planar shock wave with a dense particle curtain: Modeling and experiments, Physics of Fluids. 24 (1) (2012) 113301.

13. **Regele J.D., Rabinovitch J., Colonius T., Blanquart G.,** Unsteady effects in dense, high speed, particle laden flows, International Journal of Multiphase Flow. 61 (May) (2014) 1–13.

14. **Liu H., Guo Y,, Lin W.,** Simulation of shock-powder interaction using kinetic theory of granular flow, Powder Technology. 273 (March) (2015) 133–144.

15. **Houim R.W., Oran E.S.,** A multiphase model for compressible granular-gaseous flows: Formulation and initial tests, J. Fluid Mech. 789 (25 February) (2016) 166–220.

16. **Ben-Dor G., Britan A., Elperin T., et al.,** Experimental investigation of the interaction between weak shock waves and granular layers, Experiments in Fluids. 22 (6) (1997) 432–443.

17. **Ben-Dor G., Britan A., Elperin T., et al.,** Mechanism of compressive stress formation during weak shock waves impact with granular materials, Experiments in Fluids. 22 (6) (1997) 507–518.

18. **Zhu F., Chou C.C., Yang K.H.,** Shock enhancement effect of lightweight composite structures and materials, Composites. Part B: Engineering. 42 (5) (2011) 1202–1211.

19. **Utkin P.S.,** Nekotoryye vychislitelnyye aspekty modelirovaniya vzaimodeystviya udarnoy volny s oblakom chastits v ramkakh dvukhzhidkostnoy modeli [Some computational aspects of modeling the interaction of a shock wave with a cloud of particles in the terms of a two-fluid model], Goreniye i Vzryv [“Burning and Explosion”– Russian Journal]. 10 (3) (2017) 53 – 57.

20. **Godunov S.K., Zabrodin A.V., Ivanov M.Ya., et al.,** Rйsolution numйrique des problèmes multidimensionnels de la dinamique des gaz, Mir, Moscou, 1979.

Received 17.09.2019, accepted 05.11.2019.

THE AUTHORS

BULOVICH Sergei V.
Peter the Great St. Petersburg Polytechnic University
29 Politechnicheskaya St., St. Petersburg, 195251, Russian Federation
bulovic@yandex.ru

MASIUKEVICH Aleksei V.
The Ioffe Institute of the Russian Academy of Sciences
26 Polytekhnicheskaya St., St. Petersburg, 194021, Russian Federation
79313165906@yandex.ru

СПИСОК ЛИТЕРАТУРЫ

1. **Kitagawa K., Takayama K.** Attenuation of shock waves propagating in polyurethane foams // Shock Waves. 2006. Vol. 15. No. 6. Pp. 437–445.

2. **Seitz W.M., Skews B.W.** Effect of compressible foam properties on pressure amplification during shock wave impact // Shock Waves. 2006. Vol. 15. No. 3–4. Pp. 177–197.

3. **Boiko V.M., Kiselev V.P., Kiselev S.P., Papyrin A.N., Poplavsky S.V., Fomin V.M.** Shock wave interaction with a cloud of particles // Shock Waves. 1997. Vol. 7. No. 5. Pp. 275–285.

4. **Rogue X., Rodriguez G., Haas J.F., Saurel R.** Experimental and numerical investigation of the shock-induced fluidization of a particles bed // Shock Waves. 1998. Vol. 8. No. 1. Pp. 29–45.

5. **Баренблатт Г.И., Ентов В.М., Рыжик В.М.** Теория нестационарной фильтрации жидкости и газа. М.: «Недра», 288 .1972 с.

6. **Нигматулин Р.И.** Динамика многофазных сред. Ч. I. М.: Наука, 1987. 464 с.

7. **Нигматулин Р.И.** Динамика многофазных сред. Ч. II. М.: Наука, 1987. 360 с.

8. **Britan A., Elperin T., Igra O., Jiang J.P.** Acceleration of a sphere behind planar shock waves // Experiments in Fluids. 1995. Vol. 20. No. 2. Pp. 84–90.

9. **Sun M., Saito T., Takayama K., Tanno H.** Unsteady drag on a sphere by shock wave loading // Shock Waves. 2004. Vol. 14. No. 1–2. Pp. 3–9.

10. **Parmar M., Haselbacher A., Balachandar S.** Modeling of the unsteady force for shock-particle interaction // Shock Waves. 2009. Vol. 19. No. 4. Pp. 317–329.

11. **Wagner J.L., Beresh S.J., Kearney S.P., Trott W.M., Castaneda J.N., Pruett B.O., Baer M.R.** A multiphase shock tube for shock wave interactions with dense particle fields // Experiments in Fluids. 2012. Vol. 52. No. 6. Pp. 1507–1515.

12. **Ling Y., Wagner J.L., Beresh S.J., Kearney S.P., Balachandar S.** Interaction of a planar shock wave with a dense particle curtain: Modeling and experiments // Physics of Fluids. 2012. Vol. 24. No. 1. P. 113301.

13. **Regele J.D., Rabinovitch J., Colonius T., Blanquart G.** Unsteady effects in dense, high speed, particle laden flows // International Journal of Multiphase Flow. 2014. Vol. 61. May. Pp. 1–13.

14. **Liu H., Guo Y,, Lin W.** Simulation of shock-powder interaction using kinetic theory of granular flow // Powder Technology. 2015. Vol. 273. March. Pp. 133–144.

15. **Houim R.W., Oran E.S.** A multiphase model for compressible granular-gaseous flows: Formulation and initial tests // J. Fluid Mech. 2016. Vol. 789. 25 February. Pp. 166–220.

16. **Ben-Dor G., Britan A., Elperin T., O. Igra O., Jiang J.P.** Experimental investigation of the interaction between weak shock waves and granular layers // Experiments in Fluids. 1997. Vol. 22. No. 6. Pp. 432–443.

17. **Ben-Dor G., Britan A., Elperin T., Igra O., Jiang J.P.** Mechanism of compressive stress formation during weak shock waves impact with granular materials // Experiments in Fluids. 1997. Vol. 22. No. 6. Pp. 507–518.

18. **Zhu F., Chou C.C., Yang K.H.** Shock enhancement effect of lightweight composite structures and materials // Composites. Part B: Engineering. 2011. Vol. 42. No. 5. Pp. 1202–1211.

19. **Уткин П.С.** Некоторые вычислительные аспекты моделирования взаимодействия ударной волны с облаком частиц в рамках двухжидкостной модели // Горение и взрыв. 2017. Т. 3 № .10. С. 53–57.

20. **Годунов С.К., Забродин А.В., Иванов М.Я., Крайко А.Н., Прокопов Г.П.** Численное решение многомерных задач газовой динамики. М.: Наука, 400 .1976 с.

Статья поступила в редакцию 17.09.2019, принята к публикации 05.11.2019.

СВЕДЕНИЯ ОБ АВТОРАХ

БУЛОВИЧ Сергей Валерьевич – *кандидат физико-математических наук, доцент кафедры «Гидроаэродинамика, горение и теплообмен» Санкт-Петербургского политехнического университета Петра Великого.*

195251, Российская Федерация, г. Санкт-Петербург, Политехническая ул., 29
bulovic@yandex.ru

МАСЮКЕВИЧ Алексей Владимирович – *инженер Физико-технического института им. А.Ф. Иоффе РАН.*

194021, Российская Федерация, г. Санкт-Петербург, Политехническая ул., 26
79313165906@yandex.ru